Inaugural dissertation

for
obtaining the doctoral degree
of the
Combined Faculty of Mathematics, Engineering and
Natural Sciences
of the
Ruprecht - Karls - University
Heidelberg

Presented by

M.Sc. Steffen Klein

born in Tübingen

Oral examination:

19th of September 2023

In situ cryo-correlative light and electron tomography of influenza A virus entry and its inhibition by IFITM3

Referees:
Prof. Dr. med. Dr. h.c. Hans-Georg Kräusslich
Dr. Petr Chlanda

For Paul.

Summary

The innate immune system is the first wall of defense against many infectious pathogens, such as viruses or bacteria. The antiviral interferon-induced transmembrane protein 3 (IFITM3) is one of the key players against enveloped viruses like the influenza A virus. IFITM3 is localized in the endosomal-lysosomal system and is known to prevent viral cytoplasmic entry. Different hypotheses on the mode of action of IFITM3 were proposed, but the underlying molecular mechanism still needs to be fully understood. Here, I am using a combination of cryo-light microscopy and *in situ* cryo-electron tomography to study the antiviral function of IFITM3 within the natural cellular environment in the context of an influenza A virus infection. To visualize the antiviral actions of IFITM3, I established a novel cryo-correlative light and electron microscopy method. This novel approach allowed me to localize trapped influenza A virus particles in the endosomal-lysosomal system of an IFITM3-overexpressing human epithelial lung cell line A549, which allowed me to study them by cryo-electron tomography. Structural analysis of IFITM3-positive multivesicular bodies revealed that IFITM3 does not alter the ultrastructural morphology of the endosomal-lysosomal system and does not modulate the number of intraluminal vesicles (ILVs). These results contradict the 'fusion decoy hypothesis,' which suggests that an increased number of ILVs in the late endosomal lumen could redirect viral membrane fusion from the limiting late endosomal membrane to fusion with ILVs. High-resolution *in situ* cryo-electron tomography of influenza A virus particles within late endosomes revealed that IFITM3 traps influenza A virus particles in a hemifusion state at the limiting late endosomal membrane and ILVs. These findings support the previously formulated 'hemifusion stabilization' hypothesis as they are the first direct proof of IFITM3-mediated hemifusion stabilization within the natural cellular environment. Furthermore, ultrastructural characterization of the hemifusion sites revealed the post-fusion form of the viral fusion protein hemagglutinin (HA). Thus, IFITM3 does not inhibit low-pH triggered HA conformational changes, indicating that IFITM3 inhibits membrane fusion indirectly by modulating the membrane properties of the late endosomal-lysosomal system and thus stabilizing hemifusion.

Zusammenfassung

Das angeborene Immunsystem ist die erste Verteidigungslinie gegen viele infektiöse Krankheitserreger, wie Viren oder Bakterien. Das antivirale Protein 'Interferon induziertes Transmembranprotein 3' (IFITM3) spielt eine essenzielle Rolle gegen umhüllte Viren wie das Influenza A Virus. IFITM3 befindet sich im endosomalen-lysosomalen System der Zelle und verhindert den zytoplasmatischen Eintritt des Virus. Es wurden verschiedene Hypothesen über die Wirkungsweise von IFITM3 aufgestellt, aber der zugrunde liegende molekulare Mechanismus ist immer noch nicht verstanden. In dieser Arbeit nutze ich eine Kombination aus Kryo-Lichtmikroskopie und Kryo-Elektronentomographie, um die antivirale Funktion von IFITM3 innerhalb der natürlichen zellulären Umgebung und im Kontext einer Influenza A Virusinfektion zu untersuchen. Um die antivirale Aktivität von IFITM3 zu visualisieren, habe ich eine neue kryo-korrelative Licht- und Elektronenmikroskopie Methode entwickelt. Diese Entwicklung ermöglichte es mir, inhibierte Influenza A Viruspartikel im endosomalen-lysosomalen System von IFITM3-überexprimierenden menschlichen Lungenepithelzellen zu lokalisieren. Die Strukturanalyse von IFITM3-positiven multivesikulären Körpern ergab, dass IFITM3 die ultrastrukturelle Morphologie des endosomalen-lysosomalen Systems nicht verändert und die Anzahl der intraluminalen Vesikel gleichbleibt. Diese Ergebnisse widersprechen der 'Fusion-Decoy-Hypothese', die vermutet, dass eine erhöhte Anzahl von intraluminalen Vesikeln im späten endosomalen Lumen die virale Membranfusion von der endosomalen Membran zur Fusion mit ntraluminalen Vesikeln umleiten könnte. Hochauflösende Kryo-Elektronentomographie von Influenza A Viruspartikeln innerhalb von späten Endosomen zeigte, dass IFITM3 Influenza A Viruspartikel in einem Hemifusionszustand sowohl an der endosomalen Membran als auch an intraluminalen Vesikeln stabilisiert. Diese Ergebnisse liefern den direkten Nachweis, dass IFITM3 die virale Membranfusion von Influenza A Viruspartikeln in einem Hemifusionszustand stabilisiert. Diese Ergebnisse unterstützen die zuvor formulierte 'Hemifusions-Stabilisierungs'-Hypothese. Darüber hinaus offenbart die ultrastrukturelle Charakterisierung der Hemifusionsstellen die Post-Fusionsform des viralen Fusionsproteins Hämagglutinin. Dies zeigt, dass IFITM3 nicht die übliche Membranfusion-induzierende Rückfaltung von HA2 hemmt, was darauf hindeutet, dass IFITM3 die Membranfusion indirekt hemmt, indem es die Membraneigenschaften des späten endosomalen-lysosomalen Systems moduliert und somit die Hemifusion stabilisiert.

Acknowledgements

First, I want to thank Petr for the opportunity to work together on this exciting project and for his outstanding support throughout my Ph.D. Your positive attitude and enthusiasm for viruses and cryo-electron microscopy are inspiring. I am grateful for everything you taught me during long discussions and the many hours spent together at the Krios and Aquilos. Thanks for always allowing me to widen my scientific horizon during many scientific conferences and for your constant support of my personal development. I also want to thank my TAC members Hans-Georg and Thomas for their support and constructive feedback throughout the years. Many thanks also to Vibor for setting up the amazing microscopy facility at CIID and allowing me to be part of the IDIP team.

Of course, I want to thank all members of the Chlanda Lab for being such a fantastic group of people and creating a very positive, fun, and enjoyable atmosphere in the lab. Thanks, Sophie, for sharing many great moments in the lab, during conferences, and at the Boulderhaus. Thanks for the great discussions over many cups of coffee (or sometimes beer). I am grateful that we went through the journey of Ph.D. life together! I want to thank Niki for always being supportive. Moritz, thanks for the daily nerd talk and your absolute enthusiasm about everything related to programming! Thanks, Liv, Sarah, Melina, and Jana, for sharing this journey with me. During my Ph.D., I had the privilege to work with amazingly talented students, and I want to thank Bene and Carmen for being such great master students. I also want to thank all my supervised interns: Nina, Carmen, and Romy. I am grateful for the fruitful collaboration with Gonen and Fabio on the IFITM3 project.

Most importantly, I want to thank my family and friends who supported me my whole life. I want to thank my parents for their love and never-ending support and my brother Alex who is always there for me. I want to thank Claudia for our great friendship and journey since the first semester. I am indescribably grateful that Anna-Maria accompanied me all these years, supported me throughout all the ups and downs, and always believed in me. Thanks for all your love.

Danksagung

Zunächst möchte ich Petr für die Möglichkeit danken, an diesem spannendenden Projekt zusammenzuarbeiten, sowie für seine herausragende Unterstützung während meiner Promotion. Deine positive Einstellung und Begeisterung für Viren und Kryo-Elektronenmikroskopie sind inspirierend. Ich bin dankbar für alles, was du mir während langen Diskussionen und der vielen Stunden, die wir gemeinsam am Krios und Aquilos verbracht haben, beigebracht hast. Danke, dass du mir immer erlaubt hast, meinen wissenschaftlichen Horizont während vieler wissenschaftlicher Konferenzen zu erweitern, und für deine ständige Unterstützung meiner persönlichen Entwicklung. Ich möchte auch meinen TAC-Mitgliedern Hans-Georg und Thomas für ihre Unterstützung und konstruktives Feedback im Laufe der Jahre danken. Vielen Dank auch an Vibor, der die erstklassige Mikroskopie-Facility am CIID aufgebaut hat und mir erlaubt hat, Teil des IDIP-Teams zu sein. Natürlich möchte ich mich bei allen Mitgliedern des Chlanda Labors bedanken. Dafür, dass ihr eine so fantastische Gruppe von Menschen seid und eine so positive und angenehme Atmosphäre im Labor geschaffen habt. Danke, Sophie, dass wir viele großartige Momente teilen konnten, im Labor, während Konferenzen und im Boulderhaus. Danke für die großartigen Diskussionen bei vielen Tassen Kaffee (oder manchmal Bier). Ich bin dankbar, dass wir gemeinsam die Doktorandenzeit erlebt haben! Ich möchte Niki dafür danken, dass sie mich immer unterstützt hat. Moritz, danke für die täglichen Nerd-Gespräche und deine absolute Begeisterung für alles, was mit Programmierung zu tun hat! Danke, Liv, Sarah, Melina und Jana, dass ihr diese Reise mit mir geteilt habt. Während meiner Promotion hatte ich das Privileg, mit unglaublich talentierten Studenten zusammenzuarbeiten, und ich möchte Bene und Carmen dafür danken, dass sie großartige Masterstudenten waren. Ich möchte auch allen Praktikanten danken, die ich währen dieser Zeit betreuen durfte: Nina, Carmen und Romy. Ich bin dankbar für die großartige Zusammenarbeit mit Gonen und Fabio während des IFITM3 Projekts. Am wichtigsten ist es mir, meiner Familie und meinen Freunden zu danken, die mich mein ganzes Leben lang unterstützt haben. Ich möchte meinen Eltern für ihre Liebe und ihre unermüdliche Unterstützung danken und meinem Bruder Alex, der immer für mich da ist. Ich möchte Claudia für unsere großartige Freundschaft und die gemeinsame Reise seit dem ersten Semester danken. Ich bin unbeschreiblich dankbar, dass Anna-Maria mich all die Jahre begleitet hat, und mich während aller Höhen und Tiefen unterstützt und immer an mich geglaubt hat. Danke für deine Liebe.

Contents

List of Figures

Publications

In the context of this dissertation, I developed a novel *in situ* cryo-CLEM method, which was published in

Klein S, Wachsmuth-Melm M, Winter SL, Kolovou A & Chlanda P (2021). Cryo-correlative light and electron microscopy workflow for cryo-focused ion beam-milled adherent cells. *Methods Cell Biol* **162**, 273–302. DOI: 10.1016/bs.mcb.2020.12.009.

This method was further used to study the structure of lamellar bodies in human lung epithelial cells, which was published in

Klein S[1], Wimmer BH[1], Winter SL, Kolovou A, Laketa V & Chlanda P (2021). Post-correlation on-lamella cryo-CLEM reveals the membrane architecture of lamellar bodies. *Commun Biol*, 137. DOI: 10.1038/s42003-020-01567-z.

I further used *in situ* cryo-CLEM for the main project of this dissertation, which focused on the antiviral properties of IFITM3 in the context of an influenza A virus infection. This work was published in

Klein S[1], Golani G[1] Lolicato F[1], Lahr C, Beyer D, Herrmann A, Wachsmuth-Melm M, Reddmann N, Brecht R, Hosseinzadeh M, Kolovou A, Makroczyova J, Peterl S, Schorb M, Schwab Y, Brügger B, Nickel W, Schwarz US & Chlanda P. IFITM3 blocks influenza virus entry by sorting lipids and stabilizing hemifusion. *Cell Host Microbe* **31.4**. DOI: 10.1016/j.chom.2023.03.005.

In 2019 the world faced the challenge of a coronavirus pandemic caused by the severe acute respiratory syndrome coronavirus (SARS-CoV)-2. During this challenging time, I supported the Center of Infectious Diseases diagnostic department at the University Clinics of Heidelberg, where we developed a viral RNA extraction protocol for high-throughput diagnostics against SARS-CoV-2. This protocol was published in

Klein S[1], Müller TG[1], Khalid D, Sonntag-Buck V, Heuser AM, Glass B, Meurer M, Morales I, Schillak A, Freistaedter A, Ambiel I, Winter SL, Zimmermann L, Naumoska T, Bubeck F, Kirrmaier D, Ullrich S, Barreto Miranda I, Anders S, Grimm D,

Schnitzler P, Knop M, Kräusslich HG, Dao Thi VL, Börner K & Chlanda P (2020). SARS-CoV-2 RNA Extraction Using Magnetic Beads for Rapid Large-Scale Testing by RT-qPCR and RT-LAMP. *Viruses* **12.8**. DOI: 10.3390/v12080863.

Furthermore, we used *in situ* cryo-ET to structurally characterize the viral replication cycle of this novel SARS-CoV-2 in the native cellular environment. This study was published in

Klein S[1], Cortese M[1], Winter SL[1], Wachsmuth-Melm M, Neufeldt CJ, Cerikan B, Stanifer ML, Boulant S, Bartenschlager R & Chlanda P (2020). SARS-CoV-2 structure and replication characterized by *in situ* cryo-electron tomography. *Nat Commun* **11.1**, 5885. DOI: 10.1038/s41467-020-19619-7

This dissertation will not discuss the projects related to SARS-CoV-2 in detail, but a summary of both projects can be found in Appendices I and II.

[1]These authors contributed equally.

1 Introduction

1.1 Influenza A virus

1.1.1 *Orthomyxoviridae*

The family *Orthomyxoviridae* consists of negative-sense RNA viruses with a total of seven genera: *Alphainfluenzaviruses*, *Betainfluenzaviruses*, *Gammainfluenzaviruses*, and *Deltainfluenzaviruses* as well as *Quaranjaviruses*, *Thogotoviruses*, and *Isaviruses* (Schoch *et al.* 2020). The first *Alphainfluenzavirus* was discovered by W. Smith in 1933 (W Smith *et al.* 1933). *Alphainfluenzaviruses* cause seasonal influenza outbreaks and occasional pandemics with devastating public health consequences. *Betainfluenzaviruses* show a lower potential for pandemics due to the lack of a natural reservoir in animals. However, they are a high burden due to significant childhood morbidity and mortality (Zaraket *et al.* 2021). Like *Betainfluenzaviruses*, *Gammainfluenzaviruses* mainly infect humans and cause respiratory disease with cold-like symptoms in children (Matsuzaki *et al.* 2006). *Deltainfluenzaviruses* mainly infect animals, with known cases in swine (Hause, Ducatez, *et al.* 2013) and cattle (Hause, Collin, *et al.* 2014). The nomenclature of the influenza viruses follows a universal naming scheme: First, the type (A, B, C, D) is stated, followed by the place and year of isolation. Furthermore, the subtypes of the two viral surface glycoproteins hemagglutinin (HA) and neuraminidase (NA) are indicated. For *Alphainfluenzaviruses*, 18 HA and 11 NA subtypes have been identified (Tong *et al.*

2013). Most of these subtypes have been identified in wild aquatic birds, the most important natural reservoir of *Alphainfluenzaviruses*. Thus, at least 198 different HA-NA combinations are possible, although, in humans, only a small number of subtypes can be found. In the following section, the biology of influenza A viruses (IAVs) will be discussed in detail, focusing on the progression of influenza disease, the viral morphology, the genome organization, and the viral life cycle.

1.1.2 Influenza

IAV is the only species of the genus *Alphainfluenzavirus* and causes influenza in humans and animals, a respiratory disease with mild symptoms in the upper respiratory tract that usually include fever, headache, muscle pain, and sore throat (Krammer *et al.* 2018). A more severe disease outcome is possible when the lower respiratory tract is infected or if secondary bacterial infections lead to life-threatening pneumonia. Furthermore, nonrespiratory symptoms from infection of other organs, such as the heart or central nervous system, are possible (Sellers *et al.* 2017). The main risk factors for influenza are chronic diseases such as diabetes mellitus or chronic pulmonary conditions. Furthermore, people with weak immunity, primarily young children and older adults, show a high risk of severe influenza (Thompson *et al.* 2004). In addition, obesity was found to be an essential risk factor for severe disease progression with a higher risk of secondary infections (Van Kerkhove *et al.* 2011). Several genetic host factors have been identified, with gene mutations related to interferon (IFN) strongly impacting the infection's severity. The most important genes are interferon-induced transmembrane proteins (IFITMs) (Everitt *et al.* 2012), which are discussed in detail in Section 1.3.3.1. IAV shows a high mutation rate of approximately 1×10^{-3} to 1×10^{-8} substitutions per site per year (R Chen & Holmes 2006), which leads to a gradual accumulation of mutations mainly in the two surface glycoproteins HA and NA (Webster *et al.* 1992). This so-called 'antigenic drift' allows the virus to evade preexisting immunity, leading

to seasonal influenza outbreaks and the need to adapt the vaccination every year. To date, two circulating human IAV subtypes, H1N1 and H3N2, cause seasonal influenza, with three to five million severe cases yearly, causing 300 to 650 thousand deaths (Iuliano *et al.* 2018). In addition to antigenic drift, IAV can alter its genome by 'antigenic shift,' the reassortment of gene segments from different viral strains when co-infection of the same cell occurs. This reassortment can also occur between human and animal influenza strains. The main natural IAV reservoir is found in wild aquatic birds, where IAV infections are mostly asymptomatic. However, mutations in the viral surface glycoprotein HA can lead to lethal infections in birds (Perkins & Swayne 2002). In addition to birds, IAV can also infect swine, where infection can cause respiratory symptoms similar to those in humans. Apart from the intraspecies transmission between animals, zoonotic transmissions from animal to human were also observed. Antigenic shift events can lead to pandemics and often result in the extinction of any previously circulating strain. In the last century, four IAV pandemics occurred due to such events: The most devastating influenza pandemic, known as the 'Spanish flu' or 'great influenza,' occurred in 1918 with a death toll of over 40 million (Palese *et al.* 2006) and rendered the H1N1 subtype predominant. Further IAV pandemics occurred in 1957 (H2N2) and 1968 (H3N2). The latest pandemic occurred in 2009 (H1N1), commonly known as the 'swine flu.' This new H1N1 variant evolved by genetic reassortment of endemic human strains and at least two endemic swine strains (Christman *et al.* 2011).

To date, two main antiviral drugs against IAV are available. The first type is matrix protein 2 (M2) ion channel inhibitors, although most circulating strains developed resistance against them (Bright *et al.* 2005). Neuraminidase inhibitors are the second class and are currently the most widely used antiviral drug against IAV. However, annual vaccinations are the most effective countermeasure against IAV.

1.1.3 Virus morphology and genome organization

IAVs belong to the family *Orthomyxoviridae* and are single-stranded negative-sense RNA viruses with a segmented genome. Each of the eight RNA segments is complexed with viral nucleoproteins (NPs) and the RNA-dependent RNA polymerase (RDRP) complex, composed of polymerase subunit 1 (PB1), polymerase subunit 2 (PB2), and polymerase acidic protein (PA). This RNA-protein complex is called viral ribonucleoprotein (vRNP). Each viral RNA segment encodes for at least one viral protein. In total, there are eight structural proteins (PB1, PB2, PA, NP, M1, M2, HA, NA) that are packed into viral particles. In addition, several non-structural proteins (NSPs) are expressed in the host cell. They are important in modulating viral replication and evading the host cell's immune defense (Hao *et al.* 2020). To date, nine NSPs have been identified (NS1, NS2/NEP, NS3, PB1-F2, NS40, PB2-S1, PA-X, PA-N155, PA-N182). Most NSPs are transcribed by alternative splicing (PB2-S1, M42, NS2/NEP, NS3), others by alternative transcription initiation (PB1-N40, PA-N155, PA-N182), using alternative reading frames (PB1-F2) or by ribosomal frameshifting (PA-X). Table 1.1 summarizes all vRNP segments and corresponding viral proteins and their function.

IAVs are pleomorphic enveloped viruses (**Figure 1.1**). Just below the viral lipid bilayer, M1 forms a scaffolding layer that defines the viral shape (Peukes *et al.* 2020), which can range from spherical virus particles, like for A/WSN/1933(H1N1), with a diameter between 80 and 120 nm to long filamentous virus particles with a length of several micrometers (Kilbourne & Murphy 1960). The two membrane-anchored glycoproteins HA and NA are located on the viral surface, with HA being the predominant glycoprotein. NA usually forms clusters, and in the case of filamentous viruses, these clusters are found on one distal side of the viral particle. The eight vRNPs are localized in the viral lumen and interact directly with the scaffolding M1 layer (Elster *et al.* 1997). M2 forms an ion channel localized in the viral envelope (Manzoor *et al.* 2017).

Table 1.1: Overview of RNA segments and viral proteins of IAV.

Segment	Protein	Function	Transcription	Refernce
(1) PB2	PB2	mRNA cap recognition	canonical transcription	Guilligay *et al.* (2008)
	PB2-S1	RIG-I inhibition	alternative splicing	Yamayoshi *et al.* (2016)
(2) PB1	PB1	RNA polymerase activity	canonical transcription	M Kobayashi *et al.* (1996)
	PB1-F2	pro-apoptotic activity	+1 reading frame	W Chen *et al.* (2001)
	PB1-N40	unknown	alternative initiation	Wise, Foeglein, *et al.* (2009)
(3) PA	PA	endonuclease activity	canonical transcription	Dias *et al.* (2009)
	PA-X	repression of host gene expression	ribosomal frameshift	Jagger *et al.* (2012)
	PA-N155	increases replication activity	alternative initiation	Muramoto *et al.* (2013)
	PA-N182	increases replication activity	alternative initiation	Muramoto *et al.* (2013)
(4) HA	HA	receptor binding; membrane fusion	canonical transcription	Edinger *et al.* (2014)
(5) NP	NP	RNA binding; nuclear import	canonical transcription	Eisfeld *et al.* (2015)
(6) NA	NA	sialic acid cleavage; virus release	canonical transcription	McAuley *et al.* (2019)
(7) M	M1	scaffolding, virus release	canonical transcription	Peukes *et al.* (2020)
	M2	ion channel; virus uncoating	alternative splicing	Manzoor *et al.* (2017)
	M42	ion channel	alternative splicing	Wise, Hutchinson, *et al.* (2012)
(8) NS	NS1	antagonist to interferon response	canonical transcription	Hale *et al.* (2008)
	NS2/NEP	export of viral RNA from nucleus	alternative splicing	O'Neill *et al.* (1998)
	NS3	host adaption	alternative splicing	Selman *et al.* (2012)

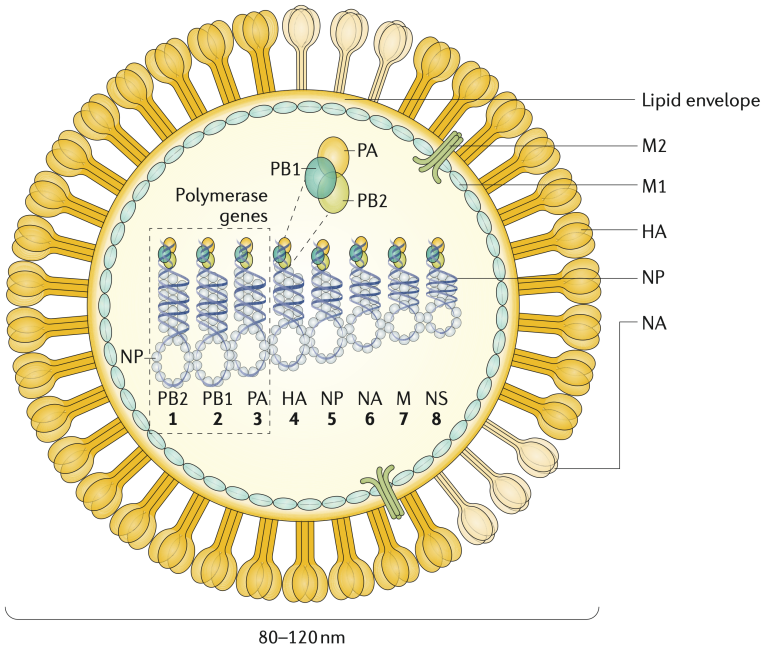

Figure 1.1: IAV morphology. All viral structural proteins of an IAV particle are schematically shown for a spherical virus. The two glycoproteins hemagglutinin (HA) and neuraminidase (NA) are located on the viral lipid envelope. Matrix protein 1 (M1) forms a scaffolding layer below the viral envelope. The ion channel matrix protein 2 (M2) spans the viral envelope. The eight viral ribonucleoproteins (vRNPs) are localized in the viral lumen and are composed of single-stranded viral RNA (blue strings), complexed with nucleoprotein (NP). The RNA-dependent RNA polymerase (RDRP) complex is located on one distal site of each vRNP and is composed of polymerase subunit 1 (PB1), polymerase subunit 2 (PB2) and polymerase acidic protein (PA). This figure is reprinted with permission from Springer Nature: Nature Reviews Disease Primers, 'Influenza' by Krammer *et al.* (2018) ©2018.

1.1.4 Replication cycle

In this section, all steps of the viral replication cycle of IAV will be discussed with a focus on viral entry, genome replication, viral protein expression, and finally, assembly and release of new virus particles. The replication cycle is also summarized in **Figure 1.2**.

1.1.4.1 Entry

The cell entry is the first step of the IAV replication cycle. The main cell types for viral entry are epithelial cells of the respiratory tract. The trimeric glycoprotein HA binds to sialic acids on the cell surface. Sialic acids are a family of sugar units with a backbone composed of nine carbon atoms. They are ubiquitously distributed throughout cell types and are generally found at the utmost ends of the glycan chains on the cell surface (Schauer 2000). HA mediated binding to sialic acids is specific to the glycosidic linkage and sialic acid type (Stencel-Baerenwald *et al.* 2014), which also defines the tropism of IAV subtypes. HA commonly binds to N-acetylneuraminic acid (Neu5Ac) with either an α2,3-link in case of avian strains or an α2,6-link in case of human IAV strains. α2,6 linked sialic acids are found primarily in the upper respiratory tract in humans (Yamada *et al.* 2006). The first barrier the virus has to overcome is the pulmonary surfactant in the respiratory tract, which is important to reduce the surface tension of the liquid-air interphase and is detrimental to breathing (Fessler & Summer 2016). In addition, the surfactant functions as a first mechanical barrier against various pathogens, such as IAV. There are various antimicrobial factors present in the surfactant. Surfactant protein A (SP-A), for example, is a sialylated glycoprotein that can bind to the viral HA and thus neutralize the virus, reducing the overall viral load of an infection (Benne *et al.* 1995). Virus particles eventually penetrate the pulmonary surfactant and bind to sialic acids on the surface of epithelial lung cells, upon which the bound viral particles are internalized by clathrin-mediated endocytosis (Matlin *et al.* 1981). This process is dynamin-dependent, essential for the final fission of the endocytosed vesicles (Roux *et al.* 2006). Clathrin-mediated endocytosis is limited to particles with a diameter smaller than 200 nm (Rejman *et al.* 2004). Thus it is only suitable for spherical IAV particles. As filamentous IAV particles can reach a length of several micrometers, filamentous virions are usually internalized by macropinocytosis (Vries *et al.* 2011).

After internalization, IAV particles are transported through the endosomal-lysosomal

system. The endosomal lumen is acidic in the late endosomal stage, with a pH between 5 and 6. This low pH environment induces structural rearrangements of the HA (Skehel, Bayley, *et al.* 1982). The pH stability of HA glycoproteins differs between IAV strains and determines the viral tropism (Krammer *et al.* 2018). The M2 ion channel in the viral envelope further allows protons and potassium ions to pass through, leading to acidification of the viral lumen, which weakens the interactions between the scaffolding matrix protein 1 (M1) layer and vRNPs and the M1 scaffolding layer eventually disassembles. This process is called priming (Stauffer *et al.* 2014). An extended HA intermediate is formed upon extensive refolding of HA, exposing the N-terminal fusion peptide, which can anchor to the endosomal membrane (Benton, Nans, *et al.* 2018). HA subsequently folds back to a more stable post-fusion state and thus provides energy to fuse the viral and endosomal membrane, finally forming a fusion pore that allows the release of the viral genome into the cytoplasm. Viral-induced fusion mechanisms are further discussed in Section 1.2.

After entering the cytoplasm, vRNPs are imported into the nucleus, which can take up to one hour (Dou *et al.* 2018). This process is mediated by the classical importin-α (IMPα)-importin-β1 (IMPβ1) nuclear import pathway (Eisfeld *et al.* 2015). IMPα binds to nuclear localization signal (NLS) motifs that are found in all viral proteins of the vRNP complex (NP, PB1, PB2, PA) (Eisfeld *et al.* 2015). These vRNP-IMPα complexes subsequently bind to IMPβ1. This complex finally docks to the nuclear pore complex (NPC), and vRNPs are actively transported into the nucleus.

1.1.4.2 Genome replication and viral gene expression

After nuclear import, vRNPs are distributed throughout the nucleus (Chou *et al.* 2013). Here, two distinct processes occur: First, viral messenger RNA (mRNA) is synthesized to induce translation in the cytoplasm to express viral proteins. Second, the viral genome is replicated to be incorporated into newly formed viral particles. The transcription of viral mRNA depends on the viral RDRP complex and the host

cell's RNA-polymerase II (RNAP II). As the viral RDRP cannot add a 5'-cap to RNA molecules (Plotch *et al.* 1978), it relies on a process called cap-snatching: PB2, which is part of the RDRP, binds to the 5'-cap of nascent host mRNA at the RNAP II (Guilligay *et al.* 2008) and the endonuclease PA subsequently cleaves the 5'-cap 10 – 15 basepairs downstream, and the viral transcription is initiated by the viral polymerase PB1. Polyadenylation of the nascent viral mRNA is achieved by PB1 stuttering (Poon *et al.* 1999). Viral mRNA is exported to the cytoplasm. Newly transcribed viral proteins are either reimported to the nucleus to accelerate viral genome replication or are transported to the plasma membrane for viral assembly and release.

Viral genome replication is driven by the viral polymerase PB1 which is part of the viral RDRP complex, PA and PB2 are not involved in the viral genome replication. The negative sense viral RNA (vRNA) is copied by PA into an intermediate positive sense complementary RNA (cRNA) by a primer-independent mechanism (Deng *et al.* 2006). This intermediate copy is further used by PA as a template to synthesize new negative sense vRNAs. As PA does not inherit any proof-reading activity, viral genome replication shows a high mutation rate of approximately 1×10^{-3} to 1×10^{-8} substitutions per site per year (R Chen & Holmes 2006), resulting in antigenic drift (Webster *et al.* 1992) and allows the virus to evade immunity which leads to yearly influenza epidemics. After genome replication, NPs, the three components of the RDRP complex (PA, PB1, PB2) and the newly synthesized vRNA form new vRNP complexes in the nucleus, which are in turn exported to the cytoplasm (Krischuns *et al.* 2021).

1.1.4.3 Assembly and release

New influenza A virus particles assemble and bud off the plasma membrane (Rossman & Lamb 2011). The viral membrane-bound structural proteins HA, NA, and M2 are synthesized at the rough endoplasmic reticulum (ER), where they are folded. HA form trimers, whereas NA and M2 form tetramers. The two viral surface proteins

HA and NA are glycosylated (Doms *et al.* 1993) at the ER. In the *cis*-Golgi network HA and M2 are further palmitoylated (Sugrue *et al.* 1990; Veit & MF Schmidt 1993). Finally, in the *trans*-Golgi network, HA is proteolytically cleaved by furin into HA1 and HA2 at the multibasic cleavage site. This priming is essential for a functional membrane fusion activity of HA. The viral proteins are subsequently transported to the plasma membrane. HA and NA cluster on lipid drafts, where viral assembly takes place (Barman *et al.* 2001). vRNPs are trafficked via recycling endosomes to the plasma membrane (Vale-Costa & Amorim 2017). A bundle of the eight vRNPs is formed in liquid organelles at ER exit sites, where RNA-RNA interactions between individual vRNPs stabilize the bundle (Alenquer *et al.* 2019). These vRNP bundles and the other structural viral proteins (M1, M2, NA, HA) form new viral particles at the plasma membrane, where M2 mediates membrane scission (Rossman, Jing, *et al.* 2010). The proteolytic activity of NA prevents the binding of nascent viral particles to sialic acid residues of the host cells, allowing for an efficient release of virions (McAuley *et al.* 2019).

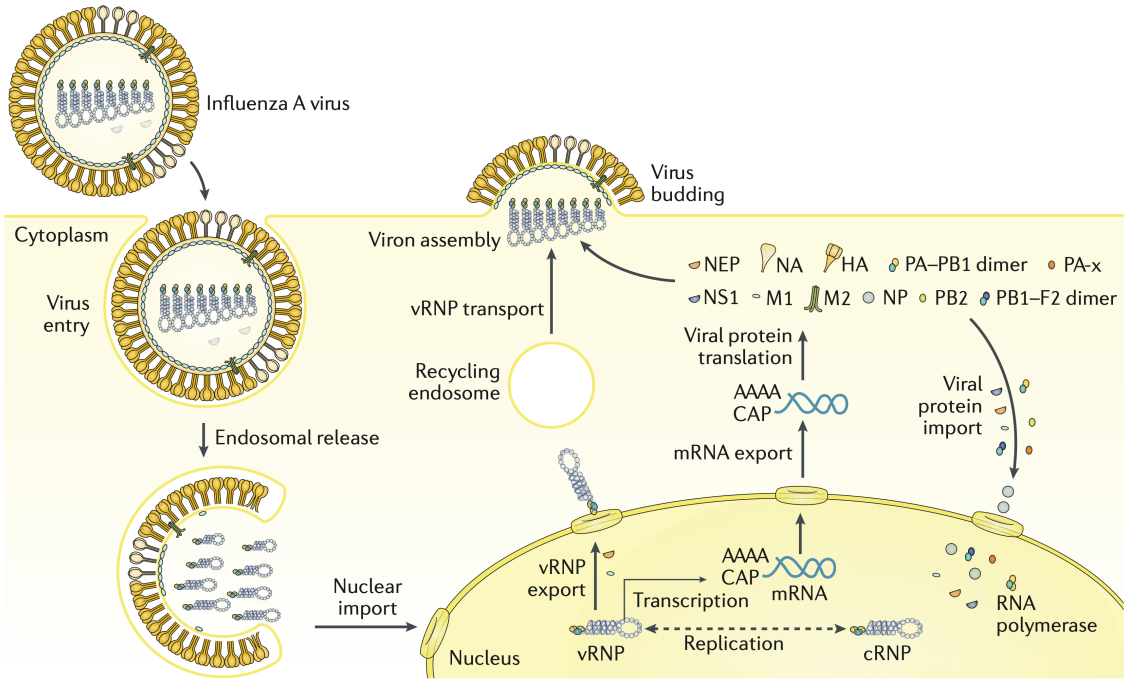

Figure 1.2: IAV replication cycle. IAV enters the cell by clathrin-mediated endocytosis or macropinocytosis (*Virus entry*) and gets released in late endosomes by viral induces membrane fusion (*Endosomal release*). vRNPs get transported to NPCs and are imported into the nucleus (*Nuclear import*). Inside the nucleus, two processes take place: First, viral mRNA is generated and exported into the cytoplasm (*Transcription*). Secondly, the viral genome is replicated (*Replication*). Viral proteins are expressed in the cytoplasm (*Viral protein translation*) and either transported to the plasma membrane or reimported into the cytoplasm to accelerate viral genome replication and transcription. New vRNPs are formed and transported via recycling endosomes to the plasma membrane (*vRNP transport*). Finally, new viral particles form and are released at the plasma membrane (*Virus budding*). This figure is reprinted with permission from Springer Nature: Nature Reviews Disease Primers, 'Influenza' by Krammer *et al.* (2018) ©2018.

1.2 Viral membrane fusion

For enveloped viruses, one of the most decisive steps during viral entry is the fusion of the viral and cellular membrane, as it is essential to release the viral genome into the host cell's cytoplasm. Membrane fusion can occur either at the plasma membrane, like for human immunodeficiency viruses (HIVs) (B Chen 2019) or in

the endosomal-lysosomal system, like for IAVs or Ebolaviruses (EBOVs). Various mechanisms for viral membrane fusion evolved, although a fusion protein is always involved (White & Whittaker 2016). Viral fusion proteins of enveloped viruses are classified into three classes (I – III) based on their structure: Class I fusion proteins are mainly composed of α-helixes, whereas class II fusion proteins are primarily composed of β-sheets. Finally, class III fusion proteins show both α-helixes and β-sheets (Kielian 2014). Another fourth class of viral fusion proteins can be found in non-enveloped reoviruses, which trigger cell-cell fusion (Shmulevitz & Duncan 2000). Despite the striking structural difference, all viral fusion proteins function similarly, with distinct steps during the fusion process. In **Figure 1.3**, these individual steps are depicted schematically. Viral membrane fusion is highly regulated to ensure fusion activity only during viral entry. In general, this specificity is achieved by cellular triggers, which lead to the exposure of the fusion peptide. Typical triggers for viral fusion protein activation are binding to viral receptors, low pH environments like the endosomal-lysosomal system, or proteolytic cleavage. After the fusion peptide is exposed, it can bind to the host cell's target membrane, bringing the viral and host membrane in close proximity. For phospholipid bilayer distances below 20 Å, repulsive hydration forces prevent spontaneous membrane fusion (Rand & Parsegian 1989). This energy barrier is overcome by the mechanical work of the viral fusion protein, derived from the back folding of the fusion protein to a stable post-fusion state. This brings the two phospholipid bilayers close together, overcoming the repulsive hydration forces and allowing the membranes to form a hemifusion stalk (Chernomordik, Zimmerberg, *et al.* 2006). The hemifusion stalk further expands to a hemifusion diaphragm which subsequently transitions to a membrane pore due to mechanical stress in the diaphragm. The transitional state between the hemifusion diaphragm and complete pore formation is called 'flickering pore' (Chanturiya *et al.* 1997). Finally, the fusion pore expands until the viral genome can be released into the cytoplasm.

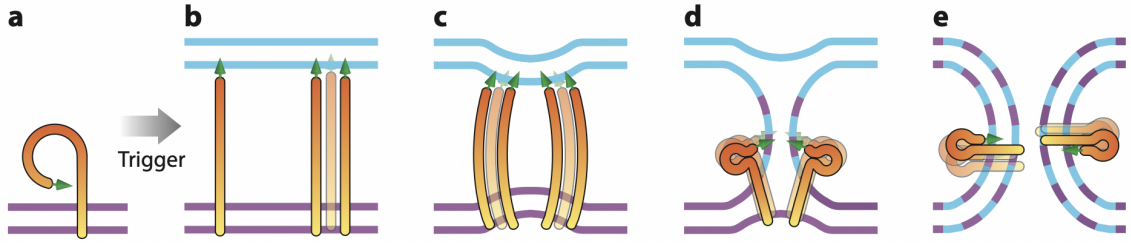

Figure 1.3: Schematic model of viral membrane fusion. **(a)** Viral fusion proteins (orange) are membrane-anchored and are located in the viral envelope (purple). The fusion peptide (green arrowhead) is inaccessible due to the tertiary structure of the viral fusion protein. **(b)** A cellular trigger, like a drop in pH, is necessary to expose the fusion peptide by unfolding the viral fusion protein. Once exposed, the fusion peptide binds to the cellular membrane (blue). **(c)** This interaction brings the cellular and viral membranes in close proximity. **(d)** The repulsive forces between the two membranes are overcome by a back-folding of the fusion protein to its post-fusion conformation. This irreversible structural rearrangement of the fusion protein provides energy to overcome the energy barrier by repulsive forces, forming a hemifusion site. In this unstable intermediate state, phospholipids of the outer leaflets of both membranes can mix. **(e)** Mechanical stress in the hemifusion site finally leads to the formation of a full fusion pore. This figure is reprinted with permission of Annual Reviews, Inc. from 'Mechanisms of Virus Membrane Fusion Proteins' by Kielian (2014) ©2014; permission conveyed through Copyright Clearance Center, Inc.

1.2.1 Hemagglutinin

HA is a class I viral fusion protein of IAV. The glycoprotein mediates membrane fusion of IAV particles with the endosomal membrane during viral entry (Skehel & Wiley 2000). HA is a 13.5 nm trimeric protein with two subunits, HA1 and HA2, linked by two disulfide bonds per subunit (Zhou *et al.* 2014). Thus, the trimeric protein, in total, consists of six subunits. HA1 mediates sialic-acid receptor binding, whereas HA2 is essential for viral membrane fusion and contains an amphipathic fusion peptide at the N-terminus (Brunner 1989). A schematic representation of the process of HA-mediated membrane fusion is shown in Figure 1.4. In neutral pH, the fusion peptide is not accessible as it is located in a hydrophobic pocket in the core of the HA trimer. After IAV cell entry by endocytosis or macropinocytosis, the low pH in late endosomes triggers structural rearrangements, exposing the fusion peptide

and leading to the dissociation of the HA1 subunit (Garcia *et al.* 2015). Although HA1 dissociates from HA2, HA1 stays flexibly attached through both disulfide bonds (Harrison 2015). Upon disassociation of HA1, an unstructured section of HA2, called B-loop, refolds into a coiled-coil confirmation, which results in an elongated HA2 intermediate (Stegmann *et al.* 1991). These structural rearrangements from the pre-fusion to the elongated form of HA were studied by single-particle cryo-electron microscope (EM) (Benton, Gamblin, *et al.* 2020), revealing intermediated dilated forms (**Figure 1.5**). With the fusion peptide located on the N-terminal domain of HA2, the fusion peptide binds to the endosomal membrane. A globular domain of HA2 unfolds and binds to a groove on the coiled-coil extended helix and induces the back folding of the extended form by the interaction of hydrophobic patches along HA2 (Boonstra *et al.* 2018). This back folding of HA2 is the energy-providing step during viral membrane fusion, which allows to overcome the repulsive hydration forces between the two membranes, leading to the formation of a hemifusion stalk. Finally, the fusion peptides and transmembrane domains of HA associate and form a 6-helix bundle, which facilitates pore formation by inducing defects to the hemifusion stalk (Lai & Freed 2015).

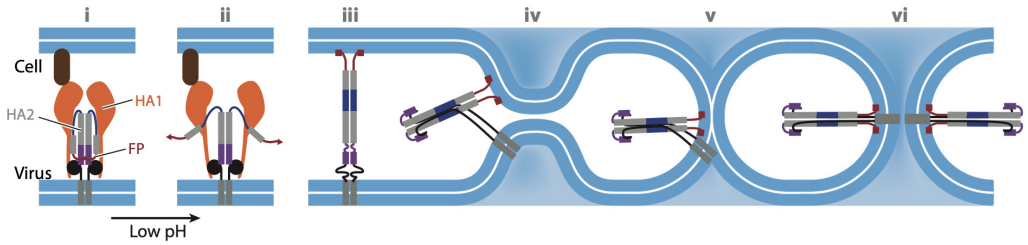

Figure 1.4: Schematic model of HA-induced membrane fusion. Schematic represenation of the canonical HA-mediated membrane fusion. For clarity, only two of the three HA subunits are shown. HA1 is not shown in steps *iii* – *vi*. Low pH triggers structural rearrangements, exposing the fusion peptide (FP, red), and disassociates HA1 (orange) (*ii*). The B-loop of HA2 (blue) rearranges to a coiled-coil form, which leads to the formation of an extended intermediate HA2. The extended form enables the fusion peptide to bind to the cellular membrane (*iii*). After fusion peptide binding, the hinge region of HA2 (purple) folds back and brings the viral and cellular membrane in close proximity (*iv*). Further unfolding of the globular domain of HA2 (black) allows to overcome the repulsive hydration forces, forming a hemifusion stalk (*v*). The fusion peptide and the transmembrane domain of HA2 (dark grey) further associate, forming a 6-helix bundle, and thus facilitate pore formation (*vi*). This figure is reproduced with permission of 'Annual Review,' from 'Hemagglutinin-Mediated Membrane Fusion: A Biophysical Perspective' by Boonstra *et al.* (2018); permission conveyed through Copyright Clearance Center, Inc."

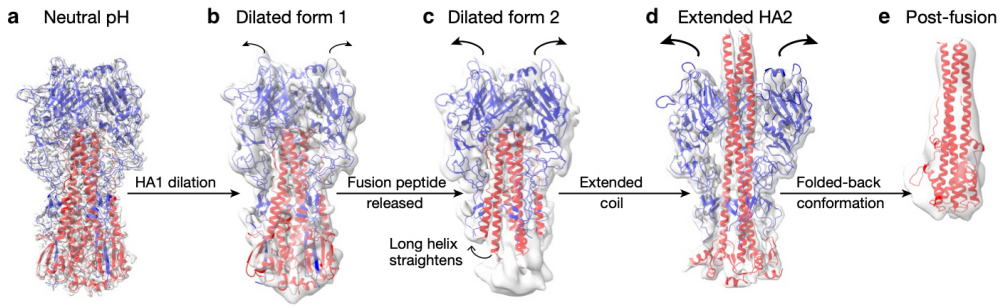

Figure 1.5: Strucutral rearrangements in HA. Different intermediate forms of HA were resolved by single particle cryo-EM. The resulting cryo-EM maps are shown in grey. Fitted models of HA1 (blue) and HA2 (red) are shown as ribbon representations. Purified HA were treated with low pH for 10 – 20 seconds to resolve an HA form indistinguishable from the neutral-pH state (**a**), intermediate dilated forms (**b and c**), and extended HA2 (**d**). To resolve the post-fusion HA structure, the sample was treated with 2-mercaptoethanol to break the disulfide bonds and subsequently incubated at low pH for 30 min (**e**). This figure is reproduced with permission from Springer Nature from 'Structural transitions in influenza haemagglutinin at membrane fusion pH' by Benton, Gamblin, *et al.* (2020)

1.3 Innate immunity

Host cell restriction factors are the first defense against a wide range of pathogens that enter the cell and are an essential barrier of the innate immune system. These diverse restriction factors target all steps of the pathogen life cycle, including entry, replication, and release. The innate immune response against IAV will be discussed in this section, with a focus on IFITM3, one of the essential restriction factors against IAV.

1.3.1 Pattern recognition receptors

All pathogens feature unique pathogen-associated molecular patterns (PAMPs), which can be recognized by cellular pattern recognition receptors (PRRs), which subsequently activate the secretion of type I IFN (IFN-α and IFN-β) (Takeuchi & Akira 2010). PAMPs can be any conserved molecular structure present in pathogens that are not present in the host cell and range from lipopolysaccharides (LPSs) in the outer membrane of gram-negative bacteria over cell wall components of fungi to viral single-stranded RNA (ssRNA) and glycoproteins (Cavaillon 2017).

During the IAV life cycle, different PRRs of the innate immune system can sense a virus infection. Toll-like receptor (TLR) 3 is constitutively expressed in human airway epithelial cells (AESs) and various other cell types and is localized in endosomes, where it recognizes IAV particles during viral entry (Guillot *et al.* 2005). It is known that TLR3 can sense viral double stranded RNA (dsRNA) (Bouteiller *et al.* 2005), but since IAV has a ssRNA genome, there might be another yet unknown mechanism in IAV recognition by TLR3. Two other PRRs of the TLR family which recognize viral ssRNA during an IAV infection are expressed by immune cells: TLR7 is mainly found in plasmacytoid dendritic cells (pDCs) (Diebold *et al.* 2004), whereas TLR8 mainly in macrophages and monocytes (Ablasser *et al.* 2009). Another important PRR family are RIG-I-like receptors (RLRs) which recognize viral RNA in the cytoplasm.

Retinoic acid-inducible gene I (RIG-I) is expressed in AESs, dendritic cells (DCs) and macrophages (Kato *et al.* 2005) and is known to recognizes 5'-triphosphates of vRNA in the cytoplasm (Pichlmair *et al.* 2006; Reikine *et al.* 2014). In the case of IAV, RIG-I seems to specifically recognizes unique secondary hairpin structures of IAV's genome (G Liu *et al.* 2015), which are formed by base pairing of the viral ssRNA (Dadonaite *et al.* 2019). Melanoma differentiation-associated gene (MDA)-5, another member of the RLR family, also recognizes viral RNA in the cytoplasm, although with another mechanism that targets mostly long, base-paired viral RNA (Dias Junior *et al.* 2019).

1.3.2 Interferon secretion

Upon activation, PRRs induce the expression of type I IFNs via different signaling pathways, as depicted in **Figure 1.6**. IFNs are a family of cytokines that are classified into three main groups (I – III) (Mazewski *et al.* 2020). Type I IFNs have a total of eight family members, although IFNα and IFNβ are predominant. IFNα is expressed in pDCs, which are a rare type of immune cells (Laustsen *et al.* 2021), but are able to express large quantities of IFNα upon a viral infection. In comparison to type I IFN, type II IFN has only one family member (IFNγ), which has mainly a regulatory role on the immune system (Tau & Rothman 1999). Type III IFNs have four members and show similar antiviral functions as type I IFN, but with lower inflammatory properties and slower kinetics (Lazear *et al.* 2019).

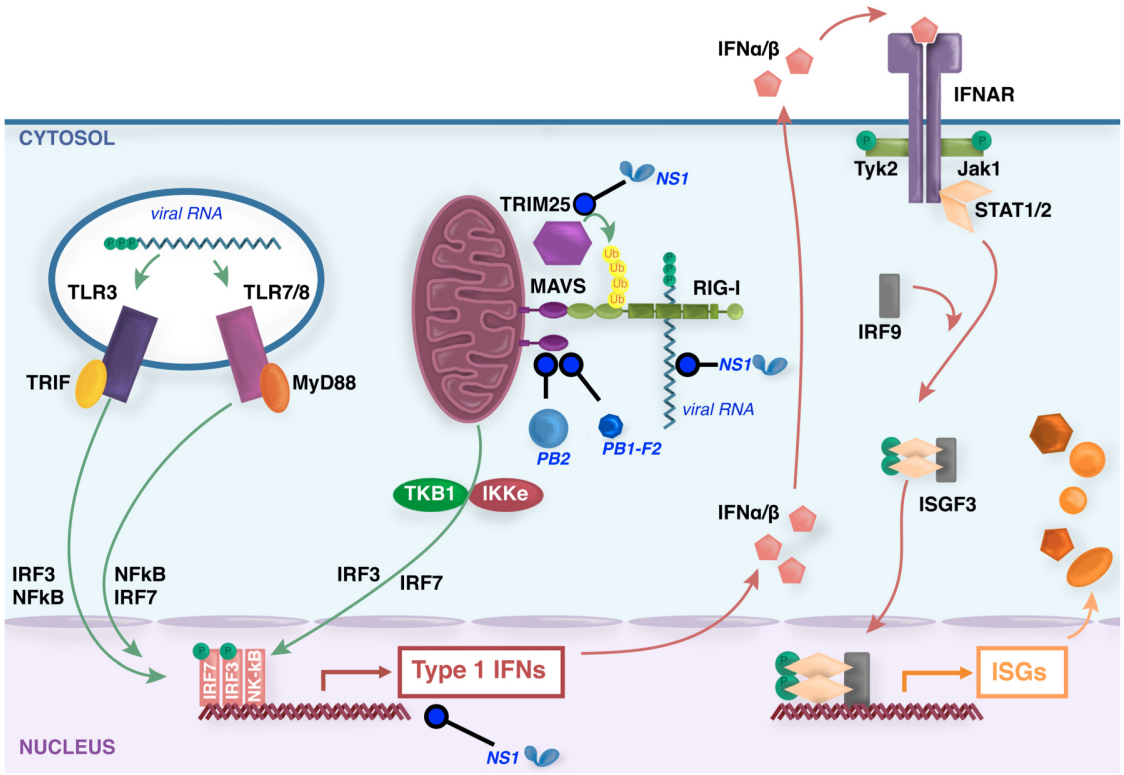

Figure 1.6: Overview of PRRs and interferon stimulation during IAV infection. PAMPs like the viral RNA are recognized by various PRRs like TLR3, TLR7/8, or RIG-I. Activated PRRs activate the expression of type I IFNs, which are secreted in the extracellular space. IFNs subsequently bind to interferon-α/β receptors (IFNARs) at the plasma membrane and induce through a signal cascade the expression of ISGs. This figure is reprinted under the Attribution 4.0 International (CC BY 4.0) license: 'Host Cell Restriction Factors that Limit Influenza A Infection' by Villalón-Letelier *et al.* (2017).

1.3.3 Interferon stimulated genes

Upon PRR induced IFN secretion, IFNs bind to cellular receptors to induce the expression of interferon stimulated genes (ISGs). The IFNAR is a ubiquitous, heteromeric membrane receptor, and upon type I IFN binding, the two subunits IFNAR1 and IFNAR2 are dimerized, which in turn induces the autophosphorylation of Janus kinase (JAK) 1 (Platanias 2005). Activated JAK1 further phosphorylates signal transducers and activators of transcription (STAT) 1 and STAT2, allowing their

dimerization. STAT1/2 form a complex with the interferon regulatory factor (IRF) 9. This complex is called interferon stimulated gene factor (ISGF) 3 and is translocated to the nucleus. Upon binding to interferon stimulated response elements (ISREs), the transcription of ISGs is induced (Lukhele *et al.* 2019). This pathway is known as the 'canonical type I IFN signaling pathway.' In addition, IFNAR can activate several other signaling pathways, summarized as 'non-canonical pathways.'

To date, hundreds of ISGs were identified (Schoggins 2019) with either a broad antiviral activity or specific activity against individual viral families. The main ISGs, which show antiviral properties during the IAV life cycle, are summarized in **Figure 1.7**. One of these ISGs is viperin, identified in 1997, showing antiviral properties against a broad spectrum of viruses (Zhu *et al.* 1997). Viperin was reported to disrupt lipid rafts at the plasma membrane and thus inhibit viral budding of IAV (Wang *et al.* 2007). A second antiviral mechanism was reported by which viperin can terminate the RNA synthesis of viral RDRPs (Rivera-Serrano *et al.* 2020). Another important example for an ISG is myxovirus-resistance protein (Mx) A, which is a GTPase protein (Martens & Howard 2006). The mouse analog Mx1 was first described in 1963, reporting antiviral properties against mycoviruses (Lindemann *et al.* 1963). MxA shows antiviral properties against various virus families. During the IAV life cycle, two distinct antiviral mechanisms were reported. First, it was shown that MxA blocks the transport of incoming vRNPs to the cytoplasm (Xiao *et al.* 2013), although other IFNs might be necessary as a cofactor. Second, an inhibitory effect on the amplification of vRNA from cRNA was reported (Zimmermann *et al.* 2011), likely by sequestering newly synthesized PB2 and NP in the cytoplasm. However, the exact mechanism is not completely understood yet (Zimmermann *et al.* 2011). Some of the most effective ISGs are part of the IFITM family, which will be discussed in detail in the following section.

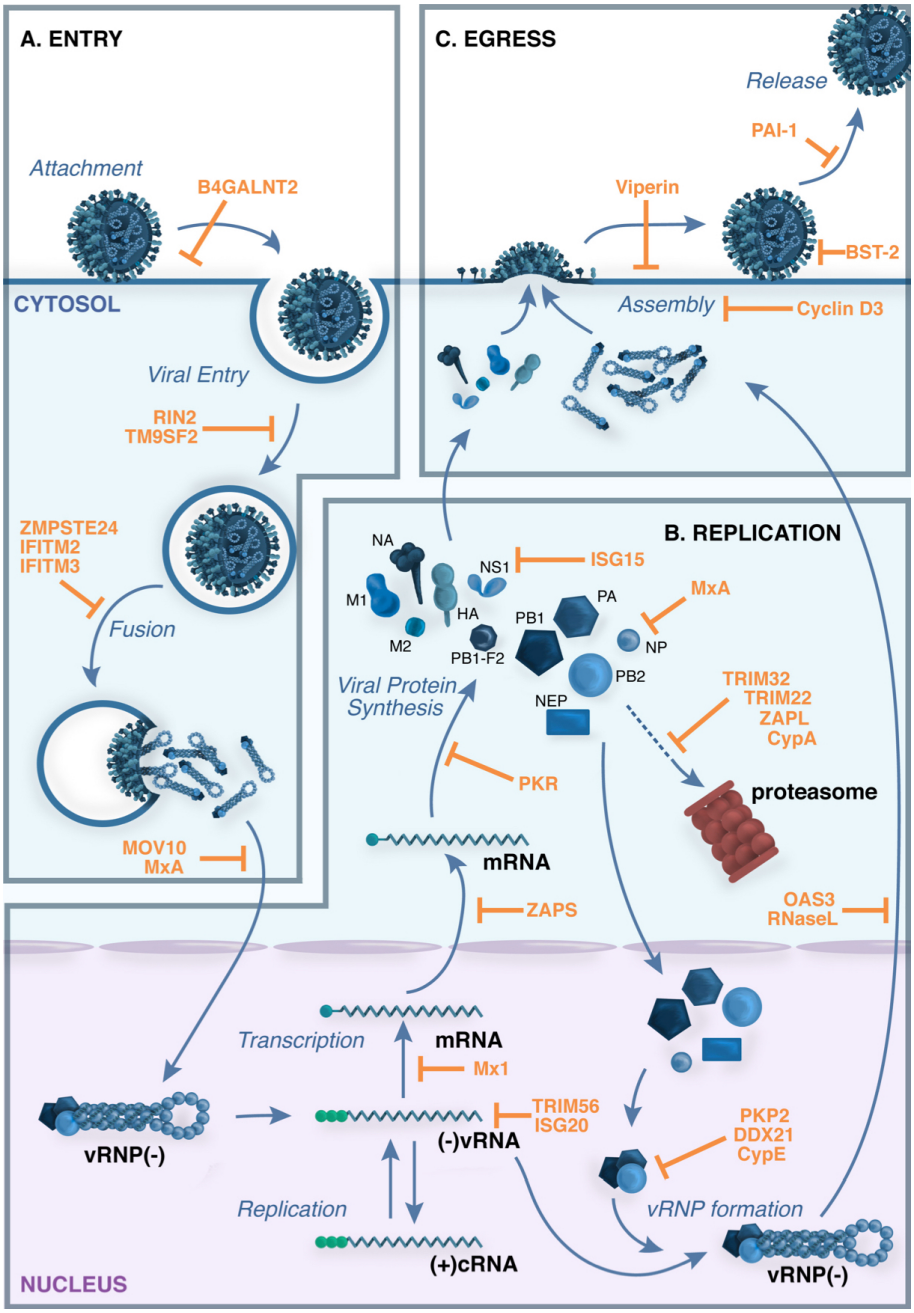

Figure 1.7: Overview of ISGs during the viral replication cycle of IAV. IFN induces the expression of a wide variety of ISGs, which interfere with every step of IAV's replication cycle starting from viral attachment, cell entry, membrane fusion, transcription, and translation in the nucleus, viral protein synthesis to assembly and release at the plasma membrane. The most important ISGs which affect IAV and their specific activity are indicated in orange. This figure is reprinted under the Attribution 4.0 International (CC BY 4.0) license: 'Host Cell Restriction Factors that Limit Influenza A Infection' by Villalón-Letelier *et al.* (2017).

1.3.3.1 Interferon-induced transmembrane protein 3

1.3.3.1.1 The IFITM protein family

IFITM is a gene family with a total of five family members (*ifitm1*, *ifitm2*, *ifitm3*, *ifitm5* and *ifitm10*) in humans, all encoded by chromosome 11 (Yánez *et al.* 2020). IFITM1–3 are known to play a significant role in the IFN-induced innate immune response and effectively inhibit viral entry by blocking membrane fusion (Bailey, Zhong, *et al.* 2014). IFITM5 and 10, on the other hand, have no known antiviral properties (Liao *et al.* 2019) and are also not induced by IFN although the name would suggest so. IFITMs are found in a wide variety of species ranging from reptiles, birds, and fish to mammals (Hickford *et al.* 2012). This broad prevalence indicates an essential and well-conserved function of IFITMs. IFITM1–3 are viral-restriction factors, with cellular localization at the plasma membrane (IFITM1) or in the endosomal-lysosomal system (IFITM2–3) (Diamond & Farzan 2013). The cellular location of the IFITM type also defines the specificity against different viruses. IFITM1, for example, is localized at the plasma membrane (SE Smith *et al.* 2019) and thus blocks viral entry of enveloped viruses that enter the cell by viral membrane fusion with the plasma membrane, such as HIV-1 (Lu *et al.* 2011) or several bunyaviruses like the La Crosse encephalitis virus (LACV) (Mudhasani *et al.* 2013). Enveloped viruses that enter the cell via membrane fusion in the endosomal-lysosomal system are inhibited by IFITM2 and 3. The specificity of IFITM depends on the fusion-inducing pH optimum of the virus. IAV or SARS-CoV, for example, fuse in early to late endosomes, where IFITM3 is preferentially localized. On the other hand, viruses with a lower pH optimum for membrane fusion, like EBOV or Marburg virus (MARV), fuse in later stages of the endosomal maturation process, and thus IFITM2 has a more potent antiviral effect, as it is localized in late endosomes and early lysosomes. The following section will discuss IFITM3 in more detail.

1.3.3.1.2 Impact of IFITM3 on influenza severity

Several single-nucleotide polymorphisms (SNPs) in the *ifitm3* gene were linked to

more severe IAV infections. SNP rs12252-C leads to the expression of a truncated form of IFITM3 (Everitt *et al.* 2012), whereas SNP rs34481144 results in lower mRNA levels and thus a lower IFITM3 expression (Allen *et al.* 2017). *ifitm3* knockout mice were found to be more susceptive for IAV infection and showed a more severe disease progression (Bailey, Huang, *et al.* 2012). As IFITM3 shows a broad antiviral effect, these SNPs also show a more severe disease outcome for various other viruses such as Dengue virus (DENV), EBOV, HIV and SARS-CoV-2 (Brass *et al.* 2009; Nikoloudis *et al.* 2020; Y Li *et al.* 2022).

1.3.3.1.3 IFITM3 structure

IFITM3 is a small transmembrane protein with a size of approximately 15 kDa. The protein structure of IFITM3 was not solved yet at a molecular resolution, but several studies indicate that IFITM3 shows a type II transmembrane topology with one transmembrane domain (TMD) and a cytoplasmic N-terminal domain (NTD) based on epitope-tagging (Bailey, Kondur, *et al.* 2013) and solution nuclear magnetic resonance (NMR) (Ling *et al.* 2016) (**Figure 1.8**). In addition to the TMD, two amphipathic domains were identified that localize at the cytosolic side of the protein and incorporated in the outer phospholipid monolayer of the endosomal membrane (Chesarino, Compton, *et al.* 2017). This combination of TMD and amphipathic domains is a conserved feature of the CD225 protein superfamily and was acquired from prokaryotes by horizontal gene transfer (Sällman Almén *et al.* 2012). Recent studies showed that the amphipathic domains are essential for the antiviral properties of IFITM3 (Chesarino, Compton, *et al.* 2017). IFITM3 was found to be post-translationally modified. Palmitoylation sites at Cys71, Cys72, and Cys105 were identified (Yount *et al.* 2010; Thinon *et al.* 2018), and it was shown that these post translational modifications (PTMs) are essential for the correct integration of the amphipathic helices by stabilizing the interaction with the phospholipid monolayer of the late endosomal membrane (Garst *et al.* 2021). Cys72 is highly conserved in IFITM3 of different species, which indicates the important function of

its palmitoylation for the function of IFITM3 (Benfield *et al.* 2020). In addition to palmitoylation, IFITM3 also has a phosphorylation site at Tyr20, which regulates cellular localization. In phosphorylated IFITM3, the endocytotic signal is blocked, which leads to preferential localization of IFITM3 at the plasma membrane. Dephosphorylation of Tyr20 activates the endocytosis signal, and IFITM3 is transported to the late endosome (Chesarino, McMichael, *et al.* 2014).

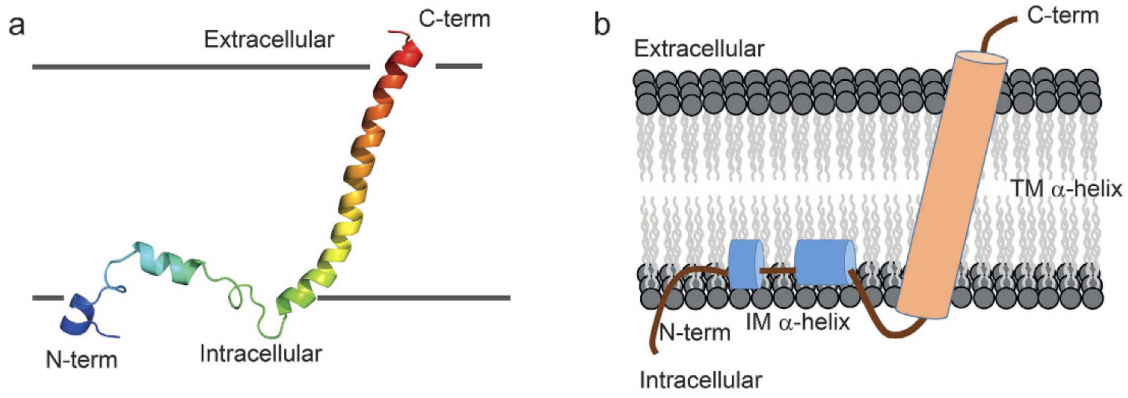

Figure 1.8: Proposed topology of IFITM3. (a) Structure of the TMD and the two amphipathic helix (AH) domains of IFITM3 based on solution NMR experiments. **(b)** Schematic representation of the proposed IFITM3 topology. A single α-helix spans the membrane and forms the TMD (orange). Two smaller α-helices are integrated into the cytoplasmic/intracellular site and form the AH domains (blue). The C-terminus faces the extracellular/late endosomal site, whereas the N-terminus faces the cytoplasmic/intracellular site. This figure is reprinted under the Attribution 4.0 International (CC BY 4.0) license: 'Combined approaches of EPR and NMR illustrate only one transmembrane helix in the human IFITM3' by Ling *et al.* (2016).

1.3.3.1.4 IFITM3 mode of action

It is widely accepted that IFITM3 blocks the release of the viral genome into the cytoplasm of the host cell, which was first reported by Brass *et al.* (2009). Further studies validated these results using different methods like fluorescence-microscopy-based lipid mixing experiments and β-lactamase (Blam)-based entry assays for IAV infection (Desai *et al.* 2014). However, the molecular mechanism which allows IFITM3 to block the viral genome release remains elusive. Several hypotheses on

the molecular mechanism were proposed, which will be discussed in more detail.

Hemifusion stabilization hypothesis

This model suggests that IFITM3 is not interacting with the first steps of the viral fusion machinery (see Section 1.2). During non-inhibitory circumstances, hemifusion is a short-lived non-stable intermediate stage during fusion pore formation. The 'hemifusion stabilization hypothesis' suggests that IFITM3 can inhibit the formation of complete fusion pores by stabilizing the hemifusion stage. This hypothesis is in line with the observed lipid exchange between the viral and endosomal membranes in IFITM3 expressing cells (Desai *et al.* 2014). As the fusion process is strongly dependent on the biophysical properties of the target membrane, hemifusion could be stabilized by IFITM3 if it could modulate the late endosomal membrane properties. One important lipid known to modulate the stiffness and curvature of membranes is cholesterol (Teissier & Pécheur 2007), and several studies showed that IFITM3 expression leads to altered cholesterol levels in late endosomes. It was demonstrated that IFITM3 prevents the interaction between VAMP-associated protein A (VAPA) and oxysterol-binding protein 1 (OSBP) and thus disrupts the cholesterol homeostasis of the cells and subsequently increases the late endosomal cholesterol levels (Amini-Bavil-Olyaee *et al.* 2013). Another study showed that an IFITM3-independent increase in late endosomal cholesterol levels is sufficient to restrict viral entry (Kühnl *et al.* 2018), further confirming the critical role of optimal cholesterol levels for viral membrane fusion in late endosomes. Recently, it was further shown by *in vitro* experiments that cholesterol directly binds to the AH domain of IFITM3 which is directly correlated with the depth of the AH domain insertion (Rahman, Datta, *et al.* 2022). Other direct or indirect ways on how IFITM3 might alter the membrane properties were proposed: IFITM3 might directly induce negative membrane curvature and membrane stiffness, as shown by *in vitro* experiments of reconstituted IFITM3 in giant unilamellar vesicles (GUVs) (Guo *et al.* 2021). Recently, the motif GxxxG was found to drive multimerization of IFITM3, which

might increase the membrane stiffness (Rahman, Coomer, *et al.* 2020). Another study indicates that IFITM3 might also be dependent on other cofactors to stabilize the hemifusion state (Fu *et al.* 2017). Still, no direct experimental proof exists that hemifusion is stabilized by IFITM3. Furthermore, this hypothesis does not give a molecular explanation of how the hemifusion state is stabilized.

Late endosome acidification hypothesis

In comparison to the 'hemifusion stabilization hypothesis' Wee *et al.* (2012) suggest that IFITM3 interferes earlier in the entry process by decreasing the pH of late endosomes through direct interaction with the proton pump vacuolar-type ATPase (v-ATPase) at the late endosomal membrane. This shift in pH could prevent the activity of the pH-sensitive viral fusion proteins and thus inhibit viral membrane fusion.

Fusion-decoy hypothesis

Two independent studies reported that IFITM3 overexpression increases the volume of acidic compartments found in the endosomal-lysosomal system (Feeley *et al.* 2011; Amini-Bavil-Olyaee *et al.* 2013). Based on these observations, Desai *et al.* (2014) formulated the hypothesis that an increased number of intraluminal vesicles (ILVs) in the late endosomal lumen could redirect viral membrane fusion from the limiting late endosomal membrane to fusion with ILVs. If IFITM3 would additionally block the back fusion of ILVs to the late endosomal membrane, as suggested by Amini-Bavil-Olyaee *et al.* (2013), this would effectively block the release of the viral genome into the cytoplasm. This hypothesis would also be compatible with the observed lipid mixing between endosome and virus (Desai *et al.* 2014).

In summary, various studies on the antiviral properties of IFITM3 proposed different modes of action on how IFITM3 can block the release of the viral genome. All these studies only provided indirect evidence of a certain mechanism or used *in vitro* systems. Thus, the molecular mechanism of the antiviral properties of IFITM3 remains undetermined.

1.4 Cryo-transmission electron microscopy of biological samples

1.4.1 The transmission electron microscope

In transmission electron microscopy (TEM) an image is created by the interaction of accelerated electrons with the sample. The basic principles of TEM are reviewed in detail by Williams & Carter (1996). The most important concepts will be discussed here. A TEM (**Figure 1.9**) generates electrons by an electron source like a tungsten filament, CeB_6 or LaB_6 crystals, or a field emission gun. An accelerator stack of anodes accelerates the electrons to generate a high-energy electron beam. The typical acceleration voltage in TEM is 100 – 300 kV and determines the velocity of the accelerated electrons. Electron microscopes need to be operated in a high vacuum to avoid the interaction of the accelerated electrons with molecules. Vacuum pumps maintain the high vacuum in the microscope column. Electromagnetic lenses can focus electrons, similar to optical lenses in light microscopy. A set of condenser lenses generate a parallel electron beam that travels through the sample. Electrons can pass the specimen without any interaction (unscattered electrons) or by interaction with the atoms of the specimen (elastic and inelastic scattering). The amount of scattering depends on the sample's thickness, density, and composition. Contrast formation by electron scattering is discussed in more detail in **Section 1.4.2**. After the parallel electron beam travels through the sample, the electron beam is collected by the objective lens and generates the first magnified image plane. In the back focal plane, the electron diffraction pattern can be observed. Here, the objective aperture is positioned, which blocks highly scattered electrons and thus increases contrast. A set of lenses further magnifies the image and finally projects it to an electron detector at the bottom of the microscope. Modern TEM systems are often composed of a more complex setup of lenses and incorporate corrections for aberration and astigmatism. In addition, electromagnetic deflection coils allow the modulation of

beam tilt and shift.

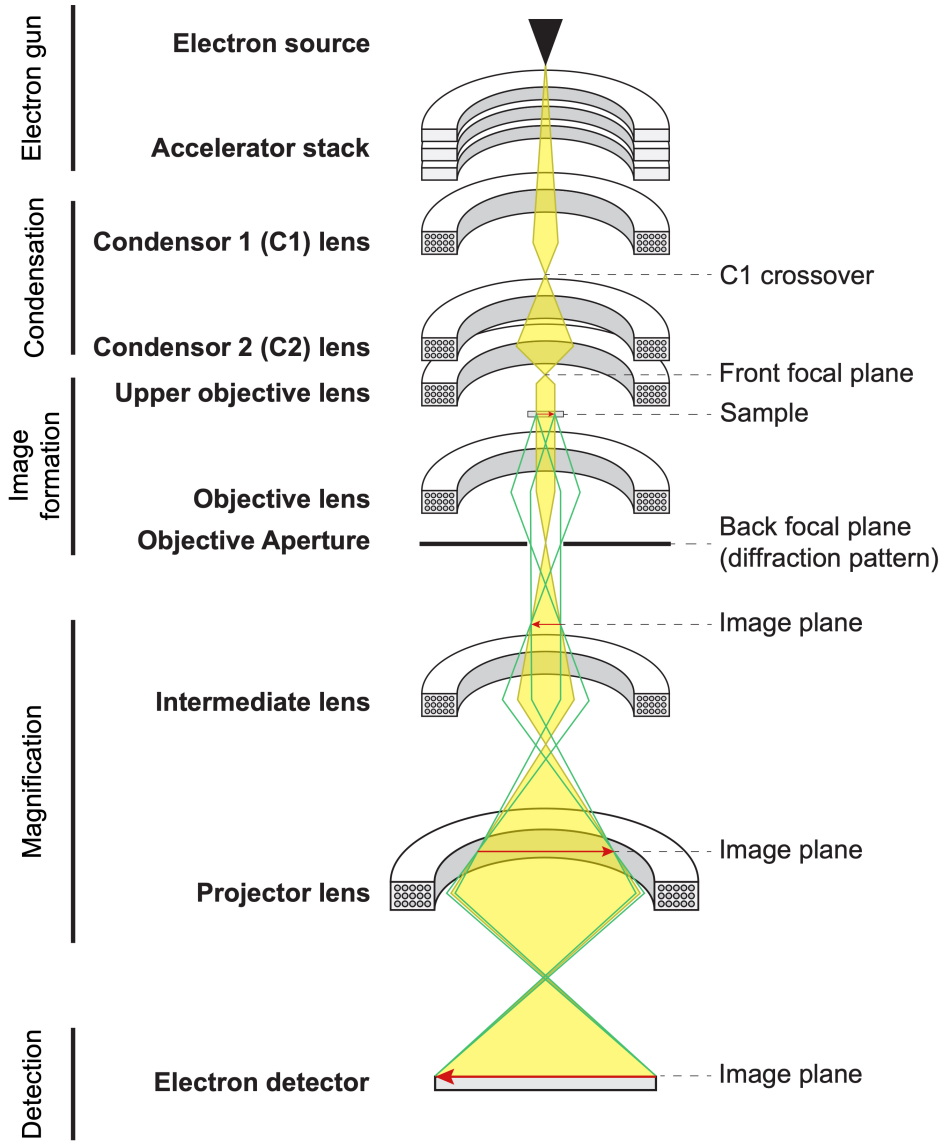

Figure 1.9: Schematic of a transmission electron microscope. An exemplary setup of a typical transmission electron microscope is shown. The unscattered electron beam path is shown in yellow, and two exemplary electron beam paths of scattered electrons are shown in green. Image planes are indicated with red arrows. The main optical elements are indicated: Electron source, accelerator stacks, different electromagnetic lenses, apertures, and the electron detector. This figure is based on Williams & Carter (1996) & Franken *et al.* (2020).

1.4.2 Contrast formation

1.4.2.1 Interaction of accelerated electrons with matter

Accelerated electrons interact with the specimen, which modulates the trajectory of the electrons in different ways (**Figure 1.10a**). The interaction of incident electrons with the sample in TEM was reviewed in detail by Orlova & Saibil (2011). Unscattered electrons do not interact with the sample, and thus its electron path is unaltered. Incident electrons can interact with the atoms of the sample, which scatters the electrons and thus can alter their trajectory. There are two main types of interactions: Inelastic and elastic scattering.

1.4.2.1.1 Inelastic scattering

Inelastic scattering occurs when an incident electron directly interacts with an electron of an atom in the sample. This interaction leads to a deflection of the incident electron, resulting in energy transfer from the incident electron to the sample. Since part of the energy is transferred, the incident electrons lose energy and thus velocity. The transferred energy causes the specimen's electron to move to a higher energy level. The excited electron drops down to its original energy state and releases the energy during this process by the emission of X-rays. If the transferred energy is high enough, electrons can even be ejected from the atom, resulting in the release of secondary electrons and ionization of the atom. These effects lead to undesired radiation damage to the sample and impair high-resolution imaging. Due to the lower velocity of the inelastically scattered electrons, they focus in a different plane compared to nonscattered or elastically scattered electrons, leading to a blurred image. Thus inelastically scattered electrons do not contribute to the formation of phase contrast (see section 1.4.2.3). Since inelastic scattering damages the sample, in TEM of biological samples, the negative effects are minimized by using thin samples and minimizing the total electron dose during image acquisition ("low dose mode"). Inelastically scattered electrons do not contribute to phase

contrast but introduce noise. Thus, energy filters are used to filter inelastically scattered electrons. This is achieved by selectively allowing only electrons of certain energies to reach the electron detector and thus filter inelastically scattered electrons (**Figure 1.10b**).

1.4.2.1.2 Elastic scattering

During elastic scattering, on the other hand, incident electrons do not directly interact with the electrons of an atom but are attracted by the positive charge of the atomic nucleus, which redirects the indecent electron without energy transfer, thus without altering the velocity of the electrons. Since no energy is transferred to the sample, elastic electron scattering is not damaging the specimen. In contrast to inelastically scattered electrons, elastically scattered electrons can be focused on the same plane as nonscattered electrons. At the back focal plane, elastically scattered electrons interfere with nonscattered electrons, creating phase contrast (**Section 1.4.2.3**).

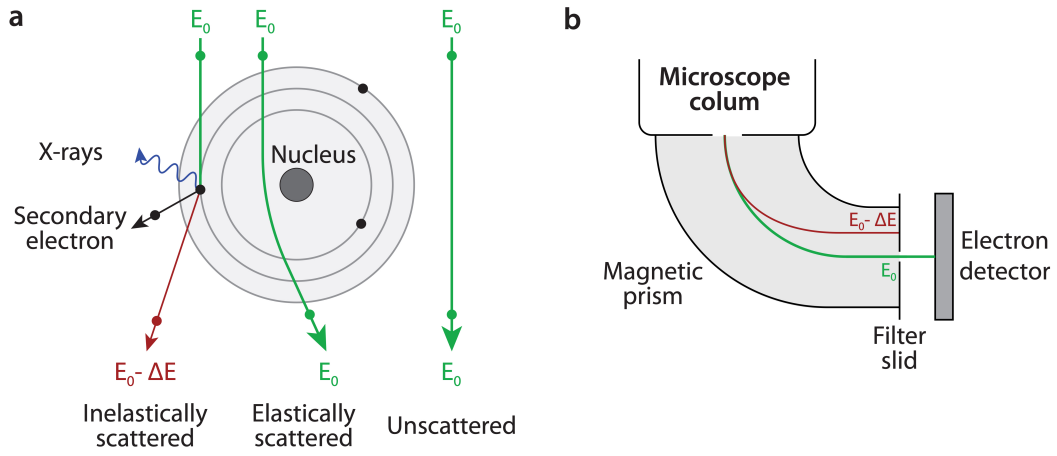

Figure 1.10: Schematic interaction of accelerated electrons with an atom. **a** Interaction of an accelerated electron with an atom by inelastic and elastic scattering. **b** Schematic depiction of an energy filter used in TEM. A magnetic prism bends incident electrons based on the energy. Zero-loss electrons (E_0) are bent less than electrons with lost energy due to inelastic scattering ($E_0 - \Delta E$). A tunable filter slit allows the selection of only zero-loss electrons. Panel **a** of this figure is based on Williams & Carter (1996) & Orlova & Saibil (2011), and panel **b** is based on Gubbens *et al.* (2010).

1.4.2.2 Amplitude contrast

Amplitude contrast is based on the concept that a certain amount of incident electrons are blocked by the specimen and do not reach the electron detector, resulting in a lower electron count for areas of the sample with high density at the focused image plane of the electron detector, resulting in contrast formation. This type of contrast can only be achieved for samples that generate highly scattered electrons, which can be filtered by apertures and energy filters and thus are not reaching the electron detector. Both inelastically and elastically scattered electrons contribute to amplitude contras. Since biological samples are mainly composed of light atoms (C, H, N, O), they only produce weak amplitude contrast. Thus, it is necessary to stain samples with electron-dense stain in order to be imaged using amplitude contrast. Typical biological samples are purified virus samples, negatively stained with an electron-dense solution like phosphotungstic acid (PTA). Chemically fixed cell sections are typically stained with uranyl acetate or lead citrate, introducing contrast to cellular features.

1.4.2.3 Phase contrast

In comparison to amplitude contrast, phase contrast does not rely on high-angle scattered electrons. This allows imaging of unstained biological samples. Phase contrast relies on the interference between low-angle scattered and nonscattered electrons to generate contrast. This is possible due to the wave-particle duality (Greiner 2001) of the accelerated electron, allowing them to be described as a particle and a wave at the same time. Elastically scattered electrons have a different beam path compared to nonscattered electrons (compare beam paths in **Figure1.9**) which allows the modulation of their phases independently. Scattered and nonscattered electron waves interfere at the back focal plane of the objective lens, which generates a diffraction pattern in the back focal plane. Interference of the two waves results in a lower amplitude of the resulting wave. This results in different intensities

detected at the image plane, creating contrast. In a theoretical optimal microscope setup with perfect focus, the phases of scattered and nonscattered electron waves are identical, leading to solely positive interference and, thus, no change in the amplitude of the resulting wave. Since electromagnetic lenses used in TEM typically show some amount of spherical aberration, the different paths of scattered and unscattered electrons lead to a relative phase shift of the two electron waves, which leads to interference. Since aberrations decrease the achievable resolution of a TEM system, in modern TEM systems, they are corrected by advanced optical setups, minimizing their effect on phase shift. Thus, the phase shift between elastically scattered and nonscattered electron waves is introduced deliberately by defocus or the use of phase plates like the Zernike phase plate (Danev & Nagayama 2001) or Volta phase plate (Fukuda *et al.* 2015).

1.4.2.4 Contrast transfer function

In TEM, the micrograph recorded by the electron detector is affected by the optical system of the microscope. The most important parameters to consider are lens aberrations and defocus. Thus, the recorded image can be described as a real image convoluted by a point spread function (PSF) specific to the optical system of the microscope (Heimowitz *et al.* 2020). This concept is equivalent to the optical transfer function (OTF) in light microscopy. Fourier transformation of the PSF describes the modulation in the frequency space and is called contrast transfer function (CTF). The CTF can be described as (Erickson & Klug 1971; Wade 1992; Zanetti *et al.* 2009):

$$CTF(f) = A(\sin(\pi\lambda f^2(\Delta z - 0.5\lambda^2 f^2 c_s)) + B\cos(\pi\lambda f^2(\Delta z - 0.5\lambda^2 f^2 c_s))) \quad (1.1)$$

with the spatial frequency (f), defocus-dependent envelope function (A), fraction of amplitude contrast (B), electron wavelength (λ), defocus (z), and spherical aberration c_s.

A theoretical optimal microscope without any aberrations would show a CTF function that is not modulating the signal for any frequency (**Figure 1.11a**, blue dotted curve). In reality, high-frequency information is dampened due to imperfect spatial and temporal coherence of the electron beam, which is described by the envelope function (**Figure 1.11a**, red dotted curve), resulting in an upper information limit. Furthermore, aberrations and defocus lead to wave interferences depending on the frequency, resulting in an oscillating sinusoidal CTF curve with zero crossings (**Figure 1.11a**, green curve). This results in concentrical rings visible in the Fourier-transformed micrographs, known as Thon rings (Thon 1966). At frequencies with zero crossings, the information content is lost and can not be recovered. Higher defocus results in the first zero crossing being shifted towards lower frequencies, resulting in a higher number of zero crossings for a given frequency range and, subsequently, higher information lost. Thus, image acquisition at lower defocus values preserves more information content with the compromise of reduced phase contrast.

Computational methods were developed to estimate the CTF from the electron power spectrum of the micrograph (Xiong *et al.* 2009). To that aim, variables of the CTF function (**Equation 1.1**) are estimated based on the microscope setup. The parameters are further refined by fitting the curve to the power spectrum of the micrograph. Higher contrast results in a better CTF estimation. The resulting CTF estimation allows partial recovery of the real signal from the convoluted micrograph by phase flipping (**Figure 1.11b**) and amplitude correction by Wiener-filtering (Penczek 2010). CTF correction is essential to recover high-frequency information of the micrographs. For cryo-electron tomography, more complex CTF correction methods are necessary due to the defocus gradient in tilted micrographs (Fernández *et al.* 2006; Turoňová, Schur, *et al.* 2017).

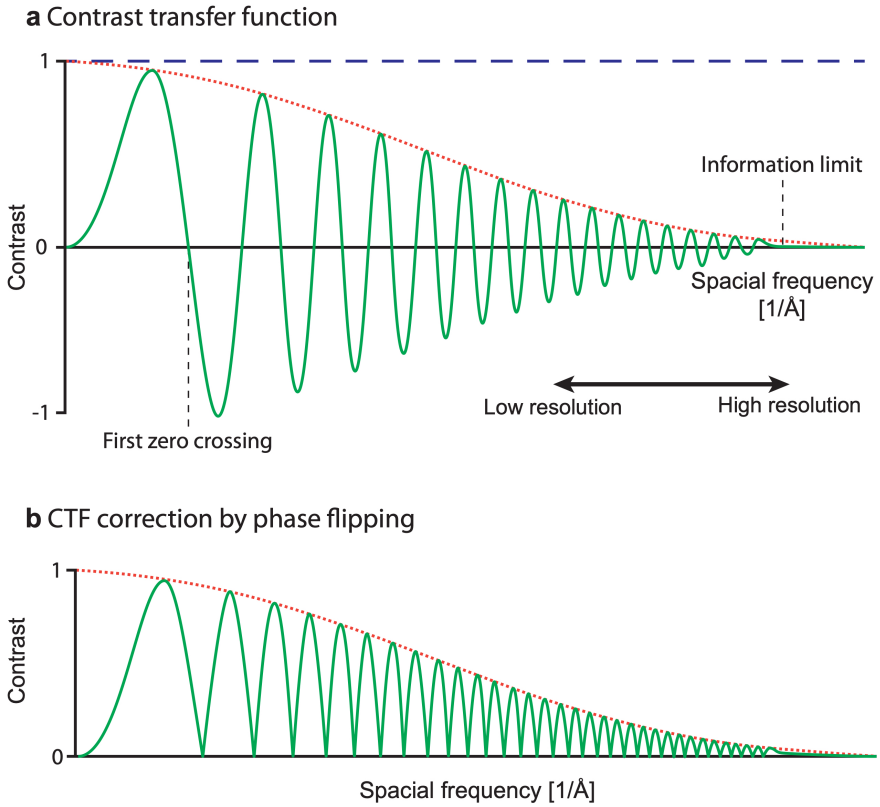

Figure 1.11: Contrast transfer function. a Plot showing a schematic CTF function. The blue dotted line indicates a CTF of a perfect theoretical microscope that does not modulate the signal. In reality, high-frequency information is dampened by the imperfect spatial and temporal coherence of the electron beam. This effect is described by the envelope function (red dotted curve). Spherical aberrations and defocus introduce oscillating positive and negative contrast dependent on the spatial frequency (green curve). **b** CTF correction by phase flipping: Sections of the uncorrected CTF with negative contrast transfer are multiplied by -1 to recover the correct phase. This figure is based on Costa *et al.* (2017).

1.4.3 *In situ* cryo-electron tomography (ET)

Cryo-EM revolutionized the field of structural biology due to advancements in sample preparation (Dubochet *et al.* 1988), the development of novel direct electron detectors (McMullan *et al.* 2009; X Li *et al.* 2013), and improvements in image processing (Frank *et al.* 1995; Frank 2009). Jacques Dubochet, Joachim Frank,

and Richard Henderson were awarded the Nobel Prize for Chemistry in 2017 for contributions to the development of cryo-EM. These breakthroughs lead to the so-called 'Resolution Revolution' (Kühlbrandt 2014), enabling atomic structure determination of macromolecular structures by single particle analysis (SPA) (Yip *et al.* 2020; Nakane *et al.* 2020). However, SPA is limited to *in vitro* structural analysis of purified samples. The development of cryo-ET further allowed the ultrastructural characterization of heterogenous structures like enveloped viruses and small prokaryotic cells. The introduction of cryo-focused ion beam (FIB) milling (Marko *et al.* 2007; Rigort *et al.* 2012) further enabled *in situ* cryo-ET of larger eukaryotic cells. Combined with subtomogram averaging (STA) analysis, these developments enable high-resolution structure determination within the natural cellular environment, bridging the gap between cellular and structural biology (Xue *et al.* 2022; PC Hoffmann *et al.* 2022). In this chapter, I will discuss the method of *in situ* cryo-ET in more detail with a focus on sample preparation, data acquisition, and reconstruction.

1.4.3.1 Preparation of biological samples for *in situ* cryo-ET

Biological samples for cryo-EM are physically fixed or vitrified, as developed by Dubochet *et al.* (1988). This method allows to vitrify the sample by rapid cooling, resulting in amorphous ice. This vitrification process avoids the formation of hexagonal and cubic ice during freezing and is essential for high-resolution cryo-EM, as cubic ice shows a high electron absorbance and causes electron diffraction. In addition, the formation of cubic ice can damage the biological sample. Fast freezing prevents ice crystal formation, and the water molecules are fixed in a metastable transient state, which is electron-transparent and preserves the ultrastructure of the biological sample. To achieve fast freezing, the sample is directly plunged into liquid ethane at a temperature just above its melting temperature of -182.8 °C. The high thermal conductivity of ethane allows rapid heat transfer from the sample, resulting in the formation of amorphous ice. This method is limited to thin biological samples

like monodisperse cells with a height of approximately 5 µm. For thicker samples like organoids or tissue, high pressure freezing (HPF) is an alternative vitrification method (Studer *et al.* 2008).

The electron beam of a typical 300 kV cryo-TEM can penetrate biological samples with a maximum thickness of approximately 500 nm (Baumeister 2005). Thinner samples further reduce the chance of inelastically scattered electrons and enable high-resolution structure determination. Thus, samples of 150 – 200 nm are typically used of *in situ* cryo-ET. Since monodisperse eukaryotic cells are too thick for direct imaging, methods for sample thinning were developed. The first method was based on the cryo-sectioning of vitrified samples using a diamond knife (Al-Amoudi *et al.* 2004). However, this method suffered from cutting artifacts like knife marks and sample compression. FIB milling, a method widely used in material science, was adapted to frozen-hydrated biological specimens to allow sample thinning without cutting artifacts (Marko *et al.* 2007; Rigort *et al.* 2012). To thin the sample, a focused ion beam, like Ga^+, is used to iteratively sputter off material from the specimen. During this process, the sample thinning is monitored by scanning electron microscopy (SEM) until a final thickness of 150 – 300 nm is reached. The resulting thin section of a cell is called lamella and allows for high-resolution cryo-ET imaging. Cryo-FIB milling is now routinely used for *in situ* cryo-ET sample preparation.

1.4.3.2 Cryo-ET data acquisition

High-resolution structure analysis of purified macromolecular complexes by SPA cryo-EM relies on 2D TEM projections with individual particles ideally in random orientations within a thin amorphous ice film. Averaging a large number of randomly oriented 2D projections and classification allows atomic structure determination (Boekema *et al.* 2009). Cryo-ET, on the other hand, utilizes a series of tilted projections, which allows the reconstruction of a three-dimensional volume by back

projection without the need for averaging. This dramatically widens the possibility of cryo-EM as it allows for structural characterization of heterogeneous samples like viruses, small prokaryotic cells, and cryo-FIB milled cell sections. Cryo-ET can also be utilized for purified macromolecular complexes with a preferred orientation, which inhibits structure determination by SPA. Since cryo-ET needs to image the same section of the sample at different angles, typically from +60° to -60°, it is essential to minimize the total accumulated dose to minimize radiation damage. It is also important to consider that the accumulated radiation damage will degrade high-frequency information, and thus the information content of the tilts decrease during tilt series acquisition. A second consideration is the increased travel length of the electrons at high tilts, decreasing the signal-to-noise ratio. Classical tilting schemes used for ET are continuous or bidirectional (**Figure 1.12a and b**). To maximize the transfer of high-resolution information during a tilt series in cryo-ET, a dose-symmetric tilting scheme was developed (Hagen *et al.* 2017) (**Figure 1.12c**). Here, the first acquired projections are symmetrically distributed around the zero-degree tilt to allow for image acquisition of the high-frequency containing low-angle tilts with minimum radiation damage.

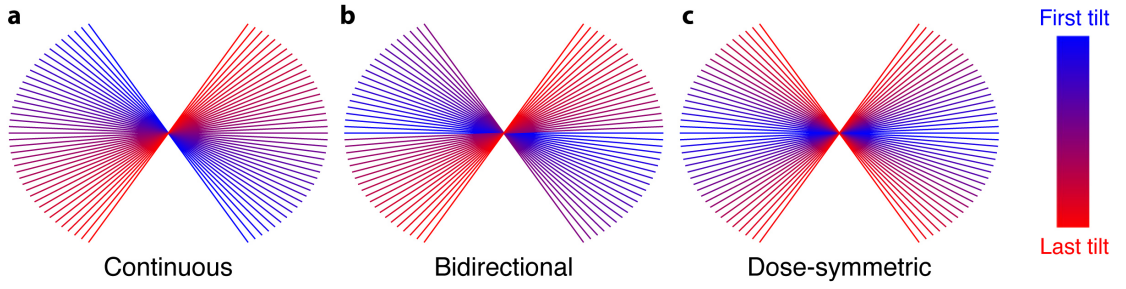

Figure 1.12: Different tilting schemes for ET. Overview of three different tilt acquisition schemes used in ET. The sequence of tilt acquisition is indicated by color, with blue for the first tilt and red for the last acquired tilt. This figure is a modified reprint under the Attribution 4.0 International (CC BY 4.0) license: 'Benchmarking tomographic acquisition schemes for high-resolution structural biology' by Turoňová, Hagen, *et al.* (2020).

1.4.3.3 Three-dimensional reconstruction and subtomogram averaging (STA)

Based on the Fourier Slice Theorem, individual tilts of the acquired tilt series (**Figure 1.13a and b**) can be combined to reconstruct a three-dimensional volume representation of the specimen (**Figure 1.13c**) (De Rosier & Klug 1968). This reconstructed volume is called a tomogram. Due to the geometry of the sample and the increasing beam path at high tilts, cryo-ET is limited to maximum tilting angles of 70°. The missing projections at higher tilts result in missing information in the frequency space of a reconstructed tomogram. This phenomenon is called a 'missing wedge' and results in an anisotropic resolution along the Z-axis of a reconstructed tomogram (Lučič *et al.* 2013). Different algorithms for tomogram reconstruction were developed, like weighted back projection (Radermacher 1992) and simultaneous iterative reconstruction technique (SIRT) (Gilbert 1972).

STA (**Figure 1.13d**) combines *in situ* cryo-ET with concepts of SPA and allows high-resolution structural analysis of macromolecular complexes within the native environmental environment of the cell. It allows the study of large multiprotein complexes like ribosomes with a close-atomic resolution (Xue *et al.* 2022). Furthermore, STA enables the study of the structural dynamics and interactions within the cellular environment. In comparison to SPA, the macromolecular structure of interest is not purified but instead localized within cellular tomograms by different computational methods like template matching by cross-correlation analysis or by the use of deep learning networks for particle picking (Teresa-Trueba *et al.* 2023; Rice *et al.* 2023). Iterative alignment of a large number of such extracted subvolumes increases the signal-to-noise ratio (SNR) and thus achieves higher resolution. In addition, the averaging completes the missing information of the frequency space due to limited tilting (missing wedge), resulting in an isotropic resolution of the average. There are different STA packages available with Dynamo (Castaño-Díez *et al.* 2012) and Relion (Zivanov *et al.* 2022).

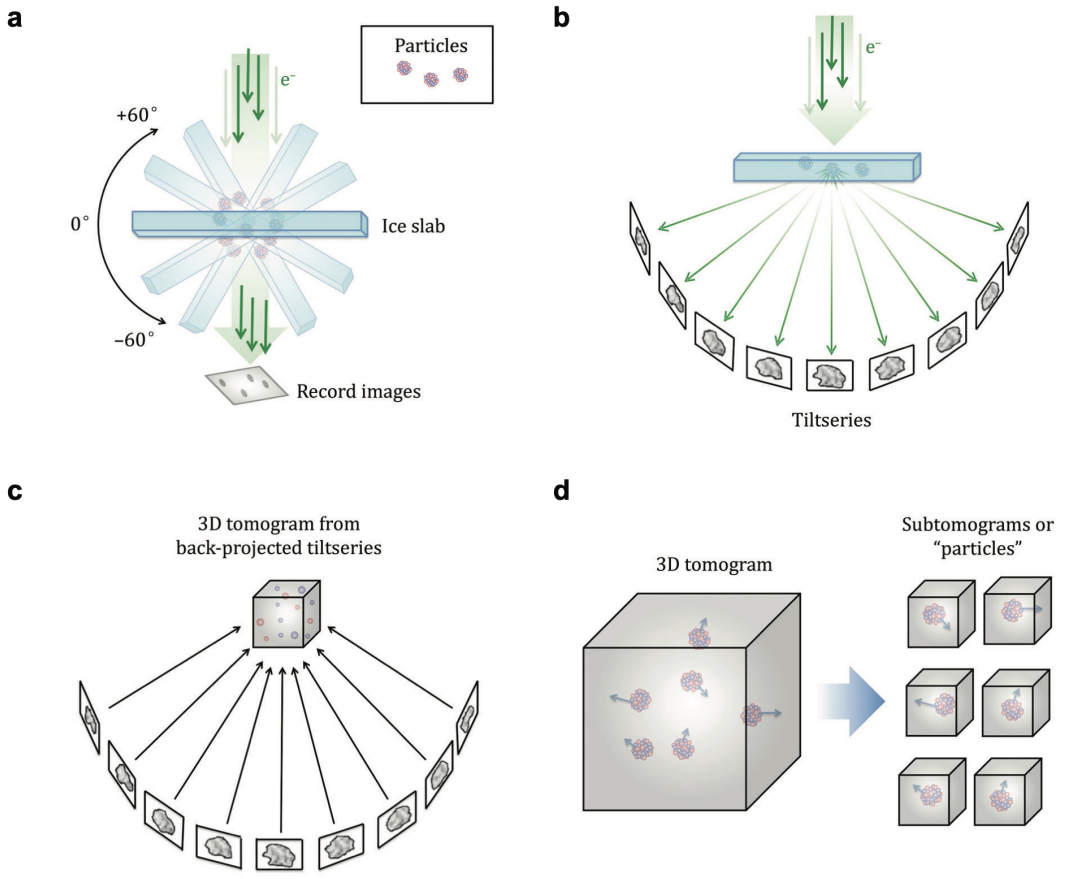

Figure 1.13: Schematic workflow for cryo-ET and STA. a A thin, vitrified sample like purified particles or thin sections of a cell (cryo-lamellae) are imaged by cryo-TEM in different angles, typically ranging from -60° to 60°, with a step size of 2 – 3°. **b** The acquired data is called a tilt series. **c** By different reconstruction methods, like weighted back-projection, a three-dimensional volume representation of the sample can be calculated. The limited tilting range during data acquisition results in a missing wedge in the frequency space of the reconstructed tomogram and results in anisotropic resolution. **d** STA analysis allows average extracted subtomograms of an identical structure, resulting in an isotropic, high-resolution average. This figure is a modified reprint under the Attribution 4.0 International (CC BY 4.0) license: 'The advent of structural biology in situ by single particle cryo-electron tomography' by Galaz-Montoya & Ludtke (2017).

2 Aims of this study

The first defense against infectious pathogens, such as viruses or bacteria, is orchestrated by the innate immune system. A critical step in viral infection is the release of the viral genome into the host cell's cytoplasm. An essential player in this innate immune response is the protein IFITM3, which notably inhibits the entry of many enveloped viruses, including IAV. Despite our knowledge of IFITM3's protective role, the precise molecular mechanisms underpinning its antiviral properties remain unknown, with various hypotheses proposed and discussed (see **Section 1.3.3.1.4**). This project aims to gain a deeper knowledge of the antiviral mechanism of IFITM3 on the ultrastructural level, utilizing *in situ* cryo-ET in the context of an IAV infection.

Visualizing the antiviral actions of IFITM3 within the dense native cellular environment of infected cells necessitates a complex methodological approach. I have therefore combined the imaging capabilities of cryo-light microscopy with the 3D structural information provided by *in situ* cryo-ET. To accomplish this, I have innovated a new cryo-CLEM method, alongside the requisite data processing workflows, during the first phase of my doctoral project. I have established the following specific aims:

- The implementation of an optimized data acquisition workflow that integrates cryo-light microscopy, cryo-FIB milling, and *in situ* cryo-ET.
- The establishment of a downstream data processing workflow to correlate all image modalities with the highest feasible precision.

- Assessment of the correlation precision and success rate of the newly developed method.

This development has enabled me, during the second phase of my Ph.D. project, to structurally characterize the antiviral properties of IFITM3, thereby fostering a deeper understanding of its molecular mechanisms. I have established the following specific aims:

- Establishment of the human epithelial lung cell line A549 stably overexpressing IFITM3 and rigorous validation of its antiviral properties.
- Characterization of the cellular localization of IFITM3 and its impact on cellular morphology.
- Development of fluorescently labeled IAV particles for utilization in *in situ* cryo-CLEM.
- Investigation of the IAV entry timeline to determine the optimal point for *in situ* cryo-CLEM analysis of infected cells.
- Identification of the localization of IAV particles in IFITM3 expressing cells and characterization of viral entry inhibition at the ultrastructural level.

3 Materials and Methods

3.1 Cell culture

The adenocarcinoma human alveolar basal epithelial cell line A549 is commonly used as a model system for IAV infections and is derived from carcinomatous lung tissue (Giard *et al.* 1973). A549 cells were obtained from American Type Culture Collection (ATCC) and cultured at 37 °C, 5 % CO_2 using Dulbecco's modified eagle medium (DMEM)-F12 supplemented with 10 % fetal calf serum (FCS) and 1 % penicillin/streptomycin (P/S). Human embryonic kidney cells expressing the SV40 large T-antigen (HEK293Ts) were obtained from ATCC and cultured at 37 °C, 5 % CO_2 using DMEM medium supplemented with GlutaMAX-I, 10 % FCS and 1 % P/S. HEK293T master cell bank cells (HEK293T-MCBs) were a gift from Dr. Marco Binder (DKFZ, Heidelberg, Germany) and cultured at 37 °C, 5 % CO_2 using DMEM medium supplemented with GlutaMAX-I, 10 % FCS and 1 % P/S. Madin-Darby canine kidney cells (MDCKs) were a gift from Prof. João Amorim (Instituto Gulbenkian de Ciência, Portugal) and cultured at 37 °C, 5 % CO_2 using DMEM-F12 medium supplemented with 10 % FCS and 1 % P/S.

3.2 Generation of stable A549-IFITM3 cell lines

As described in this section, I established a stable cell line using lentiviral transduction to characterize the effect of IFITM3 expressions in adenocarcinomic human alveolar basal epithelial cells (A549) cells. Romy Brecht and Nina Reddmann were lab rotation students in the lab and supported this process under my supervision.

3.2.1 Cloning

The gene sequence of IFITM3 from the complementary DNA (cDNA) entry vector pENTR221-clone3728-IFITM3 was transferred to a destination vector pWPI-IRES-Puro. For this, 150 ng of each the entry vector and the destination vector were combined, and 1 µl Gateway LR Clonase Enzyme Mix (ThermoFisher Scientific, Invitrogen) was added. The volume was topped up to 5 µl with TE buffer (10 mM Tris, 0.1 mM EDTA, pH 8). The cloning mix was incubated for 2 h at 25 °C. The cloning reaction mix was added to 50 µl *E. coli* cells (Stellar competent cells, Takara) and incubated for 30 min on ice. Cells were heat shocked for 45 sec at 42 °C, and subsequently, 450 µl SOC medium (ThermoFisher Scientific, Invitrogen) was added. Transduces cells were incubated for 1 h at 37 °C on a shaker at 180 rounds per minute (rpm) in a 14 ml round bottom tube. Cells were plated on a 1.5 % lysogeny broth (LB) agar plate with 50 $\mu g/ml$ ampicillin (AMP) and incubated for 12 h at 37 °C. Using the QIAprep Spin Miniprep Kit (QIAGEN), plasmids were purified following the manufacturer's protocol, and colonies were sequenced by Sanger sequencing (Microsynth) using the primer TATAGACAAACGCACACCG.

3.2.2 Lentiviral production

Lentiviruses were generated for cell transduction using a second-generation lentiviral packaging system comprised of an envelope plasmid (pCMV-VSV-G), packaging plasmid (psPAX2), and the cloned transfer plasmid (pWPI-IFITM3). 4×10^5 HEK293T-MCB cells per well were seeded in a 6-well plate. The next day, cells were transfected with the following transfection mix: 0.375 µg envelope plasmid, 0.75 µg packaging plasmid, 1.25 µg pIFITM3-transfer plasmid, 0.125 µg pAdVantage plasmid was added to a total of 250 µl Opti-MEM medium (ThermoFisher Scientific, Gibco). 7.5 µl TransIT-2020 (Mirus Bio) transfection reagent was added, and the transfection mix was incubated for 30 min. Next, the incubated transfection mix was added to the previously seeded cells. After 6 h, the virus-containing medium was replaced with fresh medium, and cells were incubated for 48 h. The supernatant, containing the lentivirus, was harvested, sterile-filtered using a 0.45 µCME filter (Roth), and stored at -80 °C.

3.2.3 Lentiviral transduction

For lentiviral transduction, 2×10^4 A549 cells were seeded in a 12-well plate. The next day, 350 µl lentivirus was added to each well. To increase the infection rate, 5 µg/ml polybrene (Merck, Sigma-Aldrich) was added. After two days, the medium was exchanged, and 0.8 µg/ml puromycin was added to start the cell selection. On day 4, the puromycin concentration was further increased to 1.2 µg/ml. All cells in a non-transduced control were fully detached on day six, so the selection was stopped. Transduced cells were detached from the dish by trypsinization and transferred to a new 10 cm cell culture dish. After two more days in a selection medium with 1.5 µg/ml puromycin, individual cell colonies were observed and separated by cloning cylinders (Sigma-Aldrich) to establish several monoclonal A549-IFITM3 cell lines.

3.3 Influenza A/WSN/1933(H1N1) virus production

For the infection experiments conducted in this study, I produced A/WSN/1933 (H1N1) viruses using a reverse genetics system (E Hoffmann *et al.* 2000), as described in the following section.

3.3.1 Reverse genetics system

4×10^6 HEK293T cells were seeded in a 10 cm culture dish and transfected with the following transfection mix: 2.5 µg of each plasmid (pHW2000-PB1-WSN, pHW2000-PB2-WSN, pHW2000-PAWSN, pHW2000-NP-WSN, pHW2000-NA-WSN, pHW2000-M-WSN, pHW2000-NS-WSN, pHW2000-HA-WSN) were diluted in 2 ml Opti-MEM medium, and 60 µl TransIT-293 (Mirus Bio) transfection reagent was added. The next day, the cell culture medium was exchanged with an FBS-free infection medium (DMEM-GlutaMAX-I with 1 % P/S, 0.3 % bovine serum albumin (BSA), and 2 $\mu g/ml$ TPCK-trypsin). The next day, the supernatant was centrifuged (10 min at 1,000 ×g), aliquoted, shock frozen in liquid nitrogen (LN_2), and stored at passage 0 (P0) at -80 °C.

3.3.2 Virus propagation and sucrose purification

To propagate the virus recovered by the reverse genetics system, 4×10^6 MDCK cells were seeded in a T175 cell culture flask. The next day, 10 ml of a 1:10 dilution of the P0 virus stock was added to the cells and incubated for 1 h at 37 °C with 5 % CO_2. Cells were washed and 40 ml infection medium (DMEM-GlutaMAX-I with 1 % P/S, 0.3 % BSA, and 2 $\mu g/ml$ TPCK-trypsin) was added. After three days, the supernatant was centrifuged three times (15 min at 2,200 × g) to remove the cell debris. 5 ml of 30 % sucrose solution in HNE buffer (10 mM HEPES, 1 mM EDTA, 100 mM NaCl

ar pH 7.4) was added to a thin-walled centrifugation tube, and 33 ml supernatant was overlaid. The sample was centrifuged in an Optima L-90K (Beckman Coulter) ultracentrifuge using an SW32 swing-out rotor (90 min at 83,018 ×g, 4 °C). After centrifugation, the supernatant was discarded, and the pellet was resuspended using 1 ml HNE buffer. The resuspended sample was centrifuged in an Optima TLX (Beckman Coulter) ultracentrifuge using a TLA-120.2 fixed-angle rotor (30 min at 15,728 ×g, 4 °C). After centrifugation, the supernatant was discarded, and the pellet was resuspended using 200 µl HNE buffer. The purified virus was aliquoted, shock-frozen in LN_2, and stored as passage 1 (P1) at -80 °C.

3.3.3 Plaque assay

A plaque assay was performed to determine the virus stock's viral titer. 1×10^6 MDCK cells were seeded in a 6-well plate and incubated for one day. The viral stock was diluted in infection medium (DMEM-GlutaMAX-I with 1 % P/S, 0.3 % BSA, and 2 $\mu g/ml$ TPCK-trypsin) in a dilution series between 10^{-3} to 10^{-9} and 800 µl of each dilution was added to one well of the 6-well plate and incubated for 1 h at 37 °C with 5 % CO_2. Wells were washed two times and overlaid with 3 ml of a plaque medium (DMEM-GlutaMAX -I, 0.5 % P/S, 0.15 % BSA, 1 µg/ml TPCK-trypsin, 1.2 % Avicel RC-581). After two days, cells were fixed with 1 % glutaraldehyde (GA) for 30 min and stained with a 1 % crystal violet solution (Sigma-Aldrich) for 10 min. For each well, all plaques were manually counted, and the viral titer was calculated:

$$T_{virus} = \frac{n_{plaque}}{d * V} \tag{3.1}$$

with the viral titer T_{virus}, the number of counted plaques n_{plaque}, the dilution factor d, and the volume of used virus dilution V. The titer for all wells was determined, and the average titer was calculated and used as the viral titer for all further experiments.

3.3.4 Fluorescent labeling of influenza A viruses

For the *in-situ* cryo-CLEM workflow, I established a protocol to fluorescently label influenza A/WSN/1933(H1N1) using the fluorescent membrane dye neuro- (nDiO) (Biotium) of sucrose purified virus particles, as described in this section. 200 µl sucrose purified A/WSN/1933(H1N1) was fluorescently labeled with 5 µl 'Cellbrite Green' (Biotium) for 1 h on a rotation wheel at room temperature (RT). The labeled virus was again purified by sucrose purification. 500 µl of a 10 % sucrose solution in HNE buffer was added to thick-walled centrifugation tubes, and 200 µl labeled virus solution was overlaid. The sample was centrifuged in an Optima Max (Beckman Coulter) ultracentrifuge using a TLS-55 swing-out rotor (90 min at 107,000 ×g, 4 °C). After centrifugation, the supernatant was discarded, and the pellet was resuspended in 1 ml HNE buffer. The resuspended sample was centrifuged in an Optima TLX (Beckman Coulter) ultracentrifuge using a TLA-120.2 fixed-angle rotor (30 min at 15,728 ×g, 4 °C). After centrifugation, the supernatant was discarded, and the pellet was resuspended in 200 µl HNE buffer. The purified virus was aliquoted, shock-frozen in LN_2, and stored at -80 °C.

3.4 Generation of fluorescent reporter viruses A/WSN/1933(H1N1)-PA-mScarlet

To assess successful virus infection, I generated an influenza A/WSN/1933(H1N1) reporter virus expressing a mScarlet-tagged PA, which is based on the work of Tran *et al.* (2013). To increase the stability of the fluorescent tag, I codon-optimized the gene sequence on mScarlet by substituting TpA and CpG sites to reduce the recognition by the antiviral Zinc-finger restriction factor (Odon *et al.* 2019). This fluorescent reporter virus was jointly established with Carmen Lahr, a Master's student, and Nina Reddmann, a rotation student, I supervised.
Using the GenSmart codon optimization software, the mScarlet sequence (Bindels

et al. 2017) was optimized for mammalian expression systems. In an additional manual step, all TpA and CpG sites were identified and changed to another codon without changing the amino acid sequence. This new codon-optimized mScarlet sequence was synthesized and inserted into a pcDNA3.4 plasmid backbone by the GeneArt synthesis service (ThermoFisher Scientific). 1 µl of the plasmid pHW2000-PA-mScarlet was digested with 1 unit XbaI (New England Biolabs) and 1.33 unit BssHII (New England Biolabs) in a total volume of 50 µl 1×CutSmart buffer (New England Biolabs) for 15 min at 37 °C. The reaction was stopped by a heat inactivation step at 65 °C for 20 min. The product of the restriction digestion was separated on an agarose gel (0.7 %), and the linearized plasmid was purified with the NucleoSpin Gel and PCR Clean-up kit (Macherey-Nagel). The mScarlet sequence of the reverse genetics plasmid pHW2000-PA-mScarlet (gift by Prof. Dr. Andrew Mehle) was exchanged with the codon-optimized mScarlet sequence by In-Fusion cloning (Takara), following the manufacturer's protocol. Therefore, an overhang-PCR was performed using 0.2 µM of a forward primer (CCCACGCCCTGCGCGCGGCAGCAATGGTGTCCAAGGGTGAAGC) and a reverse primer (AAGCAGTTTTCTAGATCACTTGTACAGCTCATCCATTCCAC), 1 ng of the codon-optimized pcDNA3.4-mScarlet plasmid, 12.5 µl CloneAmp HiFi PCR Premix (Takara) and 1 µl DMSO in a total of 25 µl volume. The PCR reaction was run in a thermocycler with the following parameters: 35 cycles; denaturation: 98 °C for 10 sec; annealing: 64 °C for 15 sec; elongation: 72 °C for 10 sec. 20 µl of the PCR product was mixed with 8 µl Cloning Enhancer (Takara) and incubated for 15 min at 37 °C. The reaction was stopped by an inactivation step at 80 °C for 15 min. The In-Fusion reaction mix was prepared by adding 25 ng of the codon-optimized mScarlet PCR fragment with overhangs, 50 ng of the linearized pHW2000-PA-mScarlet plasmid, and 1 µl In-Fusion enzyme mix (Takara) in a total volume of 5 µl in H_2O. The In-Fusion reaction was run for 15 min at 50 °C. 5 µl of the In-Fusion reaction product was added to 50 µl *E. coli* cells (Stellar competent cells, Takara) and incubated for 30 min on ice. Cells were heat shocked for 45 sec at 42 °C, and subsequently, 450 µl SOC medium (ThermoFisher Scientific,

Invitrogen) was added. Transduces cells were incubated for 1 h at 37 °C on a shaker at 180 rpm in a 14 ml round bottom tube. Cells were plated on a 1.5 % LB agar plate with 50 µg/ml AMP and incubated for 12 h at 37 °C. Using the QIAprep Spin Miniprep Kit (QIAGEN), plasmids were purified, and colonies were sequences using a forward primer (GGCAAACAACAGATGGCTGGCAAC) and reverse primer (GTATGCATCTCCACAACTAGAAGG).
Using the reverse genetics system (see section 3.3.1), a fluorescent reporter virus was recovered by exchange of the plasmid pHW2000-PA-WSN with the newly generated condon-optimized pHW2000-PA-WSNmScarlet plasmid.

3.5 Immunoblotting

Immunoblotting was used to quantify the expression levels of IFITM3 in different cell lines. Therefore, 1×10^6 cells were cultured in 10 cm cell culture dishes. After two washing steps with cold PBS, 650 µl RIPA lysis buffer (50 mM Tris-HCL, 150 mM NaCl, 1 % v/v Triton X-100, 0.5 % v/v sodium deoxycholate, 0.1 % v/v SDS, 1 ×protease inhibitor cocktail (ThermoFisher Scientific, Roche) in H_2O) was added to the cells and incubated for 20 min on ice. Cell debris was removed from the lysate by centrifugation (12,000 ×g for 20 min at 4 °C). Using the Pierce BCA protein assay kit (ThermoFisher Scientific), the protein concentration of the lysate was determined.
Protein extracts were diluted to a final concentration of 0.7 µg/µl in RIPA buffer. 200 µl sample was combined with 66.7 µl 4 ×Laemmli buffer (supplemented with 0.2 M dithiothreitol, Bio-Rad) and incubated for 8 min at 90 °C. A precast polyacrylamide gel (4 – 15 %, Bio-Rad) was loaded with 40 µl sample and 10 µl broad range color pre-stained protein standard (New England BioLabs). The samples were separated by gel electrophoresis using the Mini-PROTEAN electrophoresis chamber (BioRad) filled with 1×TGS running buffer (Bio-Rad) for 60 min at 120 V. The samples were transferred from the polyacrylamide gel to a 0.2 µm PVDF membrane (Bio-Rad)

using the Trans-Blot Turbo transfer system (Bio-Rad) with a constant 2.5 A for 7 min.
The PVDF membrane was washed three times with TBS supplemented with 0.1 % v/v Tween-20 (TBS-T) and blocked in 5 % BSA in TBS-T for 1 h. The primary antibody was diluted in TBS-T, and the PVDF membrane was incubated for 1 h at RT. Next, the PVDF membrane was washed three times with TBS-T and subsequently incubated with a secondary antibody, diluted in TBS-T. PVDF membrane was washed three times and incubated for 5 min in Clarity Western ECL substrate working solution (Bio-Rad). The chemiluminescence signal was measured with the Azure 400 imaging system (Azure Biosystems). Expression levels were quantified using the Gel Analyzer plugin of FIJI (Schindelin et al., 2012) using the housekeeping gene actin as a loading control.

3.6 Immunofluorescence labeling and confocal fluorescent light microscopy

5×10^4 cells were seeded on microscopy coverslips (12 mm, No.1, Marienfeld) in a 6-well plate. After one day, cells were fixed with 4 % paraformaldehyde (PFA) in phosphate buffered saline (PBS) for 15 min at RT. The sample was washed three times with PBS at RT, like all following washing steps. The PFA was quenched by incubation with 20 mM glycine in PBS for 10 min. After three more washing steps, the cells were permeabilized with 0.2 % Triton X-100 in PBS for 5 min. After three washing steps, the sample was blocked with 3 % BSA in PBS-T for 1 h. After three washing steps, cells were incubated with a primary antibody diluted in 1 % BSA in PBS-T for 1 h. After three washing steps, cells were incubated with a secondary antibody diluted in 1 % BSA in PBS-T for 1 h. After three washing steps, nuclei were fluorescently labeled with 1 µg/µl Hoechst 33342 (Sigma-Aldrich) in PBS for 5 min. The sample was washed three times with PBS and one time with deionized

water. The coverslips were mounted on microscopy slides using 7 µl ProLong Glass Antifade mounting medium (ThermoFisher Scientific, Invitrogen). After 24 h of curing, fluorescent microscopy data was acquired on an SP8 TCS laser scanning confocal microscope (Leica) equipped with a 63×/1.4 HC PL APO CS2 oil immersion objective using a UV laser with an excitation wavelength of 405 nm (for Hoechst 33342) and a helium-neon laser with an excitation wavelength of 633 nm (for Alexa Fluor 633) in sequential acquisition mode with 4× line accumulation. Acquired image stacks were deconvolved using a theoretical PSF using the AutoQuant X3 (Media Cybernetics) software in 10 iterations with these settings: lens immersion refractive index 1.515; sample embedding refractive index 1.52; sample distance from coverslip of 0 nm; emission wavelength of 461 nm (for Hoechst 33342) or 647 nm (for Alexa Fluor 633) and appropriate settings for the used objective (NA 1.4; objective lens magnification 63×). Deconvolced image stacks were segmented using the surface segmentation function of the Imaris (Verison 9.8.2, Oxford Instruments) software.

3.7 Colocalization analysis

Using immunofluorescence and confocal microscopy, the colocalization between IFITM3 and Ras-related protein 7 (Rab7) or lysosomal-associated membrane protein 1 (LAMP1) was evaluated in the A549-IFITM3 cell line. A549-IFITM3 cells were grown on 12 mm coverslips in a 6-well plate in complete growth medium. The following day, the cells were transfected with either pC1-Rab7-eGFP or pN1-LAMP1-eGFP using a transfection mix of 2.5 µg plasmid, 7.5 µl transfection reagent, and 250 µl OptiMEM. The transfection mix was added to the cells and incubated for 30 min at RT. The cells were then incubated at 37 °C for 24 h in a 5% CO_2 environment. The cells were fixed with 4 % PFA in PBS for 30 min and washed three times with PBS. Cells were then permeabilized by incubation with 0.2 % Triton X-100 in PBS for 5 min, followed by 3 washes with PBS for 5 min each. The cells were

incubated with blocking buffer (3% BSA in PBS with 0.1 % Tween-20) for 1 h and then incubated with a primary antibody against IFITM3 (diluted 1:200 in 1 % BSA in PBS with Tween-20) for 1 h. After 3 washes with PBS with Tween-20 for 5 min each, the cells were incubated with a secondary antibody (goat anti-rabbit Alexa Fluor 633, diluted 1:2,000 in dilution buffer) for 1 h. The cells were washed three times with PBS with Tween-20 for 5 min each and then incubated with 1 µg/µl 4',6-diamidino-2-phenylindole (DAPI) in BSA for 1 min to label the nuclei. The cells were washed three times with PBS for 5 min each, followed by a short wash with deionized water. The coverslips were mounted on microscopy slides with 7 µl ProLong Glass Antifade mounting medium and allowed to cure for 24 h at RT. Confocal microscopy was performed using an SP8 TCS laser scanning confocal microscope (Leica) equipped with a 63×/1.4 HC PL APO CS2 oil immersion objective. A UV laser with an excitation wavelength of 405 nm (for DAPI), an argon laser with an excitation wavelength of 488 nm (for eGFP), and a helium-neon laser with an excitation wavelength of 633 nm (for Alexa Fluor 633) were used in sequential acquisition mode with 4 ×line accumulation. The pixel size was set at 72.1 nm, and Z-stacks were acquired using a Z-spacing of 200 nm. Image stacks were deconvolved with AutoQuant X3 (Media Cybernetics) using a theoretical and adaptive point spread function (PSF) for 10 iterations. The following parameters were used: lens immersion refractive index of 1.515, sample embedding refractive index of 1.52, sample distance from coverslip of 0 nm, an emission wavelength of 461 nm (for DAPI), 507 nm (for eGFP), or 647 nm (for Alexa Fluor 633), and appropriate settings for the objective used (NA 1.4, objective lens magnification 63×). The colocalization between IFITM3 and Rab7, LAMP1, or DAPI was analyzed by calculating the Pearson and Manders correlation coefficients (Manders *et al.* 1993) using the 'coloc2' tool in ImageJ/FIJI (Schindelin *et al.* 2012). The analysis was performed on a manually selected region of interest for each cell. Before the correlation analysis, the background signal was subtracted using a rolling ball algorithm (radius = 30 px) (Sternberg 1983) implemented in ImageJ/FIJI

(Schindelin *et al.* 2012).

3.8 Infection assay

Using the A/WSN/1933(H1N1)-PA-mScarlet reporter cell line (see section 3.4), an infection was performed to quantify the percentage of infected cells. This infection assay was jointly performed with Carmen Lahr, a Master's student I supervised. 5×10^5 cells were seeded on microscopy coverslips (12 mm, No.1, Marienfeld) in a 24-well plate and grown for 24 h at 37 °C. The reporter virus stock was diluted in the serum-free DMEM-F12 medium and added to the cells to achieve the desired multiplicity of infection (MOI). Cells were incubated for 1 h at 37 °C and washed with complete growth medium three times. Cells were incubated for 24 h and fixed with 4 % PFA in PBS for 30 min. Cells were immunolabeled as described in section 3.6 against the viral protein M2. Samples were imaged using the automated high-throughput wide-field microscope Celldiscoverer 7 (Zeiss) equipped with a 20×/0.95 NA PL APO COR objective and Axiocam 712 camera. The acquired images were stitched, and nuclei were automatically segmented using the StarDist plugin (U Schmidt *et al.* 2018) in ImageJ/FIJI. The average signal intensity of PA-mScarlet and M2 were quantified for each segmented region. Thresholds for the signal intensity of PA-mScarlet and M2 for non-infected cells were determined using a non-infected control sample. Each segmented cell exceeding one of the thresholds was counted as infected, and the infection rate was calculated.

3.9 Blam membrane fusion assay

A Blam-based fusion assay was utilized to quantify the viral cytoplasmic entry. The viral fusion assay was jointly performed with Romy Brecht, a rotation student I supervised.

3.9.1 Influenza A Blam-VLP production

First, Influenza virus like particles (VLPs) expressing a M1-Blam were produced as follows: 2.7×10^6 HEK293T cells were seeded in a 10 cm cell culture dish. The next day, cells were transfected to produce VLPs. 1.48 µg pCAGGS-A/Hong Kong/1968-HA plasmid, 1.40 µg pCAGGS-A/Singapore/1957-NA, and 7.12 µg pCAGGS-M1-Blam plasmid were added in a total of 1 ml Opti-MEM medium. 30 µl polyethylenimine (PEI) (1 µg/µl, Polysciences) transfection reagent was added, and the transfection mix was incubated for 30 min and added to the cells. After 6 hours, the medium was exchanged with fresh complete growth medium, and cells were incubated for 48 h at 37 °C. The supernatant was centrifuged (1,000 ×g for 10 min) to remove the cell debris, and 2.5 µl TPCK-Trypsin (10 µg/µl, Sigma-Aldrich) was added to the cleared supernatant and incubated for 30 min at 37 °C. 7 µl trypsin inhibitor (5 µg/µl in PBS, Sigma-Aldrich) was added and incubated for another 10 min at 37 °C. The VLP-containing supernatant was aliquoted and stored at -80 °C.

3.9.2 Blam assay

A black-walled 96-well plate (Corning) was coated by adding 25 µl per well of a 57.2 µg/ml fibronectin solution in PBS and incubated for 6 h. Cells were washed with PBS, and 1.2×10^4 cells per well were seeded. The next day, cells were infected by adding 190 µl influenza VLPs expressing M1-Blam to each well. The efficiency of VLP infection was increased by spinoculation of the 96-well plate (250 × g for 1 h at RT). Cells were washed once with PBS, and 90 µl per well of Opti-MEM (supplemented with 1 % P/S and 20 mM HEPES) was added, and cells were incubated for 3 h at 37 °C. 20 µl of Blam-staining solution (6 µM CCF4AM in Blam loading solution, ThermoFisher Scientific) was added to each well. Cells were incubated for 12 h at 8 °C. The fluorescent signal was acquired with an excitation wavelength of 410 nm (9 nm bandwidth) and emission wavelengths of 450 nm or 520 nm (20 nm bandwidth) using the Infinite 200 plate reader (Tecan) with a manual gain of 160

and 3×3 reads per well and an integration time of 20 µs and 50 reads per position. The background emission signal was measured in a sample with only medium and subtracted from each measurement. The $^{450\,nm}/_{520\,nm}$ ratio was determined and averaged for each triplicate. In addition to the quantitative plate reader readout, fluorescent microscopy images of the samples were acquired on a Nikon Eclipse Ts2 fluorescent microscope equipped with a DS-Fi3 camera, 20× / 0.4 NA lens equipped with a Blam-optimized filter set.

3.10 Viral entry half-time determination

To quantify the entry half-time of IAV in A549 cells, I utilized a NH_4Cl add-in infection time course experiment. This viral entry assay was jointly performed with Carmen Lahr, a Master's student I supervised. NH_4Cl neutralizes the pH of the endosomal system, and thus IAV-mediated membrane fusion can be halted, as it is dependent on the low pH of the endosome. By adding NH_4Cl at different time points post-infection, it is possible to determine the infection rate depending on the entry time. In the following section, I will describe the method in detail.

First, 5 $\times 10^4$ A549 or A549-IFITM3 cells were seeded on 12 mm coverslips in a 24-well plate in complete growth media. After 24 h, the cells were infected with the established IAV reporter virus A/WSN/1933PA-mScarlet, using a MOI = 3. For a synchronized infection, the infection was performed on ice for 1 h. After three washing steps with PBS, cells were incubated at 37 °C. After different time points post-infection, cells were treated with 50 mM NH_4Cl. I analyzed the following time points: 0 mpi, 15 mpi, 30 mpi, 60 mpi, and 120 mpi. After 12 h incubation, cells were fixed with 4 % PFA in PBS for 30 min. After three washing steps with PBS, cells were immunolabeled against M2. Nuclei were fluorescently labeled with DAPI. Using an automated fluorescent microscope (Celldiscoverer 7, Zeiss), the samples on the coverslip were imaged using a tile scan. The individual tiles were stitched

in FIJI, and nuclei were automatically segmented using the StarDist plugin in FIJI (Zhao *et al.* 2022). For each segmentation, the average PA-mScarlet and M2 signal was calculated. Using a non-infected control, maximum average intensities were determined and used as a threshold for non-infected cells. I determined 750 au and 600 au as thresholds for M2 and PA-mScarlet, respectively. Every segmentation with one of the two thresholds exceeded was counted as an infected cell. For each time point, the infection rate was calculated and plotted against the NH_4Cl add-in time point. A four-parameter logistic (4PL) curve was fitted, and the inflection point (IC50) was determined for the viral penetration at half-time.

3.11 Room-temperature transmission electron tomography

To characterize the cellular ultrastructure, ET on HPF/freeze substitution (FS) samples was performed as described in this section. The sample preparation steps (HPF/FS, ultramicrotomy, and immunolabeling) were performed by Androniki Kolovou. The ET acquisition was performed by Martin Schorb (Electron Microscopy Core Facility, EMBL Heidelberg).

3.11.1 High-pressure freezing and freeze substitution

2.8×10^5 A549 cells were seeded on carbon-coated sapphire discs (Leica) in a 6-well plate. The next day, cells were fixed by HPF using an EM ICE HFP system (Leica). Type A and B carriers (Leica) were coated with 1-hexadecane, the carriers were filled with a complete growth medium, and the sapphire disc with the cells was inserted and high-pressure frozen. After HPF, the samples were resin-embedded by automatic freeze substitution (AFS). A Lowicryl HM20 solution (34.04 g monomer E, 5.96 g crosslinker D, 200 mg initiator C) was prepared in different dilutions from

10 % to 100 %. In addition, a 0.1 % uranyl acetate (UA) solution in acetone was prepared. The automated freeze substitution system AFS2 (Leica) was prepared by adding all reagents and samples, and the automated freeze substitution protocol was performed, as detailed in Table 3.1.

Table 3.1: Freeze substitution protocol.

Step	Temp start	Temp end	Slope	Time	Reagent	Transfer	Agitation	UV
1	-90 °C	-90 °C		48 h	0.1 % UA	stay	off	off
2	-90 °C	-45 °C	5 °C/h	9 h	0.1 % UA	stay	off	off
3	-45 °C	-45 °C		5 h	0.1 % UA	stay	off	off
4	-45 °C	-45 °C		10 min	Acetone	exch/fill	off	off
5	-45 °C	-45 °C		10 min	Acetone	exch/fill	off	off
6	-45 °C	-45 °C		10 min	Acetone	exch/fill	off	off
7	-45 °C	-45 °C		4 h	10 % Lowicryl	mix	on	off
8	-45 °C	-45 °C		4 h	25 % Lowicryl	mix	on	off
9	-45 °C	-35 °C	2.5 °C/h	4 h	50 % Lowicryl	mix	on	off
10	-35 °C	-35 °C	2.5 °C/h	4 h	75 % Lowicryl	mix	on	off
11	-35 °C	-35 °C		10 h	100 % Lowicryl	exch/fill	off	off
12	-35 °C	-35 °C		10 h	100 % Lowicryl	exch/fill	off	off
13	-35 °C	-35 °C		10 h	100 % Lowicryl	exch/fill	off	off
14	-35 °C	-35 °C		48 h	100 % Lowicryl	stay	off	on
15	-35 °C	20 °C	5 °C/h	9 h	100 % Lowicryl	stay	off	on
16	20 °C	20 °C		48 h	100 % Lowicryl	stay	off	on
17	20 °C	20 °C		72 h	100 % Lowicryl	stay	off	off

3.11.2 Ultramicrotomy

The resin-embedded samples were manually trimmed, and subsequently, 250 nm sections were cut using a diamond knife (DiATOME) using a UC7 ultramicrotome (Leica). Individual sections were placed on an EM copper slot grid with a 1 % formvar film (2 ×1 mm, Glider), which was previously coated with 2 nm carbon

using the ACE600 sputter coater (Leica).

3.11.3 Immunolabeling of sections

The 250 nm sections of the resin-embedded samples were blocked in blocking buffer (0.8 % BSA and 0.1% fish skin gelatin (FSG) in PBS) for 30 min, followed by incubation with the primary IFITM3 antibody diluted blocking buffer for 1 h. The sample was washed five times with PBS and incubated with 10 nm protein A gold (PAG) (Aurion) diluted in a blocking buffer (1:50). Sections were finally washed five times in PBS and five times in H_2O.

3.11.4 Image acquisition and data analysis

Using a Tecnai F30 (FEI) equipped with a Gatan OneView 4K camera, tilt series were acquired with 1° tilting steps from -60° to +60° using the software SerialEM (Mastronarde 2005) with a pixel spacing of 1.03 nm. Using the IMOD software (Kremer *et al.* 1996), tilt series were reconstructed using patch tracking for alignment and R-weighted back-projection for reconstruction. The endosomal membrane and individual ILVs were manually segmented using IMOD. The segmentation was jointly performed with Mehdi Hosseinzadeh, a student assistant I supervised. The segmented volume of each endosome was measured, and the total number of ILVs per endosome was quantified and normalized to the endosomal volume.

3.12 *In-situ* cryo-correlative light and electron tomography of cryo-focused ion beam milled adherent cells

3.12.1 Sample preparation and vitrification

1.8×10^5 A549 or A549-IFITM3 cells were seeded on glow-discharged EM grids (200 mesh gold with SiO_2 film and R1/4 spacing, Quantifoil). The next day, cells were infected with A/WSN/1933(H1N1)-nDiO virus using a MOI of 200. To that aim, the EM grids were blotted on filter paper (No.1, Whatman) and placed on parafilm on an 8 °C cooling block. 20 µl of virus (in DMEM-F12, 20 mM HEPES) was added to each grid and incubated for 30 min to allow attachment of virus particles to the cell surface. Grids were transferred to a 35 mm cell culture dish, washed five times, and incubated for 1 h at 37°C, 5% CO_2 in complete growth medium with 100 nM Lipi-Blue (Dojindo), which allows fluorescent labeling of lipid droplets (LDs). After incubation, grids were washed two times with complete growth medium and vitrified by plunge freezing using the EM GP2 plunge freezer (Leica) with the following plunging parameters: air temperature: 25 °C; ethane temperature: -183 °C; air humidity: 70 %, blotting time: 3.5 sec from the back with filter paper (No. 1, Whatman).

3.12.2 Cryo-light microscopy of plunge frozen samples

Using the cryoCLEM fluorescent wide-field microscope (Leica) (Schorb, Gaechter, *et al.* 2017), the vitrified grids were mapped in a central 1.2×1.2 mm square of the grid. Using the LAS X Navigator, volume stacks with a thickness of 30 µm and a Z-spacing of 300 nm were acquired. The fluorescence volume data were deconvolved using AutoQuant X3 (Media Cybernetics) with the following parameters: iterations:

100; lens immersion refractive index: 1; sample embedding refractive index: 1.31; sample distance from coverslip: 0 nm; emission wavelength: 460 nm for Lipi-Blue, 525 nm for nDiO; numerical aperture: 0.9; objective lens magnification: 50×. Maximum intensity projections (MIPs) of each tile was calculated, and tiles were stitched using the cryo-CLEM toolbox (Klein, Wachsmuth-Melm, *et al.* 2021).

3.12.3 Sample thinning by cryo-focused ion beam milling

Using a dual-beam cryo-FIB/SEM microscope (Aquilos, Thermo Fisher Scientific), the grid was first mapped by cryo-SEM and the stitched cryo-LM map was imported and correlated to the cryo-SEM map using the MAPS software (Schorb & Sieckmann 2017). Cells that showed a nDiO signal were selected for FIB-milling. The sample was coated with an organo-metallic platinum layer for 5 sec, and cells were subsequently milled using an angle between 15° and 18° using a Gallium ion beam. The milling process was performed in five distinct steps with a final nominal thickness of 150 nm (Wagner *et al.* 2020) (Table 3.2). To increase the stability of the lamellae, a micro-expansion joint milling pattern was utilized (Wolff *et al.* 2019).

Table 3.2: Steps for cryo-FIB milling

Step	Thickness [µm]	Lamella width [µm]	Current [nA]
1	5	15	1
2	2.5	14	0.5
3	1.2	13	0.1
4	0.5	12	0.05
5	0.15	11	0.03 – 0.01

3.12.4 Cryo-electron tomography

Tomograms were acquired on the cryo-FIB milled samples on a 300 kV cryo-TEM (Krios, Thermo Fisher Scientific), which was equipped with a direct electron detector (K3, Gatan) and an energy filter (Quanta Imaging Filter, Gatan) set to 20 eV. First, lamellae were mapped at 8,700× (equivalent to 10.64 Å pixel spacing) with a defocus of 50 µm using the serialEM software (Mastronarde 2005). Sites for tomogram acquisition were selected, and tilt series were acquired at 33,000× (equivalent to 2.67 Å pixel spacing) with a defocus of 3 µm and an electron dose of 3 $e^{-}/Å^{2}$ using a dose-symmetric tilting scheme (Hagen *et al.* 2017) with 3° increments with a tilting range from -52° to 68°. For each tilt, gain-corrected frames were saved.

3.12.5 Cryo-light microscopy of cryo-FIB milled samples

After cryo-ET of cryo-FIB milled samples, for each lamella, one cryo-LM volume stack with a thickness of 30 µm and a Z-spacing of 300 nm was acquired and deconvolved using AutoQuant X3 (Media Cybernetics) as described above (Section 3.12.2).

3.12.6 Data processing

3.12.6.1 Tilt series reconstruction

Frames for each tilt were split into an even and odd subset, which were motion-corrected using MotionCor2 (Zheng *et al.* 2017) and combined into an even and odd tilt series. Both tilt series were reconstructed using identical parameters in etomo (Kremer *et al.* 1996) using patch tracking for tilt alignment. 3D CTF-correction and a dose-symmetric filter were applied using the etomo implementation. The final tomogram reconstruction was performed using weighted back-projection with a SIRT-like filter equivalent to five iterations. Using the two reconstructed tomograms

from the even and odd tilt series, noise2noise image restoration (Lehtinen *et al.* 2018) was applied using the cryoCARE software package (Buchholz *et al.* 2019).

3.12.6.2 Stitching of overview cryo-EM maps of lamellae

Each lamella is mapped at 8,700× magnification (section 3.12.4) using a 10 % tile overlap. The individual tiles are stitched with the 'Align Serial Sections/Blend Montages' function of etomo (Kremer *et al.* 1996) and exported as a single 16-bit tif file.

3.12.6.3 Correlation analysis

3.12.6.3.1 Image registration of pre- and post-LM maps in three-dimensional space

For each volume stack of a lamella, which was acquired after cryo-FIB milling ('pre-LM map,' section 3.12.5), the corresponding tile was extracted from the cryo-LM dataset acquired before cryo-FIB milling ('post-LM map,' section 3.12.2). The volumes were aligned by 3D registration using the *imregtform* function of Matlab (MathWorks) using a custom Matlab script (supplementary data 5.6.1). The transmitted light (TL)-bright field (BF) channel of the post-LM map was combined with the aligned fluorescent channels of the pre-LM map to generate a new composite-LM map.

3.12.6.3.2 Lamella tilt compensation

As cryo-FIB milling is performed at an angle between 15° and 18° (section 3.12.3), the fluorescent signal corresponding to the lamella is located in different Z-slices of the aligned composite-LM map (section 3.12.6.3.1). To compensate for the tilted lamella, the composite volume is manually tilt-corrected. The organometallic platinum-layer visible in the TL-BF channel was used to measure the exact lamella tilt, and the complete volume was rotated accordingly using the image transformation

tool implemented in FIJI (Schindelin *et al.* 2012).

3.12.6.3.3 Extraction of Z-slice

After lamella tilt compensation (section 3.12.6.3.2), the fluorescent signal of the lamella is located in a single Z-slice of the image volume. To identify the Z-slice corresponding to the lamella position, LDs on the cryo-TEM map of the lamella were identified. Using the Lipi-Blue fluorescent signal, the Z-slice of the image volume, which comprises the corresponding LDs, was manually identified and extracted from the volume stack using FIJI (Schindelin *et al.* 2012).

3.12.6.3.4 Image registration of TEM-map and cryo-LM map

The stitched cryo-TEM map of the lamella (section 3.12.6.2) and the tilt-corrected Z-slice of the cryo-LM map (section 3.12.6.3.3) were correlated using the eC-CLEM (Paul-Gilloteaux *et al.* 2017) plugin in icy (Chaumont *et al.* 2012). LDs on both maps were manually selected as reference points for correlation. A rigid transformation was calculated, and a new composite image composed of the transformed fluorescent channels and the cryo-TEM map was generated.

3.12.6.3.5 Analysis of correlation precision

The distance between the center of the Lipi-Blue fluorescent signal and the center of the LD on the cryo-TEM map was measured to quantify the correlation precision.

3.12.6.3.6 Analysis of out-of-lamella-signal

To quantify the 'correlation success rate,' the total number of LDs present on the cryo-TEM map was divided by the total number of Lipi-Blue fluorescent signals on the correlated cryo-LM map.

To quantify the 'out-of-lamella signal,' the total number of Lipi-Blue fluorescent signals on the correlated cryo-LM map was divided by the number of Lipi-Blue fluorescent signals which do not correlate to any LD on the cryo-TEM map.

3.12.6.4 Tomogram segmentation and quantification

The reconstructed cryo-electron tomograms were segmented using the software Amira (Thermo Fisher Scientific). The cryoCARE denoised tomogram was further filtered by applying a non-local means and membrane enhancement filter. Using the Top-hat segmentation tool, membranes were segmented and manually refined. Different membrane types, like LE membrane, ILV membrane, and viral membranes, were colored differently.

3.12.6.5 Analysis of hemifusion symmetry

Each hemifusion site, situated at either the limiting LE membrane or within ILVs, was analyzed by measuring the length of the hemifusion diaphragm and both the inner and outer angles. To position the hemifusion site on a single XY plane, the tomogram was resliced using the slicer tool in IMOD (Kremer *et al.* 1996). All angular measurements were conducted using the 'angle tool' provided by ImageJ/FIJI software (Schindelin *et al.* 2012). For measuring the length of the hemifusion diaphragm, a line profile of 10-pixel width was plotted. Subsequent to this, the average signal corresponding to the late endosomal lumen was subtracted. The diaphragm length was then determined by identifying the difference between the zero-crossing points and was reported accordingly. In this manner, the reported measurement accounts for the presence of the phospholipid monolayers.

3.12.7 Subtomogram averaging

Electron densities, frequently observed at the hemifusion sites, were characterized using STA. A total of 30 distinct densities were manually identified and extracted. This was accomplished by employing a dipole model in Dynamo (Castaño-Díez *et al.* 2012), utilizing a box size of 192 pixels, equivalent to a physical dimension of 51.28 nm. An initial reference model was constructed by averaging all subvolumes.

The subvolumes were oriented based on the information obtained from the dipole model. To facilitate the even distribution of the missing wedge from individual subvolumes during the initial model creation, azimuth angles were randomized. The first round of averaging was computed without a symmetry operation (C1) and made use of a spherical mask. The resultant average from this first subtomogram averaging was used as a new template for the second averaging process. For the second averaging, a tightly constrained mask around the central density was used, and a C3 symmetry operation was applied. The numerical parameters for the first and second averaging were kept consistent (**Table 3.3**).

Table 3.3: Numerical parameters used in the Dynamo software package for STA analysis

	Round 1	**Round 2**	**Round 3**	**Round 3**
Iterations	1	1	1	1
References	1	1	1	1
Cone aperture [°]	120	30	10	2
Cone Sampling [°]	30	10	2	0.5
Azymuth rotation range [°]	360	90	30	5
Azymuth rotation sampling [°]	90	30	5	1
Refine	2	2	2	2
Refine factor	2	2	2	2
High pass filter [°]	2	2	2	2
Low pass filter [pixel]	32	32	32	32
Symmetry	C1/C3	C1/C3	C1/C3	C1/C3
Particle dimensions	192	192	192	192
Shift limits in X, Y, and Z [pixel]	12,12,12	6,6,6	4,4,4	2,2,2
Shift limiting way	1	2	2	2
Separation in tomogram	0	0	0	0
Basic MRA	0	0	0	0
Threshold parameter	0.8	0.8	0.8	0.8
Threshold modus	5	5	5	5

4 Results

4.1 Novel method for *in situ* cryo-correlative light and electron microscopy

4.1.1 Rationale

In situ cryo-ET allows the ultrastructural analysis of the cellular environment in its native state. One major limitation of this method is the lack of labeling and unambiguous identification of features of interest. To overcome this shortcoming, I aimed to develop an *in situ* cryo-correlative light and electron microscopy workflow that combines high-resolution cryo-ET with fluorescent microscopy, allowing localizing a fluorescently labeled structure of interest on cryo-FIB milled adhered eukaryotic cells. This method is intended to be suitable for adherent eukaryotic cells directly grown on cryo-EM grids and be compatible with commercially available widefield cryo-LM systems. To that aim, features of interest are fluorescently labeled by overexpressing fluorescent fusion proteins or fluorescent dyes for specific cellular components like LDs. The labeled cells are subsequently vitrified by plunge freezing. An overview of the complete workflow is visualized in **Figure 4.1**. All necessary steps for this newly developed correlation workflow are described in detail in this chapter.

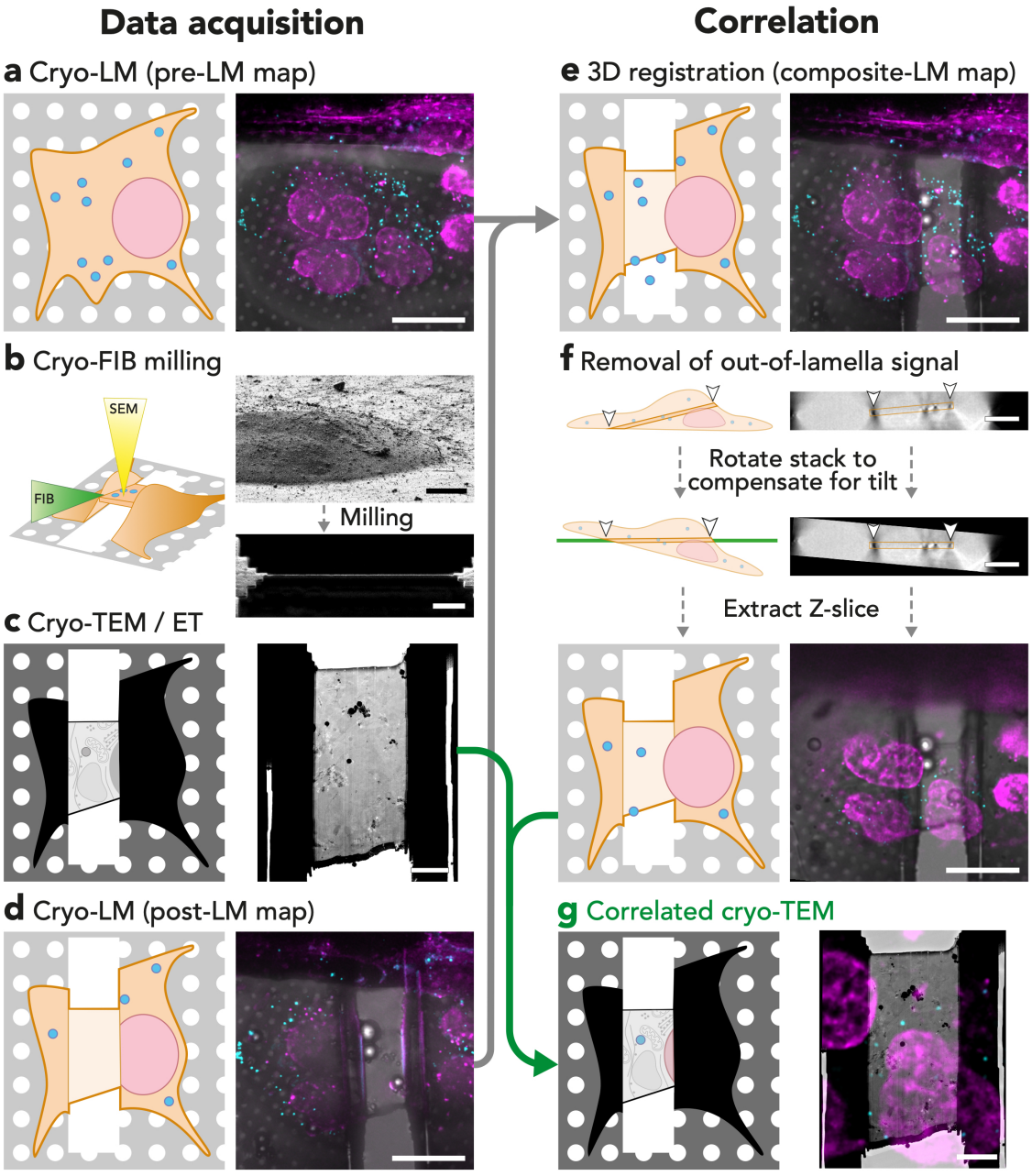

Figure 4.1: (Captions on next page)

Figure 4.1: (Previous page) *In situ* cryo-correlative light and electron microscopy workflow. Adherent A549 cells were grown on a holey SiO_2 grid. The nucleus and LDs were fluorescently labeled, and the sample was subsequently vitrified by plunge freezing. This figure shows each step of the *in situ* cryo-correlative light and electron microscopy workflow, with a schematic representation on the left and a biological example on the right. The workflow can be separated into 'data acquisition' (a – d) and 'correlation' (e – g). **(a)** After plunge freezing, volume fluorescence light microscopy data was acquired using a cryo-LM. A maximum intensity projection is shown with TL-BF signal in grayscale, the nucleus in magenta, and LDs in magenta. Scale bar: 20 µm. **(b)** The cryo-LM data from (a) is used to perform a rough correlation with the SEM map of the sample to identify a cell of interest. Using a cryo-FIB, a 150 nm thin lamella is created by an iterative FIB-milling process. Scale bars: 20 µm. **(c)** After cryo-FIB/SEM, the created lamella is mapped using a cryo-TEM and tomograms are acquired on sites of interest. Scale bar: 5 µm. **(d)** After cryo-TEM acquisition, the same area is mapped again by cryo-LM. Compared to (a), the lamella's area no longer shows any fluorescent signal. Scale bar: 20 µm. The acquired cryo-LM data (a and d) will be correlated to the cryo-TEM (c) in the following steps: **(e)** The previously acquired pre- and post-cryo-LM datasets (a and d) are registered and aligned in three dimensions. A composite map is generated by combining the fluorescent channels from the pre-LM map with the aligned TL-BF channel from the post-LM map. Scale bar: 20 µm. **(f)** Due to the tilted milling geometry during FIB-milling (b), the lamella (shown in dark orange) is not horizontally aligned. The actual lamella tilt is measured using the TL-BF channel of the composite map (e). The tilt is corrected, and the Z-slice corresponding to the lamella is extracted from the three-dimensional composite volume. Scale bar: 20 µm **(g)** Finally, LDs on the cryo-TEM map (c) and the tilt corrected cryo-LM map (f) are used as fiducial markers to correlate both maps. Scale bar: 5 µm. This figure is a modified reprint from *Methods in Cell Biology*, Volume 162 by Klein, Wachsmuth-Melm, *et al.* (2021), 'Cryo-correlative light and electron microscopy workflow for cryo-focused ion beam milled adherent cells', ©2021, with permission from Elsevier.

4.1.2 Data acquisition

Using a wide-field cryo-LM, a volume image of the sample is acquired. The microscope is operated at temperatures below the devitrification temperature of -138.15 °C (McDowall *et al.* 1983; Schorb, Gaechter, *et al.* 2017) to avoid devitrification of the sample. This volume image is essential for a subsequential *a posteriori* correlation step, allowing high-precision correlation after cryo-ET acquisition of lamellae.

At first, the map is used for targeted cryo-FIB milling in two dimensions (X–Y). To that aim, a maximum projection of the volume fluorescent image stack is generated. The sample is transferred to a dual-beam cryo-FIB/SEM microscope, and the grid is mapped by cryo-SEM. The MIP-fluorescence map is correlated in two dimensions with the SEM-map (Schorb & Sieckmann 2017), which allows identifying features of interest based on the fluorescence information and selecting positions for cryo-FIB milling accordingly (**Figure 4.1b**). This step allows selecting milling areas with the feature of interest present and increases the chance that the feature of interest is present in the prepared lamella. In the next step, the sample is transferred to a cryo-TEM system, and all lamellae are mapped at a magnification 8,700× (pixel size = 10.64 Å). This medium magnification allows evaluating the quality of the lamella (thickness, devitrification, ice contamination) (**Figure 4.1c**). Tomogram sites are selected based on visual features on the acquired TEM maps, like viral particles. If the structure of interest can not be localized by features on the cryo-TEM map, other correlation approaches might be necessary, as discussed in Section 5.1. The here described correlation method allows high-precision correlation of the cryo-TEM map after the cryo-ET acquisition, thus enabling target validation. To achieve this high precision *a posteriori* correlation, the volume fluorescent signal is acquired a second time by cryo-LM after tomogram acquisition (**Figure 4.1d**). This volume map is called post-LM map, as it is acquired post-cryo-ET acquisition.

4.1.3 Data correlation

In the post-LM map, the fluorescent signal on the lamellae is not detectable anymore. However, the surrounding fluorescent signal of the remaining cell body is still present (**Figure 4.1d**). This remaining signal is sufficient to align the pre- and post-LM using three dimensions by cross-correlation. The Matlab code used for this step can be found in the supplementary data 5.6.1. A strong contrast signal like LDs is used for the image registration. Furthermore, both the pre- and post-cryo-LM volumes

were deconvolved to increase the SNR, as shown in **Figure 4.2**.

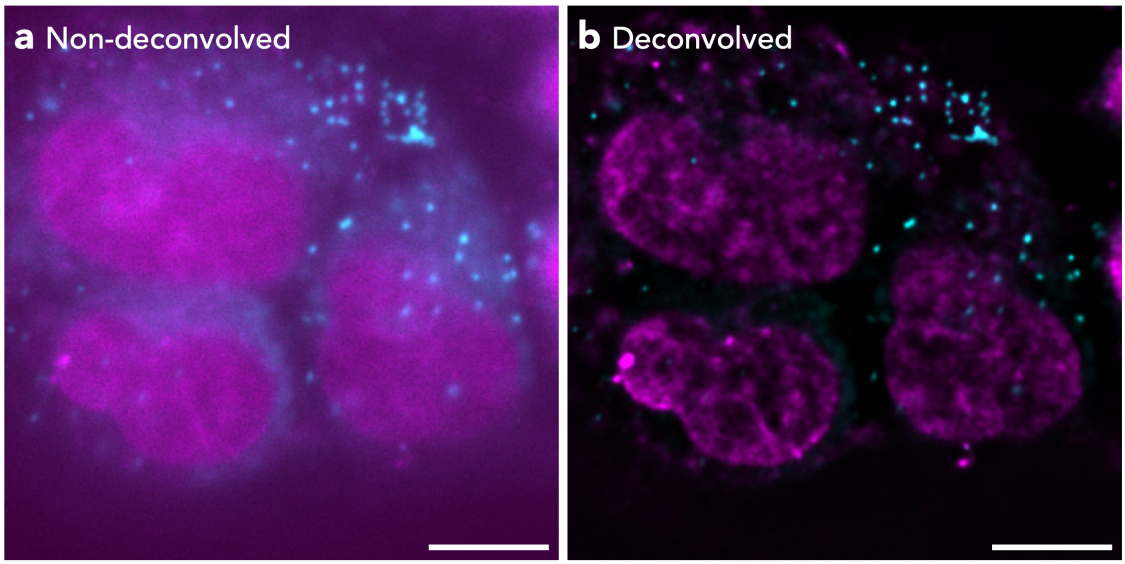

Figure 4.2: Deconvolution of cryo-LM data. (a) MIP of non-deconvolved cryo-LM volume data of A549 cells. Nuclei (magenta) and LDs (cyan) are fluorescently labeled. **(b)** Same volume cryo-LM data as shown in (a) after deconvolution. Scale bars: 10 µm. This figure is a modified reprint from *Methods in Cell Biology*, Volume 162 by Klein, Wachsmuth-Melm, *et al.* (2021), 'Cryo-correlative light and electron microscopy workflow for cryo-focused ion beam milled adherent cells', ©2021, with permission from Elsevier.

This 3D registration step combines the pre-LM map's fluorescent signal, which includes the complete cellular fluorescent signal before cryo-FIB milling, with the bright field signal of the post-LM map, which includes the exact lamella position. This correlated and combined map is called composite-LM map (**Figure 4.1e**). It includes all information necessary for high precision correlation with the cryo-TEM map of the lamella, namely (a) the complete volume fluorescent information of the cell and (b) the lamella position in this volume dataset. Due to the milling geometry of the cryo-FIB/SEM microscope, the produced lamella typically shows a tilt-offset between 8 and 11° relative to the sample (Wagner *et al.* 2020). This results in a Z-height difference of the two lamella ends of over 3.5 µm when assuming a typical lamella length of 20 µm and an effective milling angle of 10°. Thus, the fluorescent signal corresponding to the lamella is found in different Z-planes of

the composite-LM map. This tilt offset is corrected to extract only the fluorescent signal corresponding to the lamella position. The exact lamella tilt is manually measured using the TL-BF channel of the composite-LM map, and the complete volume is rotated accordingly (**Figure 4.1f**). This ensures that all fluorescent signals of the lamella can be found in a single Z-plane of the volume stack. In the following data processing step, one Z-plane of the tilt-corrected composite-LM map is extracted, corresponding to the lamella position. To increase the precision of this extraction step, LDs are used as fiducial markers. To that aim, all LDs on the lamella's cryo-TEM map are identified. Next, the image volume is manually examined in the Z-direction to find the previously identified LDs (**Figure 4.3**). The determined Z-slice is subsequently extracted from the image volume. Finally, the cryo-TEM map is correlated with this extracted Z-slice of the tilt-corrected cryo-LM map using rigid image transformation. LDs and other distinctive features like the corners of the lamella are used as reference points for the transformation.

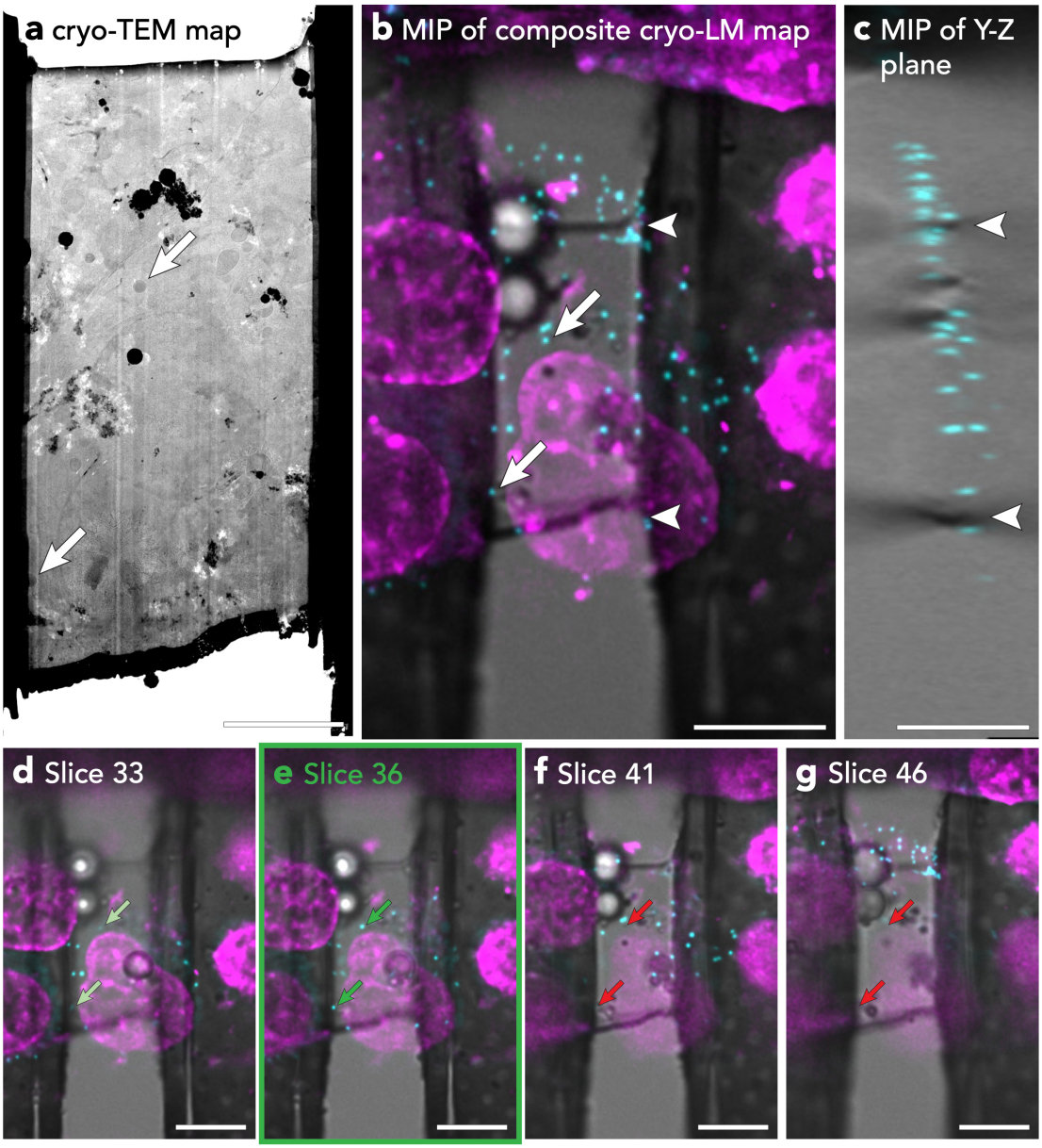

Figure 4.3: (Captions on next page)

Figure 4.3: (Previous page) Correction of lamella tilt. In this figure, the Z-slice extraction, as shown in **Figure 4.1f**, is described in detail. **(a)** Cryo-TEM of the lamella. Two recognizable LDs are marked with white arrows. Scale bar: 5 µm. **(b)** MIP of the cryo-LM map of the same area as the lamella. The TL-BF signal is shown in grayscale, fluorescently labeled nuclei are shown in cyan, and LDs in magenta. The platinum coating can be recognized as dark lines at the borders of the lamella, as indicated by the white arrowheads. The fluorescent signal of the two LDs can already be identified by their location. Scale bar: 10 µm. **(c)** Side view of the MIP of the cryo-LM map (c). The nucleus signal is not shown here. The white arrowheads indicate the platinum coating of the lamella. **(d – f)** Different slices of the volume cryo-LM data (b). The arrows represent the XY-position of the two identified LDs as shown in (a and b). Green arrows indicate slices where the fluorescent signal of the two LDs are visible; red arrows indicate missing fluorescent signal. In Slice 36, the signal intensity of the LD is strongest. Thus, this slice is selected to be extracted from the image volume. Scale bars: 10 µm. This figure is a modified reprint from *Methods in Cell Biology*, Volume 162 by Klein, Wachsmuth-Melm, *et al.* (2021), 'Cryo-correlative light and electron microscopy workflow for cryo-focused ion beam milled adherent cells', ©2021, with permission from Elsevier.

4.1.4 Correlation result

The final correlation result of the example used in this chapter is shown in **Figure 4.4**. The lamella comprises two adjacent A549 cells with their plasma membranes in tight contact (**Figure 4.4a**), and both nuclei partially comprised on the lamella. Nuclei of the cells were fluorescently labeled with SYTO DeepRed, and the correlated fluorescent signal correlates with the nuclei of the cryo-TEM map (**Figure 4.4b**). Besides other cellular organelles, two LDs are localized in one of the two cells on the lamella. The fluorescent signal of LipiBlue, precisely localize with these the LDs. This example shows the precision of the newly developed *in situ* cryo-CLEM workflow. In the next section, the correlation results are further benchmarked.

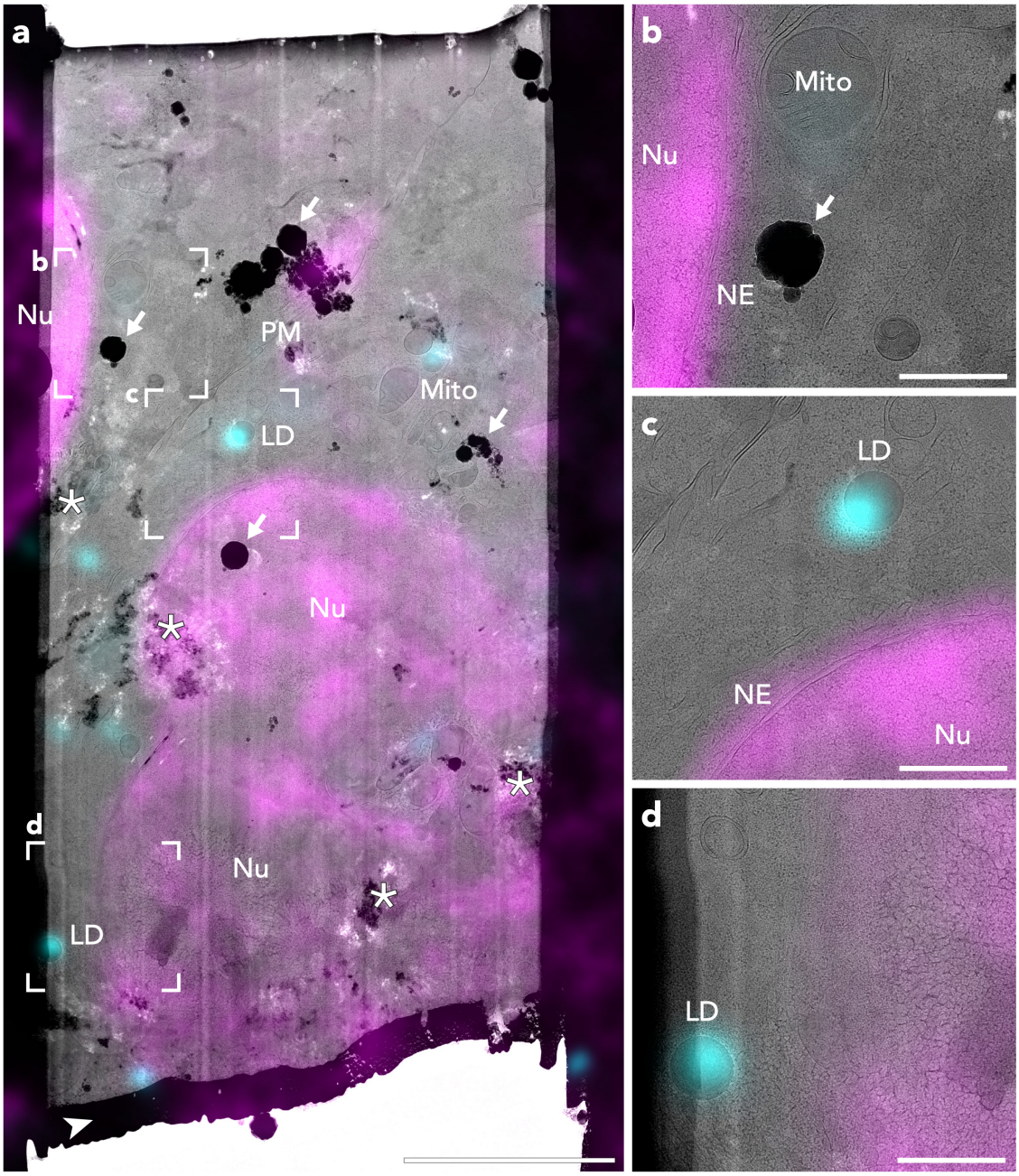

Figure 4.4: (Captions on next page)

Figure 4.4: (Previous page) Example of correlation using the *in situ* cryo-CLEM workflow. A549 cells were grown on EM-grids, nuclei, and LDs were fluorescently labeled. After plunge freezing, the *in situ* cryo-CLEM workflow (**Figure 4.1**) was used to correlate the cryo-TEM and cryo-LM signal. **(a)** Overview of the correlated map. The cryo-TEM map is overlayed with the fluorescent signal of nuclei (magenta) and LDs (cyan). Cellular structures are indicated: Nucleus (Nu), nuclear envelope (NE), plasma membrane (PM), mitochondria (Mito), and lipid droplet (LD). With arrows indicate ice contaminations on the lamella. White asterisks indicate devitrified areas of the lamella. The white arrowhead indicates the platinum layer. Scale bar: 5 µm. **(b – d)** Magnified views of the correlated map, as indicated in (a). Scale bars: 1 µm. This figure is a modified reprint from *Methods in Cell Biology*, Volume 162 by Klein, Wachsmuth-Melm, *et al.* (2021), 'Cryo-correlative light and electron microscopy workflow for cryo-focused ion beam milled adherent cells', ©2021, with permission from Elsevier.

4.1.5 Correlation benchmark using lipid droplets

To validate the reproducibility of the established *in situ* cryo-CLEM workflow, I benchmarked the correlation of LDs in A549 cells. Four lamellae were correlated using the described workflow (**Figure 4.5**). 11 LDs were identified on cryo-TEM maps of the four lamellae. All 11 LDs correlated to the fluorescent LipiBlue signal. To estimate the X-Y correlation precision, the distance between the center of the electron density of the LD on the cryo-TEM map and the center of the fluorescent signal was measured for all 11 LDs to be 124 nm (standard deviation (SD) = 41 nm). This correlation precision surpasses the theoretical spatial resolution of the used cryo-LM system of 248 nm for an excitation wavelength of 447 nm of LipiBlue, as calculated using the Nyquist rate and PSF calculator (Scientific Volume Imaging). Although all LDs found on the cryo-TEM map were successfully correlated, more fluorescent signals can be observed which did not correlate to any LD on the cryo-TEM map (white arrows in **Figure 4.5**). In total, 12 of these unspecific fluorescent signals were detected, which means that 52 % of the observed fluorescent signal did not colocalize to any electron density corresponding to a LD on the cryo-TEM map. As

this signal corresponds to cellular features absent in the lamella, I reference these unspecific signals as 'out-of-lamella signals.'

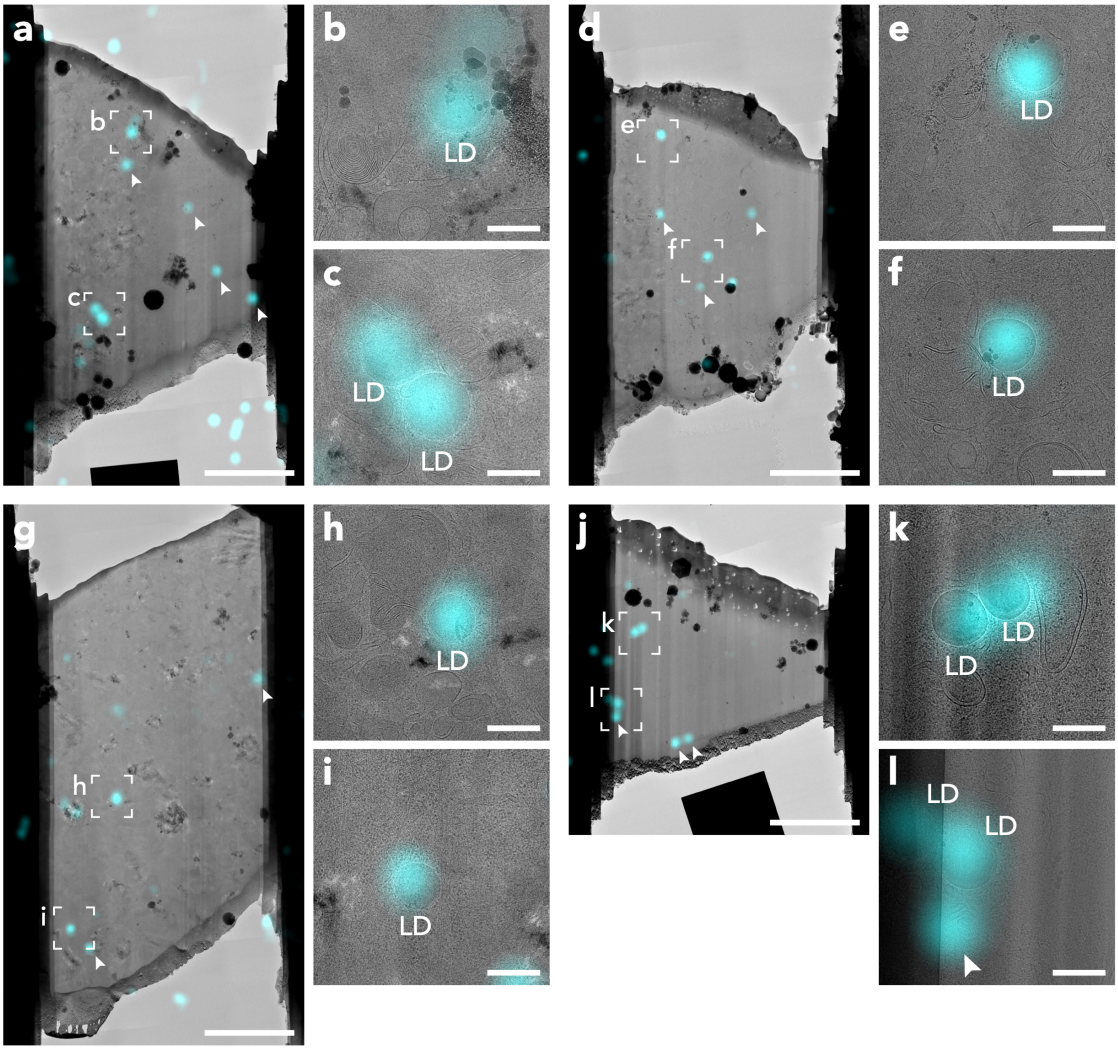

Figure 4.5: Benchmark of the *in situ* cryo-CLEM workflow. A549 cells grown on EM and LDs (cyan) were fluorescently labeled. After plunge freezing, the *in situ* cryo-CLEM workflow was (**Figure 4.1**) was used to correlate the cryo-TEM and cryo-LM signal of four different cells (a, d, g, and j). All LDs (n = 11) present on the four lamellae are shown in magnified views (b, c, e, g, h, i, k, and l). Fluorescent signals which do not correlate to any LD on the lamellae are indicated with white arrowheads. This figure is reprinted under the Attribution 4.0 International (CC BY 4.0) license: 'Post-correlation on-lamella cryo-CLEM reveals the membrane architecture of lamellar bodies' by Klein, Wimmer, *et al.* (2021).

4.1.6 Impact of Z-extraction of correlation precision

To evaluate the impact of the tilt correction and Z-slice extraction (**Figure 4.1f**) on the correlation, I performed the correlation of the same four lamellae used in **Section 4.1.5** but skipped the tilt correction and Z-slice extraction steps. Instead of the extracted Z-slice, the MIP of the cryo-LM volume image was used for the final correlation with the cryo-TEM map. In **Figure 4.6**, the different correlation results for each lamella are shown side-by-side. This comparison enables the evaluation of the impact of Z-slice extraction on the out-of-lamella signal. Instead of 12 LD signals which can not be correlated to any electron density in the cryo-TEM map in case of the complete workflow, 35 of these unspecific signals can be observed when skipping the tilt correction and Z-slice extraction steps. Thus, these two extra steps can reduce the out-of-lamella signal by 66 %.

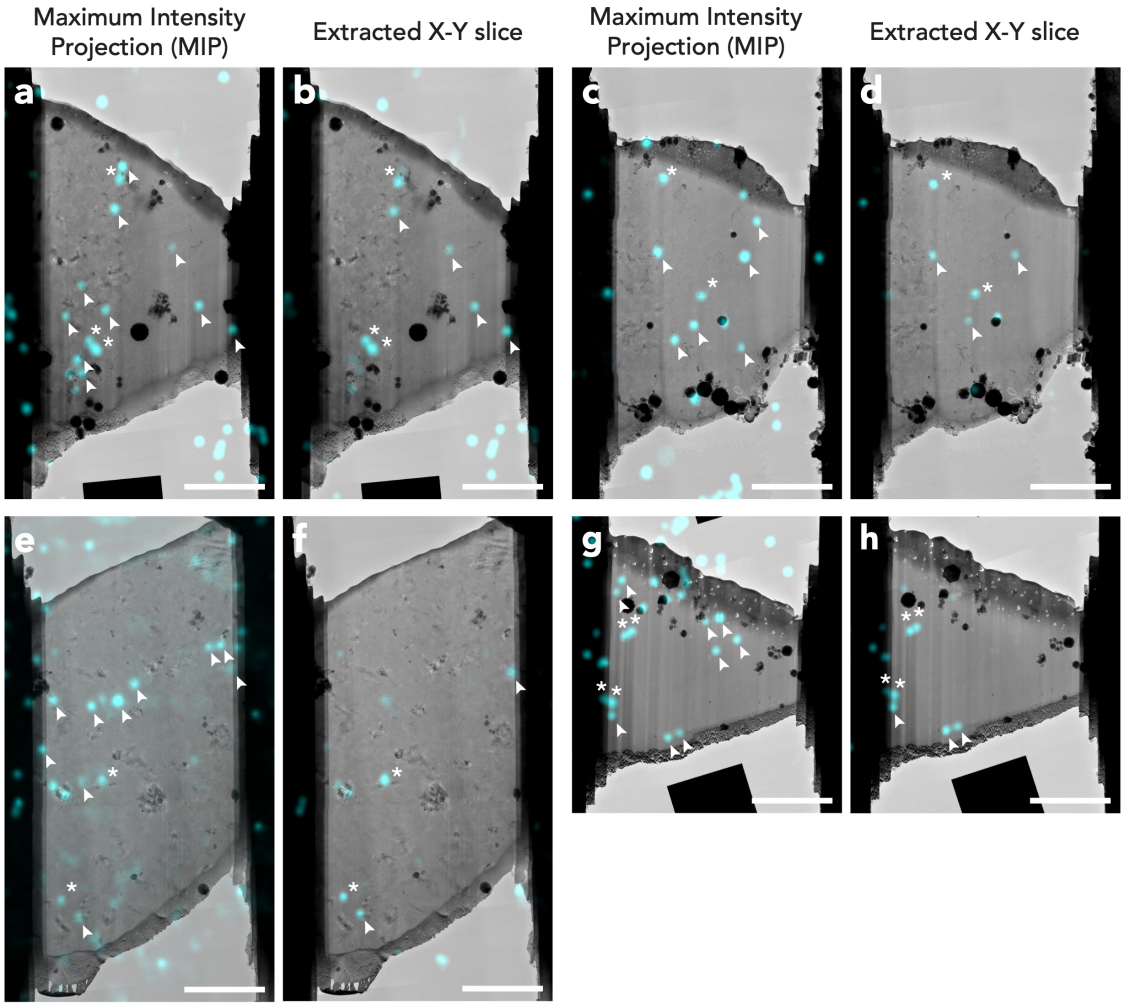

Figure 4.6: Impact of tilt-correction and Z-slice extraction on the correlation benchmark. The four correlated lamellae shown in **Figure 4.5** were processed with the *in situ* cryo-CLEM workflow (**Figure 4.1**) using either the MIP cryo-LM map (a, c, e, and g) or the tilt-corrected and extracted Z-slice of the cryo-LM map (b, d, g, and h). Correlated LDs are indicated with white asterisks, and fluorescent signals which do not correlate to any LD on the lamellae are indicated with white arrowheads. Scale bars: 5 µm. This figure is reprinted under the Attribution 4.0 International (CC BY 4.0) license: 'Post-correlation on-lamella cryo-CLEM reveals the membrane architecture of lamellar bodies' by Klein, Wimmer, *et al.* (2021).

4.2 IAV particle labeling using the fluorescent lipophilic dye nDiO

Characterization of IAV cell entry by *in situ* cryo-ET requires fluorescently labeled viral particles to localize endocytosed viral particles in endosomal organelles of the infected cell. To that aim, I utilized the fluorescent and lipophilic membrane dye nDiO to label the membranes of purified A/WSN/1933 viral particles. After labeling, the viral particles were purified again by a sucrose-purification step. I performed *in vitro* cryo-ET of viral particles mixed with fluorescent beads to characterize these labeled particles. The fluorescent beads were used as fiducial markers, enabling correlation of cryo-LM and cryo-EM signal (**Figure 4.7a**). 46 % of all observed viral particles showed a fluorescent signal (**Figure 4.7b-d**), and the other 54 % of the viral particles were not fluorescently labeled (**Figure 4.7e**). Since the viral particles are only partially fluorescently labeled, it is expected that not all viral particles can be detected by future *in situ* cryo-CLEM experiments. Furthermore, 52 % of all observed fluorescent spots could not be correlated to a virus particle, indicating that the virus preparation contains additional fluorescent material next to labeled viral particles (**Figure 4.7f**). The quantification results are shown in **Figure 4.7g**.

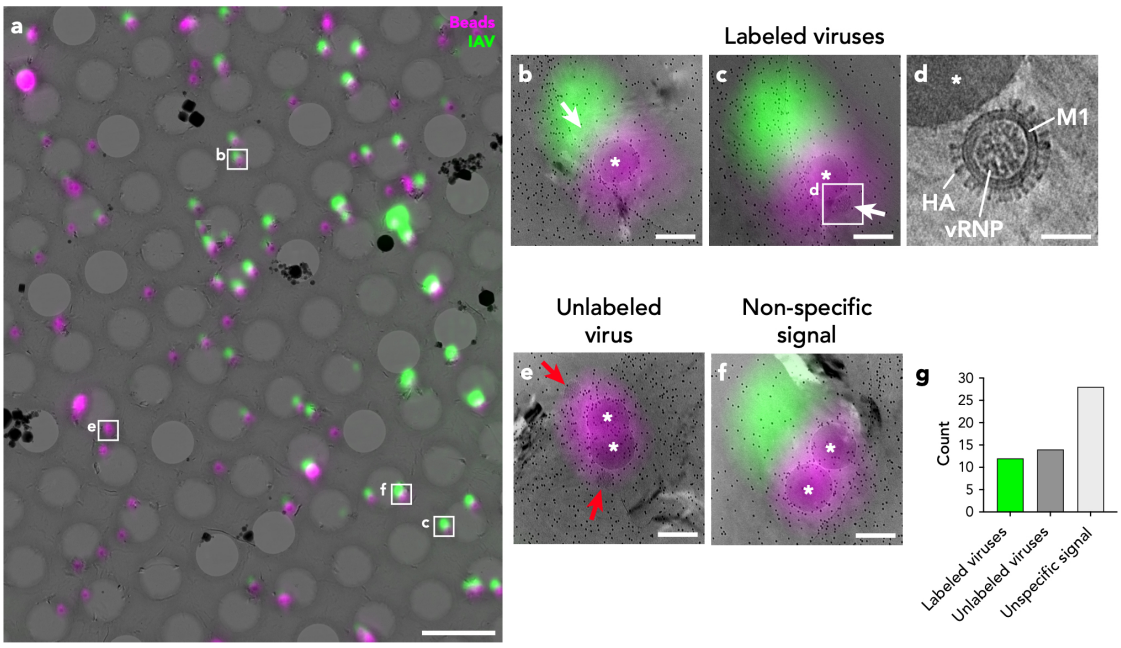

Figure 4.7: *In vitro* cryo-CLEM of influenza A/WSN/1933 (H1N1), labeled with the lipophilic dye nDiO. Fluorescently labeled virus particles were mixed with 200 nm fluorescent beads and gold particles and subsequently plunge-frozen on electron microscopy grids. **(a)** Cryo-TEM overview map correlated with the cryo-LM map. Fluorescent beads are shown in magenta, and the fluorescently labeled virus particles are in green. Scale bar: 20 µm. **(b and c)** Magnified views of the correlated map (a), showing viral particles (white arrows) which correlate to the green fluorescent signal. Scale bars: 200 nm. **(d)** Central slice of a reconstructed tomogram of a fluorescently labeled virus particle, shown in (c). The viral glycoprotein HA, the scaffolding M1 layer below the viral envelope, and the vRNPs are indicated. Scale bars: 50 nm. **(e)** Magnified view of the correlated map (a), showing viral particles (red arrow) which do not correlate to the fluorescence signal. Scale bar: 200 nm. **(f)** Magnified view of the correlated map (a), showing fluorescent signal which does not correlate to viral particles. Scale bar: 200 nm. **(g)** Classification of correlations in labeled viral particles, unlabeled viral particles, and non-specific fluorescent signals.

4.3 Interferon induced transmembrane protein 3 (IFITM3)

4.3.1 Generation of A549-IFITM3 stable cell lines

To study the antiviral properties of IFITM3, I utilized the human epithelial lung cell line A549, an established model for viral infection studies. Although IFN treatment induces IFITM3 expression in these cells (**Figure 4.8a and b**), it also upregulates various other ISGs (see **section 1.3.3**) and is, therefore, suboptimal for studying the antiviral effect of IFITM3 alone. Thus, I established two A549 cell lines stably overexpressing IFITM3. A549-IFITM3 (high) shows a 3.94-fold higher and A549-IFITM3 (low) a 1.63-fold higher expression compared to IFN treated A549 cells (**Figure 4.8a and b**). IFITM3 expression did not induced expression of IFITM1 or IFITM2 (**Figure 4.8c**). In addition to these two cell lines, I also evaluated an A549 cell line overexpressing IFITM3 tagged with the fluorescent protein neonGreen (nG) (Desai *et al.* 2014). This cell line was kindly provided by Professor Gregory B. Melikyan (Emory University, USA). Using FACS, I sorted these cells in high and low expressing populations (**Figure 4.8d and e**).

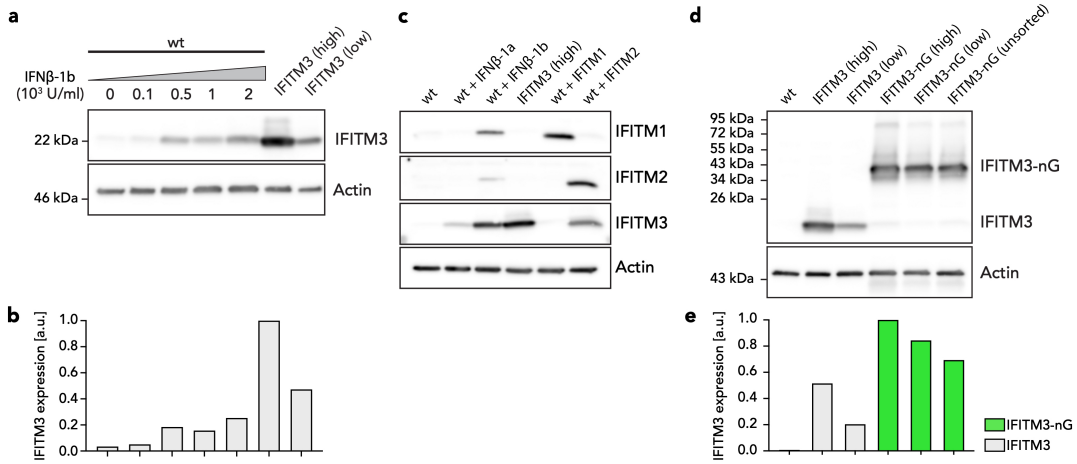

Figure 4.8: (Captions on next page)

Figure 4.8: IFITM3 expression levels of different stable A549 cell lines. (a) IFN-induces IFITM3 expression in A549 cells. A549 cells were treated with different concentrations of IFN (between 0 and 2×10^3 U/ml IFN), and the IFITM3 expression levels were analyzed by immunoblotting and compared to monoclonal A549 cells stably overexpressing non-tagged IFITM3 (high/low). Actin was used as a loading control. **(b)** Quantification of the expression levels based on the immunoblots shown in (a). Expression levels were normalized to Actin and reported as relative expression. a.u. = arbitrary unit. **(c)** The expression levels of IFITM1–3 were analyzed for A549 cells (lane 1), A549 cell treated with 1×10^3 U/ml IFNβ-1a or IFNβ-1b (lanes 2 and 3), A549-IFITM3 (high) (lane 3), and A549 cells transiently expressing IFITM1 or IFITM2 (lanes 4 and 5). **(d)** The expression level of the following A549 cell lines was analyzed by immunoblot analysis: Non-overexpression A549 cells (wt); Two clones of monoclonal A549 cells stably overexpressing non-tagged IFITM3 (high/low); Three polyclonal A549 cell lines stably overexpression IFITM3 tagged with the fluorescent nG. Cells were sorted by fluorescence-activated cell sorting (FACS) for high or low expressing cells (high/low), and non-sorted cells were also analyzed (unsorted). Actin was used as a loading control. **(e)** Quantification of the expression levels based on the immunoblots shown in (a). Expression levels were normalized to Actin and reported as relative expression. Romy Brecht and Nina Reddmann were lab rotation students in the lab and supported the establishment of the cell lines under my supervision. This figure is a modified reprint from *Cell Host Microbe*, Volume 31.4 by Klein, Golani, *et al.* (2023), 'IFITM3 blocks influenza virus entry by sorting lipids and stabilizing hemifusion', ©2023, with permission from Elsevier.

4.3.1.1 Inhibition of viral infection

To evaluate the antiviral properties of the overexpressed IFITM3 and IFITM3-nG in the established cell lines, I performed an infection assay utilizing the established reporter virus A/WSN/1933(H1N1)-PA-mScarlet. A549 cells showed an infection rate of 98.8 % (**Figure 4.9e–h**). A549-IFITM3 (high), expressing non-tagged IFITM3, showed a 11.5-fold reduced infection rate of 8.2 % (**Figure 4.9i–l**). Importantly, overexpression of the fluorescently tagged IFITM3-nG still showed an infection rate of 92.6 % (**Figure 4.9m–p**), indicating that the fluorescent tag interfered with the antiviral properties of IFITM3.

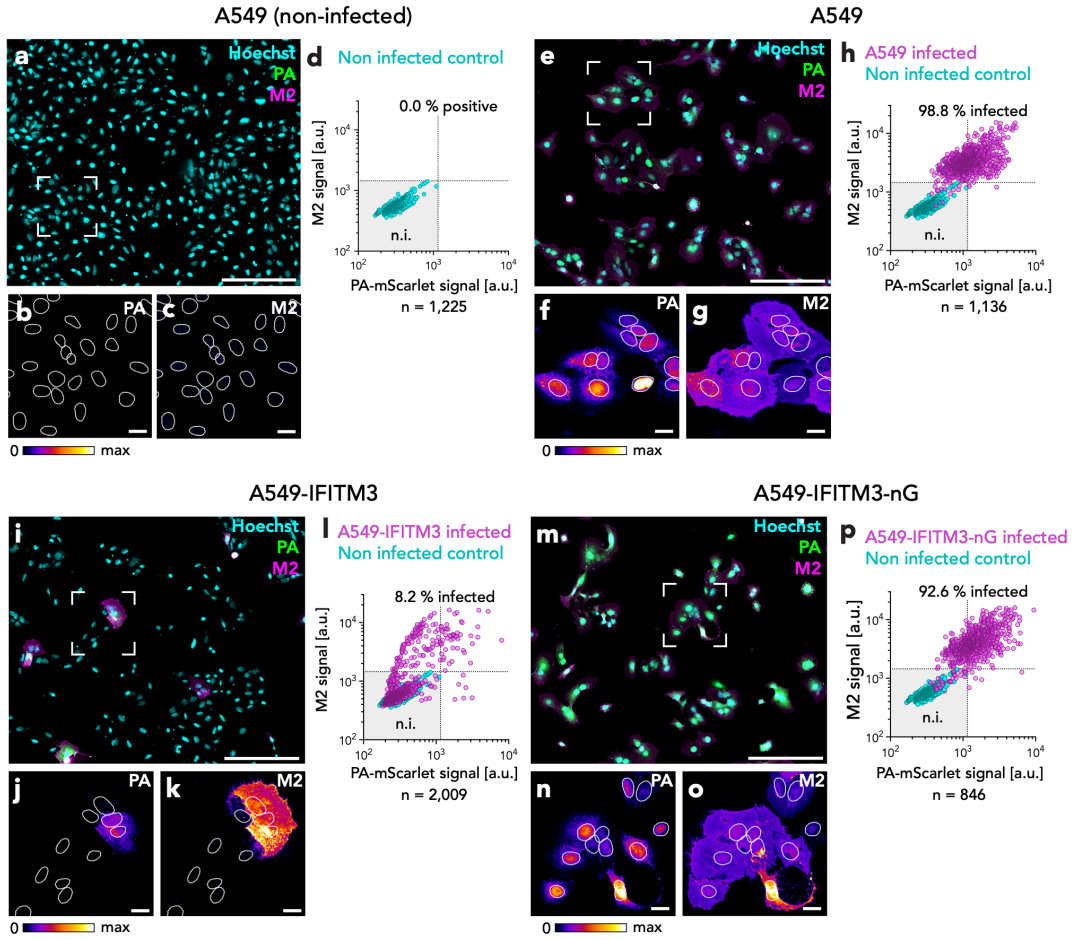

Figure 4.9: IFITM3-induced IAV infection inhibition. A549 cells (e – h), A549-IFITM3 cells (i – l), and A549-IFITM3-nG cells (m – p) were infected with the reporter virus A/WSN/1933(H1N1)-PA-mScarlet with a MOI of 3. Non-infected A549 cells (a – d) were used as a negative control. Cells were fixed after 24 hours post infection (hpi) and immunolabeled against the viral M2 protein; nuclei were fluorescently labeled using Hoechst. For each sample, widefield fluorescent maps were acquired (a, e, i, m), with the Hoechst signal shown in cyan, the PA-mScarlet signal shown in green, and the M2 signal shown in magenta. For each sample, a magnified area for PA (b, f, j, n) or M2 (c, g, k, o) signal only is shown using a fire lookup table. Nuclei were automatically segmented (white lines in magnified areas), and the average signal values in the segmented regions for PA-mScarlet and M2 were measured. Values were blotted for all analyzed cells as scatter blots (d, h, l, p). Thresholds for infected cells were determined by the non-infected control (d), and the proportion of infected cells was determined for each sample, as indicated in the scatter blots. This infection assay was jointly performed with Carmen Lahr, a Master's student I supervised. Scale bars: (a, e, i, m) 200 µm, (b, c, f, g, j, k, n, o) 20 µm. This figure is a modified reprint from *Cell Host Microbe*, Volume 31.4 by Klein, Golani, *et al.* (2023), 'IFITM3 blocks influenza virus entry by sorting lipids and stabilizing hemifusion', ©2023, with permission from Elsevier.

4.3.1.2 Inhibition of viral cell entry

Using a Blam-based membrane fusion assay, the impact of IFITM3 on the viral-induced membrane fusion in the endosomal-lysosomal system was evaluated. To that aim, influenza VLPs expressing M1-Blam were utilized (**Figure 4.10**). A fluorescence resonance energy transfer (FRET)-based readout allows the quantification of VLP entry into the host cell's cytoplasm. In line with the infection assay (**Section 4.3.1.1**), IFN treatment of A549 cells leads to an up to 8.7-fold reduced influenza VLPs entry (**Figure 4.10a and e**). Similarly, overexpression of non-tagged IFITM3 showed a similar reduction of influenza VLPs entry of 10.5-fold (**Figure 4.10b, c, and e**), indicating that IFITM3 prevents viral cell entry. The nG-tagged IFITM3 variant showed, similar to the viral infection assay (**Figure 4.9i – l**), only a weak reduction of influenza VLP entry of 20 % (**Figure 4.10d and e**), further confirming that the A549-IFITM3-nG cell line is non-functional. Thus, all further experiments are conducted with the non-tagged A549-IFITM3 (high) cell line. Since I can not use the fluorescently tagged version of IFITM3 for future cryo-CLEM experiments of IAV infected A549-IFITM3 cells, I have to rely on the signal of the fluorescently labeled viral particles (**Section 4.2**) for correlation.

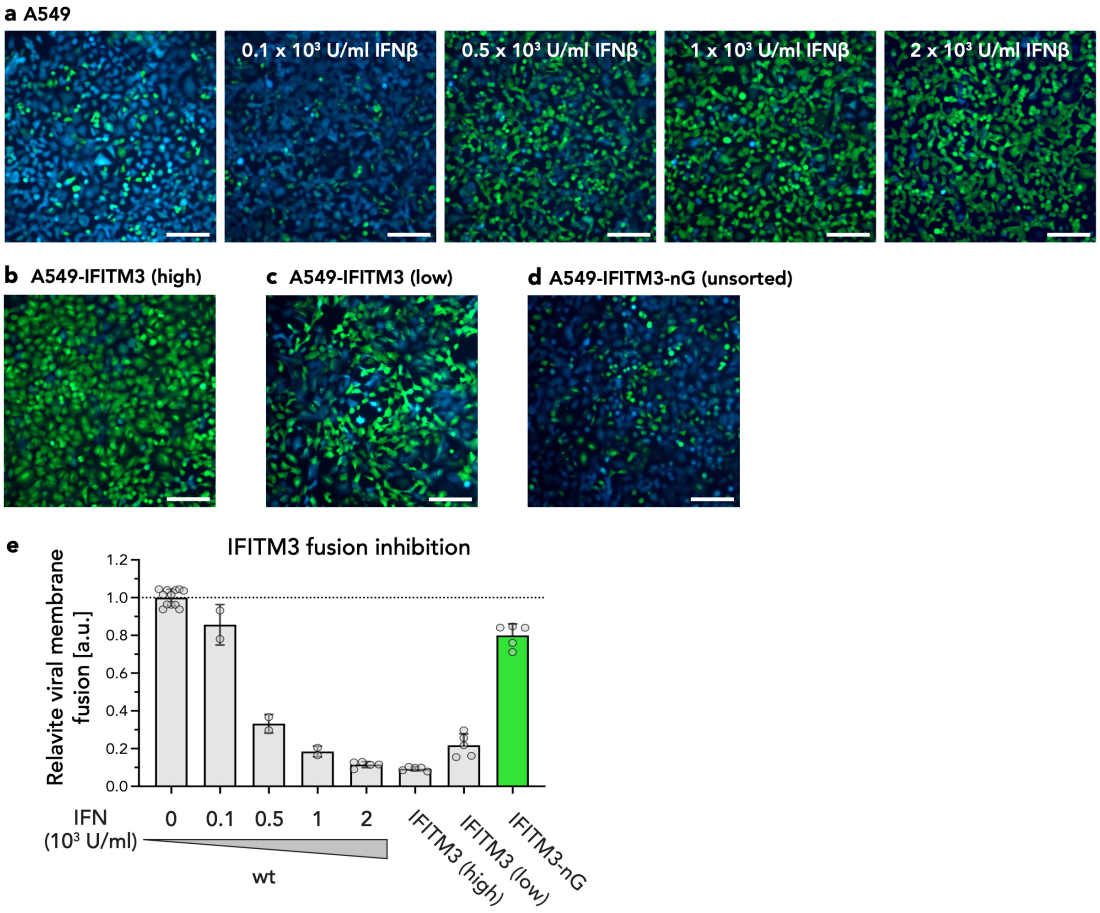

Figure 4.10: IFITM3-induced IAV entry inhibition. Blam assays were performed to quantify the cytoplasmic entry of influenza VLPs expressing M1-Blam. Cells were stained with the FRET dye CCF4-AM and subsequently infected with M1-Blam VLPs. Blam can cleave CCF4-AM, which is located in the cytoplasm, which leads to a fluorescent emission shift from green (530 nm) to blue (460 nm). The $^{460}/_{530}$ nm ratios were quantified on a plate reader **(e)**, and subsequently, qualitative fluorescence microscopy images were acquired **(a – d)**. The following samples were analyzed: A549 cells, treated with different IFN concentrations ($0 - 2 \times 10^3$ U/ml) (a). A549-IFITM3 stable cell line with a high IFITM3 levels (b). A549-IFITM3 stable cell line with a low IFITM3 level (c). A549-IFITM3-nG stable cell line (d). The viral fusion assay was jointly performed with Romy Brecht, a rotation student I supervised. Scale bars: (a – d) 100 µm. This figure is a modified reprint from *Cell Host Microbe*, Volume 31.4 by Klein, Golani, *et al.* (2023), 'IFITM3 blocks influenza virus entry by sorting lipids and stabilizing hemifusion', ©2023, with permission from Elsevier.

4.3.1.3 Cellular localization of IFITM3

IFITM3 is known to be mainly localized in the endosomal-lysosomal system (Feeley *et al.* 2011; Kummer *et al.* 2019). To validate the cellular localization of IFITM3 in the established A549-IFITM3 cell line, I performed a colocalization analysis with the late endosomal marker Rab7 (Seaman *et al.* 2009; TT Liu *et al.* 2012; Chesarino, McMichael, *et al.* 2014) and the lysosomal marker LAMP1 (Eskelinen 2006). IFITM3 showed a partial localization with both Rab7 and LAMP1 with Pearson's correlation coefficients of 0.51 ± 0.08 and 0.64 ± 0.14, respectively (**Figure 4.11**). These results indicate that overexpressed IFITM3 shows the expected cellular distribution in the endosomal-lysosomal system. This is important for future cryo-CLEM experiments of IAV infected A549-IFITM3 cells since we can not use fluorescently tagged IFITM3, as the antiviral properties are mostly lost when tagging with nG (**Sections 4.3.1.1 and 4.3.1.2**). Thus, we can not directly correlate fluorescent IFITM3 signal but have to rely on the fluorescent signal of labeled viral particles (**Section 4.2**) to localize them in endosomes during viral entry. This colocalization analysis shows that endosomal-lysosomal organelles show a strong colocalization with IFITM3, and thus it is likely that IFITM3 is present in observed events. Still, a direct validation during cryo-CLEM experiments is not possible.

I further analyzed the number and volume of IFITM3 positive organelles per cell. IFN treatment and stable IFITM3 overexpression drastically increased the number of IFITM3 positive organelles by 11-fold and 34-fold, respectively (**Figure 4.12**). The A549-IFITM3 cell line showed 801 ± 46 IFITM3-positive organelles per cell (**Figure 4.12j**) with an average volume of 0.4 µm³ (**Figure 4.12k**). The number of organelles per cell is an important consideration for *in situ* cryo-ET since after cryo-FIB milling, only 0.5 – 1 % of the cell volume is present on the lamella. Thus, between 4 and 8 IFITM3-positive organelles are expected per lamella. This range of expected events is well-suited for future cryo-CLEM experiments of IAV infected A549-IFITM3 cells.

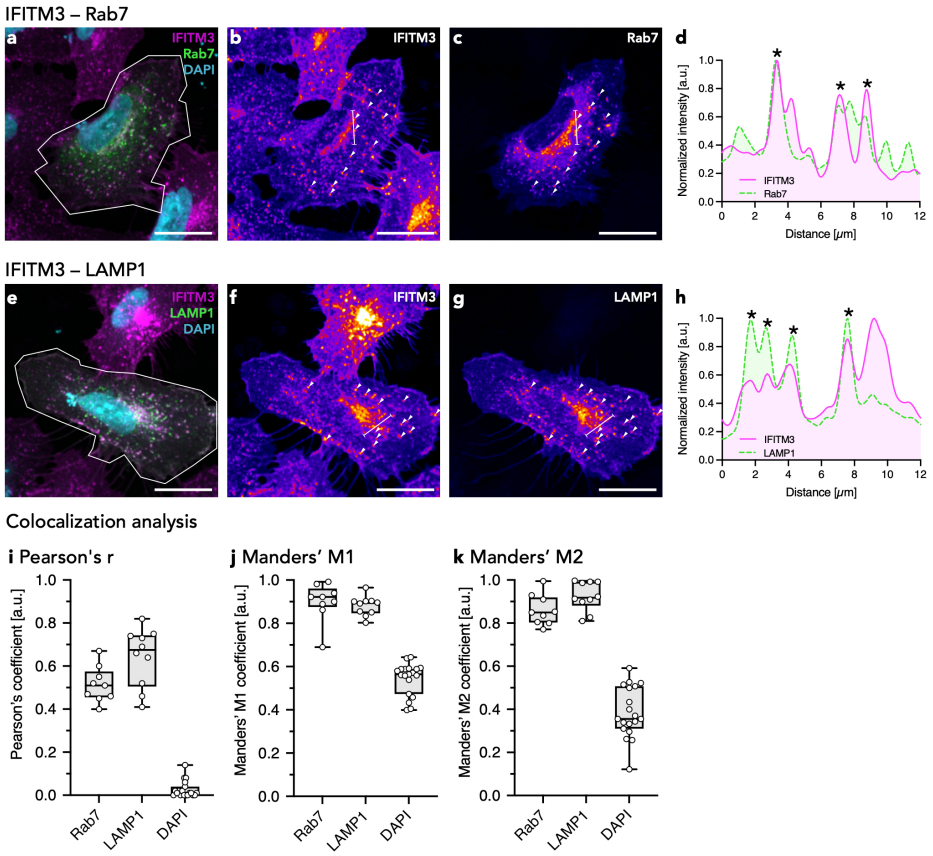

Figure 4.11: Cellular localization of IFITM3. (a – d) Colocalization analysis between IFITM3 and Rab7. Rab7-eGFP was transiently overexpressed in A549-IFITM3 cells. (a) Central slice of a composite image. IFITM3 is shown in magenta, Rab7 in green, and the nucleus in cyan. The region of interest (ROI) for colocalization analysis is indicated in white. (b and c) The fluorescent signal of IFITM3 and Rab7 are represented using a fire lookup table (LUT). Representative organelles, which show both IFITM3 and Rab7 signals, are indicated with white arrowheads in both panels. (d) Plot profile of the fluorescent signals along the line shown in (b and c). Positions where both signals correlate are indicated with an asterisk. **(e – h)** Colocalization analysis between IFITM3 and LAMP1. LAMP1-eGFP was transiently overexpressed in A549-IFITM3 cells. (a) Central slice of a composite image. IFITM3 is shown in magenta, LAMP1 in green, and the nucleus in cyan. The ROI for colocalization analysis is indicated in white. (f and g) The fluorescent signal of IFITM3 and LAMP1 are represented using a fire LUT. Representative organelles, which show both IFITM3 and LAMP1 signals, are indicated with white arrowheads in both panels. (h) Plot profile of the fluorescent signals along the line shown in (b and c). Positions where both signals correlate are indicated with an asterisk. **(i – k)** Colocalization analysis of IFITM3 with Rab7 and LAMP1 for 9 and 10 individual cells, respectively. Nuclei, fluorescently labeled with DAPI, were used as a negative control. Pearson's correlation coefficient (i) and Manders' correlation coefficients (j and k) were calculated for each cell. Data are represented as Box-Whisker plots, showing all data points, median (central line), and 25 % and 75 % quantiles (box boundaries). Scale bars: 20 µm

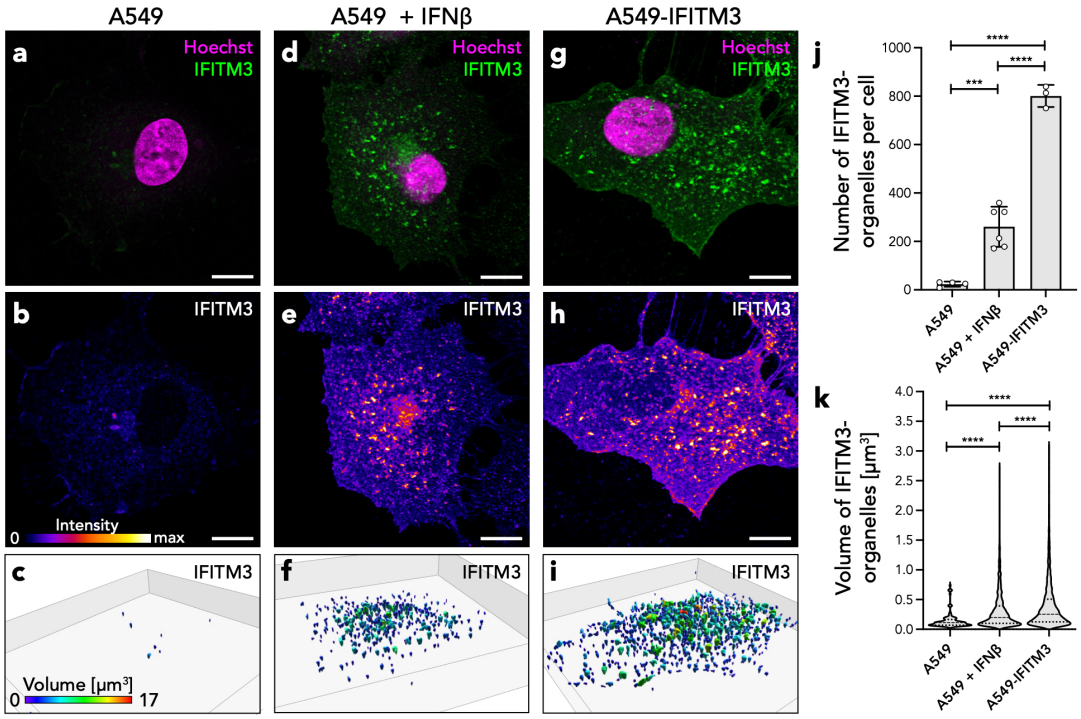

Figure 4.12: Quantification of IFITM3-positive organelles. A549 cells (a – c), A549 cells treated with 1×10^3 U/ml IFN (d – f), and A549-IFITM3 cells (g – i) were immunolabeled against IFITM3. Nuclei were fluorescently labeled with Hoechst. **(a – i)** For each sample, one representative cell is shown in the top row as a composite image, with IFITM3 in green and Hoechst in magenta (a, d, g). The middle row (b, e, h) shows only the IFITM3 signal, using a fire lookup table. The bottom row shows the three-dimensional segmentation of the IFITM3 signal. Individual segmented objects are color-coded according to their volume. **(j)** Quantification of the number of IFITM3-positive organelles. Each data point represents one segmented cell. Data is visualized as bar graphs showing the mean. Error bars represent the SD. **(k)** Quantification of the volume of individual IFITM3-positive organelles. Data is represented as a violin plot indicating the mean (dashed line) and the upper/lower quantiles (dotted lines). Statistical significances were analyzed by unpaired t-tests, with * for $p < 0.05$, ** for $p < 0.01$, *** for $p < 0.001$ **** for $p < 0.0001$. Scale bars: 10 µm. This figure is a modified reprint from *Cell Host Microbe*, Volume 31.4 by Klein, Golani, *et al.* (2023), 'IFITM3 blocks influenza virus entry by sorting lipids and stabilizing hemifusion', ©2023, with permission from Elsevier.

4.3.1.4 Ultrastructural characterization of IFITM3-positive organelles

Since fluorescent microscopy analysis revealed that IFITM3 partially localizes with both endosomal and lysosomal markers (**Figure 4.11**), I further characterized the cellular localization of IFITM3 by ET of HPF/FS samples. To localize IFITM3 on the HPF/FS sections, I utilized immunogold labeling against IFITM3 (**Figure 4.13**). I selected organelles with a multivesicular body (MVB) morphology for tomogram acquisition since this is characteristic for endosomal and lysosomal organelles (Gruenberg 2020). This allowed me to quantify the number of gold particles for A549 cells, A549 cells treated with IFN, and A549-IFITM3 cells. A549-IFITM3 showed a significant 5.3 fold increase of immunogold particles per organelle compared to A549 cells (**Figure 4.8**), which is in line with the increased IFITM3 expression level in this cell line (**Figure 4.8j**). The gold particles were found preferentially on the limiting endosomal membrane, as shown in **Figure 4.13g**. This shows that IFITM3 specifically localizes to MVB organelles like LEs.

Two independent studies reported an IFITM3 induced increase of ILVs in late endosomes (Feeley *et al.* 2011; Amini-Bavil-Olyaee *et al.* 2013), and thus the 'fusion decoy' hypothesis was formulated by Desai *et al.* (2014) (**Section 1.3.3.1.4**). It was suggested that an increased number of ILVs could redirect viral membrane fusion from the limiting late endosomal membrane to fusion with ILVs, thus blocking viral entry. Therefore, I quantified the number of ILVs per organelles in A549 cells, A549 cells treated with IFN, and A549-IFITM3 cells (**Figure 4.14**). Three-dimensional segmentation of the tomograms allowed quantification of ILVs in the volume data. The quantification showed no significant difference in the number of ILVs for the three different samples (**Figure 4.14g**), which shows that IFITM3 does not influence the number ILVs in LEs.

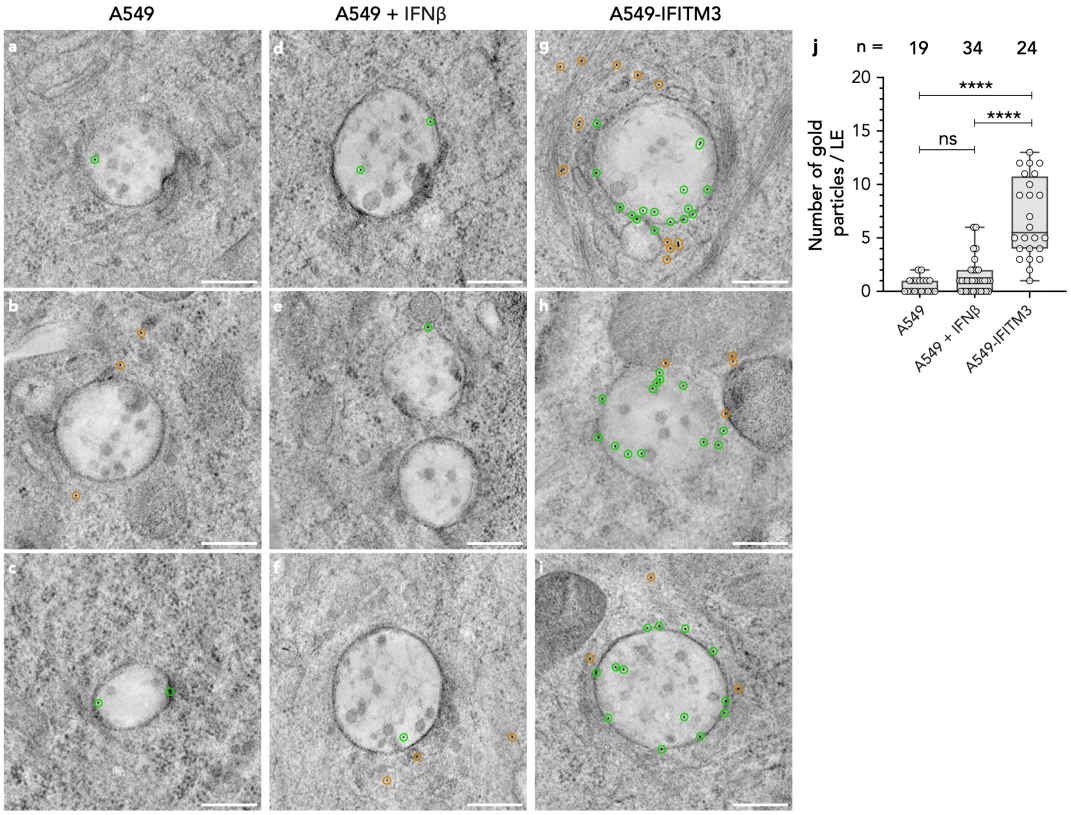

Figure 4.13: IFITM3 is localized in multivesicular organelles. (a – i) A549 cells (a – c), A549 cells treated with 2×10^3 U/ml IFN (d – f) and A549-IFITM3 cells (g – i) were structurally analyzed by ET of HPF/FS samples. In addition, immunogold labeling against IFITM3 was performed. Tomograms of LE-like organelles featuring a MVB-like morphology were acquired. For each sample, average intensity projections of three exemplary tomograms are shown, which allows the identification of gold particles. Particles indicated with green circles show anti-IFITM3 immunogold which localizes to the MVB-like organelle, whereas orange-labeled particles are localized in the cytoplasm of the cell. Scale bars: 200 nm. **(j)** Quantification of the number of gold particles per LE for the three different samples. Each data point represents one organelle. Data are represented as Box-Whisker plots, showing all data points, median (central line), and 25 % and 75 % quantiles (box boundaries). Statistical significances were analyzed by unpaired t-tests, with * for $p < 0.05$, ** for $p < 0.01$, *** for $p < 0.001$ **** for $p < 0.0001$. The sample preparation steps (HPF/FS, ultramicrotomy, and immunolabeling) were performed by Androniki Kolovou. Data acquisition was performed by Martin Schorb. The quantification was jointly performed with Mehdi Hosseinzadeh, a student assistant I supervised. This figure is a modified reprint from *Cell Host Microbe*, Volume 31.4 by Klein, Golani, *et al.* (2023), 'IFITM3 blocks influenza virus entry by sorting lipids and stabilizing hemifusion', ©2023, with permission from Elsevier.

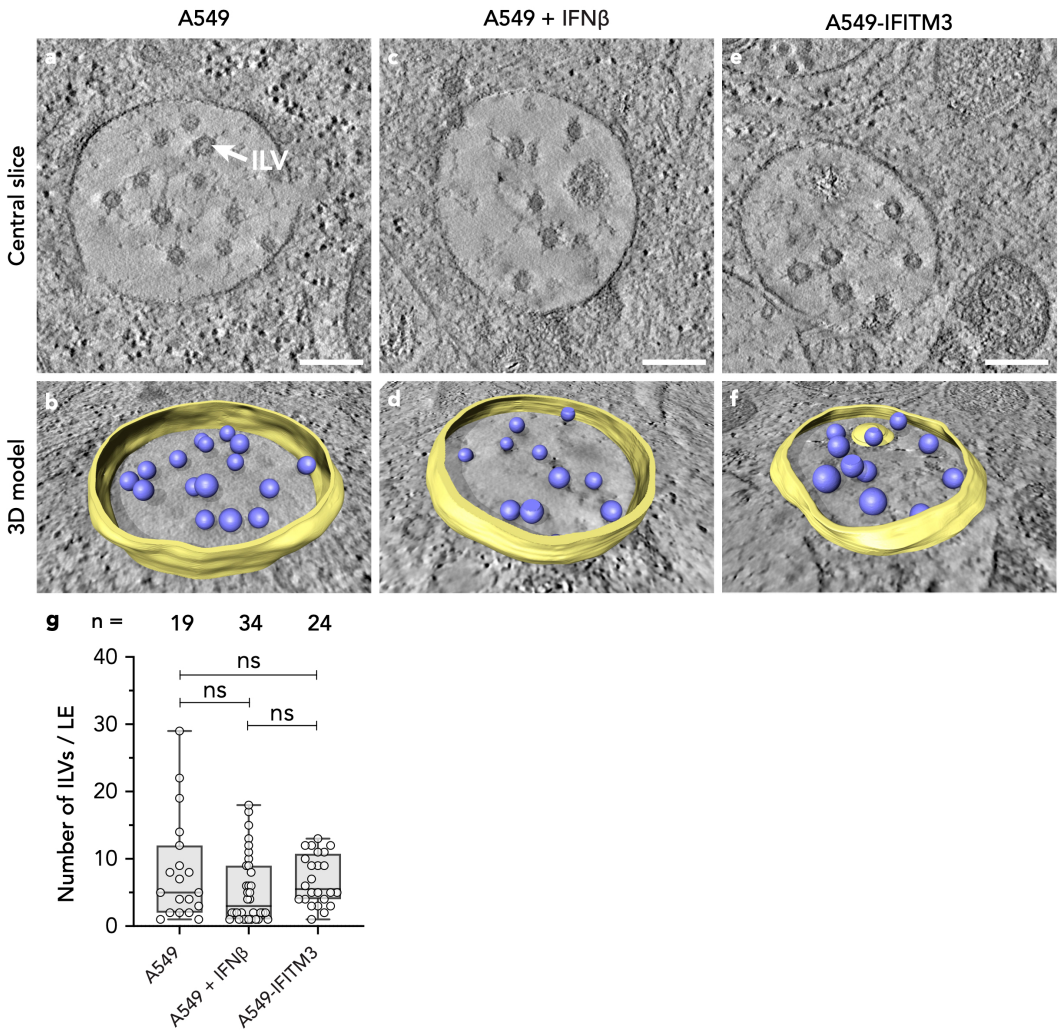

Figure 4.14: IFITM3 does not impact the number of ILVs in multivesicular organelles. A549 cells (a and b), A549 cells treated with 2×10^3 U/ml IFN (c and d) and A549-IFITM3 cells (e and f) were structurally analyzed by ET of HPF/FS samples. In addition, immunogold labeling against IFITM3 was performed. **(a – f)** Tomograms of LE-like organelles featuring a MVB-like morphology were acquired. In the top row (a, c, e), central slices of exemplary tomograms are shown. In the bottom row (b, d, g), three-dimensional segmentations of the tomograms are shown with the organelle membrane in yellow and ILVs in purple. Scale bars: 200 nm. **(g)** Quantification of the number of ILVs per LE. Data are represented as Box-Whisker plots, showing all data points, median (central line), and 25 % and 75 % quantiles (box boundaries). The significance of the difference was analyzed by an unpaired t-test with * for $p < 0.05$, ** for $p < 0.01$, *** for $p < 0.001$ **** for $p < 0.000$. The sample preparation steps (HPF/FS, ultramicrotomy, and immunolabeling) were performed by Androniki Kolovou. Data acquisition was performed by Martin Schorb. The quantification was jointly performed with Mehdi Hosseinzadeh, a student assistant I supervised. This figure is a modified reprint from *Cell Host Microbe*, Volume 31.4 by Klein, Golani, *et al.* (2023), 'IFITM3 blocks influenza virus entry by sorting lipids and stabilizing hemifusion', ©2023, with permission from Elsevier.

4.3.1.5 IAV entry half-time

To estimate the optimal timing for future cryo-CLEM experiments of IAV infected A549-IFITM3 cells, I conducted an experiment to see when the virus-induced membrane fusion occurs. I used fluorescence microscopy to track the number of infected cells over time and added NH_4Cl at different time points post-infection (**Figure 4.15**). NH_4Cl is membrane permeable and increases the endosomal pH (Ohkuma & Poole 1978). Since IAV membrane fusion depends on the low pH of the endosome, NH_4Cl treatment stops viral entry at the time of treatment. Thus, this approach allows measuring the percentage of infected cells at a given time post-infection and, in turn, allows estimating the duration of viral endocytic uptake (Lozach *et al.* 2010). Using this approach, I determined the half-time of IAV-mediated membrane fusion to be 45 min (**Figure 4.15b**). At this point, 50 % of the infected cells had completed the fusion process. Based on these data, I chose 1 hpi as a time point for future cryo-CLEM experiments of IAV infected A549-IFITM3 cells, as at this time point, the majority (69 %) of viruses are expected to be fused with the endosomal membrane in non-inhibitory conditions, and thus increases the probability of observing the impact of IFITM3 on viral entry.

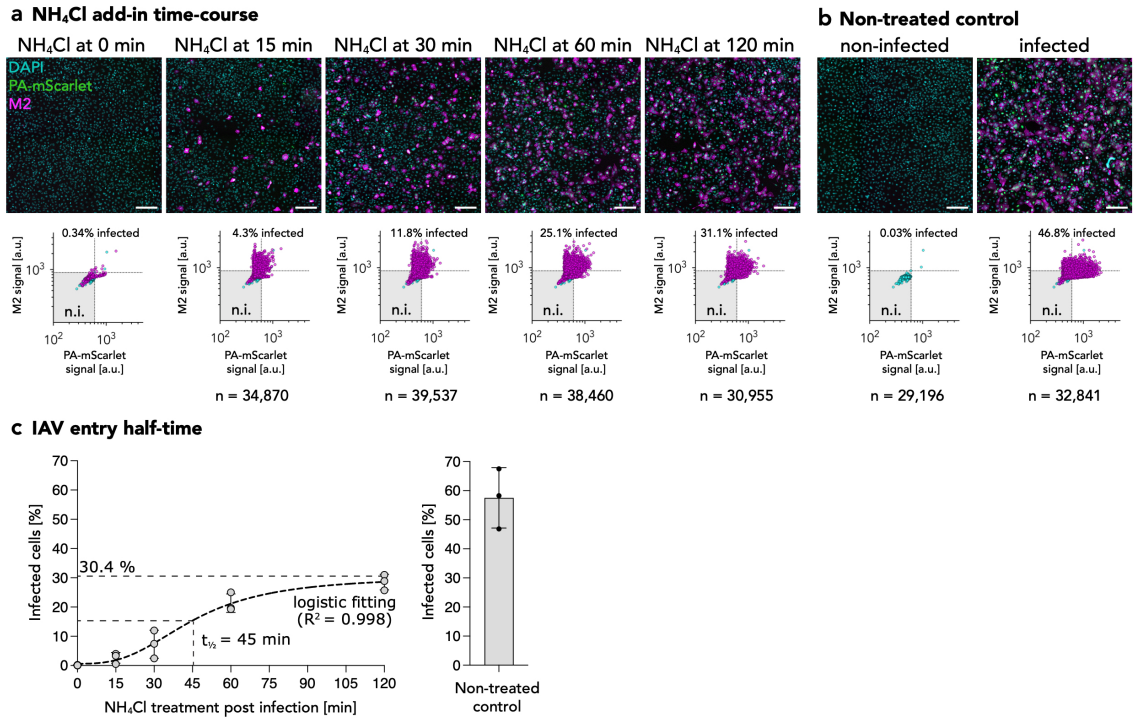

Figure 4.15: IAV entry time-course. A549 cells were infected with the reporter virus A/WSN/1933(H/N1)-PA-mScarlet using a MOI of 3 and a synchronized infection. Infected cells were treated with 50 mM NH_4Cl at different time points. Cells were fixed between 12 and 14 hpi, immunolabeled against M2, and nuclei were fluorescently labeled with DAPI. The percentage of infected cells was determined using fluorescent microscopy for all NH_4Cl add-in time points. **(a and b)** NH_4Cl add-in time-course for 0, 15, 30, 60, and 120 minutes post infection (mpi) (a). As controls, non-treated A549 cells were used (b). For each time point, one representative fluorescent image is shown with the nucleus in cyan, PA-mScarlet in green, and M2 in magenta. Each nucleus was automatically segmented, and the average PA-mScarlet and M2 signal was determined. Below each image, the scatter plot of all analyzed cells is shown. The number of analyzed cells is indicated (n). The non-treated and non-infected sample (b) was used to determine thresholds for both PA-mScarlet and M2 signals, as indicated with the dotted lines. Two data points were excluded. The percentage of infected cells for each time point was determined based on these thresholds. **(c)** The NH_4Cl add-in time-course was repeated in two independent experiments, and the percentage of infected cells was plotted against the treatment time. The data were fitted using a four-parameter logistic (4PL) curve (R2 = 0.998) (dotted line). The half-time ($t_{1/2}$) for viral penetration was determined to be 45 min. This entry assay was jointly performed with Carmen Lahr, a Master's student I supervised.

4.3.2 Ultrastructural characterization of influenza A virus infection in IFITM3 overexpressing cells

As shown previously, IFITM3 blocks the release of the viral genome into the cytoplasm of the host cell (Brass *et al.* 2009; Desai *et al.* 2014), but the molecular mechanism is not well understood. Different molecular mechanisms were proposed, as discussed in **Section 1.3.3.1.4**. To understand the antiviral process on a structural level, I utilized *in situ* cryo-ET of infected cells. To that aim, I used the previously established A549-IFITM3 cell line, which shows a stable overexpression of IFITM3 (**Figure 4.8**), effectively blocking IAV infection (**Figure 4.9**) by inhibition of viral cytoplasmic entry (**Figure 4.10**). In this cell line, IFITM3 is localized in the endosomal-lysosomal system (**Figures 4.10 and 4.11**), as shown by previous results (Feeley *et al.* 2011; Weston *et al.* 2016). To localize viral particles in tomograms of infected cells, I developed a cryo-CLEM workflow (**Section 4.1**) and established fluorescent labeling of A/WAS/1933(H1N1) particles (**Section 4.2**). These developments allow me to structurally characterize trapped viral particles in the endosomal-lysosomal system of IFITM3 overexpressing A549 cells. Since viral entry is a time-sensitive process, I determined the half-time of IAV entry in A549 cells to be 45 mpi (**Figure 4.15**). Most viral particles entered the cell by 120 mpi.

To maximize the chance of observing inhibition of viral entry in A549-IFITM3 cells by *in situ* cryo-ET, I decided to use the 60 mpi time point and used a high MOI of 200 for the infection. Cryo-TEM of cryo-FIB-milled A549-IFITM3 cells infected with fluorescently labeled influenza A virus (MOI = 200, 1 hpi) revealed endosome-like organelles on the cryo-lamellae (**Figure 4.16**). These sites were selected for cryo-ET data acquisition. Subsequent correlation using the previously established workflow showed a correlation of the fluorescent signal of the labeled viral particles to these endosome-like structures (**Figure 4.16a, b, d and f**), indicating the virus particles are localized in the endosome-like organelles.

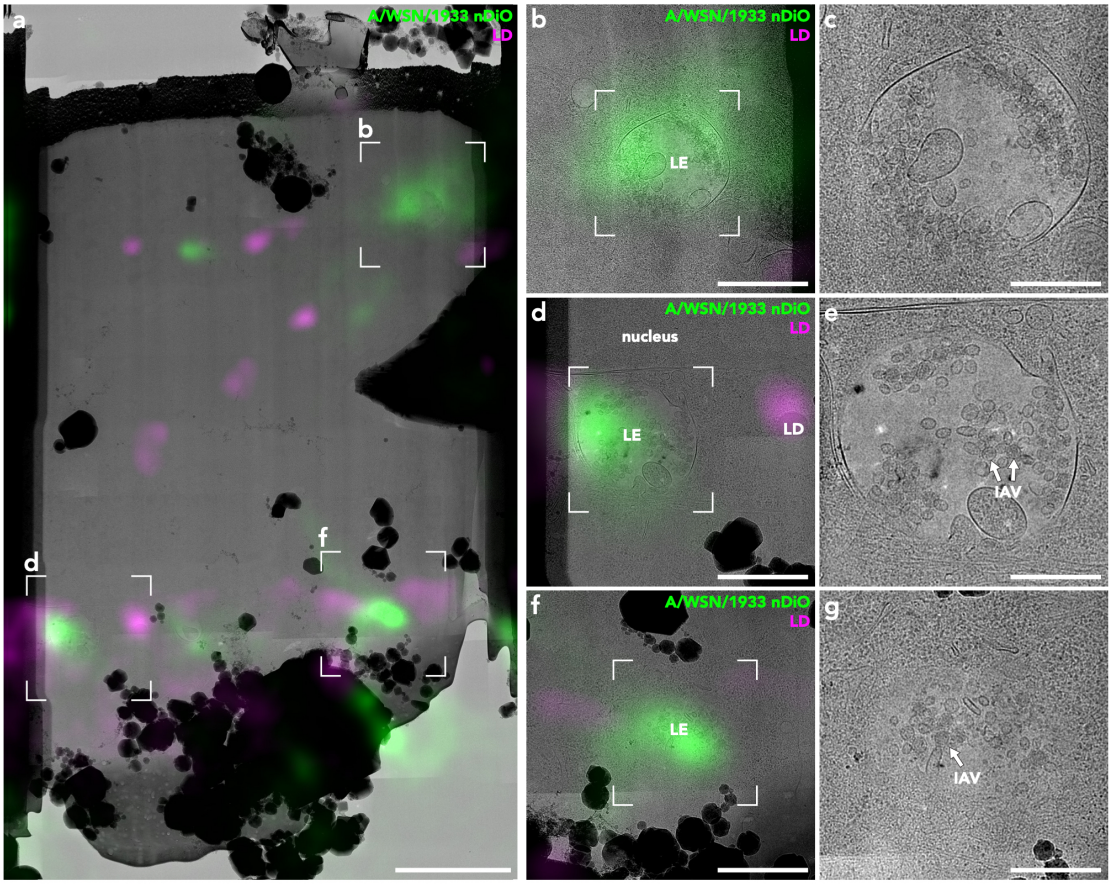

Figure 4.16: *In situ* cryo-CLEM of A549-IFITM3 cells infected with influenza A/WSN/1933(H1N1). A549-IFITM3 cells were infected with a nDiO-fluorescently labeled influenza A/WSN/1933(H1N1) virus (MOI=200, 1 hpi). The previously established *in situ* cryo-CLEM workflow (**Figure 4.1**) was used to correlate the cryo-TEM data with the fluorescence signal of the labeled IAV particles. **(a)** *In situ* cryo-TEM map of a cryo-FIB milled lamella of an infected A549-IFITM3 cell. The cryo-TEM map was correlated with the fluorescent signal of the virus (green). LDs (magenta) were also fluorescently labeled and used as fiducial markers. **(b, d, f)** The three indicated areas are magnified on the right. LEs, LDs and nuclear regions are indicated. **(c, e, and g)** Magnified cryo-TEM maps are shown without the correlated fluorescence map. IAV particles are indicated. Scale bars: (a) 3 µm, (b, d, and f) 1 µm, (c, e, and g) 500 nm. This figure is a modified reprint from *Cell Host Microbe*, Volume 31.4 by Klein, Golani, *et al.* (2023), 'IFITM3 blocks influenza virus entry by sorting lipids and stabilizing hemifusion', ©2023, with permission from Elsevier.

4.3.2.1 Stabilized hemifusion sites at late endosomal membranes

Cryo-ET of the correlated endosome-like structures (**Figure 4.16**) revealed the ultrastructural details of the virus-containing organelles. I observed ILVs, hallmarks for endosomal and lysosomal organelles with multivesicular morphology, and IAV particles regularly in close contact with the endosomal limiting membrane and ILVs (**Figure 4.17a and b**). In four different tomograms, 43 viral particles were identified within the endosomal lumen but non in the cytoplasm.
As the viral entry half-time in A549 was determined to be at 45 mpi, one would expect most virus particles to be localized already in the cytoplasm at 1 hpi. The observation of virus particles localized in endosomes in A549-IFITM3 cells indicates that due to IFITM3 overexpression, virus particles can not enter the cytoplasm and are trapped in the endosomal lumen. This is also in agreement with the observed antiviral properties of IFITM3, as shown by the infection assay (**Figure 4.9**) and membrane fusion assay (**Figure 4.10**). Viral particles observed in late endosomes showed a diameter of 87.8 nm (SD = 7.8 nm, n = 18) and a disorganized HA phenotype, as expected in a low pH environment. Furthermore, 83 % of the viral particles showed a partially disassembled M1 layer. In 9 % of the cases, the M1 layer was fully disassembled, and in the remaining 8 %, the M1 layer was found fully intact. This observation further indicates that the viral particles were exposed to the low pH environment of the endosomal-lysosomal network. Importantly, these viral particles were regularly found to be interacting with ILVs (**Figure 4.17c and d**) and the limiting LE membrane (**Figure 4.17e and f**). Interestingly, on some occasions, I observed crystal-like structures bound to viral particles (**Figure 4.17f, arrow heads**). These structures resemble cholesterol ester crystals previously observed in late endosomes (Klein, Wimmer, *et al.* 2021).

In a total of four tomograms, I observed 21 interaction sites with ILVs and 6 interactions with the limiting LE membrane (summarized in **Table 4.1**). To evaluate the type of interaction, I analyzed all observed virus membrane interactions by plot

profiles (**Figures 4.18, 4.19, 4.20, 4.21, and 4.22**). Based on the plot profiles, I classified the interactions as hemifusion or tight docking. Tight docking refers to a configuration of two membranes that are closely positioned but have separate phospholipid bilayers, a state this can be observed before hemifusion. Out of the 27 observed events, I identified 85 % (23 events) as hemifusion and 15 % (4 events) as tight docking, based on the given definition. The tight docking events displayed linear density profiles with signal peaks of two adjacent phospholipid bilayers separated by a noticeable decrease in signal. On the other hand, linear density profiles of all hemifusion events lacked adjacent phospholipid bilayers.
This analysis indicates that IFITM3 accumulates hemifusion sites between viral particles and endosomal membranes. Furthermore, I did not observe post-fusion events or vRNPs in the cytoplasm, indicating that complete viral fusion is impeded by IFITM3, and the hemifusion state is stabilized.

Table 4.1: Overview of observed virus membrane interactions in A549-IFITM3 cells

Tomogram	Interaction site	Contact site	Contact type	Figure
Tomogram 1	1	ILV	Hemifusion	4.18a
	2	ILV	Hemifusion	4.18b
	3	ILV	Hemifusion	4.18c
	4	ILV	Hemifusion	4.18d
	5	ILV	Tight docking	4.18e
	6	ILV	Hemifusion	4.18f
	7	ILV	Hemifusion	4.18g
	8	ILV	Hemifusion	4.18h
	9	ILV	Hemifusion	4.18i
	10	ILV	Hemifusion	4.18j
	11	ILV	Hemifusion	4.18k
	12	ILV	Hemifusion	4.18l
	13	ILV	Hemifusion	4.18m
	14	ILV	Hemifusion	4.18n
	15	ILV	Tight docking	4.18o
	16	Limiting LE membrane	Hemifusion	4.19a
	17	Limiting LE membrane	Hemifusion	4.19b
	18	Limiting LE membrane	Hemifusion	4.19c
Tomogram 2	19	ILV	Hemifusion	4.20c
	20	Limiting LE membrane	Tight docking	4.20d
	21	Limiting LE membrane	Hemifusion	4.20e
Tomogram 3	22	ILV	Hemifusion	4.21c
	23	Limiting LE membrane	Hemifusion	4.21d
Tomogram 4	24	ILV	Tight docking	4.22c
	25	ILV	Hemifusion	4.22d
	26	ILV	Hemifusion	4.22e
	27	ILV	Hemifusion	4.22f

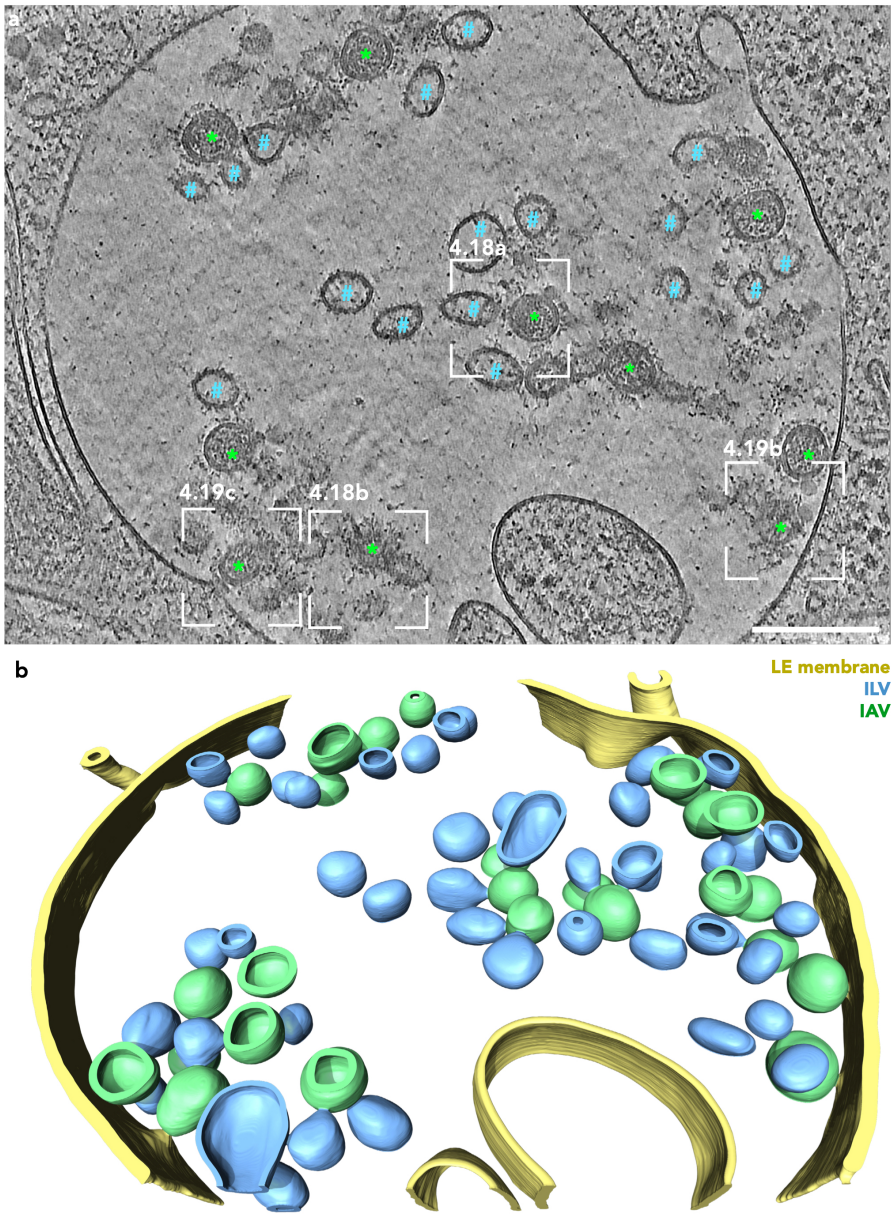

Figure 4.17: Cryo-ET of LE-like organelle reveals hemifusion sites between IAV particles and cellular membrane. (a) Central slice of a reconstructed *in situ* cryo-ET. The tomogram site was identified based on *in situ* cryo-CLEM, as shown in **Figure 4.16d and e**. ILVs (blue hashes) and ILV particles (green asterisks) are indicated. **(b)** Three-dimensional rendering of the tomogram shown in (a), showing the limiting LE membrane in yellow, ILVs in blue, and IAV particles in green. Scale bar: (a) 200 nm. This figure is a modified reprint from *Cell Host Microbe*, Volume 31.4 by Klein, Golani, *et al.* (2023), 'IFITM3 blocks influenza virus entry by sorting lipids and stabilizing hemifusion', ©2023, with permission from Elsevier.

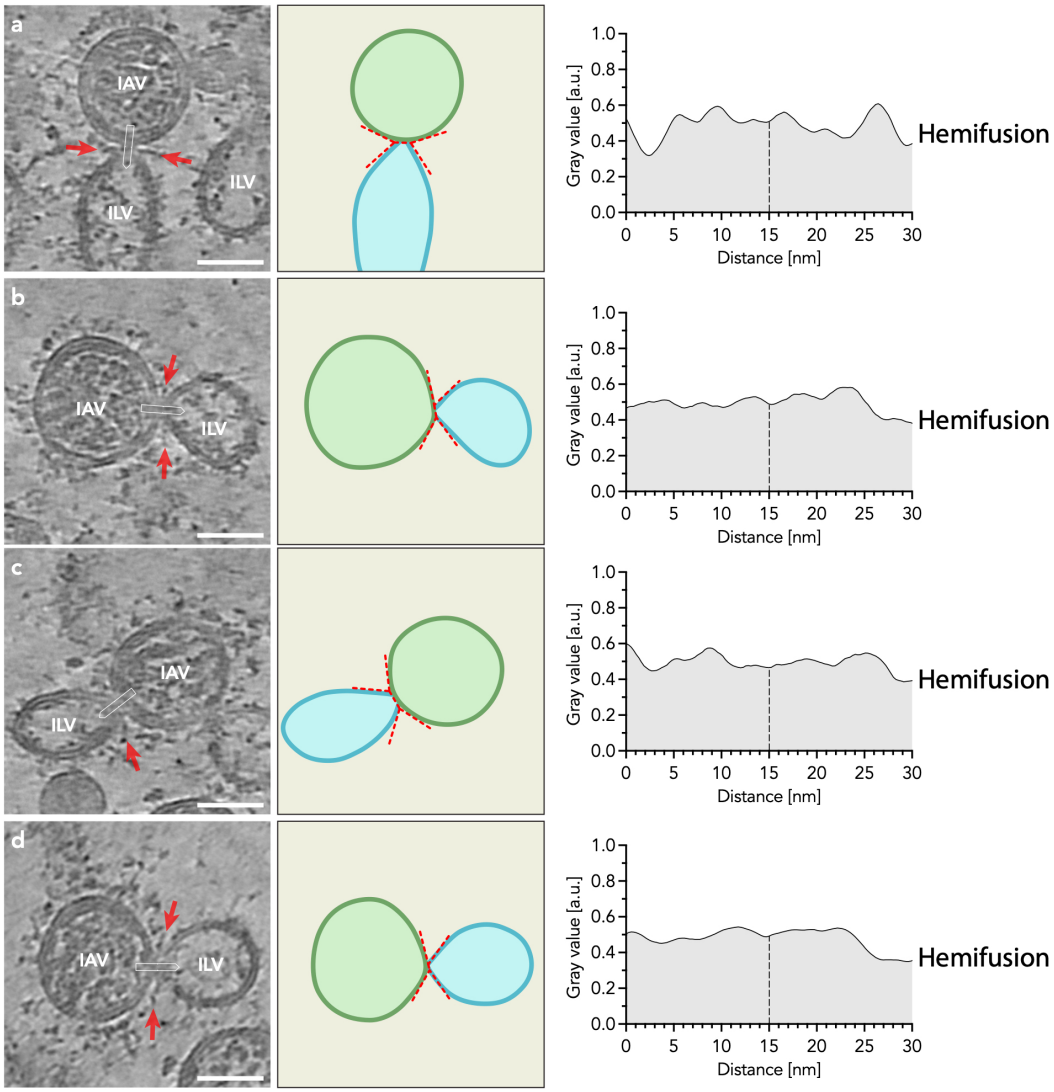

Figure 4.18: Gallery of IAV particle – membrane interaction sites at endosomal ILVs found in an IFITM3-overexpressing A549 cell shown in Figure 4.17 (Part 1/4). See page 102 for figure legend.

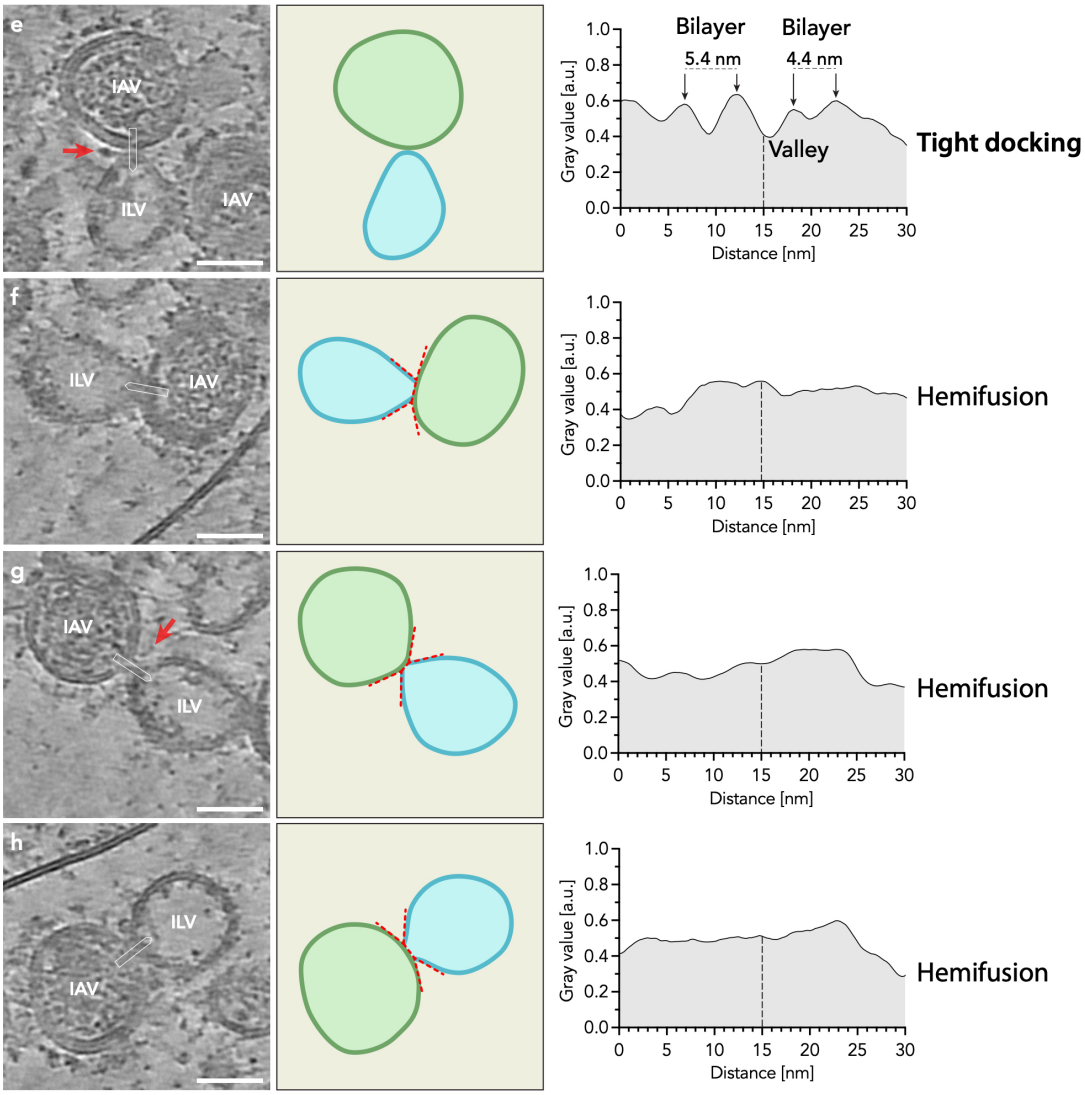

Figure 4.18: Gallery of IAV particle – membrane interaction sites at endosomal ILVs found in an IFITM3-overexpressing A549 cell shown in Figure 4.17 (Part 2/4). See page 102 for figure legend.

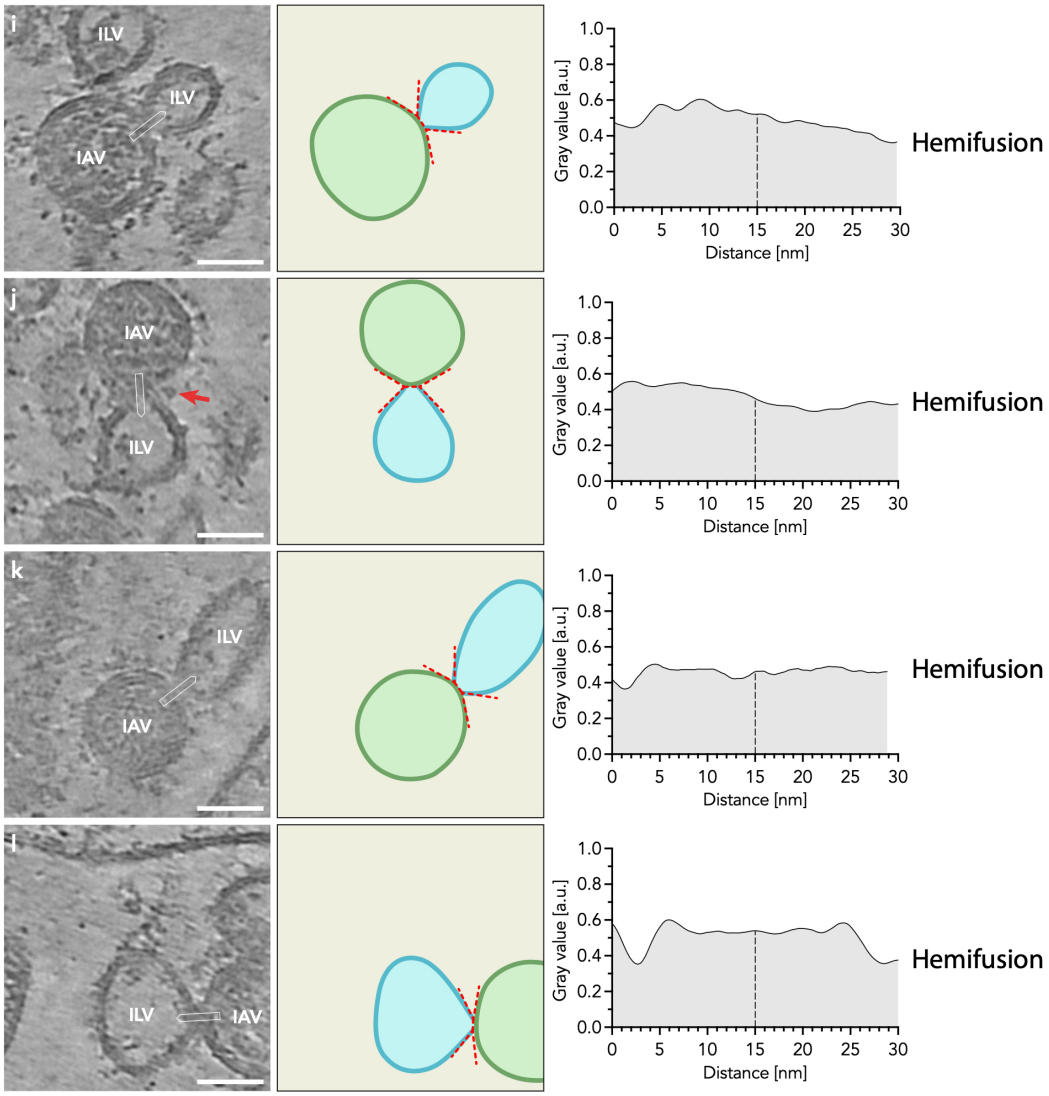

Figure 4.18: Gallery of IAV particle – membrane interaction sites at endosomal ILVs found in an IFITM3-overexpressing A549 cell shown in Figure 4.17 (Part 3/4). See page 102 for figure legend.

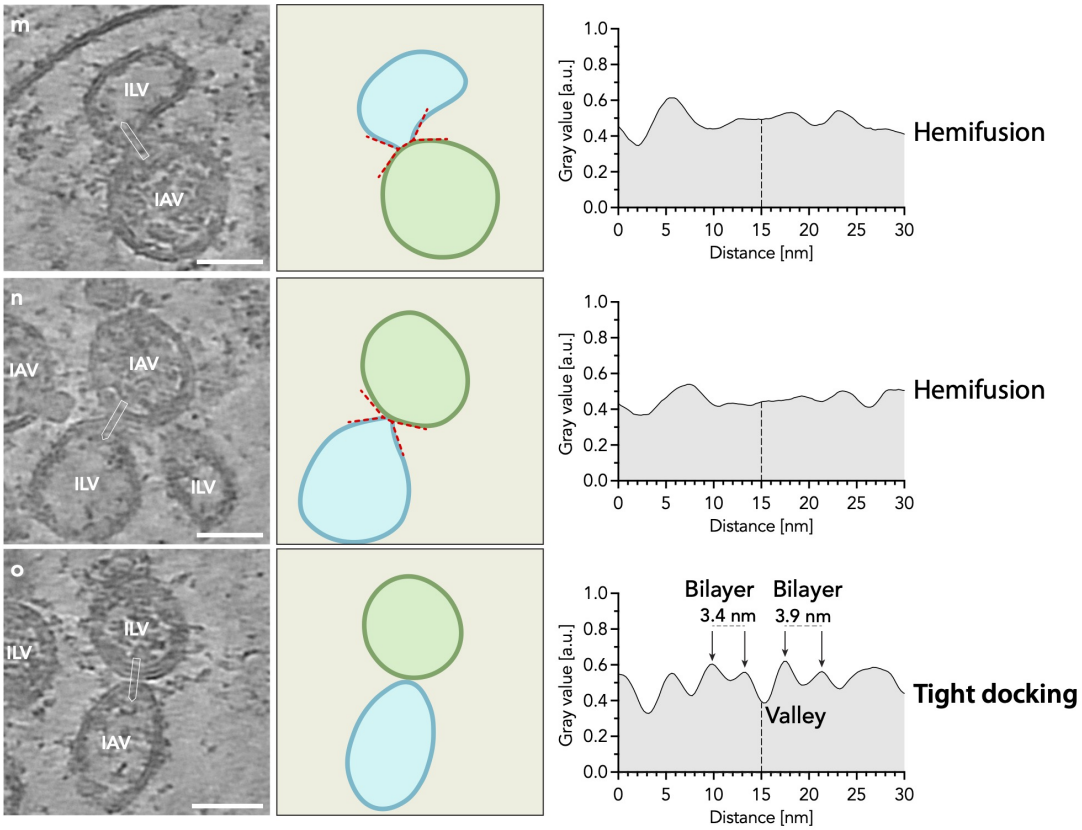

Figure 4.18: Gallery of IAV particle – membrane interaction sites at endosomal ILVs found in an IFITM3-overexpressing A549 cell shown in Figure 4.17 (Part 4/4). (a – o) Slices through reconstructed tomograms are shown with IAV particles, and ILVs indicated. Electron-dense structures at the membrane interaction site are indicated with red arrows. Next to each tomogram, a schematic representation of the membrane interaction site is shown, with IAV particles in green and ILVs in blue. Measurements for the membrane interaction diaphragm length and the inner- and outer angles are shown with red dotted lines. For each virus-membrane interaction (indicated with a white square in the tomogram), a line profile (5.34 nm width) is shown on the right. Based on the line profile features, the interaction sites were classified as tight docking (two adjacent phospholipid bilayers) or hemifusion (no apparent bilayers). Scale bars: 50 nm. This figure is a modified reprint from *Cell Host Microbe*, Volume 31.4 by Klein, Golani, *et al.* (2023), 'IFITM3 blocks influenza virus entry by sorting lipids and stabilizing hemifusion', ©2023, with permission from Elsevier.

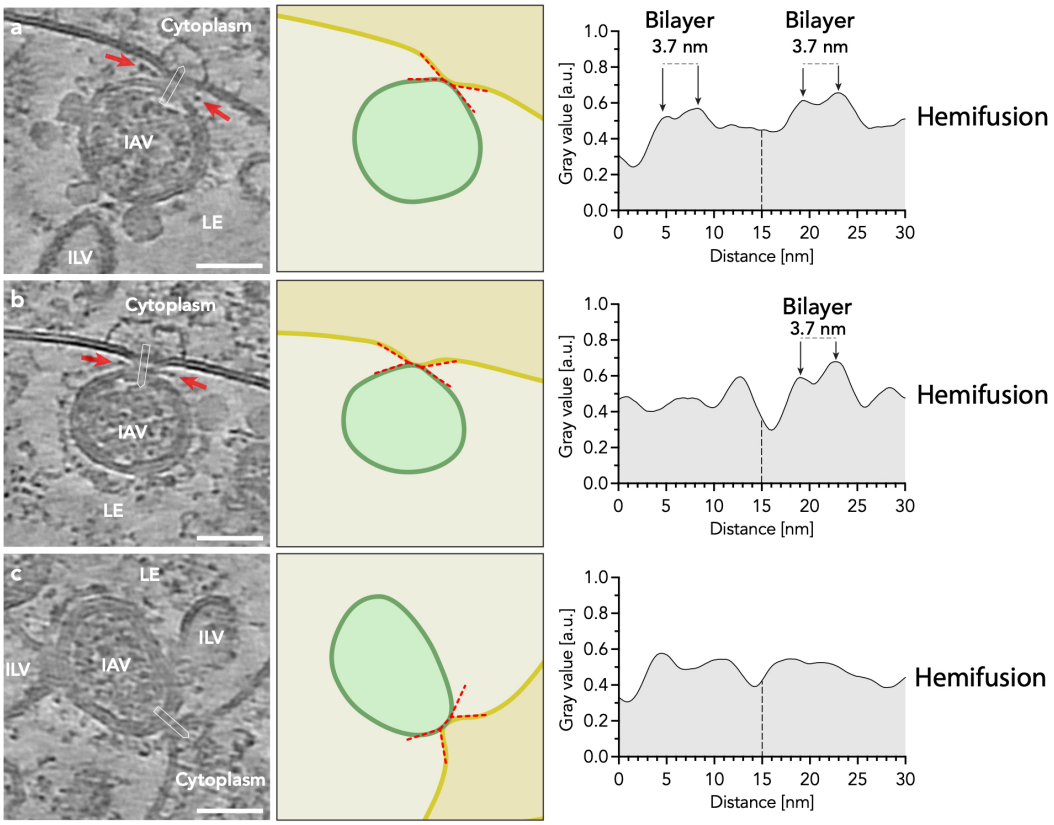

Figure 4.19: Gallery of IAV particle – membrane interaction sites at limiting LE membrane found in an IFITM3-overexpressing A549 cell shown in Figure 4.17. (a – c) Slices through reconstructed tomograms are shown with IAV particles, ILVs, LE, and cytoplam indicated. Electron-dense structures at the hemifusion site are indicated with red arrows. Next to each tomogram, a schematic representation of the hemifusion site is shown, with IAV particles in green and the limiting LEs membrane in yellow. Measurements for the hemifusion diaphragm length and the inner- and outer angles are shown with red dotted lines. For each virus-membrane interaction (indicated with a white square in the tomogram), a line profile (5.34 nm width) is shown on the right. Based on the line profile features, the interaction sites were classified as tight docking (two adjacent phospholipid bilayers) or hemifusion (no apparent bilayers). Scale bars: 50 nm. This figure is a modified reprint from *Cell Host Microbe*, Volume 31.4 by Klein, Golani, *et al.* (2023), 'IFITM3 blocks influenza virus entry by sorting lipids and stabilizing hemifusion', ©2023, with permission from Elsevier.

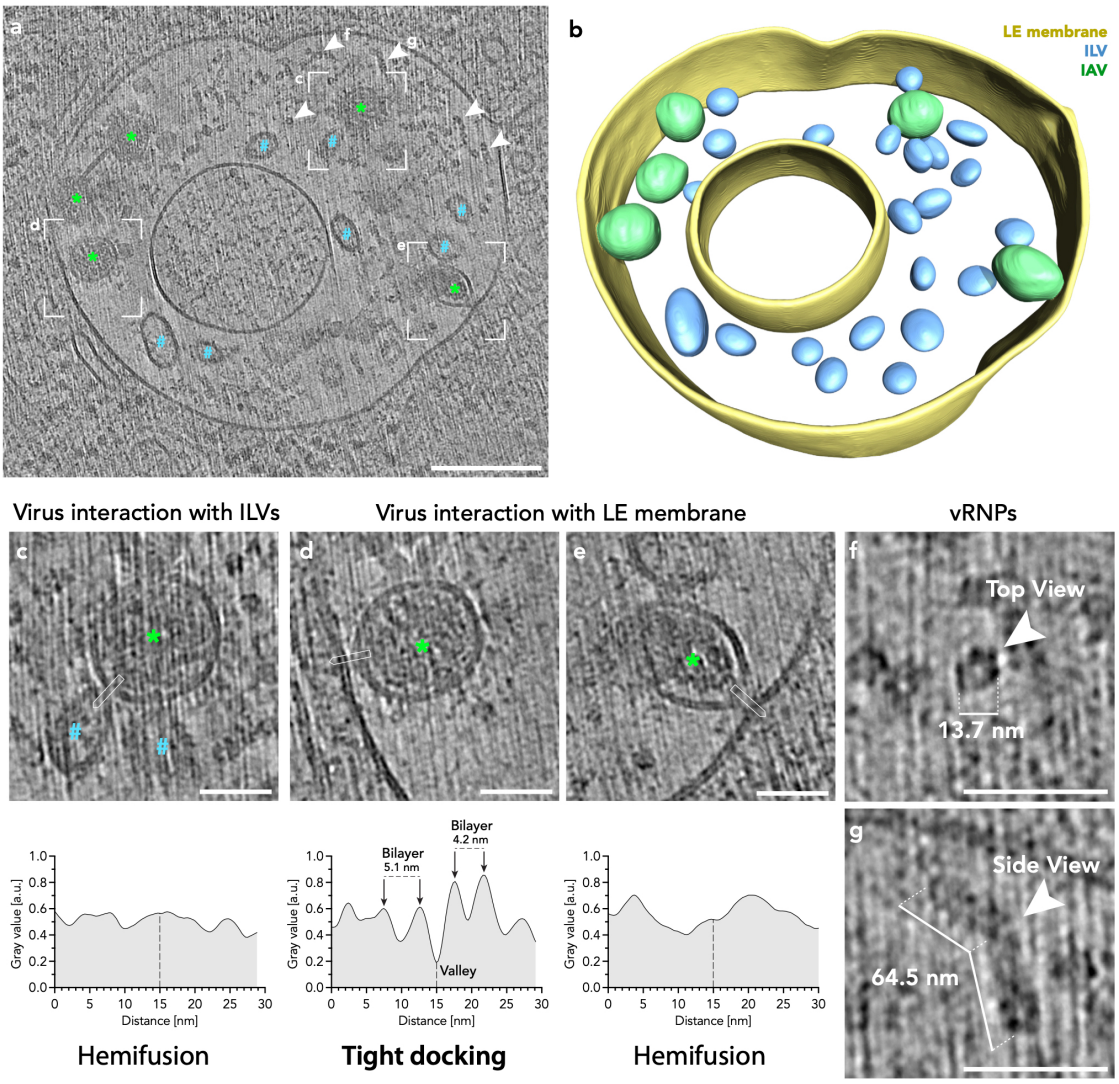

Figure 4.20: Cryo-ET of LE-like organelle reveals IAV particle – membrane interaction sites. (a) Central slice of a reconstructed *in situ* cryo-ET. The tomogram site was identified based on *in situ* cryo-CLEM, as shown in **Figure 4.16d and e**. ILVs (blue hashes), ILV particles (green asterisks), and vRNPs (white arrowheads) are indicated. **(b)** Three-dimensional rendering of the tomogram shown in (a), showing the limiting LE membrane in yellow, ILVs in blue, and IAV particles in green. **(c – e)** Magnified slices of the reconstructed tomogram, as indicated in (a). For each virus-membrane interaction (indicated with a white square), a line profile (5.34 nm width) is shown at the bottom. Based on the line profile features, the interaction sites were classified as tight docking (two adjacent phospholipid bilayers) or hemifusion (no apparent bilayers). **(f and g)** Magnified slices of the reconstructed tomogram, as indicated in (a), showing vRNPs in the endosomal lumen as a side view (f) and a top view (g). Scale bars: (a) 200 nm, (c – f) 50 nm. This figure is a modified reprint from *Cell Host Microbe*, Volume 31.4 by Klein, Golani, *et al.* (2023), 'IFITM3 blocks influenza virus entry by sorting lipids and stabilizing hemifusion', ©2023, with permission from Elsevier.

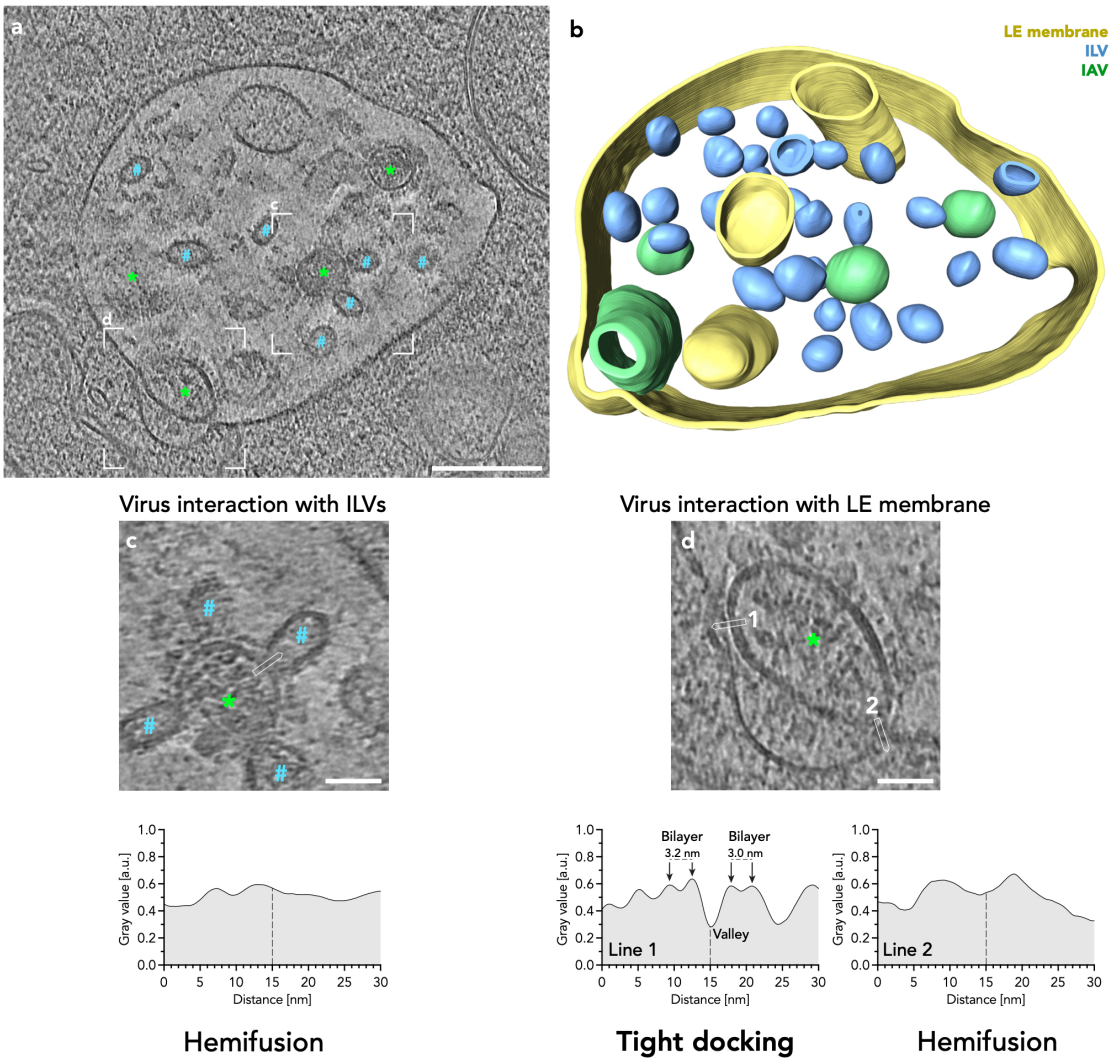

Figure 4.21: Cryo-ET of LE-like organelle reveals IAV particle – membrane interaction sites. (a) Central slice of a reconstructed *in situ* cryo-ET. The tomogram site was identified based on *in situ* cryo-CLEM, as shown in **Figure 4.16d and e**. ILVs (blue hashes) and ILV particles (green asterisks) are indicated. **(b)** Three-dimensional rendering of the tomogram shown in (a), showing the limiting LE membrane in yellow, ILVs in blue, and IAV particles in green. **(c and d)** Magnified slices of the reconstructed tomogram, as indicated in (a). For each virus-membrane interaction (indicated with a white square), a line profile (5.34 nm width) is shown at the bottom. Based on the line profile features, the interaction sites were classified as tight docking (two adjacent phospholipid bilayers) or hemifusion (no apparent bilayers). Scale bars: (a) 200 nm, (c and d) 50 nm. This figure is a modified reprint from *Cell Host Microbe*, Volume 31.4 by Klein, Golani, *et al.* (2023), 'IFITM3 blocks influenza virus entry by sorting lipids and stabilizing hemifusion', ©2023, with permission from Elsevier.

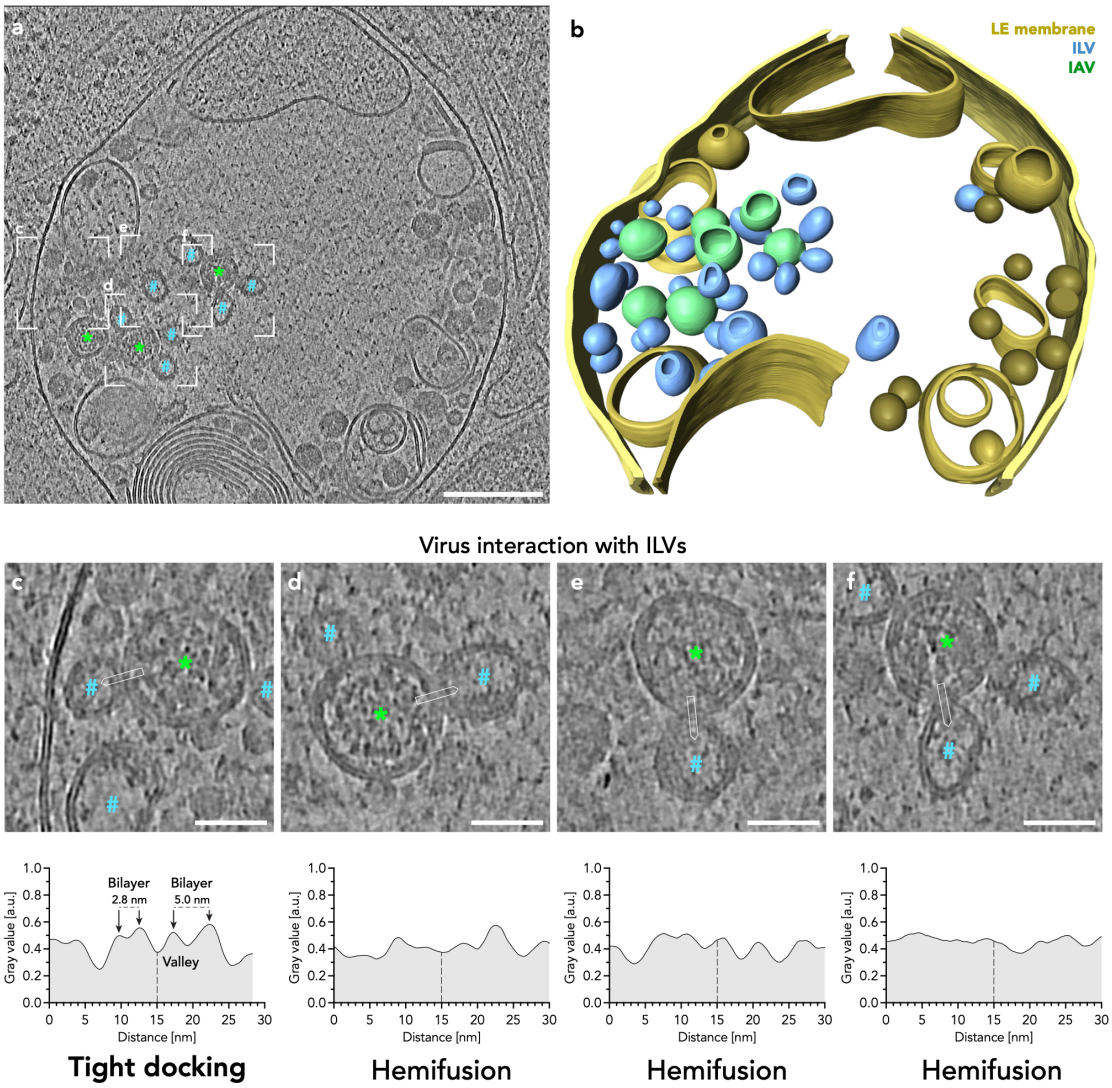

Figure 4.22: Cryo-ET of LE-like organelle reveals IAV particle – membrane interaction sites. (a) Central slice of a reconstructed *in situ* cryo-ET. The tomogram site was identified based on *in situ* cryo-CLEM, as shown in **Figure 4.16d and e**. ILVs (blue hashes) and ILV particles (green asterisks) are indicated. **(b)** Three-dimensional rendering of the tomogram shown in (a), showing the limiting LE membrane in yellow, ILVs in blue, and IAV particles in green. textbf(c – f) Magnified slices of the reconstructed tomogram, as indicated in (a). For each virus-membrane interaction (indicated with a white square), a line profile (5.34 nm width) is shown at the bottom. Based on the line profile features, the interaction sites were classified as tight docking (two adjacent phospholipid bilayers) or hemifusion (no apparent bilayers). Scale bars: (a) 200 nm, (c – f) 50 nm. This figure is a modified reprint from *Cell Host Microbe*, Volume 31.4 by Klein, Golani, *et al.* (2023), 'IFITM3 blocks influenza virus entry by sorting lipids and stabilizing hemifusion', ©2023, with permission from Elsevier.

4.3.2.2 Geometric analysis of hemifusion sites

I further quantified the geometry of the observed hemifusion sites between viral particles and endosomal membranes by measurement of the inner and outer angles as well as the hemifusion diaphragm size (**Figure 4.23**), as shown in **Figures 4.18, 4.19, 4.20, 4.21, and 4.22**. The analysis revealed a symmetric geometry around the central axis, which inner angles of 157° (SD = 12) and 140° (SD = 13) for the viral and cytoplasmic side and a more narrow outer angle of 63° (SD = 12) (**Figure 4.23b**). No significant difference between the opposing angles was observed, which means that the observed hemifusion sites are stabilized in a symmetric geometry. Furthermore, measurements of the hemifusion diaphragm size revealed an average length of 16.5 nm (SD = 5.3 nm, n = 17) (**Figure 4.23c**).

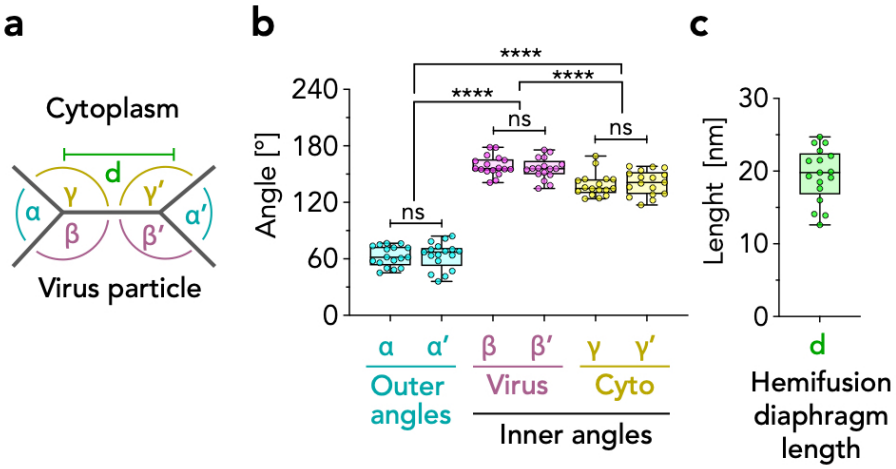

Figure 4.23: Geometrical analysis of hemifusion diaphragm. (a) Schematic representation of a hemifusion diaphragm between a virus particle and cellular membrane at the late endosomal lumen. The measured parameters for angles (α, β, and γ), and diaphragm length d are indicated. **(b)** Measurement of the outer angles (α and α), the inner angles facing the viral lumen β and β) and the inner angles facing the cytoplam γ and γ). **(c)** Measurement of the hemifusion diaphragm length d. This figure is a modified reprint from *Cell Host Microbe*, Volume 31.4 by Klein, Golani, *et al.* (2023), 'IFITM3 blocks influenza virus entry by sorting lipids and stabilizing hemifusion', ©2023, with permission from Elsevier.

4.3.2.3 Post-fusion HA glycoprotein is localized at hemifusion sites

During the ultrastructural characterization, I regularly observed additional electron-dense structures at the hemifusion sites (**Figures 4.18, 4.19, 4.20, 4.21, and 4.22**, red arrows). The cylindrical structures were found mostly orthogonal to the hemifusion diaphragm. Since the viral fusion protein HA plays an essential role during IAV membrane fusion, I structurally characterized the observed densities by STA to elucidate their identity. Therefor, I extracted 30 subvolumes of individual potential HA glycoproteins at hemifusion sites. Iterative averaging of the subvolumes (**Figure 4.24a and b**) without imposing symmetry revealed a rod-shaped structure and the phospholipid bilayers of the viral and endosomal membranes (**Figure 4.24a, green dotted lines**). Line profile measurement of the phospholipid bilayers revealed a typical phospholipid monolayer distance of a membrane with 4.5 nm and 5.1 nm, respectively **Figure 4.24c**). In a second iterative averaging step (**Figure 4.24c**), I used a tight mask, only focusing on the rod-shape structure, and I imposed a C3 symmetry since HA is a trimeric protein. As evident from the top view, the membranes are not resolved anymore, but the central density is more refined, revealing a structure composed of a head and stalk region with a total dimension of 13.6 × 5.1 × 5.0 nm (**Figure 4.24d**). I fitted the post-fusion HA2 structure (PDB: 1QU1, J Chen, Skehel, *et al.* (1999)) to the electron density of the STA. The fitting showed a high accuracy, as 97% of the atoms were found within the isosurface of the STA. This indicates that the densities found at the hemifusion sites likely represent the post-fusion HA2 subdomain. Interestingly, no densities of an HA1 subunit were revealed by the STA analysis, indicating that the HA1 subdomain was already dissociated due to the reducing conditions of the endosomal lumen.

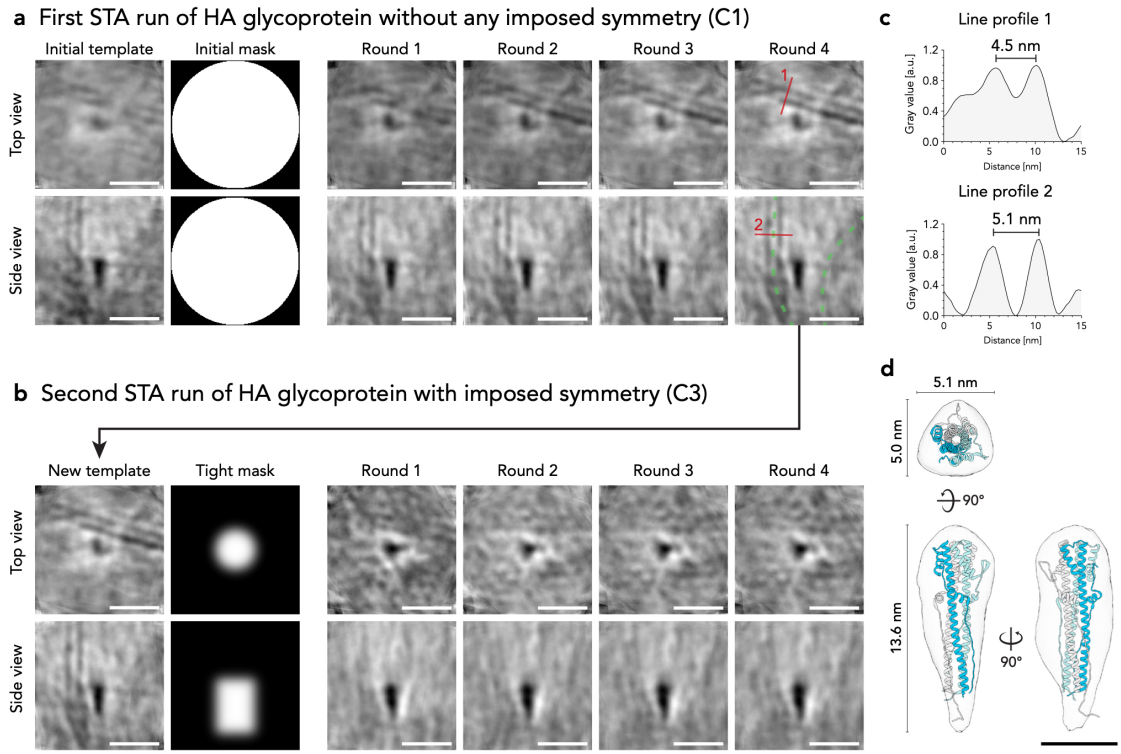

Figure 4.24: Subtomogram average of the post-fusion HA glycoprotein localized at hemifusion sites. A total of 30 subvolumes of post-fusion HA glycoproteins were extracted and averaged. **(a)** First, the subvolumes were iteratively averaged without imposing any symmetry and using an arbitrary spherical initial mask. The results of round 4 show the post-fusion HA close to membranes, as indicated with dotted green lines. **(b)** In the second round of averaging, a threefold symmetry was applied, and a tighter mask was used to only average the post-fusion HA. **(c)** Two line profiles of the membranes shown in (a, as indicated with red lines) were plotted, and the distance between the two maxima, representing each a phospholipid monolayer of the membrane, was measured. **(d)** Isosurface of the final average. The post-fusion HA structure (PDB: 1QU1, J Chen, Skehel, *et al.* (1999)) was fitted into the isosurface. Scale bars: (a and b) 10 nm, (d) 5 nm. This figure is a modified reprint from *Cell Host Microbe*, Volume 31.4 by Klein, Golani, *et al.* (2023), 'IFITM3 blocks influenza virus entry by sorting lipids and stabilizing hemifusion', ©2023, with permission from Elsevier.

5 Discussion

5.1 *In-situ* cryo-correlative light and electron microscopy

The combination of fluorescent and electron microscopy is a powerful tool to answer many biological questions, as it allows to utilize the information on protein identity and localization (fluorescence microscopy) with the cellular ultrastructural (ET). Such CLEM approaches are already well established for room-temperature ET of chemically fixed, or HPF/FS cell sections (Kukulski *et al.* 2011). For *in situ* cryo-ET data, robust correlative workflows are lacking. Here, I successfully established a novel method for *in situ* cryo-CLEM that combines high-resolution cryo-ET with fluorescent microscopy. This method allows for localizing fluorescently labeled structures of interest on cryo-FIB milled cells. The workflow involves fluorescently labeling features of interest, vitrifying the cells by plunge freezing, and acquiring volume fluorescence light microscopy data using a cryo-LM. The sample is then transferred to a dual-beam cryo-FIB/SEM microscope for targeted cryo-FIB milling. After cryo-TEM acquisition, the acquired cryo-LM data is correlated to the cryo-TEM map using fiducial markers like LDs. In summary, the described method provides a workflow for *in situ* cryo-CLEM, combining cryo-ET with fluorescent microscopy to enable the ultrastructural analysis of cellular environments in their native state. This approach enhances the identification and analysis of features of interest in adherent eukaryotic cells, offering a powerful tool for investigating biological processes at

high resolution. I successfully applied this method to localize fluorescently labeled IAV particles in LEs of infected A549 cells, as described in **Chapter 4.3**.

5.1.1 Correlation precision

The here-established cryo-CLEM method was benchmarked using LDs, revealing a correlation precision of 124 nm (SD = 41 nm) (**Section 4.1.5**). Several factors limit the accuracy of correlation between cryo-widefield-LM and cryo-TEM images. One of the main limitations of correlation precision is chromatic aberrations between the cryo-LM emission wavelength of the target structure and the feature used as a fiducial marker. This offset between different channels directly reduces correlation precision, as the coordinates between the features in the different channels show an offset. The correlation can be improved by developing cryo-LM systems utilizing objectives with superior chromatic aberration correction. Another possible solution to this problem could be incorporating multi-channel fluorescent beads (like TetraSpecks, ThermoFisher Scientific), which would allow for correcting chromatic aberrations during data processing. Another limitation is the diffraction limit of the used objective lens of the cryo-LM, which limits the resolution of the system. Since the NA of air objectives is limited to NA = 1, the resolution of a microscopy system can be improved using immersion objectives with higher NA. Cryogenic immersion fluorescence microscopy was accomplished before using the cryo-immersion medium HFE-7200 (Faoro *et al.* 2018). However, this system is not optimized for samples on cryo-EM grids. Furthermore, there might be a risk of damaging the thin lamellae during immersion. Thus, we are currently limited to air objectives with a typical NA of 0.9. In addition, stage drift can limit the achievable resolution. Since the sample and stage must be operated at temperatures below the devitrification temperature of water at all times, the stage is usually directly or indirectly cooled by (LN2), which can induce such stage drift. Developing novel cryo-stages with improved stability to minimize drift could improve the correlation precision.

Despite this limitation, moving from widefield systems to confocal microscopy systems with array detectors (like the Zeiss LSM900 with AiryScan2 detector and Linkam cryo-stage CMS196) can increase the resolution by a factor of 2.12× in all dimensions (Scientific Volume Imaging 2023). In addition, array detectors show a higher sensitivity than confocal systems due to the combination of a wide-open pinhole and a sensitive detector array.

5.1.2 Benefits and limitations of an *a posteriori* correlation approach

Sample thinning using cryo-FIB is necessary for cryo-TEM image acquisition due to the limited penetration depth of the electrons below 1 µm (Grimm *et al.* 1998). To achieve higher resolutions, an optimal sample thickness is 150 nm (Grimm *et al.* 1998). Due to this thinness of cryo-lamellae, no fluorescence signal can be detected on lamella using a cryo-widefield system, which could be used to localize the region of interest prior to cryo-TEM (see **Figure 4.1d**). The reason could be the insufficient sensitivity of the camera to detect the fluorescent signal of the remaining fluorophores in a 150 nm thin lamella. Furthermore, fluorophores close to the lamella surface might be damaged due to the FIB beam. A recent publication quantified the depth of FIB-beam-induced damage on ribosomes up to 60 nm from the lamella surface of a 200 nm lamella (Lucas & Grigorieff 2023). If this FIB-beam-induced damage also affects fluorophore properties remains to be determined. The inability to detect a fluorescent signal on lamella with a widefield cryo-LM system prevented the possibility of on-lamella cryo-CLEM and motivated me to develop the here-described *a posteriori* approach where I computationally extract the fluorescence signal corresponding to the lamella position from the fluorescence volume image acquired before cryo-FIB milling. Thus, the here described cryo-CLEM method allows correlation of thin lamellae in all three dimensions without the need to directly detect on-lamella fluorescent signal.

The main shortcoming of such an approach is the uncertainty of the lamella localization within this volume. Here we rely on the presence of cellular structures to be used as fiducial markers for correlation, such as LDs. The correlation precision is impaired if no such structure is present in the lamella. One approach to overcome this limitation could be the introduction of fluorescent beads into cells before plunging that could be used as fiducial markers for correlation. Import via endocytosis or active import by electroporation could be evaluated as strategies for cellular delivery.

A second limitation of this method is the limited Z-resolution of the widefield cryo-LM system of 814 nm (Scientific Volume Imaging 2023), which is more than 5-times the thickness of a typical cryo-lamellae of 150 nm. Thus, it is expected that in the final correlation, the fluorescent signal (here termed as 'out-of-lamella signal') from fluorophores in close proximity to the lamella position is still present. Improved microscopy systems, like confocal microscopy systems with array detectors, can increase the Z-resolution to 384 nm, which would be only 2.5× the thickness of a typical lamella. By developing cryo-immersion methods for cryo-EM grids, one could further improve the Z-resolution to 238 nm, which would further decrease the amount of expected out-of-lamella signal from the here described *a posteriori* cryo-CLEM method.

An alternative correlative method to the here developed *a posteriori* approach for lamella correlation is side-specific milling (Arnold *et al.* 2016). Here, the fluorescence 3D volume is correlated with the low-angle cryo-FIB image of the sample just prior to cryo-FIB milling. Fluorescent beads are utilized to calculate the three-dimensional coordinate transformations between the two image modalities. This allows the determination of the cryo-FIB milling position to target a specific fluorescent signal within the cell. In comparison to the here developed *a posteriori* cryo-CLEM method, site-specific milling increases the chance that the target of interest is within the small cryo-lamella volume and thus renders this method particularly useful for low abundant targets. Furthermore, it allows correlation prior to

cryo-TEM and thus can be used to perform cryo-ET on specified regions with the ROI. The targeted milling success is mainly limited by two factors: (1) The precision of the correlation step is limited by the Z-resolution of the used cryo-LM system. Here, confocal systems are preferred due to their increased Z resolution. (2) Any sample movement that occurs after calculating the three-dimensional coordinate transformation leads to an offset of the determined milling position and target position. Such movements can be induced by stage drift or sagging of the cells during the first steps of cryo-FIB milling. Compared to side-specific milling, the here developed cryo-CLEM workflow allows correlation and validation of targeted structures after cryo-FIB milling. Combining both side-specific milling and *a posteriori* cryo-CLEM would merge the advantage of both methods into one workflow, enabling targeted milling and correlation validation.

5.1.3 Alternative methods and future developments

The here-developed cryo-CLEM method was based on a widefield cryo-LM microscopy system. With the discussed limitations of such a system, the here described *a posteriori* cryo-CLEM methods proved to be a valuable and practical tool for in-cell cryo-CLEM to study IAV entry in native conditions (see **Chapter 4.3**). In recent years, new hardware developments allowed the development of novel cryo-CLEM workflows. New commercial confocal cryo-LM systems with array detectors allowed on-lamella cryo-CLEM and integrated light microscopy systems into cryo-FIB/SEM systems allow targeted cryo-FIB milling. Furthermore, active developments for cryo-super resolution microscopy will further advance the evolving field of cryo-CLEM. This chapter will discuss these current and future developments in more detail.

5.1.3.1 Integrated cryo-light microscopy and cryo-FIB/SEM systems

The development of cryo-FIB/SEM systems with an integrated cryo-LM module is further improving the correlative workflow (see **Table 5.1**). Integrating both image modalities in one system reduces the sample transfers and thus can minimize sample damage due to ice contamination, devitrification, and mechanical damage. Furthermore, the possibility to perform cryo-LM image acquisition during cryo-FIB milling enables the possibility of targeted milling and real-time monitoring of the fluorescent signal during the milling process. The initial development enabled retrofitting of a widefield cryo-LM into cryo-FIB/SEM systems (Gorelick *et al.* 2019) and was made commercially available (Smeets *et al.* 2021; ThermoFisher Scientific 2021). These implementations have two main shortcomings: (1) The systems are currently only available with widefield optics, limiting their resolution. (2) The focal points of the cryo-LM and cryo-FIB are not coinciding. This means the sample must be moved to another position within the microscopy chamber for each imaging modality. This prevents the live monitoring of the fluorescent signal during cryo-FIB milling. The second shortcoming was addressed by the development of systems with the cryo-LM objective positioned opposing the cryo-FIB source (S Li *et al.* 2023; ThermoFisher Scientific 2022), allowing for the same coincidence focal point between cryo-LM and cryo-FIB, enabling simultaneous cryo-FIB milling and cryo-LM acquisition, which allows live monitoring of the milling process. Still, the cryo-LM system used is limited to widefield. The most recent development to date is the implementation of a confocal cryo-LM system (W Li *et al.* 2023), although the focal points are not coinciding. Future developments might incorporate advanced optics, like confocal systems with array detectors with the same focal point as the cryo-FIB system, thus resolving all shortcomings of currently available systems, rendering external cryo-LM systems obsolete.

Table 5.1: Overview of integrated cryo-light microscopy and cryo-FIB/SEM systems

System	Magnification	NA	Coincidence	Confocality	Reference
PIE-scope	Up to 50×	Up to 0.95	No	Widefield	Gorelick *et al.* (2019)
iFLM	20×	0.7	No	Widefield	ThermoFisher Scientific (2021)
Meteor	Up to 100×	Up to 0.95	No	Widefield	Smeets *et al.* (2021)
Arctis	100×	0.75	Yes	Widefield	ThermoFisher Scientific (2022)
cryo-STAR	100×	0.8	Yes	Widefield	S Li *et al.* (2023)
cryoCLIEM	100×	0.9	No	Confocal	W Li *et al.* (2023)

5.1.3.2 Cryo-super resolution

The resolution of confocal cryo-LM systems (Arnold *et al.* 2016) can be further improved by applying super-resolution light microscopy methods. One important factor to consider for cryo-EM samples is the energy of the used lasers, as the transferred energy can head up the sample above the devitrification temperature of water. Thus, low-dose methods like single-molecule localization microscopy (SMLM) (Tuijtel *et al.* 2019), super-resolution optical fluctuation imaging (SOFI) (Moser *et al.* 2019) and structured illumination microscopy (SIM) (Phillips *et al.* 2020) are currently exploited for cryo-CLEM applications. In comparison, stimulated emission depletion (STED) microscopy (Hell & Wichmann 1994) might be unsuitable for cryo-CLEM due to the necessary high-intensity lasers. SMLM methods rely on photoswitching fluorescent molecules (Lelek *et al.* 2021). As the photoswitching activity might be altered at low temperatures, further research is necessary to develop photoswitching molecules optimized for cryo-CLEM applications. Since SMLM relies on stochastic detection of single molecules over a long acquisition time, stage drift needs to be avoided, which needs to be solved by using stable cryo-stages optimized for cryo-SMLM applications.

5.2 Interferon induced transmembrane protein 3 (IFITM3)

IFITM3 is an essential player of the innate immune system and efficiently inhibits infection of various virus species (**Section 1.3.3.1**). Despite its clinical importance, the molecular mechanism of IFITM3 is not well understood. To shed light on the antiviral function of this protein, I studied IFITM3 in the context of IAV infection in human epithelial lung cells A549. First, I established stable IFITM3 cell lines and showed that IFITM3 expression inhibits viral infection by blocking viral membrane fusion in late endosomes (**Figures 4.9 and 4.10**). I further characterized the cellular localization of IFITM3 and found the protein predominantly localized in the late endosomal-lysosomal system using confocal microscopy (**Figure 4.11**) and ET (**Figure 4.12**). I further quantified the number of ILVs within multivesicular organelles of the endosomal-lysosomal system. The analysis showed that expression of IFITM3 does not impact the number of ILVs, contradicting the previously formulated 'fusion decoy' hypothesis as the mechanism of IFITM3 (**Section 1.3.3.1.4**). To study the impact of IFITM3 on the viral replication cycle on a structural level, I used a cryo-CLEM approach, which I established in the context of this thesis (**Section 4.1**). Based on a viral entry time course (**Figure 4.15**), I determined the half-time of IAV-mediated membrane fusion to be 45 mpi. Based on these results, I choose a time point of 1 hpi for the structural characterization of IAV infection in IFITM3-expressing cells. Cryo-CLEM allowed me to localize fluorescently labeled IAV particles in LEs of A549-IFITM3 cells (**Section 4.16**). *In situ* cryo-ET of these sites revealed the ultrastructural details of these virus-containing organelles. I regularly observed viral particles in a hemifusion state at both the limiting LE membrane and ILVs (**Table 4.1**). The accumulation of hemifusion sites at this late entry point indicates that IFITM3 traps the viral particles in the usually short-lived hemifusion state. Further analysis of the hemifusion site revealed rod-shaped structures in close proximity to the hemifusion diaphragm. The subtomogram average of these

structures revealed a shape and size matching the post-fusion form of HA (**Figure 4.24**), further indicating that these hemifusion sites are indeed stabilized.

In summary, these findings indicate that IFITM3 blocks IAV entry by stabilizing the hemifusion state during viral-induced membrane fusion in late endosomes. In the following chapter, I will discuss these findings in more detail.

5.2.1 Establishment and validation of IFITM3 cell line

To study the antiviral effect of IFITM3, I established an IFITM3 overexpressing A549 cell lines using lentiviral transduction. Evaluation of the expression level (**Figure 4.8**) revealed stable expression of IFITM3 for both the high and low expressing cell lines. Importantly, the stable overexpression of IFITM3 does not induce the expression of IFITM1 or IFITM2. Thus, the observed antiviral mechanisms can be attributed solely to IFITM3. I further evaluated the antiviral properties and could show an 11.5-fold reduced infection rate compared to A549 cells (**Figure 4.9**). This result is in agreement with previously reported antiviral properties of IFITM3 (Brass *et al.* 2009). Using a Blam-based cell entry assay, I further validated the cell line. As expected, influenza VLP entry was reduced by 10.5-fold compared to A549 cells (**Figure 4.10**). These results match with previous studies showing IFITM3-mediated inhibition of IAV cytosolic entry (Feeley *et al.* 2011; Desai *et al.* 2014). In summary, I established an A549 cell line stably overexpressing IFITM3 and validated its antiviral properties.

Since I aimed to utilize cryo-CLEM to study the antiviral properties of IFITM3, fluorescently labeled IFITM3 would allow me to correlate the localization of IFITM3 with *in situ* cryo-ET. Thus, I obtained an A549 cell line expressing a fusion protein of IFITM3 with the fluorescent protein nG (Desai *et al.* 2014). This cell line was kindly provided by Professor Gregory B. Melikyan (Emory University, USA). Similar

to the established A549-IFITM3 cell line, I evaluated the antiviral properties with an infection assay (**Figure 4.9**) and Blam-based viral entry assay (**Figure 4.10**). Both assays showed only a minimal reduced viral infection and entry. These results indicate that the fluorescently tagged IFITM3 lost its antiviral activity. While IFITM3 is a small transmembrane protein with a size of only around 15 kDa, its larger, fluorescent fusion partner nG (26.6 kDa) might sterically inhibit its antiviral activity. Based on these results, I decided to use the fully functional non-tagged A549-IFITM3 cell line for further cryo-CLEM experiments and utilize fluorescently labeled IAV for cryo-CLEM instead.

5.2.2 Impact of IFITM3 on the cellular morphology

The cellular localization of IFITM3 was reported to be in the endosomal-lysosomal system (Feeley *et al.* 2011; Narayana *et al.* 2015; Weston *et al.* 2016; Kummer *et al.* 2019). To further validate the A549-IFITM3 cell line, I utilized colocalization analysis with the late endosomal marker Rab7 (Seaman *et al.* 2009; TT Liu *et al.* 2012; Chesarino, McMichael, *et al.* 2014) and lysosomal marker LAMP1 (Eskelinen 2006), and I could validate partial colocalization with both markers (**Figure 4.11**). To better understand the number and size of IFITM3 positive organelles in the A549-IFITM3 cell line for *in situ* cryo-ET, I performed 3D segmentation of confocal microscopy stacks (**Figure 4.12**), revealing an average of 801 IFITM3-positive organelles per cell with an average volume of 0.4 µm³. This corresponds well to a typical late endosomal volume of up to 0.5 µm³ (Huotari & Helenius 2011). IFITM3-positive organelles are distributed throughout the cell with a preference for the perinuclear region. The number and distribution are well suited for cryo-FIB milling, as it is likely for those organelles to be present in a cryo-lamellae. Thus, a targeted milling approach is not needed, provided that in a large fraction of IFITM3 positive organelles, virus particles are localized. To achieve this, I decided to use a high MOI of 200 for the cryo-CLEM experiments.

To further analyze cellular IFITM3 localization on the structural level, I utilized HPF/FS cell sections for room temperature ET. IFITM3 was labeled with immunogold to localize them in the tomograms. As expected from the colocalization analysis, immunogold was predominantly localized to cellular organelles with a MVB-like morphology (**Figure 4.13**), typical for LEs (Gruenberg 2020). This morphological characterization is important for *in situ* cryo-CLEM experiments, as we do not have fluorescently labeled IFITM3 for correlation. Thus, I aim to localize fluorescently labeled IAV particles within cellular organelles with a MVB-like morphology.

5.2.3 IFITM3 mode of action

5.2.3.1 Fusion decoy hypothesis

The 'fusion decoy hypothesis' (**Section 1.3.3.1.4**) assumes an increased number of ILVs in the late endosomal lumen that could redirect viral membrane fusion from the limiting late endosomal membrane to fusion with ILVs. If IFITM3 would, in addition, block the back fusion of ILVs to the late endosomal membrane, as suggested by Amini-Bavil-Olyaee *et al.* (2013), this would effectively block the release of the viral genome into the cytoplasm but still would be compatible with the observed lipid mixing between endosome and virus (Desai *et al.* 2014). To challenge this hypothesis, I utilized HPF/FS cell sections for room temperature ET and quantified the number of ILVs per MVB (**Figure 4.14**), which showed that IFITM3 does not alter the number of ILVs. This result contradicts the fusion decoy hypothesis, indicating that IFITM3 does not modulate the endosomal morphology.

5.2.3.2 Hemifusion stabilization

To structurally characterize the antiviral properties of IFITM3 in the native cellular environment, I utilized *in situ* cryo-ET. Since fluorescent labeling of IFITM3 renders

the protein non-functional, I used fluorescently labeled IAV particles for correlation. *In vitro* cryo-CLEM analysis of the purified labeled viral particles (**Figure 4.7**) showed that 46 % of the viral particles were fluorescently labeled. By using a high MOI of 200 for viral infection, the chance of localizing a labeled viral particle within the cell is still reasonable. To estimate the optimal time point for *in situ* cryo-ET of infected cells, I performed an entry time course in A549 cells (**Figure 4.15**) and determined the entry half-time to be 45 min. Thus, I decided to analyze infected A549-IFITM3 cells at 1 hpi. Using *in situ* cryo-ET, I was able to localize fluorescently labeled IAV particles in MVBs (**Figure 4.16**) and could observe IAV particles within the endosomal lumen. In four different cells, I observed a total of 43 viral particles. All observed viral particles show a disorganized HA phenotype similar to *in vitro* cryo-ET studies (Fontana *et al.* 2012). This indicates that the observed IAV particles were exposed to a low pH environment, typical for late endosomes. Thus, IFITM3 does not alter the late endosomal pH. This finding is in accordance with Weston *et al.* (2016). 27 of the 43 viral particles were in close contact with the limiting LE lumen or ILVs (**Table 4.1**). Using line profile analysis of the interaction site, I found 24 viral particles in a hemifusion state. This finding strongly indicates that IFITM3 stabilizes viral particles in the hemifusion state. The observed hemifusion sites show a similar phenotype of hemifusion observed by *in vitro* cryo-ET (Lee 2010; Chlanda, Mekhedov, *et al.* 2016; Gui *et al.* 2016; Calder & Rosenthal 2016). HA-mediated membrane fusion is a rather fast process. Based on single-particle kinetic assays, the time from pH drop to the formation of a fusion pore is in the range of minutes (Boonstra *et al.* 2018), with the hemifusion being a short-lived transitional state. The accumulation of hemifusion sites in IFITM3 expressing cells indicates that the hemifusion state is a stabilized endpoint, inhibiting full membrane fusion and, thus, the release of the viral genome into the cytoplasm. IAV membrane fusion was reported to occur within 10 – 15 min after uptake (Matlin *et al.* 1981; Patterson & Bingham 1976; Dou *et al.* 2018). For A549 cells, I determined the half-time for viral entry

to be 45 min (**Figure 4.15**). Since I observed the hemifusion sites at an even later time point of 1 hpi, this further supports IFITM3-mediated stabilized hemifusion. Interestingly, the majority of hemifusion sites were observed at ILVs within the endosomal lumen. This unexpected result shows that ILVs are a fusion target of IAV particles. ILVs are in a dynamic equilibrium with the limiting late endosomal membrane and can retrofuse with the limiting late endosomal membrane (Perrin *et al.* 2021). Thus, IAV membrane fusion with ILVs and subsequent retrofusion would result in the release of the viral genome to the cytoplasm. If this alternative entry pathway is typically occurring during IAV infection is currently not understood and needs further investigation. Immunogold labeling of room temperature ET (**Figure 4.13**), shows that IFITM3 is localized at ILVs. Taken together, the findings show that IFITM3 is localized at ILVs and stabilizes the hemifusion state. Detailed analysis of the hemifusion site geometry (**Figure 4.23**) revealed an axial symmetric hemifusion site around the central axis, indicating that the hemifusion sites were formed by symmetric expansion or converged into a symmetric geometry (Risselada & Grubmüller 2021). The observed average hemifusion diameter of 16.5 nm is similar to stable hemifusion sites observed *in vitro* (Chlanda, Mekhedov, *et al.* 2016). I regularly observed additional densities orthogonal to the hemifusion sites. STA of 30 subvolumes revealed a rod-shaped structure with stalk and head, consistent with post-fusion HA shape and size (Benton, Gamblin, *et al.* 2020). I fitted the post-fusion HA structure (J Chen, Skehel, *et al.* 1999) to the STA density with high accordance, further confirming the overall consistent shape with post-fusion HA. Due to the small number of observed structures, STA did not resolve any secondary structure, and thus it is not possible to unambiguously determine the identity of the observed structures to HA. Since IAV membrane fusion is mediated by HA (**Section 1.2.1**), and the hemifusion state can only be reached after the back folding of the elongated HA2 intermediate to the post-fusion form, it is likely that the observed structure is indeed post-fusion HA.

Taken together, the direct observation of hemifusion sites between IAV particles and the endosomal membrane directly supports the 'hemifusion stabilization' hypothesis as the antiviral mechanism of IFITM3 (Feeley *et al.* 2011; Desai *et al.* 2014). Structures similar to post-fusion HA further indicate that IFITM3 does not affect the fusogenic activity of HA, which also supports the broad countermeasure of IFITM3 against a wide variety of viruses entering the cell via the late endosomal pathway, such as respiratory syncytial virus, chikungunya virus, West Nile virus(Zani & Yount 2018), tick-borne encephalitis virus (Chmielewska *et al.* 2022), Sindbis and Semliki Forest virus (Weston *et al.* 2016), and filoviruses (Huang *et al.* 2011). Specificity of IFITM3 rather relies on the cellular localization in late endosomes. Other members of the IFITM family show different localization patterns, thus a specific against other virus types. IFITM1, for example, is localized at the plasma membrane (SE Smith *et al.* 2019) and blocks viruses like HIV (Lu *et al.* 2011) that directly fuse there. Since other IFITMs show a similar protein structure, it can be speculated that the mode of action is similar for the different IFITM members, but this needs further experimental validation.

5.2.3.3 IFITM3 induced local lipid sorting stabilizes the hemifusion state

By utilizing *in situ* cryo-CLEM, I could show that IFITM3 stabilizes the hemifusion state during HA-mediated viral fusion and thus inhibits the release of the viral genome to the cytoplasm, effectively inhibiting viral infection. This is the first direct visualization of hemifusion within the native cellular environment of the cell and proves 'hemifusion stabilization' as the molecular mechanism of IFITM3. However, these results can not directly explain how the hemifusion is stabilized. STA analysis indicates that post-fusion HA is present at the hemifusion sites. Thus it is unlikely that IFITM3 inhibits the function of the viral fusion protein. Based on these results, it is likely that IFITM3 modulates the properties of the endosomal

membrane, which hinders fusion pore formation. Fusion pore opening is inhibited by lipids with negative spontaneous curvatures like cholesterol and promoted by lipids with positive, spontaneous curvatures such as lysophosphatidylcholine (LPC) (Chernomordik & Kozlov 2003). Previous studies reported that IFITM3 modulates the cholesterol levels in late endosomes (Amini-Bavil-Olyaee *et al.* 2013). To better understand the impact of IFITM3 on the endosomal lipid composition, I collaborated with Dr. Fabio Lolicato (Heidelberg University Biochemistry Center) and Dr. Gonen Golani (Institute for Theoretical Physics, University Heidelberg) utilizing molecular dynamics (MD) simulations and continuum membrane modeling (Klein, Golani, *et al.* 2023). Atomistic MD simulations (**Figure 5.1a**) were used to analyze the interaction of an IFITM3 molecule with lipids of a complex membrane, mimicking the LE membrane composition. This experiment showed that in the vicinity of IFITM3, the local cholesterol concentration was significantly reduced by 14.2 %. The local concentration of the phospholipids 1-palmitoyl-2-oleoyl-sn-glycero-3-phosphocholine (POPC) and lysobisphosphatidic acid (LBPA) (T Kobayashi *et al.* 2002) were, in turn, increased by 5.9 % and 6.0 %, respectively (**Figure 5.1b**). Although overall cholesterol is repelled by IFITM3, the palmitoylation site at Cys72 shows a high affinity to cholesterol. A recent study showed that Cys72 is essential for the antiviral function of IFITM3 and allows correct insertion of the protein into the membrane (Garst *et al.* 2021). This could explain how IFITM3 can be localized in the cholesterol-rich endosomal membrane and, at the same time, repel cholesterol from its vicinity. Due to the transmembrane domain of IFITM3, the protein is excluded from the hemifusion diaphragm. The cholesterol repulsion of IFITM3 thus results in a local increase in the cholesterol concentration at the hemifusion diaphragm. Due to the negative spontaneous curvature of cholesterol, an increase in cholesterol concentration at the hemifusion site will reduce the mean intrinsic curvate of the hemifusion diaphragm, thus reducing mechanical stress in the diaphragm. This, in turn, will stabilize the hemifusion state and increase the energy barrier for fusion pore formation. Continuum membrane modeling of the hemifusion site showed that

IFITM3-induced cholesterol repulsion increases the fusion pore formation energy barrier by 26 $^{k_BT}/_{mol_{IFITM3}\%}$. For an IFITM3 concentration of 0.32 % $^{\text{IFITM3}}/_{\text{lipids}}$ in the endosomal membrane, this would lead to an increase of the fusion pore formation energy barrier of 8 k_BT (**Figure 5.1c**), resulting in an increased hemifusion dwell time of 3 orders of magnitude. Even with a lower IFITM3 concentration of 0.16 % $^{\text{IFITM3}}/_{\text{lipids}}$, the dwell time of fusion pore formation is increased by 33×. This increased energy barrier stabilizes the hemifusion state, as fusion pore formation is inhibited.

In summary, atomistic MD simulations and continuum membrane modeling predicts that IFITM3-mediated cholesterol repulsion and the resulting change in the endosomal membrane composition leads to an increased energy barrier for fusion pore formation, which stabilizes the hemifusion state and increases the dwell time of fusion pore formation. Thus, virus particles are trapped in a hemifusion state during viral membrane fusion and are subject to degradation in the endosomal-lysosomal system. These theoretical results provide a molecular mechanism of IFITM3-induced hemifusion stabilization as observed by *in situ* cryo-ET.

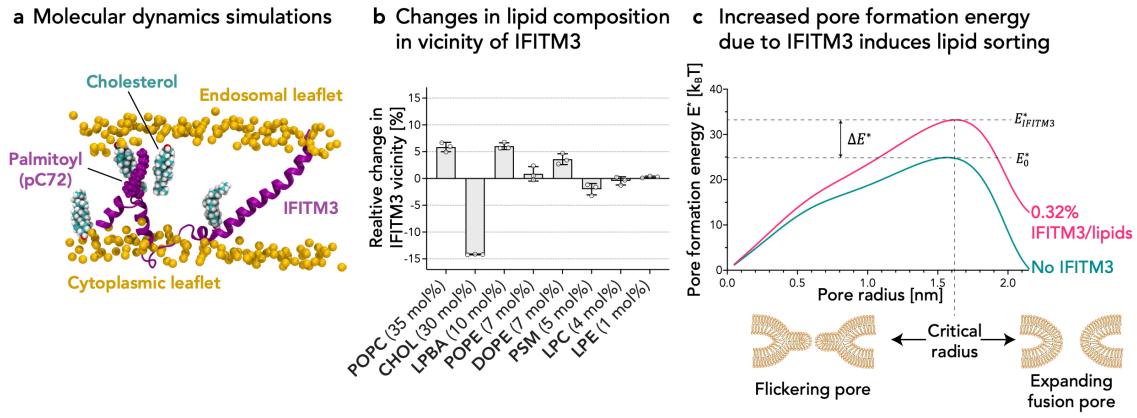

Figure 5.1: (Captions on next page)

Figure 5.1: IFITM3-induced cholesterol repulsion leads to an increased energy barrier for fusion pore formation. a Snapshot of atomistic MD simulation. IFITM3 is shown in magenta. The palmitoylated Cys72 is shown as an atom sphere model. Phorshoporus atoms of the lipid head groups are depicted in yellow, lipid tails are not shown. Cholesterol in the vicinity of IFITM3 are shown as atom sphere models. **b** Graph showing the relative changes in lipid concentration in the vicinity of IFITM3 based on three independent atomistic MD simulations with an accumulated simulation time of 18 µs. **c** Based on continuum membrane modeling, the pore formation energy E^* is shown as a function of the pore radius for a system without IFITM3-mediated lipid sorting (blue-green graph) and with a 0.32% $^{\text{IFITM3}}/_{\text{lipids}}$ ratio (magenta graph). The IFITM3-induced change in lipid composition at the hemifusion site increases the energy barrier for fusion pore formation at the critical radius by $\Delta E^* = 8k_BT$. This figure is a modified reprint from *Cell Host Microbe*, Volume 31.4 by Klein, Golani, *et al.* (2023), 'IFITM3 blocks influenza virus entry by sorting lipids and stabilizing hemifusion', ©2023, with permission from Elsevier.

5.3 Conclusion

IFITM3 is an essential protein of the innate immune system, and with its broad antiviral function, it substantially contributes to cellular resilience against infections. Despite its clinical importance, the antiviral mechanisms are not yet fully understood. Using a novel *in situ* cryo-CLEM method, I aimed to shed light on the molecular mechanism of the antiviral properties of IFITM3. To that aim, I established a suitable cell culture system with stable IFITM3 overexpression and fluorescent labeling of IAV particles. Structural analysis of IFITM3 positive endosomal-lysosomal organelles showed that the expression of IFITM3 does not modulate the organelle morphology or the number of ILVs in the endosomal lumen. These results contradict the 'fusion decoy' hypothesis and indicate that IFITM3's mode of action is not to modulate the number of ILVs. Using the established *in situ* cryo-CLEM workflow, I was able to localize and identify individual IAV particles within the natural cellular environment. Ultrastructural characterization by cryo-ET revealed that most of the observed viral particles were in a hemifusion state. Since hemifusion is a short-lived intermediate

and due to the late time point after infection, this data strongly indicates that the observed hemifusion sites are stalled. The direct observation of stabilized hemifusion sites during IAV infection in the natural cellular environment is the first direct proof of the previously postulated 'hemifusion stabilization' hypothesis. STA analysis of the hemifusion sites revealed densities with a size and shape comparable to the post-fusion form of HA. Although the resolution was not sufficient to unambiguously prove the identity as post-fusion HA, it is an indication that the energy-giving back folding of HA2 is not inhibited by IFITM3. These results indicate that IFITM3 might not inhibit viral fusion proteins but rather prevent fusion pore formation, likely due to an increased energy barrier for fusion pore formation. This energy barrier is highly dependent on the lipid composition of the membrane. To understand the impact of IFITM3 on the endosomal lipid composition, I collaborated with Dr. Gonen Golani and Dr. Fabio Lolicato on atomistic MD simulation and continuum membrane modeling. The results indicate that IFITM3 induces local lipid sorting by cholesterol repulsion. Since IFITM3 is excluded from hemifusion sites due to its transmembrane domain, cholesterol will accumulate at the hemifusion sites. Continuum membrane modeling showed that this change in lipid composition could increase the energy barrier for fusion pore formation and effectively stabilize the hemifusion state during viral membrane fusion.

In conclusion, I was able to prove hemifusion stabilization as the antiviral mechanism of IFITM3 and identified putative post-fusion HA at the hemifusion sites indicating that IFITM3 does not impact the viral fusion machinery but rather indirectly stabilizes hemifusion by modulating the mechanical properties of the endosomal membrane (**Figure 5.2**). These new findings make a significant contribution to the understanding of the antiviral mechanism of IFITM3.

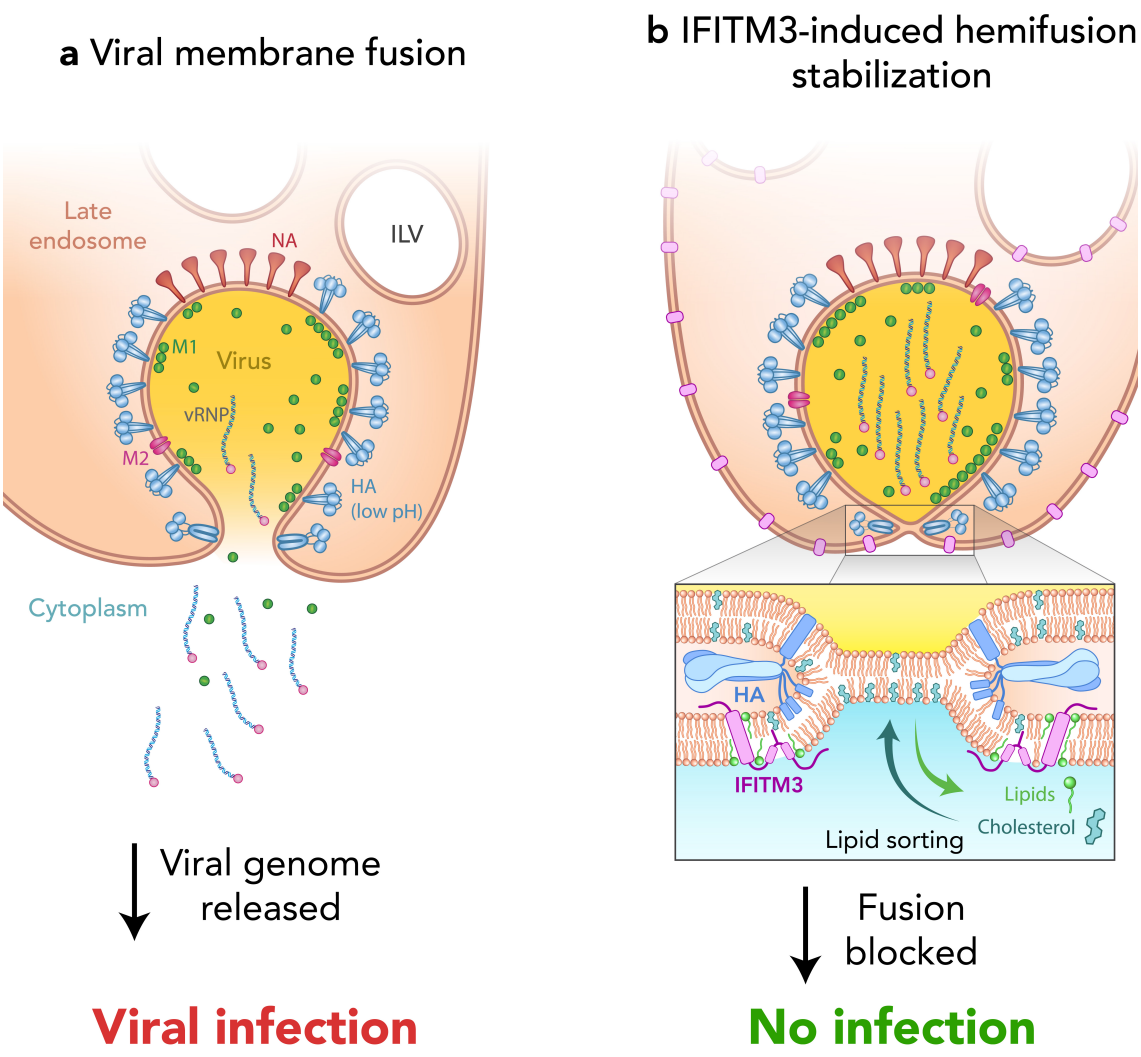

Figure 5.2: Schematic of the antiviral mechanism of IFITM3. **a** In the absence of IFITM3, HA-mediated membrane fusion allows the release of the viral vRNPs to the viral cytoplasm. **b** IFITM3 is part of the innate immune system and is induced by IFN. IFITM3 is localized at late endosomes and blocks the release of vRNPs by stabilizing the intermediate hemifusion state during viral membrane fusion. IFITM3 modulates the lipid composition of the late endosomal membrane by local lipid sorting, which increases the energy barrier for fusion pore formation, and thus stabilizes the hemifusion state. This figure is a modified reprint from *Cell Host Microbe*, Volume 31.4 by Klein, Golani, *et al.* (2023), 'IFITM3 blocks influenza virus entry by sorting lipids and stabilizing hemifusion', ©2023, with permission from Elsevier.

5.4 Outlook

Here, I was able to structurally characterize the antiviral mechanism of IFITM3 by *in situ* cryo-CLEM and could directly prove hemifusion stabilization as IFITM3's antiviral mode of action. To that aim, I utilized an IFITM3 overexpressing A549 cell line, which allowed me to attribute the antiviral mechanism specifically to IFITM3. To further validate my findings, the antiviral mechanism could be studied in the next step using more complex model systems like primary lung cells or organoid model systems for lung diseases (J Chen & Na 2022). Due to the larger size of organoids, vitrification by plunge freezing is not possible, but rather HPF with cryo-FIB lift-out could be utilized (Mahamid *et al.* 2015). Other members of the IFITM protein family show a similar topology to IFITM3 (Bailey, Zhong, *et al.* 2014). Thus it is plausible that the mode of action is shared within the family. But this remains to be evaluated.

To increase the chance of observing individual virus particles during viral entry by cryo-ET, I decided to utilize a high MOI of 200 infectious virus particles per cell. Structural studies could be performed with a decreasing number of viruses to exclude the possibility that this high virus load leads to non-physiological mechanisms. As cryo-FIB milling is a time-consuming and primarily manual procedure, this screening approach was unreasonable. Recent developments in automated cryo-FIB milling (Zachs *et al.* 2020; Buckley *et al.* 2020) and faster cryo-ET data acquisition schemes (Eisenstein *et al.* 2023) will allow such screening approaches in the future. For the same reason, I also opted to analyze only one time-point post-infection to structurally study the antiviral properties of IFITM3. Based on an entry-time course, I chose a time point for analysis at 1 hpi, just 15 min after the determined entry-half time of 45 mpi, which allowed me to observe accumulated hemifusion sites. In future experiments, it would be informative to study different time points post-infection, allowing to follow virus particles from viral cell entry to degradation in lysosomes in IFITM3-expressing cells.

Interestingly, hemifusion sites were mainly observed at ILVs rather than the limiting late endosomal membrane. This result was surprising, as it is commonly believed that IAV fuses directly with the limiting endosomal membrane (Krammer *et al.* 2018). Based on these results, a future study with a focus on IAV entry pathways in the endosome could answer the question if ILV retrofusion is a viable entry pathway of IAV. Room-temperature ET of IFITM3-immunogold labeled cell sections indicated that IFITM3 is also localized at ILVs, which would explain the observed stabilized hemifusion at the ILV membrane. Further studies using super-resolution light microscopy like MINFLUX (R Schmidt *et al.* 2021) could allow the study of the cellular localization of IFITM3 within endosomes in more detail.

At the hemifusion sites, I observed structures with an overall size and shape compatible with the post-fusion form of HA (J Chen, Skehel, *et al.* 1999), but the low resolution STA structure did not allow for unambiguous identification. Since these structures were observed at the hemifusion site between the endosomal membrane and IAV particles, HA is expected to be found, thus the assumption that the structures represent post-fusion HA is reasonable. Still, acquiring a more extensive dataset would allow for a higher resolution STA structure, resolving secondary structures and thus allowing for unambiguous identification. Furthermore, such a study would allow determining the native post-fusion HA structure in the natural cellular environment. Current single-particle cryo-EM structures of the post-fusion HA were purified, and the sample was treated with 2-mercaptoethanol to break the disulfide bonds and subsequently incubated at low pH for 30 min (Benton, Gamblin, *et al.* 2020). Due to this harsh treatment, the observed structure might not resemble the native post-fusion HA.

The results of atomistic MD simulation and continuum membrane modeling (Klein, Golani, *et al.* 2023) indicate that IFITM3 induces local lipid sorting in late endo-

somes, resulting in an increased cholesterol concentration at hemifusion sites, which in turn increases the hemifusion dwell time, and thus stabilizing the hemifusion state. This inhibition is highly dependent on the cholesterol concentration within endosomes. Measurements of the endosomal cholesterol concentration would allow to better estimate the impact of local lipid sorting on hemifusion stabilization. Furthermore, it would answer the question if IFITM3 also modulates the overall cholesterol concentration of late endosomes. Identification of local lipid sorting by cholesterol repulsion presents a novel mode of action and might be present in more transmembrane proteins to regulate fusion events in the cell. Further MD simulation studies on a broad range of transmembrane proteins could answer the question if local lipid sorting represents a previously unknown common mechanism.

In the future, it might be possible to utilize the gained knowledge of IFITM3's antiviral mechanism to develop antiviral drugs, like small peptides mimicking IFITM3, that specifically block viral-induced membrane fusion.

Supplementary data

5.5 List of materials

Table 5.2: List of primary antibodies used in this study.

Antibody	Source	Identifier	Dilution for WB	Dilution for IF
Actin	Merck, Sigma-Aldrich	A5441	1:4,000	
IFITM3	Proteintech Group Inc.	11714-1-AP	1:2,000	1:200
M2	Santa Cruz Biotechnology, Inc.	sc-32238		1:50

Table 5.3: List of secondary antibodies used in this study.

Antibody	Source	Identifier	Dilution
Anit-Mouse IgG-HRP	Santa Cruz Biotechnology, Inc.	sc-516102	1:1,000
Mouse anti-Rabbit IgG-HRP	Santa Cruz Biotechnology, Inc.	sc-2357	1:1,000
Goat anti-Rabbit IgG (H+L) Alexa Fluor 680	ThermoFisher Scientific, Invitrogen	A21076	1:2,000
Goat anti-Rabbit IgG (H+L) Alexa Fluor 633	ThermoFisher Scientific, Invitrogen	A21071	1:2,000

Table 5.4: List of cell lines, bacterial stock, and viral stock used in this study.

Antibody	**Source**	**Identifier**
A549 cells	American Type Culture Collection (ATCC)	CCL-185
E. coli competent cells 'Stellar'	Takara Bio Inc.	636763
HEK293T cells	American Type Culture Collection (ATCC)	CRL-3216
HEK293T-MCB cells	Dr. Marco Binder (DKFZ, Heidelberg, Germany)	N/A
Influenza A/WSN/1933(H1N1) virus	E Hoffmann *et al.* (2000)	N/A
MDCK cells	Prof. João Amorim (Instituto Gulbenkian de Ciência, Portugal)	N/A

Table 5.5: List of chemicals and reagents used in this study. (1/2)

Reagent	Source	Identifier
1-Hexadecen	Merck, Sigma-Aldrich	822064
Avicel	FMC Corporation	RC-581
Benzonase Nuclease HC	Merck, Millipore	71206-25KUN
Biotin Azide	ThermoFisher Scientific	B10184
Bovine Serum Albumin (BSA)	Merck, Sigma-Aldrich	A7030
CellBrite Green Cytoplasmic Membrane Dye (Neuro-DiO)	Biotium	30021
Color Prestained Protein Standard	New England Biolabs	P7719
Color Prestained Protein Standard	New England Biolabs	P7712S
cOmplete, Mini, EDTA-free Protease Inhibitor Cocktail	ThermoFisher Scientific, Roche	4693159001
Crystal violet solution, 1%, aqueous solution	Merck, Sigma-Aldrich	V5265
$CuSO_4$	Merck, Sigma-Aldrich	203165
CutSmart Buffer	New England Biolabs	B7204
DAPI	Merck, Sigma-Aldrich	D9542
DMEM	ThermoFisher Scientific, Gibco	11965092
DMEM, high glucose, GlutaMAX	ThermoFisher Scientific, Gibco	61965026
DMEM/F12	ThermoFisher Scientific, Gibco	11320033
DMSO	Merck, Sigma-Aldrich	D2650
Fetal bovine serum (FBS)	ThermoFisher Scientific, Gibco	10270-106
Fish skin gelatine (FSG)	Merck, Sigma-Aldrich	G7765
Glutaraldehyde	Merck, Sigma-Aldrich	G5882
Glycine	ThermoFisher Scientific	10070150
HEPES	Carl Roth GmbH & Co. KG	9105.2
Hoechst 33342	Merck, Sigma-Aldrich	B2261
Interferon beta (IFNβ)	ImmunoTools GmbH	11343524
Laemmli Sample Buffer (4x)	Bio-Rad Laboratories Inc.	1610747
Bacto Yeast Extraxt (LB)	ThermoFisher Scientific, Gibco	212750
Lowicryl HM20 Non-polar, Hydrophobic	Polysciences Inc.	15924-1
Methanol	Honeywell	32213
Opti-MEM medium	ThermoFisher Scientific, Gibcon	31985062
Formaldehyde 37% (PFA)	Bernd Kraft GmbH	BK19916
Sylgard 184	Dow Corning Inc.	1673921
PBS	Merck, Sigma-Aldrich	D8537

Table 5.6: List of chemicals and reagents used in this study. (2/2)

Reagent	Source	Identifier
Penicillin-Streptomycin (P/S) (10.000 units/ml)	ThermoFisher Scientific	15140122
Pierce High Capacity NeutrAvidin Agarose	ThermoFisher Scientific	29202
Polybrene infection reagent	Merck, Sigma-Aldrich	TR-1003-G
Polyethylenimine (PEI)	Polysciences	23966-1
ProLong Glass Antifade Mountant	ThermoFisher Scientific, Invitrogen	P36982
Protease inhibitor cocktail	Roche	11873580001
Protein-A gold 10 nm	Aurion	PA-80830/1
Puromycin	Merck, Sigma-Aldrich	P8833
Restriction Endonuclease BssHII	New England Biolabs	R0199S
Restriction Endonuclease XbaI	New England Biolabs	R0145S
S.O.C. medium	ThermoFisher Scientific, Invitrogen	15544034
SDS	Serva	20765.03
Sodium deoxycolate	D6750-25G	D6750
TBTA	Merck, Sigma-Aldrich	C4706
TCEP	Merck, Sigma-Aldrich	678937
TGS buffer (10x)	Bio-Rad	1610772
Trypsin from bovine pancreas, TPCK-treated	Merck, Sigma-Aldrich	T1426
Trans-Blot Turbo Mini 0.2 µm PVDF	Bio-Rad	1704156
TransIT-2020 Transfection Reagent	Mirus Bio	MIR 5400
TransIT-293 Transfection Reagent	Mirus Bio	MIR 2700
TransIT-LT1 Transfection Reagent	Mirus Bio	MIR 2300
Triton X-100	Merck, Sigma-Aldrich	X100
Trypsin inhibitor from Glycine max (soybean)	Merck, Sigma-Aldrich	T9128
Tween 20	Carl Roth GmbH & Co. KG	9127.1
Precision Plus Protein All Blue Protein Standard	Bio-Rad	1610373
Uranyl acetate	SERVA Electrophoresis GmbH	77870

Table 5.7: List of commercial kits used in this study.

Kit	Source	Identifier
In-fusion HD Cloning Kit	Takara Bio Inc.	639649
CloneAmp HiFi PCR Premix	Takara Bio Inc.	638500
Cloning Enhancer	Takara Bio Inc.	639615
Gateway LR Clonase Enzyme Mix	ThermoFisher Scientific, Invitrogen	11791019
Tricine gel	ThermoFisher Scientific	EC66252BOX
NucleoSpin Gel and PCR Clean-up Kit	MACHEREY-NAGEL	740609.5
QIAprep Spin Miniprep Kit	QIAGEN	27104
Beta-Lactamase Loading Solutions Kit	ThermoFisher Scientific, Invitrogen	K1085
LiveBLAzer FRET B/G (CCF4-AM)	ThermoFisher Scientific, Invitrogen	K1089
Pierce BCA Protein Assay Kit	ThermoFisher Scientific	23227
QIAGEN Plasmid Maxi Kit	QIAGEN	12163
Lenti-X GoStix	Takara Bio Inc.	631280

Table 5.8: List of consumables used in this study.

Kit	Source	Identifier
14 ml round bottom tube	Greiner Bio-One	187261
0.45 µm CME filter	Carl Roth GmbH & Co. KG	KH55.1
Microscopy cover slip NO. 1	Paul Marienfeld GmbH & Co. KG	111520
Microscopy slides, 76 ×26 mm	Diagonal GmbH & Co. KG	ISO NORM 8037/1
96 well assay plate, black, clear bottom	Corning Incorporated	3603
Sapphire discs for HPF/FS, ∅3 ×0.05 mm	Leica Microsystems	16702766
Quantifoil EM grid, 200 mesh gold, R1/4 SiO_2 film	Plano GmbH	S211R14A20 0
EM slot grids 2×1 mm, copper	Gilder	G2010-Cu
Cloning cylinder, glass, 150 µl	Merck, Sigma-Aldrich	C1059-1EA

Table 5.9: List of oligonucleotides used in this study.

Name	Sequence
Reverse sequencing primer IRES-rev	TATAGACAAACGCACACCG
Forward overhang primer for cloning	CCCACGCCCTGCGCGCGGCAGCAATGGTGTCCAAGGGTGAAGC
Reverse overhang primer for cloning	AAGCAGTTTTCTAGATCACTTGTACAGCTCATCCATTCCAC
Forward primer for sequencing	GGCAAACAACAGATGGCTGGCAAC
Reverse primer for sequencing	GTATGCATCTCCACAACTAGAAGG

Table 5.10: List of plasmids used in this study.

Name	Source
pCAGGS-A/Hong Kong/1968-HA	Chlanda, Schraidt, *et al.* (2015)
pCAGGS-A/Singapore/1957-NA	Chlanda, Schraidt, *et al.* (2015)
pCAGGS-M1-Blam	Tscherne *et al.* (2010)
pENTR221-clone3728-IFITM3	Dr. Marco Binder (DKFZ, Heidelberg, Germany)
pWPI-IRES-Puro	Dr. Marco Binder (DKFZ, Heidelberg, Germany)
pWPI-IFITM3	Cloned as described in Section 3.2
pCMV-VSV-G	addgene (#8454)
psPAX2	addgene (#12260)
pAdVantage	Promega (#E1711)
pHW2000-PB1-WSN	Dr. Ervin Fodor (University of Oxford, UK)
pHW2000-PB2-WSN	Dr. Ervin Fodor (University of Oxford, UK)
pHW2000-PA-WSN	Dr. Ervin Fodor (University of Oxford, UK)
pHW2000-NP-WSN	Dr. Ervin Fodor (University of Oxford, UK)
pHW2000-NA-WSN	Dr. Ervin Fodor (University of Oxford, UK)
pHW2000-M-WSN	Dr. Ervin Fodor (University of Oxford, UK)
pHW2000-NS-WSN	Dr. Ervin Fodor (University of Oxford, UK)
pHW2000-HA-WSN	Dr. Ervin Fodor (University of Oxford, UK)
pHW2000-PA-WSN-mScarlet	Andrew Mehle (University of Wisconsin – Madison, USA)
pcDNA3.4-mScarlet-codon-optimized	Established as described in Section 3.4
pHW2000-PA-WSN-mScarlet-codon- optimized	Cloned as described in Section 3.4
pC1-Rab7-eGFP	Dr. Pierre-Yves Lozach (CIID, University of Heidelberg, Germany)
pN1-LAMP1-eGFP	Dr. Pierre-Yves Lozach (CIID, University of Heidelberg, Germany)

Table 5.11: List of instruments used in this study.

Name	Manufactorer	Identifier
UV irradiation system	Vilber Lourmat GmbH	BIO-SUN
Sonicator	Bandelin Sonorex	N/A
Ultracentrifuge	Beckman Coulter, Inc.	Optima L-90K
Rotor for Optima L-90K	Beckman Coulter, Inc.	SW32
Ultracentrifuge	Beckman Coulter, Inc.	Optima TLX
Rotor for Optima TLX	Beckman Coulter, Inc.	TLA-120.2
Mini-PROTEAN Tetra Vertical Electrophoresis Cell	BioRad	1658005
Trans-Blot Turbo Transfer System	BioRad	1704150
Azure 400 chemiluminescent imager	Azure Biosystems	Azure 400
Plate reader	Tecan Trading AG	Infinite 200
High-pressure freezing system	Leica Microsystems	EM ICE
Freeze substitution system	Leica Microsystems	EM AFS2
Sputter coater	Leica Microsystems	EM ACE600
Ultramicrotome	Leica Microsystems	EM UC7
Diamond knife	DiATOME	DU3520
Fluorescent confocal microscope	Leica Microsystems	SP8
63×/1.4 NA HC PL APO CS2 oil immersion objective for SP8	Leica Microsystems	
Fluorescent wide-field microscope	Zeiss	CellDiscoverer 7 (CD7)
20×/0.95 NA plan-apochromat air objective for CD7	Zeiss	
Fluorescent wide-field microscope	Nikon	TS2-FL DS-Fi3
CFI Achro LWD ADL 20XF (20×/ 0.4 NA air objective for TS2	Nikon	MRP46202
Blam-assay filter set for Nikon Eclipse TS2	Chroma Technology	ET395/25x; 59001bs; 59001m
CryoCLEM with 60×/0.9 NA objective	Leica Microsystems	
Cryo-TEM Titan Krios, Gatan K3 camera, GIF	ThermoFisher Scientific	
Cryo-FIB/SEM Acquilos	ThermoFisher Scientific	
TEM Tecnai F30, Gatan OneView 4K camera	FEI	

Table 5.12: List of software used in this study.

Name	Source
GenSmart Codon Optimization	GenScripts
FIJI	Schindelin *et al.* (2012)
IMOD	Kremer *et al.* (1996)
icy	Chaumont *et al.* (2012)
Dynamo	Castaño-Díez *et al.* (2012)
LAS X	Leica Microsystems
MAPS	Schorb & Sieckmann (2017)
Prism	GraphPad Software
Imaris	Oxford Instruments
Post-correlation cryo-CLEM toolbox	Klein, Wachsmuth-Melm, *et al.* (2021)
cryoCARE	Buchholz *et al.* (2019)
Amira	ThermoFisher Scientific
Motioncor2	Zheng *et al.* (2017)
MATLAB 2020B	MathWorks
AutoQuant X3	Media Cybernetics, Inc.
SerialEM	Mastronarde (2005)
Magellan	Tecan Trading AG

5.6 Program code

5.6.1 3D image registration of cryo-LM data

```
% Set filenames of fixed and moving image
% pre_LM_stack: path to the image stack before milling / EM acquisition -> fixed image
pre_LM_stack = 'stack_before_milling.tif';
% post_LM_stack: path to the image stack after milling / EM acquisition -> moving image
post_LM_stack = 'stack_after_milling.tif';

% Set channel information
% channels: total number of channels in the tif file
channels = 3;
% channel_for_alignment: number of the channel that should be used for registration (one-indexed)
% small fiducial markers like lipiblue work best
channel_for_alignment = 3;

% Set pixel size of files in microns
% xy_resUM: pixel size in X/Y
```

```
xy_resUM = 0.13;
% z_resUM: pixel size in Z
z_resUM = 0.3;

% Extract image dimensions from imported files
[size_X_fixed, size_Y_fixed] = size(imread(pre_LM_stack));
size_Z_fixed = (size(imfinfo(pre_LM_stack), 1) / channels);
size_fixed = [size_X_fixed, size_Y_fixed, size_Z_fixed];
clear size_X_fixed size_Y_fixed size_Z_fixed;

size_Z_moving = (size(imfinfo(post_LM_stack), 1) / channels);
[size_X_moving, size_Y_moving] = size(imread(post_LM_stack));
size_moving = [size_X_moving, size_Y_moving, size_Z_moving];
clear size_X_moving size_Y_moving size_Z_moving;

% Create a 3D reference object which holds dimension information for both
% images
fixed_reference = imref3d(size_fixed, xy_resUM, xy_resUM, z_resUM);
moving_reference = imref3d(size_moving, xy_resUM, xy_resUM, z_resUM);

% Read multichannel tif image_after into fixed_image cell array
fixed_image = init_cell(channels, size_fixed(1), size_fixed(2), size_fixed(3));

k = 1;
for i = 1:size_fixed(3)
    for j = 1:channels
        fixed_image{j}(:, :, i) = imread(pre_LM_stack, k);
        k = k + 1;
    end
end

% Read multichannel tif of image_before into moving_image cell array
moving_image = init_cell(channels, size_moving(1), size_moving(2), size_moving(3));

k = 1;
for i = 1:size_moving(3)
    for j = 1:channels
        moving_image{j}(:, :, i) = imread(post_LM_stack, k);
        k = k + 1;
    end
end

disp('finished importing images');
toc;

% Use imregtform to calculate transformation matrix based on the fiducial
% map using translation and rotation only.

% Setup parameters
optimizer = registration.optimizer.RegularStepGradientDescent;
optimizer.GradientMagnitudeTolerance = 1e-5;
optimizer.MinimumStepLength = 5e-6;
optimizer.MaximumStepLength = 0.05;
optimizer.MaximumIterations = 5000;
optimizer.RelaxationFactor = 0.6;
metric = registration.metric.MattesMutualInformation;

% calculate the transformation matrix
transformation_matrix = imregtform(moving_image{channel_for_alignment}, moving_reference, fixed_image{channel_for_alignment},
fixed_reference, 'rigid', optimizer, metric, 'DisplayOptimization', true);
```

```
disp('finished calculating transformation matrix');
toc;

% Transform all channels of moving_image, clear untransformed stack
% from memory

moving_image_transformed = init_cell(channels, size_fixed(1), size_fixed(2), size_fixed(3));

for i = 1:channels
    [moving_image_transformed{i}, ~] = imwarp(moving_image{i}, moving_reference, transformation_matrix, 'OutputView', fixed_reference);
end

clear moving_image new_ref;

disp('finished transforming image stack');
toc;

% Save transformation_matrix
csvwrite('transformation_matrix.csv', transformation_matrix.T);

% Save transformed and fixed stack as one greyscale TIF per channel.

export_stack(fixed_image);
export_stack(moving_image_transformed);

disp('export complete');
toc;

% Functions down here: init_cell initializes a cell array of specified
% dimensions, export_stack writes tif stacks which work with FIJI.
function c = init_cell(ch, sizeX, sizeY, sizeZ)
    c = cell(1, ch);
    c(:) = {zeros(sizeX, sizeY, sizeZ, 'uint16')};
end

function export_stack(image)
     channels = size(image, 2);
     stack = size(image{1}, 3);
    for i = 1:channels
        export_filename = strcat(inputname(1), '_ch_', int2str(i), '.tif');
        imwrite(image{i}(:, :, 1), export_filename, 'Compression', 'lzw');
        for j = 2:stack
            imwrite(image{i}(:, :, j), export_filename, 'WriteMode', 'append', 'Compression', 'lzw');
        end
    end
end
```

Acronyms

A549	adenocarcinomic human alveolar basal epithelial cells
AES	airway epithelial cell
AFS	automatic freeze substitution
AH	amphipathic helix
AMP	ampicillin
ATCC	American Type Culture Collection
BF	bright field
Blam	β-lactamase
BSA	bovine serum albumin
cDNA	complementary DNA
CLEM	correlative light and electron microscopy
cRNA	complementary RNA
CTF	contrast transfer function
DAPI	4',6-diamidino-2-phenylindole
DC	dendritic cell
DENV	Dengue virus
DMEM	Dulbecco's modified eagle medium
dsRNA	double stranded RNA
EBOV	Ebolavirus
EM	electron microscope
ER	endoplasmic reticulum
ERGIC	endoplasmic reticulum – Golgi intermediate compartment
ET	electron tomography
FACS	fluorescence-activated cell sorting
FCS	fetal calf serum
FIB	focused ion beam
FRET	fluorescence resonance energy transfer
FS	freeze substitution
FSG	fish skin gelatin
GA	glutaraldehyde
GUV	giant unilamellar vesicle

HA	hemagglutinin
HEK293T	human embryonic kidney cell expressing the SV40 large T-antigen
HEK293T-MCB	HEK293T master cell bank cell
HIV	human immunodeficiency virus
HPF	high pressure freezing
hpi	hours post infection
IAV	influenza A virus
IFITM	interferon-induced transmembrane protein
IFN	interferon
IFNAR	interferon-α/β receptor
ILV	intraluminal vesicle
IMPα	importin-α
IMPβ1	importin-β1
IRF	interferon regulatory factor
ISG	interferon stimulated gene
ISGF	interferon stimulated gene factor
ISRE	interferon stimulated response element
JAK	Janus kinase
LACV	La Crosse encephalitis virus
LAMP1	lysosomal-associated membrane protein 1
LB	lysogeny broth
LBPA	lysobisphosphatidic acid
LD	lipid droplet
LE	late endosome
LM	light microscope
LN_2	liquid nitrogen
LPC	lysophosphatidylcholine
LPS	lipopolysaccharide
LUT	lookup table
M1	matrix protein 1
M2	matrix protein 2
MARV	Marburg virus
MD	molecular dynamics
MDA	melanoma differentiation-associated gene
MDCK	Madin-Darby canine kidney cell
MIP	maximum intensity projection
MOI	multiplicity of infection
mpi	minutes post infection
mRNA	messenger RNA
MVB	multivesicular body
Mx	myxovirus-resistance protein
NA	neuraminidase

nDiO	neuro-
Neu5Ac	N-acetylneuraminic acid
nG	neonGreen
NLS	nuclear localization signal
NMR	nuclear magnetic resonance
NP	nucleoprotein
NPC	nuclear pore complex
NSP	non-structural protein
NTD	N-terminal domain
OSBP	oxysterol-binding protein 1
OTF	optical transfer function
P/S	penicillin/streptomycin
PA	polymerase acidic protein
PAG	protein A gold
PAMP	pathogen-associated molecular pattern
PB1	polymerase subunit 1
PB2	polymerase subunit 2
PBS	phosphate buffered saline
pDC	plasmacytoid dendritic cell
PEI	polyethylenimine
PFA	paraformaldehyde
POPC	1-palmitoyl-2-oleoyl-sn-glycero-3-phosphocholine
PRR	pattern recognition receptor
PSF	point spread function
PTA	phosphotungstic acid
PTM	post translational modification
Rab7	Ras-related protein 7
RDRP	RNA-dependent RNA polymerase
RIG-I	retinoic acid-inducible gene I
RLR	RIG-I-like receptor
RNAP II	RNA-polymerase II
ROI	region of interest
rpm	rounds per minute
RT	room temperature
SARS-CoV	severe acute respiratory syndrome coronavirus
SD	standard deviation
SEM	scanning electron microscopy
SIM	structured illumination microscopy
SIRT	simultaneous iterative reconstruction technique
SMLM	single-molecule localization microscopy
SNP	single-nucleotide polymorphism
SNR	signal-to-noise ratio
SOFI	super-resolution optical fluctuation imaging
SP-A	surfactant protein A
SPA	single particle analysis

ssRNA	single-stranded RNA
STA	subtomogram averaging
STAT	signal transducers and activators of transcription
STED	stimulated emission depletion
TEM	transmission electron microscopy
TL	transmitted light
TLR	toll-like receptor
TMD	transmembrane domain
UA	uranyl acetate
VAPA	VAMP-associated protein A
v-ATPase	vacuolar-type ATPase
VLP	virus like particle
vRNA	viral RNA
vRNP	viral ribonucleoprotein

References

Ablasser A, Poeck H, Anz D, Berger M, Schlee M, Kim S, Bourquin C, Goutagny N, Jiang Z, Fitzgerald KA, Rothenfusser S, Endres S, Hartmann G & Hornung V (2009). Selection of molecular structure and delivery of RNA oligonucleotides to activate TLR7 versus TLR8 and to induce high amounts of IL-12p70 in primary human monocytes. *J Immunol* **182.11**, 6824–33. doi: 10.4049/jimmunol.0803001.

Alenquer M, Vale-Costa S, Etibor TA, Ferreira F, Sousa AL & Amorim MJ (2019). Influenza A virus ribonucleoproteins form liquid organelles at endoplasmic reticulum exit sites. *Nat Commun* **10.1**, 1629. doi: 10.1038/s41467-019-09549-4.

Allen EK, Randolph AG, Bhangale T, Dogra P, Ohlson M, Oshansky CM, Zamora AE, Shannon JP, Finkelstein D, Dressen A, DeVincenzo J, Caniza M, Youngblood B, Rosenberger CM & Thomas PG (2017). SNP-mediated disruption of CTCF binding at the IFITM3 promoter is associated with risk of severe influenza in humans. *Nat Med* **23.8**, 975–983. doi: 10.1038/nm.4370.

Amini-Bavil-Olyaee S, Choi YJ, Lee JH, Shi M, Huang IC, Farzan M & Jung JU (2013). The antiviral effector IFITM3 disrupts intracellular cholesterol homeostasis to block viral entry. *Cell Host Microbe* **13.4**, 452–64. doi: 10.1016/j.chom.2013.03.006.

Al-Amoudi A, Chang JJ, Leforestier A, McDowall A, Salamin LM, Norlén LPO, Richter K, Blanc NS, Studer D & Dubochet J (2004). Cryo-electron microscopy of vitreous sections. *EMBO J* **23.18**, 3583–8. doi: 10.1038/sj.emboj.7600366.

Arnold J, Mahamid J, Lucic V, Marco A de, Fernandez JJ, Laugks T, Mayer T, Hyman AA, Baumeister W & Plitzko JM (2016). Site-Specific Cryo-focused Ion Beam Sample Preparation Guided by 3D Correlative Microscopy. *Biophys J* **110.4**, 860–9. doi: 10.1016/j.bpj.2015.10.053.

Bailey CC, Huang IC, Kam C & Farzan M (2012). Ifitm3 limits the severity of acute influenza in mice. *PLoS Pathog* **8.9**, e1002909. doi: 10.1371/journal.ppat.1002909.

Bailey CC, Kondur HR, Huang IC & Farzan M (2013). Interferon-induced transmembrane protein 3 is a type II transmembrane protein. *J Biol Chem* **288.45**, 32184–32193. doi: 10.1074/jbc.M113.514356.

Bailey CC, Zhong G, Huang IC & Farzan M (2014). IFITM-Family Proteins: The Cell's First Line of Antiviral Defense. *Annu Rev Virol* **1**, 261–283. doi: 10.1146/annurev-virology-031413-085537.

Barman S, Ali A, Hui EK, Adhikary L & Nayak DP (2001). Transport of viral proteins to the apical membranes and interaction of matrix protein with glycoproteins in the assembly of influenza viruses. *Virus Res* **77.1**, 61–9. doi: 10.1016/s0168-1702(01)00266-0.

Baumeister W (2005). From proteomic inventory to architecture. *FEBS Lett* **579.4**, 933–7. doi: 10.1016/j.febslet.2004.10.102.

Benfield CT, MacKenzie F, Ritzefeld M, Mazzon M, Weston S, Tate EW, Teo BH, Smith SE, Kellam P, Holmes EC & Marsh M (2020). Bat IFITM3 restriction depends on S-palmitoylation and a polymorphic site within the CD225 domain. *Life Sci Alliance* **3.1**. doi: 10.26508/lsa.201900542.

Benne CA, Kraaijeveld CA, Strijp JA van, Brouwer E, Harmsen M, Verhoef J, Golde LM van & Iwaarden JF van (1995). Interactions of surfactant protein A with influenza A viruses: binding and neutralization. *J Infect Dis* **171.2**, 335–41. doi: 10.1093/infdis/171.2.335.

Benton DJ, Gamblin SJ, Rosenthal PB & Skehel JJ (2020). Structural transitions in influenza haemagglutinin at membrane fusion pH. *Nature* **583.7814**, 150–153. doi: 10.1038/s41586-020-2333-6.

Benton DJ, Nans A, Calder LJ, Turner J, Neu U, Lin YP, Ketelaars E, Kallewaard NL, Corti D, Lanzavecchia A, Gamblin SJ, Rosenthal PB & Skehel JJ (2018). Influenza hemagglutinin membrane anchor. *Proc Natl Acad Sci U S A* **115.40**, 10112–10117. doi: 10.1073/pnas.1810927115.

Bindels DS, Haarbosch L, Weeren L van, Postma M, Wiese KE, Mastop M, Aumonier S, Gotthard G, Royant A, Hink MA & Gadella Jr TWJ (2017). mScarlet: a bright monomeric red fluorescent protein for cellular imaging. *Nat Methods* **14.1**, 53–56. doi: 10.1038/nmeth.4074.

Boekema EJ, Folea M & Kouřil R (2009). Single particle electron microscopy. *Photosynth Res* **102.2-3**, 189–96. doi: 10.1007/s11120-009-9443-1.

Boonstra S, Blijleven JS, Roos WH, Onck PR, Giessen E van der & Oijen AM van (2018). Hemagglutinin-Mediated Membrane Fusion: A Biophysical Perspective. *Annu Rev Biophys* **47**, 153–173. doi: 10.1146/annurev-biophys-070317-033018.

Bouteiller O de, Merck E, Hasan UA, Hubac S, Benguigui B, Trinchieri G, Bates EEM & Caux C (2005). Recognition of double-stranded RNA by human toll-like receptor 3 and downstream receptor signaling requires multimerization and an acidic pH. *J Biol Chem* **280.46**, 38133–45. doi: 10.1074/jbc.M507163200.

Brass AL, Huang IC, Benita Y, John SP, Krishnan MN, Feeley EM, Ryan BJ, Weyer JL, Weyden L van der, Fikrig E, Adams DJ, Xavier RJ, Farzan M & Elledge SJ (2009). The IFITM proteins mediate cellular resistance to influenza A H1N1 virus, West Nile virus, and dengue virus. *Cell* **139.7**, 1243–54. doi: 10.1016/j.cell.2009.12.017.

Bright RA, Medina Mj, Xu X, Perez-Oronoz G, Wallis TR, Davis XM, Povinelli L, Cox NJ & Klimov AI (2005). Incidence of adamantane resistance among influenza A (H3N2) viruses isolated worldwide from 1994 to 2005: a cause for concern. *Lancet* **366.9492**, 1175–81. doi: 10.1016/S0140-6736(05)67338-2.

Brunner J (1989). Testing topological models for the membrane penetration of the fusion peptide of influenza virus hemagglutinin. *FEBS Lett* **257.2**, 369–72. doi: 10.1016/0014-5793(89)81574-1.

Buchholz TO, Krull A, Shahidi R, Pigino G, Jékely G & Jug F (2019). Content-aware image restoration for electron microscopy. *Methods Cell Biol* **152**, 277–289. doi: 10.1016/bs.mcb.2019.05.001.

Buckley G, Gervinskas G, Taveneau C, Venugopal H, Whisstock JC & Marco A de (2020). Automated cryo-lamella preparation for high-throughput in-situ structural biology. *J Struct Biol* **210.2**, 107488. doi: 10.1016/j.jsb.2020.107488.

Calder LJ & Rosenthal PB (2016). Cryomicroscopy provides structural snapshots of influenza virus membrane fusion. *Nat Struct Mol Biol* **23.9**, 853–8. doi: 10.1038/nsmb.3271.

Castaño-Díez D, Kudryashev M, Arheit M & Stahlberg H (2012). Dynamo: a flexible, user-friendly development tool for subtomogram averaging of cryo-EM data in high-performance computing environments. *J Struct Biol* **178.2**, 139–51. doi: 10.1016/j.jsb.2011.12.017.

Cavaillon JM (2017). "Pathogen-associated Molecular Patterns". In: *Inflammation*. John Wiley & Sons, Ltd. Chap. 2, 17–56. doi: 10.1002/9783527692156.ch2.

Chanturiya A, Chernomordik LV & Zimmerberg J (1997). Flickering fusion pores comparable with initial exocytotic pores occur in protein-free phospholipid bilayers. *Proc Natl Acad Sci U S A* **94.26**, 14423–8. doi: 10.1073/pnas.94.26.14423.

Chaumont F de, Dallongeville S, Chenouard N, Hervé N, Pop S, Provoost T, Meas-Yedid V, Pankajakshan P, Lecomte T, Le Montagner Y, Lagache T, Dufour A & Olivo-Marin JC (2012). Icy: an open bioimage informatics platform for extended reproducible research. *Nat Methods* **9.7**, 690–6. doi: 10.1038/nmeth.2075.

Chen B (2019). Molecular Mechanism of HIV-1 Entry. *Trends Microbiol* **27.10**, 878–891. doi: 10.1016/j.tim.2019.06.002.

Chen J, Skehel JJ & Wiley DC (1999). N- and C-terminal residues combine in the fusion-pH influenza hemagglutinin HA(2) subunit to form an N cap that terminates the triple-stranded coiled coil. *Proc Natl Acad Sci U S A* **96.16**, 8967–72. doi: 10.1073/pnas.96.16.8967.

Chen J & Na F (2022). Organoid technology and applications in lung diseases: Models, mechanism research and therapy opportunities. *Front Bioeng Biotechnol* **10**, 1066869. doi: 10.3389/fbioe.2022.1066869.

Chen R & Holmes EC (2006). Avian influenza virus exhibits rapid evolutionary dynamics. *Mol Biol Evol* **23.12**, 2336–41. doi: 10.1093/molbev/msl102.

Chen W, Calvo PA, Malide D, Gibbs J, Schubert U, Bacik I, Basta S, O'Neill R, Schickli J, Palese P, Henklein P, Bennink JR & Yewdell JW (2001). A novel influenza A virus mitochondrial protein that induces cell death. *Nat Med* **7.12**, 1306–12. doi: 10.1038/nm1201-1306.

Chernomordik LV & Kozlov MM (2003). Protein-lipid interplay in fusion and fission of biological membranes. *Annu Rev Biochem* **72**, 175–207. doi: 10.1146/annurev.biochem.72.121801.161504.

Chernomordik LV, Zimmerberg J & Kozlov MM (2006). Membranes of the world unite!. *J Cell Biol* **175.2**, 201–7. doi: 10.1083/jcb.200607083.

Chesarino NM, Compton AA, McMichael TM, Kenney AD, Zhang L, Soewarna V, Davis M, Schwartz O & Yount JS (2017). IFITM3 requires an amphipathic helix for antiviral activity. *EMBO Rep* **18.10**, 1740–1751. doi: 10.15252/embr.201744100.

Chesarino NM, McMichael TM, Hach JC & Yount JS (2014). Phosphorylation of the antiviral protein interferon-inducible transmembrane protein 3 (IFITM3) dually

regulates its endocytosis and ubiquitination. *J Biol Chem* **289.17**, 11986–11992. doi: 10.1074/jbc.M114.557694.

Chlanda P, Mekhedov E, Waters H, Schwartz CL, Fischer ER, Ryham RJ, Cohen FS, Blank PS & Zimmerberg J (2016). The hemifusion structure induced by influenza virus haemagglutinin is determined by physical properties of the target membranes. *Nat Microbiol* **1.6**, 16050. doi: 10.1038/nmicrobiol.2016.50.

Chlanda P, Schraidt O, Kummer S, Riches J, Oberwinkler H, Prinz S, Kräusslich HG & Briggs JAG (2015). Structural Analysis of the Roles of Influenza A Virus Membrane-Associated Proteins in Assembly and Morphology. *J Virol* **89.17**, 8957–66. doi: 10.1128/JVI.00592-15.

Chmielewska AM, Gómez-Herranz M, Gach P, Nekulova M, Bagnucka MA, Lipińska AD, Rychłowski M, Hoffmann W, Król E, Vojtesek B, Sloan RD, Bieńkowska-Szewczyk K, Hupp T & Ball K (2022). The Role of IFITM Proteins in Tick-Borne Encephalitis Virus Infection. *J Virol* **96.1**, e0113021. doi: 10.1128/JVI.01130-21.

Chou Yy, Heaton NS, Gao Q, Palese P, Singer RH, Singer R & Lionnet T (2013). Colocalization of different influenza viral RNA segments in the cytoplasm before viral budding as shown by single-molecule sensitivity FISH analysis. *PLoS Pathog* **9.5**, e1003358. doi: 10.1371/journal.ppat.1003358.

Christman MC, Kedwaii A, Xu J, Donis RO & Lu G (2011). Pandemic (H1N1) 2009 virus revisited: an evolutionary retrospective. *Infect Genet Evol* **11.5**, 803–11. doi: 10.1016/j.meegid.2011.02.021.

Costa TRD, Ignatiou A & Orlova EV (2017). "Structural Analysis of Protein Complexes by Cryo Electron Microscopy". In: *Methods in Molecular Biology*. Springer New York, 377–413. doi: 10.1007/978-1-4939-7033-9_28.

Dadonaite B, Gilbertson B, Knight ML, Trifkovic S, Rockman S, Laederach A, Brown LE, Fodor E & Bauer DLV (2019). The structure of the influenza A virus genome. *Nat Microbiol* **4.11**, 1781–1789. doi: 10.1038/s41564-019-0513-7.

Danev R & Nagayama K (2001). Transmission electron microscopy with Zernike phase plate. *Ultramicroscopy* **88.4**, 243–52. doi: 10.1016/s0304-3991(01)00088-2.

De Rosier DJ & Klug A (1968). Reconstruction of three dimensional structures from electron micrographs. *Nature* **217.5124**, 130–4. doi: 10.1038/217130a0.

Deng T, Vreede FT & Brownlee GG (2006). Different de novo initiation strategies are used by influenza virus RNA polymerase on its cRNA and viral RNA promoters during viral RNA replication. *J Virol* **80.5**, 2337–48. doi: 10.1128/JVI.80.5.2337-2348.2006.

Desai TM, Marin M, Chin CR, Savidis G, Brass AL & Melikyan GB (2014). IFITM3 restricts influenza A virus entry by blocking the formation of fusion pores following virus-endosome hemifusion. *PLoS Pathog* **10.4**, e1004048. doi: 10.1371/journal.ppat.1004048.

Diamond MS & Farzan M (2013). The broad-spectrum antiviral functions of IFIT and IFITM proteins. *Nat Rev Immunol* **13.1**, 46–57. doi: 10.1038/nri3344.

Dias A, Bouvier D, Crépin T, McCarthy AA, Hart DJ, Baudin F, Cusack S & Ruigrok RWH (2009). The cap-snatching endonuclease of influenza virus polymerase resides in the PA subunit. *Nature* **458.7240**, 914–8. doi: 10.1038/nature07745.

Dias Junior AG, Sampaio NG & Rehwinkel J (2019). A Balancing Act MDA5 in Antiviral Immunity and Autoinflammation. *Trends Microbiol* **27.1**, 75–85. doi: 10.1016/j.tim.2018.08.007.

Diebold SS, Kaisho T, Hemmi H, Akira S & Reis e Sousa C (2004). Innate antiviral responses by means of TLR7-mediated recognition of single-stranded RNA. *Science* **303.5663**, 1529–31. doi: 10.1126/science.1093616.

Doms RW, Lamb RA, Rose JK & Helenius A (1993). Folding and assembly of viral membrane proteins. *Virology* **193.2**, 545–62. doi: 10.1006/viro.1993.1164.

Dou D, Revol R, Östbye H, Wang H & Daniels R (2018). Influenza A Virus Cell Entry, Replication, Virion Assembly and Movement. *Front Immunol* **9**, 1581. doi: 10.3389/fimmu.2018.01581.

Dubochet J, Adrian M, Chang JJ, Homo JC, Lepault J, McDowall AW & Schultz P (1988). Cryo-electron microscopy of vitrified specimens. *Q Rev Biophys* **21.2**, 129–228. doi: 10.1017/s0033583500004297.

Edinger TO, Pohl MO & Stertz S (2014). Entry of influenza A virus: host factors and antiviral targets. *J Gen Virol* **95.Pt 2**, 263–277. doi: 10.1099/vir.0.059477-0.

Eisenstein F, Yanagisawa H, Kashihara H, Kikkawa M, Tsukita S & Danev R (2023). Parallel cryo electron tomography on in situ lamellae. *Nat Methods* **20.1**, 131–138. doi: 10.1038/s41592-022-01690-1.

Eisfeld AJ, Neumann G & Kawaoka Y (2015). At the centre: influenza A virus ribonucleoproteins. *Nat Rev Microbiol* **13.1**, 28–41. doi: 10.1038/nrmicro3367.

Elster C, Larsen K, Gagnon J, Ruigrok RW & Baudin F (1997). Influenza virus M1 protein binds to RNA through its nuclear localization signal. *J Gen Virol* **78 (Pt 7)**, 1589–96. doi: 10.1099/0022-1317-78-7-1589.

Erickson HP & Klug A (1971). Measurement and compensation of defocusing and aberrations by Fourier processing of electron micrographs. *Philosophical Transactions of the Royal Society of London. B, Biological Sciences* **261.837**, 105–118. doi: 10.1098/rstb.1971.0040.

Eskelinen EL (2006). Roles of LAMP-1 and LAMP-2 in lysosome biogenesis and autophagy. *Mol Aspects Med* **27.5-6**, 495–502. doi: 10.1016/j.mam.2006.08.005.

Everitt AR *et al.* (2012). IFITM3 restricts the morbidity and mortality associated with influenza. *Nature* **484.7395**, 519–23. doi: 10.1038/nature10921.

Faoro R, Bassu M, Mejia YX, Stephan T, Dudani N, Boeker C, Jakobs S & Burg TP (2018). Aberration-corrected cryoimmersion light microscopy. *Proc Natl Acad Sci U S A* **115.6**, 1204–1209. doi: 10.1073/pnas.1717282115.

Feeley EM, Sims JS, John SP, Chin CR, Pertel T, Chen LM, Gaiha GD, Ryan BJ, Donis RO, Elledge SJ & Brass AL (2011). IFITM3 inhibits influenza A virus infection by preventing cytosolic entry. *PLoS Pathog* **7.10**, e1002337. doi: 10.1371/journal.ppat.1002337.

Fernández JJ, Li S & Crowther RA (2006). CTF determination and correction in electron cryotomography. *Ultramicroscopy* **106.7**, 587–96. doi: 10.1016/j.ultramic.2006.02.004.

Fessler MB & Summer RS (2016). Surfactant Lipids at the Host-Environment Interface. Metabolic Sensors, Suppressors, and Effectors of Inflammatory Lung Disease. *Am J Respir Cell Mol Biol* **54.5**, 624–35. doi: 10.1165/rcmb.2016-0011PS.

Fontana J, Cardone G, Heymann JB, Winkler DC & Steven AC (2012). Structural changes in Influenza virus at low pH characterized by cryo-electron tomography. *J Virol* **86.6**, 2919–29. doi: 10.1128/JVI.06698-11.

Frank J, Zhu J, Penczek P, Li Y, Srivastava S, Verschoor A, Radermacher M, Grassucci R, Lata RK & Agrawal RK (1995). A model of protein synthesis based on cryo-electron microscopy of the E. coli ribosome. *Nature* **376.6539**, 441–4. doi: 10.1038/376441a0.

Frank J (2009). Single-particle reconstruction of biological macromolecules in electron microscopy–30 years. *Q Rev Biophys* **42.3**, 139–58. doi: 10.1017/S0033583509990059.

Franken LE, Grünewald K, Boekema EJ & Stuart MCA (2020). A Technical Introduction to Transmission Electron Microscopy for Soft-Matter: Imaging, Possibilities, Choices, and Technical Developments. *Small* **16.14**, e1906198. doi: 10.1002/smll.201906198.

Fu B, Wang L, Li S & Dorf ME (2017). ZMPSTE24 defends against influenza and other pathogenic viruses. *J Exp Med* **214.4**, 919–929. doi: 10.1084/jem.20161270.

Fukuda Y, Laugks U, Lučić V, Baumeister W & Danev R (2015). Electron cryotomography of vitrified cells with a Volta phase plate. *J Struct Biol* **190.2**, 143–54. doi: 10.1016/j.jsb.2015.03.004.

Galaz-Montoya JG & Ludtke SJ (2017). The advent of structural biology in situ by single particle cryo-electron tomography. *Biophys Rep* **3.1**, 17–35. doi: 10.1007/s41048-017-0040-0.

Garcia NK, Guttman M, Ebner JL & Lee KK (2015). Dynamic changes during acid-induced activation of influenza hemagglutinin. *Structure* **23.4**, 665–76. doi: 10.1016/j.str.2015.02.006.

Garst EH, Lee H, Das T, Bhattacharya S, Percher A, Wiewiora R, Witte IP, Li Y, Peng T, Im W & Hang HC (2021). Site-Specific Lipidation Enhances IFITM3 Membrane Interactions and Antiviral Activity. *ACS Chem Biol* **16.5**, 844–856. doi: 10.1021/acschembio.1c00013.

Giard DJ, Aaronson SA, Todaro GJ, Arnstein P, Kersey JH, Dosik H & Parks WP (1973). In vitro cultivation of human tumors: establishment of cell lines derived from a series of solid tumors. *J Natl Cancer Inst* **51.5**, 1417–23. doi: 10.1093/jnci/51.5.1417.

Gilbert P (1972). Iterative methods for the three-dimensional reconstruction of an object from projections. *J Theor Biol* **36.1**, 105–17. doi: 10.1016/0022-5193(72)90180-4.

Gorelick S, Buckley G, Gervinskas G, Johnson TK, Handley A, Caggiano MP, Whisstock JC, Pocock R & Marco A de (2019). PIE-scope, integrated cryo-correlative light and FIB/SEM microscopy. *Elife* **8**. doi: 10.7554/eLife.45919.

Greiner W (2001). *Quantum Mechanics*. Springer Berlin Heidelberg. doi: 10.1007/978-3-642-56826-8.

Grimm R, Singh H, Rachel R, Typke D, Zillig W & Baumeister W (1998). Electron tomography of ice-embedded prokaryotic cells. *Biophys J* **74.2 Pt 1**, 1031–42. doi: 10.1016/S0006-3495(98)74028-7.

Gruenberg J (2020). Life in the lumen: The multivesicular endosome. *Traffic* **21.1**, 76–93. doi: 10.1111/tra.12715.

Gubbens A, Barfels M, Trevor C, Twesten R, Mooney P, Thomas P, Menon N, Kraus B, Mao C & McGinn B (2010). The GIF Quantum, a next generation post-column imaging energy filter. *Ultramicroscopy* **110.8**, 962–970. doi: https://doi.org/10.1016/j.ultramic.2010.01.009.

Gui L, Ebner JL, Mileant A, Williams JA & Lee KK (2016). Visualization and Sequencing of Membrane Remodeling Leading to Influenza Virus Fusion. *J Virol* **90.15**, 6948–6962. doi: 10.1128/JVI.00240-16.

Guilligay D, Tarendeau F, Resa-Infante P, Coloma R, Crepin T, Sehr P, Lewis J, Ruigrok RWH, Ortin J, Hart DJ & Cusack S (2008). The structural basis for cap binding by influenza virus polymerase subunit PB2. *Nat Struct Mol Biol* **15.5**, 500–6. doi: 10.1038/nsmb.1421.

Guillot L, Le Goffic R, Bloch S, Escriou N, Akira S, Chignard M & Si-Tahar M (2005). Involvement of toll-like receptor 3 in the immune response of lung epithelial cells to double-stranded RNA and influenza A virus. *J Biol Chem* **280.7**, 5571–80. doi: 10.1074/jbc.M410592200.

Guo X, Steinkühler J, Marin M, Li X, Lu W, Dimova R & Melikyan GB (2021). Interferon-Induced Transmembrane Protein 3 Blocks Fusion of Diverse Enveloped Viruses by Altering Mechanical Properties of Cell Membranes. *ACS Nano* **15.5**, 8155–8170. doi: 10.1021/acsnano.0c10567.

Hagen WJH, Wan W & Briggs JAG (2017). Implementation of a cryo-electron tomography tilt-scheme optimized for high resolution subtomogram averaging. *J Struct Biol* **197.2**, 191–198. doi: 10.1016/j.jsb.2016.06.007.

Hale BG, Randall RE, Ortín J & Jackson D (2008). The multifunctional NS1 protein of influenza A viruses. *J Gen Virol* **89.Pt 10**, 2359–2376. doi: 10.1099/vir.0.2008/004606-0.

Hao W, Wang L & Li S (2020). Roles of the Non-Structural Proteins of Influenza A Virus. *Pathogens* **9.10**. doi: 10.3390/pathogens9100812.

Harrison SC (2015). Viral membrane fusion. *Virology* **479-480**, 498–507. doi: 10.1016/j.virol.2015.03.043.

Hause BM, Collin EA, Liu R, Huang B, Sheng Z, Lu W, Wang D, Nelson EA & Li F (2014). Characterization of a novel influenza virus in cattle and Swine: proposal for a new genus in the Orthomyxoviridae family. *mBio* **5.2**, e00031–14. doi: 10.1128/mBio.00031-14.

Hause BM, Ducatez M, Collin EA, Ran Z, Liu R, Sheng Z, Armien A, Kaplan B, Chakravarty S, Hoppe AD, Webby RJ, Simonson RR & Li F (2013). Isolation of a novel swine influenza virus from Oklahoma in 2011 which is distantly related to human influenza C viruses. *PLoS Pathog* **9.2**, e1003176. doi: 10.1371/journal.ppat.1003176.

Heimowitz A, Andén J & Singer A (2020). Reducing bias and variance for CTF estimation in single particle cryo-EM. *Ultramicroscopy* **212**, 112950. doi: 10.1016/j.ultramic.2020.112950.

Hell SW & Wichmann J (1994). Breaking the diffraction resolution limit by stimulated emission: stimulated-emission-depletion fluorescence microscopy. *Opt Lett* **19.11**, 780–2. doi: 10.1364/ol.19.000780.

Hickford D, Frankenberg S, Shaw G & Renfree MB (2012). Evolution of vertebrate interferon inducible transmembrane proteins. *BMC Genomics* **13**, 155. doi: 10.1186/1471-2164-13-155.

Hoffmann E, Neumann G, Kawaoka Y, Hobom G & Webster RG (2000). A DNA transfection system for generation of influenza A virus from eight plasmids. *Proc Natl Acad Sci U S A* **97.11**, 6108–13. doi: 10.1073/pnas.100133697.

Hoffmann PC, Kreysing JP, Khusainov I, Tuijtel MW, Welsch S & Beck M (2022). Structures of the eukaryotic ribosome and its translational states in situ. *Nat Commun* **13.1**, 7435. doi: 10.1038/s41467-022-34997-w.

Huang IC, Bailey CC, Weyer JL, Radoshitzky SR, Becker MM, Chiang JJ, Brass AL, Ahmed AA, Chi X, Dong L, Longobardi LE, Boltz D, Kuhn JH, Elledge SJ, Bavari S, Denison MR, Choe H & Farzan M (2011). Distinct patterns of IFITM-mediated restriction of filoviruses, SARS coronavirus, and influenza A virus. *PLoS Pathog* **7.1**, e1001258. doi: 10.1371/journal.ppat.1001258.

Huotari J & Helenius A (2011). Endosome maturation. *EMBO J* **30.17**, 3481–500. doi: 10.1038/emboj.2011.286.

Iuliano AD *et al.* (2018). Estimates of global seasonal influenza-associated respiratory mortality: a modelling study. *Lancet* **391.10127**, 1285–1300. doi: 10.1016/S0140-6736(17)33293-2.

Jagger BW, Wise HM, Kash JC, Walters KA, Wills NM, Xiao YL, Dunfee RL, Schwartzman LM, Ozinsky A, Bell GL, Dalton RM, Lo A, Efstathiou S, Atkins JF, Firth AE, Taubenberger JK & Digard P (2012). An overlapping protein-coding region in influenza A virus segment 3 modulates the host response. *Science* **337.6091**, 199–204. doi: 10.1126/science.1222213.

Kato H, Sato S, Yoneyama M, Yamamoto M, Uematsu S, Matsui K, Tsujimura T, Takeda K, Fujita T, Takeuchi O & Akira S (2005). Cell type-specific involvement of RIG-I in antiviral response. *Immunity* **23.1**, 19–28. doi: 10.1016/j.immuni.2005.04.010.

Kielian M (2014). Mechanisms of Virus Membrane Fusion Proteins. *Annu Rev Virol* **1.1**, 171–89. doi: 10.1146/annurev-virology-031413-085521.

Kilbourne ED & Murphy JS (1960). Genetic studies of influenza viruses. I. Viral morphology and growth capacity as exchangeable genetic traits. Rapid in ovo adaptation of early passage Asian strain isolates by combination with PR8. *J Exp Med* **111**, 387–406. doi: 10.1084/jem.111.3.387.

Klein S, Golani G, Lolicato F, Lahr C, Beyer D, Herrmann A, Wachsmuth-Melm M, Reddmann N, Brecht R, Hosseinzadeh M, Kolovou A, Makroczyova J, Peterl S, Schorb M, Schwab Y, Brügger B, Nickel W, Schwarz US & Chlanda P (2023). IFITM3 blocks influenza virus entry by sorting lipids and stabilizing hemifusion. *Cell Host Microbe* **31.4**, 616–633.e20. doi: 10.1016/j.chom.2023.03.005.

Klein S, Wachsmuth-Melm M, Winter SL, Kolovou A & Chlanda P (2021). Cryo-correlative light and electron microscopy workflow for cryo-focused ion beam milled adherent cells. *Methods Cell Biol* **162**, 273–302. doi: 10.1016/bs.mcb.2020.12.009.

Klein S, Wimmer BH, Winter SL, Kolovou A, Laketa V & Chlanda P (2021). Post-correlation on-lamella cryo-CLEM reveals the membrane architecture of lamellar bodies. *Commun Biol* **4.1**, 137. doi: 10.1038/s42003-020-01567-z.

Kobayashi M, Toyoda T & Ishihama A (1996). Influenza virus PB1 protein is the minimal and essential subunit of RNA polymerase. *Arch Virol* **141.3-4**, 525–39. doi: 10.1007/BF01718315.

Kobayashi T, Beuchat MH, Chevallier J, Makino A, Mayran N, Escola JM, Lebrand C, Cosson P, Kobayashi T & Gruenberg J (2002). Separation and characterization of late endosomal membrane domains. *J Biol Chem* **277.35**, 32157–64. doi: 10.1074/jbc.M202838200.

Krammer F, Smith GJD, Fouchier RAM, Peiris M, Kedzierska K, Doherty PC, Palese P, Shaw ML, Treanor J, Webster RG & García-Sastre A (2018). Influenza. *Nat Rev Dis Primers* **4.1**, 3. doi: 10.1038/s41572-018-0002-y.

Kremer JR, Mastronarde DN & McIntosh JR (1996). Computer visualization of three-dimensional image data using IMOD. *J Struct Biol* **116.1**, 71–6. doi: 10.1006/jsbi.1996.0013.

Krischuns T, Lukarska M, Naffakh N & Cusack S (2021). Influenza Virus RNA-Dependent RNA Polymerase and the Host Transcriptional Apparatus. *Annu Rev Biochem* **90**, 321–348. doi: 10.1146/annurev-biochem-072820-100645.

Kühlbrandt W (2014). Biochemistry. The resolution revolution. *Science* **343.6178**, 1443–4. doi: 10.1126/science.1251652.

Kühnl A, Musiol A, Heitzig N, Johnson DE, Ehrhardt C, Grewal T, Gerke V, Ludwig S & Rescher U (2018). Late Endosomal/Lysosomal Cholesterol Accumulation Is a Host Cell-Protective Mechanism Inhibiting Endosomal Escape of Influenza A Virus. *mBio* **9.4**. doi: 10.1128/mBio.01345-18.

Kukulski W, Schorb M, Welsch S, Picco A, Kaksonen M & Briggs JAG (2011). Correlated fluorescence and 3D electron microscopy with high sensitivity and spatial precision. *J Cell Biol* **192.1**, 111–9. doi: 10.1083/jcb.201009037.

Kummer S, Avinoam O & Kräusslich HG (2019). IFITM3 Clusters on Virus Containing Endosomes and Lysosomes Early in the Influenza A Infection of Human Airway Epithelial Cells. *Viruses* **11.6**. doi: 10.3390/v11060548.

Lai AL & Freed JH (2015). The Interaction between Influenza HA Fusion Peptide and Transmembrane Domain Affects Membrane Structure. *Biophys J* **109.12**, 2523–2536. doi: 10.1016/j.bpj.2015.10.044.

Laustsen A, Sluis RM van der, Gris-Oliver A, Hernández SS, Cemalovic E, Tang HQ, Pedersen LH, Uldbjerg N, Jakobsen MR & Bak RO (2021). Ascorbic acid supports

ex vivo generation of plasmacytoid dendritic cells from circulating hematopoietic stem cells. *Elife* **10**. doi: 10.7554/eLife.65528.

Lazear HM, Schoggins JW & Diamond MS (2019). Shared and Distinct Functions of Type I and Type III Interferons. *Immunity* **50.4**, 907–923. doi: 10.1016/j.immuni.2019.03.025.

Lee KK (2010). Architecture of a nascent viral fusion pore. *EMBO J* **29.7**, 1299–311. doi: 10.1038/emboj.2010.13.

Lehtinen J, Munkberg J, Hasselgren J, Laine S, Karras T, Aittala M & Aila T (2018). "Noise2Noise: Learning Image Restoration without Clean Data". In: *Proceedings of the 35th International Conference on Machine Learning*. Ed. by J Dy & A Krause. Vol. 80. Proceedings of Machine Learning Research. PMLR, 2965–2974. url: https://proceedings.mlr.press/v80/lehtinen18a.html.

Lelek M, Gyparaki MT, Beliu G, Schueder F, Griffié J, Manley S, Jungmann R, Sauer M, Lakadamyali M & Zimmer C (2021). Single-molecule localization microscopy. *Nat Rev Methods Primers* **1**. doi: 10.1038/s43586-021-00038-x.

Li S, Wang Z, Jia X, Niu T, Zhang J, Yin G, Zhang X, Zhu Y, Ji G & Sun F (2023). ELI trifocal microscope: a precise system to prepare target cryo-lamellae for in situ cryo-ET study. *Nat Methods* **20.2**, 276–283. doi: 10.1038/s41592-022-01748-0.

Li W, Lu J, Xiao K, Zhou M, Li Y, Zhang X, Li Z, Gu L, Xu X, Guo Q, Xu T & Ji W (2023). Integrated multimodality microscope for accurate and efficient target-guided cryo-lamellae preparation. *Nat Methods* **20.2**, 268–275. doi: 10.1038/s41592-022-01749-z.

Li X, Mooney P, Zheng S, Booth CR, Braunfeld MB, Gubbens S, Agard DA & Cheng Y (2013). Electron counting and beam-induced motion correction enable near-atomic-resolution single-particle cryo-EM. *Nat Methods* **10.6**, 584–90. doi: 10.1038/nmeth.2472.

Li Y, Wei L, He L, Sun J & Liu N (2022). Interferon-induced transmembrane protein 3 gene polymorphisms are associated with COVID-19 susceptibility and severity: A meta-analysis. *J Infect* **84.6**, 825–833. doi: 10.1016/j.jinf.2022.04.029.

Liao Y, Goraya MU, Yuan X, Zhang B, Chiu SH & Chen JL (2019). Functional Involvement of Interferon-Inducible Transmembrane Proteins in Antiviral Immunity. *Front Microbiol* **10**, 1097. doi: 10.3389/fmicb.2019.01097.

Lindemann J, Lane CA & Hobson D (1963). The Resistance of A2G Mice to Myxoviruses. *J Immunol* **90.6**, 942–51.

Ling S, Zhang C, Wang W, Cai X, Yu L, Wu F, Zhang L & Tian C (2016). Combined approaches of EPR and NMR illustrate only one transmembrane helix in the human IFITM3. *Sci Rep* **6**, 24029. doi: 10.1038/srep24029.

Liu G, Park HS, Pyo HM, Liu Q & Zhou Y (2015). Influenza A Virus Panhandle Structure Is Directly Involved in RIG-I Activation and Interferon Induction. *J Virol* **89.11**, 6067–79. doi: 10.1128/JVI.00232-15.

Liu TT, Gomez TS, Sackey BK, Billadeau DD & Burd CG (2012). Rab GTPase regulation of retromer-mediated cargo export during endosome maturation. *Mol Biol Cell* **23.13**, 2505–15. doi: 10.1091/mbc.E11-11-0915.

Lozach PY, Mancini R, Bitto D, Meier R, Oestereich L, Overby AK, Pettersson RF & Helenius A (2010). Entry of bunyaviruses into mammalian cells. *Cell Host Microbe* **7.6**, 488–99. doi: 10.1016/j.chom.2010.05.007.

Lu J, Pan Q, Rong L, He W, Liu SL & Liang C (2011). The IFITM proteins inhibit HIV-1 infection. *J Virol* **85.5**, 2126–37. doi: 10.1128/JVI.01531-10.

Lucas BA & Grigorieff N (2023). Quantification of gallium cryo-FIB milling damage in biological lamellae. *Proc Natl Acad Sci U S A* **120.23**, e2301852120. doi: 10.1073/pnas.2301852120.

Lučič V, Rigort A & Baumeister W (2013). Cryo-electron tomography: the challenge of doing structural biology in situ. *J Cell Biol* **202.3**, 407–19. doi: 10.1083/jcb.201304193.

Lukhele S, Boukhaled GM & Brooks DG (2019). Type I interferon signaling, regulation and gene stimulation in chronic virus infection. *Semin Immunol* **43**, 101277. doi: 10.1016/j.smim.2019.05.001.

Mahamid J, Schampers R, Persoon H, Hyman AA, Baumeister W & Plitzko JM (2015). A focused ion beam milling and lift-out approach for site-specific preparation of frozen-hydrated lamellas from multicellular organisms. *J Struct Biol* **192.2**, 262–9. doi: 10.1016/j.jsb.2015.07.012.

Manders EMM, Verbeek FJ & Aten JA (1993). Measurement of co-localization of objects in dual-colour confocal images. *J Microsc* **169.3**, 375–382. doi: 10.1111/j.1365-2818.1993.tb03313.x.

Manzoor R, Igarashi M & Takada A (2017). Influenza A Virus M2 Protein: Roles from Ingress to Egress. *Int J Mol Sci* **18.12**. doi: 10.3390/ijms18122649.

Marko M, Hsieh C, Schalek R, Frank J & Mannella C (2007). Focused-ion-beam thinning of frozen-hydrated biological specimens for cryo-electron microscopy. *Nat Methods* **4.3**, 215–7. doi: 10.1038/nmeth1014.

Martens S & Howard J (2006). The interferon-inducible GTPases. *Annu Rev Cell Dev Biol* **22.1**, 559–89. doi: 10.1146/annurev.cellbio.22.010305.104619.

Mastronarde DN (2005). Automated electron microscope tomography using robust prediction of specimen movements. *J Struct Biol* **152.1**, 36–51. doi: 10.1016/j.jsb.2005.07.007.

Matlin KS, Reggio H, Helenius A & Simons K (1981). Infectious entry pathway of influenza virus in a canine kidney cell line. *J Cell Biol* **91.3**, 601–13. doi: 10.1083/jcb.91.3.601.

Matsuzaki Y, Katsushima N, Nagai Y, Shoji M, Itagaki T, Sakamoto M, Kitaoka S, Mizuta K & Nishimura H (2006). Clinical features of influenza C virus infection in children. *J Infect Dis* **193.9**, 1229–35. doi: 10.1086/502973.

Mazewski C, Perez RE, Fish EN & Platanias LC (2020). Type I Interferon (IFN)-Regulated Activation of Canonical and Non-Canonical Signaling Pathways. *Front Immunol* **11**, 606456. doi: 10.3389/fimmu.2020.606456.

McAuley JL, Gilbertson BP, Trifkovic S, Brown LE & McKimm-Breschkin JL (2019). Influenza Virus Neuraminidase Structure and Functions. *Front Microbiol* **10**, 39. doi: 10.3389/fmicb.2019.00039.

McDowall AW, Chang JJ, Freeman R, Lepault J, Walter CA & Dubochet J (1983). Electron microscopy of frozen hydrated sections of vitreous ice and vitrified biological samples. *J Microsc* **131.Pt 1**, 1–9. doi: 10.1111/j.1365-2818.1983.tb04225.x.

McMullan G, Chen S, Henderson R & Faruqi AR (2009). Detective quantum efficiency of electron area detectors in electron microscopy. *Ultramicroscopy* **109.9**, 1126–43. doi: 10.1016/j.ultramic.2009.04.002.

Moser F, Pražák V, Mordhorst V, Andrade DM, Baker LA, Hagen C, Grünewald K & Kaufmann R (2019). Cryo-SOFI enabling low-dose super-resolution correlative light and electron cryo-microscopy. *Proc Natl Acad Sci U S A* **116.11**, 4804–4809. doi: 10.1073/pnas.1810690116.

Mudhasani R, Tran JP, Retterer C, Radoshitzky SR, Kota KP, Altamura LA, Smith JM, Packard BZ, Kuhn JH, Costantino J, Garrison AR, Schmaljohn CS, Huang IC, Farzan M & Bavari S (2013). IFITM-2 and IFITM-3 but not IFITM-1 restrict Rift Valley fever virus. *J Virol* **87.15**, 8451–64. doi: 10.1128/JVI.03382-12.

Muramoto Y, Noda T, Kawakami E, Akkina R & Kawaoka Y (2013). Identification of novel influenza A virus proteins translated from PA mRNA. *J Virol* **87.5**, 2455–62. doi: 10.1128/JVI.02656-12.

Nakane T *et al.* (2020). Single-particle cryo-EM at atomic resolution. *Nature* **587.7832**, 152–156. doi: 10.1038/s41586-020-2829-0.

Narayana SK, Helbig KJ, McCartney EM, Eyre NS, Bull RA, Eltahla A, Lloyd AR & Beard MR (2015). The Interferon-induced Transmembrane Proteins, IFITM1, IFITM2, and IFITM3 Inhibit Hepatitis C Virus Entry. *J Biol Chem* **290.43**, 25946–59. doi: 10.1074/jbc.M115.657346.

Nikoloudis D, Kountouras D & Hiona A (2020). The frequency of combined IFITM3 haplotype involving the reference alleles of both rs12252 and rs34481144 is in line with COVID-19 standardized mortality ratio of ethnic groups in England. *PeerJ* **8**, e10402. doi: 10.7717/peerj.10402.

O'Neill RE, Talon J & Palese P (1998). The influenza virus NEP (NS2 protein) mediates the nuclear export of viral ribonucleoproteins. *EMBO J* **17.1**, 288–96. doi: 10.1093/emboj/17.1.288.

Odon V, Fros JJ, Goonawardane N, Dietrich I, Ibrahim A, Alshaikhahmed K, Nguyen D & Simmonds P (2019). The role of ZAP and OAS3/RNAseL pathways in the attenuation of an RNA virus with elevated frequencies of CpG and UpA dinucleotides. *Nucleic Acids Res* **47.15**, 8061–8083. doi: 10.1093/nar/gkz581.

Ohkuma S & Poole B (1978). Fluorescence probe measurement of the intralysosomal pH in living cells and the perturbation of pH by various agents. *Proc Natl Acad Sci U S A* **75.7**, 3327–31. doi: 10.1073/pnas.75.7.3327.

Orlova EV & Saibil HR (2011). Structural analysis of macromolecular assemblies by electron microscopy. *Chem Rev* **111.12**, 7710–48. doi: 10.1021/cr100353t.

Palese P, Tumpey TM & Garcia-Sastre A (2006). What can we learn from reconstructing the extinct 1918 pandemic influenza virus?. *Immunity* **24.2**, 121–4. doi: 10.1016/j.immuni.2006.01.007.

Patterson S & Bingham RW (1976). Electron microscope observations on the entry of avian infectious bronchitis virus into susceptible cells. *Arch Virol* **52.3**, 191–200. doi: 10.1007/BF01348016.

Paul-Gilloteaux P, Heiligenstein X, Belle M, Domart MC, Larijani B, Collinson L, Raposo G & Salamero J (2017). eC-CLEM: flexible multidimensional registration software for correlative microscopies. *Nat Methods* **14.2**, 102–103. doi: 10.1038/nmeth.4170.

Penczek PA (2010). Image restoration in cryo-electron microscopy. *Methods Enzymol* **482**, 35–72. doi: 10.1016/S0076-6879(10)82002-6.

Perkins LEL & Swayne DE (2002). Pathogenicity of a Hong Kong-origin H5N1 highly pathogenic avian influenza virus for emus, geese, ducks, and pigeons. *Avian Dis* **46.1**, 53–63. doi: 10.1637/0005-2086(2002)046[0053:POAHKO]2.0.CO;2.

Perrin P, Janssen L, Janssen H, Broek B van den, Voortman LM, Elsland D van, Berlin I & Neefjes J (2021). Retrofusion of intralumenal MVB membranes parallels viral infection and coexists with exosome release. *Curr Biol* **31.17**, 3884–3893.e4. doi: 10.1016/j.cub.2021.06.022.

Peukes J, Xiong X, Erlendsson S, Qu K, Wan W, Calder LJ, Schraidt O, Kummer S, Freund SMV, Kräusslich HG & Briggs JAG (2020). The native structure of the assembled matrix protein 1 of influenza A virus. *Nature* **587.7834**, 495–498. doi: 10.1038/s41586-020-2696-8.

Phillips MA, Harkiolaki M, Susano Pinto DM, Parton RM, Palanca A, Garcia-Moreno M, Kounatidis I, Sedat JW, Stuart DI, Castello A, Booth MJ, Davis I & Dobbie IM (2020). CryoSIM: super-resolution 3D structured illumination cryogenic fluorescence microscopy for correlated ultrastructural imaging. *Optica* **7.7**, 802–812. doi: 10.1364/OPTICA.393203.

Pichlmair A, Schulz O, Tan CP, Näslund TI, Liljeström P, Weber F & Reis e Sousa C (2006). RIG-I-mediated antiviral responses to single-stranded RNA bearing 5'-phosphates. *Science* **314.5801**, 997–1001. doi: 10.1126/science.1132998.

Platanias LC (2005). Mechanisms of type-I- and type-II-interferon-mediated signalling. *Nat Rev Immunol* **5.5**, 375–86. doi: 10.1038/nri1604.

Plotch SJ, Tomasz J & Krug RM (1978). Absence of detectable capping and methylating enzymes in influenza virions. *J Virol* **28.1**, 75–83. doi: 10.1128/JVI.28.1.75-83.1978.

Poon LL, Pritlove DC, Fodor E & Brownlee GG (1999). Direct evidence that the poly(A) tail of influenza A virus mRNA is synthesized by reiterative copying of a U track in the virion RNA template. *J Virol* **73.4**, 3473–6. doi: 10.1128/JVI.73.4.3473-3476.1999.

Radermacher M (1992). Weighted Back-Projection Methods, 91–115. doi: 10.1007/978-1-4757-2163-8_5.

Rahman K, Coomer CA, Majdoul S, Ding SY, Padilla-Parra S & Compton AA (2020). Homology-guided identification of a conserved motif linking the antiviral functions of IFITM3 to its oligomeric state. *Elife* **9**. doi: 10.7554/eLife.58537.

Rahman K, Datta SAK, Beaven AH, Jolley AA, Sodt AJ & Compton AA (2022). Cholesterol binds the amphipathic helix of IFITM3 and regulates antiviral activity. *J Mol Biol*, 167759. doi: 10.1016/j.jmb.2022.167759.

Rand R & Parsegian V (1989). Hydration forces between phospholipid bilayers. *Biochimica et Biophysica Acta (BBA) - Reviews on Biomembranes* **988.3**, 351–376. doi: https://doi.org/10.1016/0304-4157(89)90010-5.

Reikine S, Nguyen JB & Modis Y (2014). Pattern Recognition and Signaling Mechanisms of RIG-I and MDA5. *Front Immunol* **5**, 342. doi: 10.3389/fimmu.2014.00342.

Rejman J, Oberle V, Zuhorn IS & Hoekstra D (2004). Size-dependent internalization of particles via the pathways of clathrin- and caveolae-mediated endocytosis. *Biochem J* **377.Pt 1**, 159–69. doi: 10.1042/BJ20031253.

Rice G, Wagner T, Stabrin M, Sitsel O, Prumbaum D & Raunser S (2023). TomoTwin: generalized 3D localization of macromolecules in cryo-electron tomograms with structural data mining. *Nat Methods* **20.6**, 871–880. doi: 10.1038/s41592-023-01878-z.

Rigort A, Bäuerlein FJB, Villa E, Eibauer M, Laugks T, Baumeister W & Plitzko JM (2012). Focused ion beam micromachining of eukaryotic cells for cryoelectron tomography. *Proc Natl Acad Sci U S A* **109.12**, 4449–54. doi: 10.1073/pnas.1201333109.

Risselada HJ & Grubmüller H (2021). How proteins open fusion pores: insights from molecular simulations. *Eur Biophys J* **50.2**, 279–293. doi: 10.1007/s00249-020-01484-3.

Rivera-Serrano EE, Gizzi AS, Arnold JJ, Grove TL, Almo SC & Cameron CE (2020). Viperin Reveals Its True Function. *Annu Rev Virol* **7.1**, 421–446. doi: 10.1146/annurev-virology-011720-095930.

Rossman JS, Jing X, Leser GP & Lamb RA (2010). Influenza virus M2 protein mediates ESCRT-independent membrane scission. *Cell* **142.6**, 902–13. doi: 10.1016/j.cell.2010.08.029.

Rossman JS & Lamb RA (2011). Influenza virus assembly and budding. *Virology* **411.2**, 229–36. doi: 10.1016/j.virol.2010.12.003.

Roux A, Uyhazi K, Frost A & De Camilli P (2006). GTP-dependent twisting of dynamin implicates constriction and tension in membrane fission. *Nature* **441.7092**, 528–31. doi: 10.1038/nature04718.

Sällman Almén M, Bringeland N, Fredriksson R & Schiöth HB (2012). The dispanins: a novel gene family of ancient origin that contains 14 human members. *PLoS One* **7.2**, e31961. doi: 10.1371/journal.pone.0031961.

Schauer R (2000). Achievements and challenges of sialic acid research. *Glycoconj J* **17.7-9**, 485–99. doi: 10.1023/a:1011062223612.

Schindelin J, Arganda-Carreras I, Frise E, Kaynig V, Longair M, Pietzsch T, Preibisch S, Rueden C, Saalfeld S, Schmid B, Tinevez JY, White DJ, Hartenstein V, Eliceiri K, Tomancak P & Cardona A (2012). Fiji: an open-source platform for biological-image analysis. *Nat Methods* **9.7**, 676–82. doi: 10.1038/nmeth.2019.

Schmidt R, Weihs T, Wurm CA, Jansen I, Rehman J, Sahl SJ & Hell SW (2021). MINFLUX nanometer-scale 3D imaging and microsecond-range tracking on a common fluorescence microscope. *Nat Commun* **12.1**, 1478. doi: 10.1038/s41467-021-21652-z.

Schmidt U, Weigert M, Broaddus C & Myers G (2018). "Cell Detection with Star-Convex Polygons". In: *Medical Image Computing and Computer Assisted Intervention – MICCAI 2018*. Ed. by AF Frangi, JA Schnabel, C Davatzikos, C Alberola-López & G Fichtinger. Cham: Springer International Publishing, 265–273.

Schoch CL, Ciufo S, Domrachev M, Hotton CL, Kannan S, Khovanskaya R, Leipe D, Mcveigh R, O'Neill K, Robbertse B, Sharma S, Soussov V, Sullivan JP, Sun L, Turner S & Karsch-Mizrachi I (2020). NCBI Taxonomy: a comprehensive update on curation, resources and tools. *Database (Oxford)* **2020**. doi: 10.1093/database/baaa062.

Schoggins JW (2019). Interferon-Stimulated Genes: What Do They All Do?. *Annu Rev Virol* **6.1**, 567–584. doi: 10.1146/annurev-virology-092818-015756.

Schorb M, Gaechter L, Avinoam O, Sieckmann F, Clarke M, Bebeacua C, Bykov YS, Sonnen AFP, Lihl R & Briggs JAG (2017). New hardware and workflows for semi-automated correlative cryo-fluorescence and cryo-electron microscopy/tomography. *J Struct Biol* **197.2**, 83–93. doi: 10.1016/j.jsb.2016.06.020.

Schorb M & Sieckmann F (2017). Matrix MAPS-an intuitive software to acquire, analyze, and annotate light microscopy data for CLEM. *Methods Cell Biol* **140**, 321–333. doi: 10.1016/bs.mcb.2017.03.012.

Scientific Volume Imaging (2023). *Microscopy Nyquist Rate and PSF Calculator*. url: https://svi.nl/NyquistCalculator (visited on 2023).

Seaman MNJ, Harbour ME, Tattersall D, Read E & Bright N (2009). Membrane recruitment of the cargo-selective retromer subcomplex is catalysed by the small GTPase Rab7 and inhibited by the Rab-GAP TBC1D5. *J Cell Sci* **122.Pt 14**, 2371–82. doi: 10.1242/jcs.048686.

Sellers SA, Hagan RS, Hayden FG & Fischer 2nd WA (2017). The hidden burden of influenza: A review of the extra-pulmonary complications of influenza infection. *Influenza Other Respir Viruses* **11.5**, 372–393. doi: 10.1111/irv.12470.

Selman M, Dankar SK, Forbes NE, Jia JJ & Brown EG (2012). Adaptive mutation in influenza A virus non-structural gene is linked to host switching and induces a novel protein by alternative splicing. *Emerg Microbes Infect* **1.11**, e42. doi: 10.1038/emi.2012.38.

Shmulevitz M & Duncan R (2000). A new class of fusion-associated small transmembrane (FAST) proteins encoded by the non-enveloped fusogenic reoviruses. *EMBO J* **19.5**, 902–12. doi: 10.1093/emboj/19.5.902.

Skehel JJ, Bayley PM, Brown EB, Martin SR, Waterfield MD, White JM, Wilson IA & Wiley DC (1982). Changes in the conformation of influenza virus hemagglutinin at the pH optimum of virus-mediated membrane fusion. *Proc Natl Acad Sci U S A* **79.4**, 968–72. doi: 10.1073/pnas.79.4.968.

Skehel JJ & Wiley DC (2000). Receptor binding and membrane fusion in virus entry: the influenza hemagglutinin. *Annu Rev Biochem* **69**, 531–69. doi: 10.1146/annurev.biochem.69.1.531.

Smeets M, Bieber A, Capitanio C, Schioetz O, Heijden T van der, Effting A, Piel É, Lazem B, Erdmann P & Plitzko J (2021). Integrated Cryo-Correlative Microscopy for Targeted Structural Investigation In Situ. *Microscopy Today* **29.6**, 20–25. doi: 10.1017/S1551929521001280.

Smith SE, Busse DC, Binter S, Weston S, Diaz Soria C, Laksono BM, Clare S, Van Nieuwkoop S, Van den Hoogen BG, Clement M, Marsden M, Humphreys IR, Marsh M, Swart RL de, Wash RS, Tregoning JS & Kellam P (2019). Interferon-Induced Transmembrane Protein 1 Restricts Replication of Viruses That Enter Cells via the Plasma Membrane. *J Virol* **93.6**. doi: 10.1128/JVI.02003-18.

Smith W, Andrewes C & Laidlaw P (1933). A virus obtained from influenza patients. *The Lancet* **222.5732**. Originally published as Volume 2, Issue 5732, 66–68. doi: https://doi.org/10.1016/S0140-6736(00)78541-2.

Stauffer S, Feng Y, Nebioglu F, Heilig R, Picotti P & Helenius A (2014). Stepwise priming by acidic pH and a high K+ concentration is required for efficient uncoating of influenza A virus cores after penetration. *J Virol* **88.22**, 13029–46. doi: 10.1128/JVI.01430-14.

Stegmann T, Delfino JM, Richards FM & Helenius A (1991). The HA2 subunit of influenza hemagglutinin inserts into the target membrane prior to fusion. *J Biol Chem* **266.27**, 18404–10.

Stencel-Baerenwald JE, Reiss K, Reiter DM, Stehle T & Dermody TS (2014). The sweet spot: defining virus-sialic acid interactions. *Nat Rev Microbiol* **12.11**, 739–49. doi: 10.1038/nrmicro3346.

Sternberg (1983). Biomedical Image Processing. *Computer* **16.1**, 22–34. doi: 10.1109/MC.1983.1654163.

Studer D, Humbel BM & Chiquet M (2008). Electron microscopy of high pressure frozen samples: bridging the gap between cellular ultrastructure and atomic resolution. *Histochem Cell Biol* **130.5**, 877–89. doi: 10.1007/s00418-008-0500-1.

Sugrue RJ, Belshe RB & Hay AJ (1990). Palmitoylation of the influenza A virus M2 protein. *Virology* **179.1**, 51–6. doi: 10.1016/0042-6822(90)90272-s.

Takeuchi O & Akira S (2010). Pattern recognition receptors and inflammation. *Cell* **140.6**, 805–20. doi: 10.1016/j.cell.2010.01.022.

Tau G & Rothman P (1999). Biologic functions of the IFN-gamma receptors. *Allergy* **54.12**, 1233–51. doi: 10.1034/j.1398-9995.1999.00099.x.

Teissier E & Pécheur EI (2007). Lipids as modulators of membrane fusion mediated by viral fusion proteins. *Eur Biophys J* **36.8**, 887–99. doi: 10.1007/s00249-007-0201-z.

Teresa-Trueba I de, Goetz SK, Mattausch A, Stojanovska F, Zimmerli CE, Toro-Nahuelpan M, Cheng DWC, Tollervey F, Pape C, Beck M, Diz-Muñoz A, Kreshuk A, Mahamid J & Zaugg JB (2023). Convolutional networks for supervised mining of molecular patterns within cellular context. *Nat Methods* **20.2**, 284–294. doi: 10.1038/s41592-022-01746-2.

ThermoFisher Scientific (2021). *Datasheet iFLM Correlative System*. url: https://assets.thermofisher.com/TFS-Assets/MSD/Datasheets/iflm-aquilos-datasheet-ds0366.pdf.

– (2022). *Datasheet Arctis Cryo-Plasma FIB*. url: https://assets.thermofisher.com/TFS-Assets/MSD/Datasheets/arctis-cryo-plasma-fib-ds0384-en.pdf.

Thinon E, Fernandez JP, Molina H & Hang HC (2018). Selective Enrichment and Direct Analysis of Protein S-Palmitoylation Sites. *J Proteome Res* **17.5**, 1907–1922. doi: 10.1021/acs.jproteome.8b00002.

Thompson WW, Shay DK, Weintraub E, Brammer L, Bridges CB, Cox NJ & Fukuda K (2004). Influenza-associated hospitalizations in the United States. *JAMA* **292.11**, 1333–40. doi: 10.1001/jama.292.11.1333.

Thon F (1966). Zur Defokussierungsabhängigkeit des Phasenkontrastes bei der elektronenmikroskopischen Abbildung. *Zeitschrift für Naturforschung A* **21.4**, 476–478. doi: 10.1515/zna-1966-0417.

Tong S *et al.* (2013). New world bats harbor diverse influenza A viruses. *PLoS Pathog* **9.10**, e1003657. doi: 10.1371/journal.ppat.1003657.

Tran V, Moser LA, Poole DS & Mehle A (2013). Highly sensitive real-time in vivo imaging of an influenza reporter virus reveals dynamics of replication and spread. *J Virol* **87.24**, 13321–9. doi: 10.1128/JVI.02381-13.

Tscherne DM, Manicassamy B & García-Sastre A (2010). An enzymatic virus-like particle assay for sensitive detection of virus entry. *J Virol Methods* **163.2**, 336–43. doi: 10.1016/j.jviromet.2009.10.020.

Tuijtel MW, Koster AJ, Jakobs S, Faas FGA & Sharp TH (2019). Correlative cryo super-resolution light and electron microscopy on mammalian cells using fluorescent proteins. *Sci Rep* **9.1**, 1369. doi: 10.1038/s41598-018-37728-8.

Turoňová B, Hagen WJH, Obr M, Mosalaganti S, Beugelink JW, Zimmerli CE, Kräusslich HG & Beck M (2020). Benchmarking tomographic acquisition schemes for high-resolution structural biology. *Nat Commun* **11.1**, 876. doi: 10.1038/s41467-020-14535-2.

Turoňová B, Schur FKM, Wan W & Briggs JAG (2017). Efficient 3D-CTF correction for cryo-electron tomography using NovaCTF improves subtomogram averaging resolution to 3.4Å. *J Struct Biol* **199.3**, 187–195. doi: 10.1016/j.jsb.2017.07.007.

Vale-Costa S & Amorim MJ (2017). Clustering of Rab11 vesicles in influenza A virus infected cells creates hotspots containing the 8 viral ribonucleoproteins. *Small GTPases* **8.2**, 71–77. doi: 10.1080/21541248.2016.1199190.

Van Kerkhove MD *et al.* (2011). Risk factors for severe outcomes following 2009 influenza A (H1N1) infection: a global pooled analysis. *PLoS Med* **8.7**, e1001053. doi: 10.1371/journal.pmed.1001053.

Veit M & Schmidt MF (1993). Timing of palmitoylation of influenza virus hemagglutinin. *FEBS Lett* **336.2**, 243–7. doi: 10.1016/0014-5793(93)80812-9.

Villalón-Letelier F, Brooks AG, Saunders PM, Londrigan SL & Reading PC (2017). Host Cell Restriction Factors that Limit Influenza A Infection. *Viruses* **9.12**. doi: 10.3390/v9120376.

Vries E de, Tscherne DM, Wienholts MJ, Cobos-Jiménez V, Scholte F, García-Sastre A, Rottier PJM & Haan CAM de (2011). Dissection of the influenza A virus endocytic routes reveals macropinocytosis as an alternative entry pathway. *PLoS Pathog* **7.3**, e1001329. doi: 10.1371/journal.ppat.1001329.

Wade R (1992). A brief look at imaging and contrast transfer. *Ultramicroscopy* **46.1**, 145–156. doi: https://doi.org/10.1016/0304-3991(92)90011-8.

Wagner FR, Watanabe R, Schampers R, Singh D, Persoon H, Schaffer M, Fruhstorfer P, Plitzko J & Villa E (2020). Preparing samples from whole cells using focused-ion-beam milling for cryo-electron tomography. *Nat Protoc* **15.6**, 2041–2070. doi: 10.1038/s41596-020-0320-x.

Wang X, Hinson ER & Cresswell P (2007). The interferon-inducible protein viperin inhibits influenza virus release by perturbing lipid rafts. *Cell Host Microbe* **2.2**, 96–105. doi: 10.1016/j.chom.2007.06.009.

Webster RG, Bean WJ, Gorman OT, Chambers TM & Kawaoka Y (1992). Evolution and ecology of influenza A viruses. *Microbiol Rev* **56.1**, 152–79. doi: 10.1128/mr.56.1.152-179.1992.

Wee YS, Roundy KM, Weis JJ & Weis JH (2012). Interferon-inducible transmembrane proteins of the innate immune response act as membrane organizers by influencing clathrin and v-ATPase localization and function. *Innate Immun* **18.6**, 834–45. doi: 10.1177/1753425912443392.

Weston S, Czieso S, White IJ, Smith SE, Wash RS, Diaz-Soria C, Kellam P & Marsh M (2016). Alphavirus Restriction by IFITM Proteins. *Traffic* **17.9**, 997–1013. doi: 10.1111/tra.12416.

White JM & Whittaker GR (2016). Fusion of Enveloped Viruses in Endosomes. *Traffic* **17.6**, 593–614. doi: 10.1111/tra.12389.

Williams DB & Carter CB (1996). *Transmission Electron Microscopy - A Textbook for Materials Science*. Springer US. doi: 10.1007/978-1-4757-2519-3.

Wise HM, Foeglein A, Sun J, Dalton RM, Patel S, Howard W, Anderson EC, Barclay WS & Digard P (2009). A complicated message: Identification of a novel PB1-related protein translated from influenza A virus segment 2 mRNA. *J Virol* **83.16**, 8021–31. doi: 10.1128/JVI.00826-09.

Wise HM, Hutchinson EC, Jagger BW, Stuart AD, Kang ZH, Robb N, Schwartzman LM, Kash JC, Fodor E, Firth AE, Gog JR, Taubenberger JK & Digard P (2012). Identification of a novel splice variant form of the influenza A virus M2 ion channel with an antigenically distinct ectodomain. *PLoS Pathog* **8.11**, e1002998. doi: 10.1371/journal.ppat.1002998.

Wolff G, Limpens RWAL, Zheng S, Snijder EJ, Agard DA, Koster AJ & Bárcena M (2019). Mind the gap: Micro-expansion joints drastically decrease the bending of FIB-milled cryo-lamellae. *J Struct Biol* **208.3**, 107389. doi: 10.1016/j.jsb.2019.09.006.

Xiao H, Killip MJ, Staeheli P, Randall RE & Jackson D (2013). The human interferon-induced MxA protein inhibits early stages of influenza A virus infection by retaining the incoming viral genome in the cytoplasm. *J Virol* **87.23**, 13053–8. doi: 10.1128/JVI.02220-13.

Xiong Q, Morphew MK, Schwartz CL, Hoenger AH & Mastronarde DN (2009). CTF determination and correction for low dose tomographic tilt series. *J Struct Biol* **168.3**, 378–87. doi: 10.1016/j.jsb.2009.08.016.

Xue L, Lenz S, Zimmermann-Kogadeeva M, Tegunov D, Cramer P, Bork P, Rappsilber J & Mahamid J (2022). Visualizing translation dynamics at atomic detail inside a bacterial cell. *Nature* **610.7930**, 205–211. doi: 10.1038/s41586-022-05255-2.

Yamada S *et al.* (2006). Haemagglutinin mutations responsible for the binding of H5N1 influenza A viruses to human-type receptors. *Nature* **444.7117**, 378–82. doi: 10.1038/nature05264.

Yamayoshi S, Watanabe M, Goto H & Kawaoka Y (2016). Identification of a Novel Viral Protein Expressed from the PB2 Segment of Influenza A Virus. *J Virol* **90.1**, 444–56. doi: 10.1128/JVI.02175-15.

Yánez DC, Ross S & Crompton T (2020). The IFITM protein family in adaptive immunity. *Immunology* **159.4**, 365–372. doi: 10.1111/imm.13163.

Yip KM, Fischer N, Paknia E, Chari A & Stark H (2020). Atomic-resolution protein structure determination by cryo-EM. *Nature* **587.7832**, 157–161. doi: 10.1038/s41586-020-2833-4.

Yount JS, Moltedo B, Yang YY, Charron G, Moran TM, López CB & Hang HC (2010). Palmitoylome profiling reveals S-palmitoylation-dependent antiviral activity of IFITM3. *Nat Chem Biol* **6.8**, 610–4. doi: 10.1038/nchembio.405.

Zachs T, Schertel A, Medeiros J, Weiss GL, Hugener J, Matos J & Pilhofer M (2020). Fully automated, sequential focused ion beam milling for cryo-electron tomography. *Elife* **9**. doi: 10.7554/eLife.52286.

Zanetti G, Riches JD, Fuller SD & Briggs JAG (2009). Contrast transfer function correction applied to cryo-electron tomography and sub-tomogram averaging. *J Struct Biol* **168.2**, 305–12. doi: 10.1016/j.jsb.2009.08.002.

Zani A & Yount JS (2018). Antiviral Protection by IFITM3 In Vivo. *Curr Clin Microbiol Rep* **5.4**, 229–237. doi: 10.1007/s40588-018-0103-0.

Zaraket H, Hurt AC, Clinch B, Barr I & Lee N (2021). Burden of influenza B virus infection and considerations for clinical management. *Antiviral Res* **185**, 104970. doi: 10.1016/j.antiviral.2020.104970.

Zhao Y, Fu C, Zhang W, Ye C, Wang Z & Ma HF (2022). Automatic Segmentation of Cervical Cells Based on Star-Convex Polygons in Pap Smear Images. *Bioengineering (Basel)* **10.1**. doi: 10.3390/bioengineering10010047.

Zheng SQ, Palovcak E, Armache JP, Verba KA, Cheng Y & Agard DA (2017). MotionCor2: anisotropic correction of beam-induced motion for improved cryo-electron microscopy. *Nat Methods* **14.4**, 331–332. doi: 10.1038/nmeth.4193.

Zhou Y, Wu C, Zhao L & Huang N (2014). Exploring the early stages of the pH-induced conformational change of influenza hemagglutinin. *Proteins* **82.10**, 2412–28. doi: 10.1002/prot.24606.

Zhu H, Cong JP & Shenk T (1997). Use of differential display analysis to assess the effect of human cytomegalovirus infection on the accumulation of cellular RNAs: induction of interferon-responsive RNAs. *Proc Natl Acad Sci U S A* **94.25**, 13985–90. doi: 10.1073/pnas.94.25.13985.

Zimmermann P, Mänz B, Haller O, Schwemmle M & Kochs G (2011). The viral nucleoprotein determines Mx sensitivity of influenza A viruses. *J Virol* **85.16**, 8133–40. doi: 10.1128/JVI.00712-11.

Zivanov J, Otón J, Ke Z, Kügelgen A von, Pyle E, Qu K, Morado D, Castaño-Díez D, Zanetti G, Bharat TAM, Briggs JAG & Scheres SHW (2022). A Bayesian approach to single-particle electron cryo-tomography in RELION-4.0. *Elife* **11**. doi: 10.7554/eLife.83724.

Appendix I: Viral RNA extraction for high-throughput diagnostics to detect SARS-CoV-2 infection

This study was conducted during the SARS-CoV-2 pandemic in 2019. During this time, I supported the Center of Infectious Diseases diagnostic department at the University Clinics of Heidelberg. This study presents a magnetic bead RNA extraction protocol that is based on in-house made reagents and is performed in 96-well plates supporting large-scale testing against SARS-CoV-2 infection. The protocol was benchmarked against the commercial QIAcube extraction platform and showed comparable viral RNA detection sensitivity and specificity when combined with various detection methods at high throughput. This method is an alternative to commercial RNA extraction kits, which may be limited due to the large demand for testing during the pandemic. The standard diagnostic pipeline for testing SARS-CoV-2 presence in patients with an ongoing infection is predominantly based on pharyngeal swabs. The viral RNA is extracted using commercial kits, followed by reverse transcription and quantitative PCR detection. The magnetic bead RNA extraction protocol presented in this publication provides a solution to the potential shortage of commercial RNA extraction kits. It can be quickly set up in a laboratory without access to an automated pipetting robot. It was demonstrated that this method could be used to process nasopharyngeal swab samples and yields RT-qPCR results comparable to those obtained with commercial kits. It was also shown that the RNA extraction protocol could be combined with fluorescent and colorimetric reverse transcription loop-mediated isothermal amplification (RT-LAMP) using a primer set targeting the N gene, as well as RT-qPCR using a primer set targeting the E gene.

Overall, this publication presents a valuable alternative to commercial RNA extraction kits for large-scale testing of SARS-CoV-2 presence in patients with an ongoing infection.

This study was published in: **Klein S**, Müller TG, Khalid D, Sonntag-Buck V, Heuser AM, Glass B, Meurer M, Morales I, Schillak A, Freistaedter A, Ambiel I, Winter SL, Zimmermann L, Naumoska T, Bubeck F, Kirrmaier D, Ullrich S, Barreto Miranda I, Anders S, Grimm D, Schnitzler P, Knop M, Kräusslich HG, Dao Thi VL, Börner K & Chlanda P (2020). SARS-CoV-2 RNA Extraction Using Magnetic Beads for Rapid Large-Scale Testing by RT-qPCR and RT-LAMP. *Viruses* **12.8**. DOI: 10.3390/v12080863.

Appendix II: SARS-CoV-2 structure and replication characterized by *in situ* cryo-ET

This study was also conducted during the SARS-CoV-2 pandemic in 2019. Prof. Dr. Christian Drosten (Institute of Virology, Charité Berlin) isolated SARS-CoV-2 from patient samples and provided samples to the Center of Infectious Diseases diagnostic department at the University Clinics of Heidelberg. This allowed me to structurally characterize the viral replication cycle in human A549 cells using state-of-the-art *in situ* cryo-ET. I was able to characterize different stages of the viral replication cycle and gained insights into the budding mechanism of the virus and the structure of extracellular virions. I directly visualized RNA filaments inside double-membrane vesicles, which are compartments associated with viral replication. These RNA filaments showed a diameter consistent with double-stranded RNA and frequent branching, likely representing RNA secondary structures. I further characterized viral assembly at the endoplasmic reticulum – Golgi intermediate compartment (ERGIC) membrane, with viral spike proteins found on the luminal side and vRNPs found accumulated on the cytosolic site of curved membranes, indicating that vRNP recruitment is enhanced by membrane curvature. Subtomogram averaging revealed that vRNPs are distinct cylindrical assemblies. Thus, we propose that the SARS-CoV-2 genome is packaged around multiple separate vRNP complexes, allowing for the incorporation of the unusually large coronavirus genome into the virion while maintaining high steric flexibility between the vRNPs.

In summary, this publication provides valuable insights into the structure and replication of SARS-CoV-2.

This study was published in: **Klein S**, Cortese M, Winter SL, Wachsmuth-Melm M, Neufeldt CJ, Cerikan B, Stanifer ML, Boulant S, Bartenschlager R & Chlanda P (2020). SARS-CoV-2 structure and replication characterized by *in situ* cryo-electron tomography. *Nat Commun* **11.1**, 5885. DOI: 10.1038/s41467-020-19619-7